Department of
Electronic and
Electrical
Engineering.

A grid-tied large-scale battery energy storage system: modelling from the pack level to the cell level

Zeyuan Wang

May 2022

Supervisors: Prof. Martin Foster and Dr Jonathan Davidson

Thesis submitted in partial fulfilment of the requirements for the degree of Doctor of Philosophy

Abstract

As civilization enters the twenty-first century, the ideal of sustainable development is being accepted by more and more countries in the world. The most influential countries on this planet, including the UK, are negotiating and cooperating in the 26th United Nations Climate Change conference (COP26) to achieve the zero-carbon goal by the middle of this century.

To achieve sustainable development, renewable energy sources are being widely introduced into the electricity grid which demands extra energy storage systems, such as batteries, to reduce the grid instability caused by them. In the meantime, electric vehicles are being promoted to replace traditional hydrocarbon-burning vehicles which further increases battery demand. All these ongoing changes are indicators of the importance of battery energy storage systems (BESSs) as an integral component of the technologies of the future.

To support these changes, this thesis reports on work which tackles an important aspect of battery-energy storage: the modelling and electrical properties of a large battery pack. The work focusses on grid-tied packs but the work is equally applicable to transport applications. The thesis describes the development of a simulator tool for large-scale BESSs which is able to simulate BESSs at pack level and cell level. With the University of Sheffield's grid-tied battery research platform, the *Willenhall Energy Storage System* (WESS), as an example, the study starts with the modelling of the large-scale BESS at pack level which provides three sets of equivalent circuit parameters for two different equivalent circuit models. These models are extracted directly from a large-scale BESS which provides high fidelity and can be used for the system-level modelling such as system design and investment evaluation.

The study of large-scale BESS modelling is then extended to cell level, where an efficient software tool for cell-level simulation is proposed. Cell-level simulations considering the cell-to-cell variation are conducted and the simulation and experimental results reveal some important properties of large-scale BESSs that are related to the cell voltage deviation. The findings in this section improve the understanding of the practically observed battery pack behaviour in the large-scale BESS (at Willenhall specifically, but most findings are generally applicable), especially at the cell level.

The study concludes by studying open circuit voltage (OCV) hysteresis in the large-scale battery pack inside (i.e., WESS) through experiments. The study of hysteresis based on measured performance is found to be significantly improved through the application of an

extended Kalman filter. OCV hysteresis has historically been primarily discussed and measured in small-scale batteries. This work demonstrates not only the challenges of OCV hysteresis measurement in large-scale BESS but also reveals the effects of the properties of large-scale battery systems on OCV hysteresis experiments.

Acknowledgements

Firstly, I would like to thank my supervisors Martin Foster and Jonathan Davidson for their continued support over the last four years. During the writing up stage of this thesis, both of them showed great patience with a non-native speaker. PhD is a long journey, and I could not get through it without their encouragement. I am always grateful for their timely help at the crucial moments of my PhD, especially in the first and last years. The advice that I received from them will benefit me for the rest of my life.

I would also like to thank the people in the Department of Electronic and Electrical Engineering. Matthew Smith and Zhuo Wang helped conducted the experiments on Willenhall Energy Storage System and lithium titanium oxide cells. The results from these experiments play an important role in this research. Apart from my colleagues, I would like to thank my friends in Sheffield and also Fengyi Zhang; They provided invaluable emotional support while I am pursuing my PhD. Last but not least, I must thank my family, especially my parents, for their unconditional support during my PhD.

Contents

Abstract ..... **i**

Acknowledgements ..... **iii**

List of Figures ..... **viii**

List of Tables ..... **xiv**

Chapter 1. Introduction **1**

1.1 Overview of electrical energy and challenges for the grid 1

1.2 Opportunities for battery energy storage system 2

1.3 Research purpose 4

1.4 Main contributions 5

1.5 List of publications 6

1.6 Thesis overview 7

Chapter 2. Literature review **9**

2.1 Basics of battery chemistries 9

2.1.1 Lead-acid batteries 9

2.1.2 Lithium-ion batteries 11

2.2 From cell to battery pack 14

2.2.1 Cell operation restrictions 14

2.2.2 Cell open circuit voltage and state of charge relationship 15

2.2.3 Small, medium and large scale batteries 17

2.3 Battery management system 17

2.3.1 Battery management system function 18

2.3.2 Cell balancing 18

2.3.3 State of charge estimation 21

2.4 Battery Energy storage system applications 23

2.4.1 Enhanced frequency response 23

2.4.2 Peak load lopping 24

2.5 Battery simulations 25

2.5.1 Electrochemical model 25
2.5.2 Data driven model 26
2.5.3 Equivalent circuit model 27
2.5.4 Battery pack simulation 30
2.6 Summary 32
Chapter 3. Pack-level modelling for Willenhall Energy Storage System 33
3.1 Experimental platform: Willenhall Energy Storage System 34
3.2 Equivalent circuit models and traditional parameter identification 35
3.2.1 Equivalent circuit models 35
3.2.2 Parameter identification method for a small battery 36
3.3 Experiment profiles 39
3.3.1 Controller related phenomena: inverter and current response speed 39
3.3.2 State of charge related phenomena: calculation, correction and resolution 42
3.3.3 Battery management system data related phenomena: sample rate, resolution and accessibility 43
3.3.4 Voltage response in profiles and pseudo-OCV model 43
3.4 Equivalent circuit model parameter identification 46
3.4.1 Capacity estimation 46
3.4.2 RC parameter estimation 46
3.4.3 Equivalent circuit model 1 (ECM1) parameters 48
3.4.4 Equivalent circuit model 2 (ECM2) parameters 50
3.4.5 OCV-SoC response and ECMs built with the SoC from BMS and the Coulomb-counting method 51
3.5 Simulation results 54
3.5.1 Single cell equivalent circuit model scale-up approach 55
3.5.2 Detailed comparison of model performance based on dataset parameter extraction 56
3.5.3 Verification 59
3.6 Conclusion 60

Chapter 4. Cell level battery equivalent circuit simulator 62

4.1 Internal cell connection within the Willenhall Energy Storage System 62

4.2 Traditional circuit simulator 63

4.2.1 Circuit schematic diagram and netlist in SPICE type simulators 64

4.2.2 Modified node analysis and the stamping rules 65

4.3 Novel battery pack circuit simulator for the Willenhall Energy Storage System . 72

4.3.1 The overall structure of the proposed simulator 72

4.3.2 Equivalent circuit transformation 74

4.3.3 Cell current calculation 77

4.4 The validation of the proposed battery simulator 79

4.4.1 Verification A: scale-up method and cell level simulation 80

4.4.2 Verification B: Simulink vs. proposed simulator 81

4.5 Conclusion 84

Chapter 5. Cell level modelling for Willenhall Energy Storage System 86

5.1 Cell voltage deviation phenomena observed during the operation of Willenhall Energy Storage System 87

5.1.1 Maximum allowed cell voltage deviation 87

5.1.2 Cell voltage deviation in repeated experiments 90

5.2 Preparation for cell level battery pack simulation 92

5.2.1 Equivalent circuit model parameter value identification and the extend of parameter variation 93

5.2.2 Generating equivalent circuit model parameters value 96

5.2.3 Constructing models for individual cells 98

5.3 Monte Carlo simulation: constant power load 100

5.3.1 Results from a single simulation: at the pack and cell level 101

5.3.2 Results from Monte Carlo simulation 103

5.4 Conclusion 104

Chapter 6. Open circuit voltage hysteresis in Willenhall Energy Storage System . 106

6.1 Introduction 106

6.2 Open circuit voltage hysteresis and experiment on Willenhall Energy Storage System 107

6.2.1 Background of open circuit voltage hysteresis 107

6.2.2 The effect of cell chemistry on hysteresis 109

6.2.3 The effect of experiment procedure on hysteresis 110

6.2.4 Open circuit voltage hysteresis measurement on Willenhall Energy Storage System and Preisach hysteresis model 113

6.2.5 Open circuit voltage hysteresis experiment: results 118

6.3 Improvements to the SoC estimation 122

6.3.1 Sequential probabilistic inference and Kalman filter 122

6.3.2 Linear Kalman filter 123

6.3.3 Extended Kalman filter 127

6.3.4 State of charge estimation with extended Kalman filter 128

6.4 Conclusion 132

Chapter 7. Conclusion and future work 134

7.1 Conclusion 134

7.2 Potential future work 136

References 138

Appendix A: 155

Appendix B: 156

List of Figures

Figure 1.1 Some important applications of battery energy storage systems 3

Figure 1.2 Historical global lithium-ion battery market (adapted from: [14]) 3

Figure 1.3 Willenhall Energy Storage System (source: [15]) 4

Figure 2.1 Diagram of a lead-acid battery (source: [17]) 10

Figure 2.2 Schematic diagram of different shapes of Li-ion battery cell, (a): cylindrical, (b) coin, (c) prismatic, (d) pouch (source: [23]) 11

Figure 2.3 A schematic diagram of lithium-ion batteries using $LiCoO_2$ battery as example (source: [25]) 12

Figure 2.4 The measured and modelled OCV-SoC relationship for five cells with different chemistry. LMO: $LiMn_2O_4$, NCM: $LiNi_{1/3}Mn_{1/3}Co_{1/3}O_2$, NCM&LMO: NCM and LMO mixed, LTO: $Li_4Ti_5O_{12}$, LFP: $LiFePO_4$ (source: [45]) 16

Figure 2.5 OCV and SoC relationship in a lithium–sulphur battery (adapted from [46]) ... 16

Figure 2.6 OCV and SoC relationship in a lead-acid battery (adapted from [47]) 17

Figure 2.7 Passive balancing diagram with n number of cells in series 19

Figure 2.8 Simple examples of capacitor based balancing and inductor-based balancing .. 20

Figure 2.9 Capacitor based balancing. (a): single capacitor, (b): multi-capacitor (adapted from: [67]) 20

Figure 2.10 Single hidden layer ANN structure (source: [75]) 23

Figure 2.11 EFR service 2 envelop and reference point [77] 24

Figure 2.12 A load profile in peak shaving application (source: [79]) 24

Figure 2.13 Internal resistance model (adapted from: [89]) 28

Figure 2.14 Randles' model circuit for lead-acid battery (adapted from: [91]) 28

Figure 2.15 One time constant model (adapted from: [92]) 29

Figure 2.16 Two time constant model (adapted from: [93]) 29

Figure 2.17 The process of Monte Carlo Analysis on battery pack simulation 31

Figure 3.1 Schematic diagram of cell connection inside WESS battery 34

Figure 3.2 Battery equivalent circuit models (a): ECM1; (b): ECM2 35

Figure 3.3 Simulation processes, using ECM1 as an example 36

Figure 3.4 Battery terminal voltage profile during a pulse discharge (PD) test (source: [114]) 37

Figure 3.5 Experimental real power and battery current profiles, on day 1 and day 2. (note: 'Time' refers to the time in the experiments) 40

Figure 3.6 The first pulse of the experimental real power and current profiles on day 1 and day 2. (note: 'Time' refers to the time in the experiments) 41

Figure 3.7 The SoC profiles and the pulse around 70% on day 1 and day 2. (note: 'Time' refers to the time in the experiments. DCH: discharge. RT: rest) 42

Figure 3.8 Experimental voltage profiles and pseudo-OCV. (a) and (b): battery voltage profiles from the experiments on day 1 and day 2 respectively; (c): pseudo-OCV vs. SoC from BMS obtained from six separated low current experiments (fitted with two 8th polynomial equations) 44

Figure 3.9 Curve fitting process for ECM parameter identification using the day 1 experiment at 58.5% SoC as an example: (a) voltage, (b) current, (c) step 1 of parameter identification, (d) step 2 of parameter identification 48

Figure 3.10 ECM1 and ECM2 resistance and time constants identified from the experiments on day 1 and day 2 with respective to SoC BMS. The first column: two sets of ECM1 identified from day 1 and day 2 experiment; the second column: ECM2 identified from day 2 experiment 50

Figure 3.11 The OCV value estimated from different experiments (i.e. day 1 and day 2) and ECM models (i.e. ECM1 and ECM2) with respect to SoC from (a) BMS and (b) the Coulomb-counting method 52

Figure 3.12 ECM1 and ECM2 resistance and time constants identified from the experiments on day 1 and day 2 with respective to SoC from the Coulomb-counting method. The first column: two sets of ECM1 identified from day 1 and day 2 experiment; the second column: ECM2 identified from day 2 experiment 53

Figure 3.13 A simulation voltage (a) and error (b) comparison between ECMs modelled with the BMS SoC (ECM1 (BMS)) and Coulomb-counting SoC (ECM1 (Coulomb)): using ECM1 (identified from day 2) and day 2 input as an example 54

Figure 3.14 Single Toshiba SCiB LTO cell ECM1 parameters identified from EIS experiments 56

Figure 3.15 Simulation voltage and voltage error result in sim. 1 – 8. (a - b): voltage and error of sim. 1 - 3 and 7 using day 1 as input; (c - d): voltage and error of sim. 4-6 and 8 using day 2 as input. sim. 1-6 use battery pack ECMs identified from day 1 or day 2 dataset and sim. 7 - 8 use the scale-up approach and the single cell ECM from EIS test 58

Figure 3.16 Current profile on May 3rd, 2019 and simulation results with $ECM1_{D1}$, $ECM1_{D2}$ and $ECM2_{D2}$: (a) current, (b) voltage, (c) SoC, (d) voltage error 60

Figure 4.1 Battery connection in WESS: (a) cell diagram and electrical symbol, (b) 2P12S module diagram, (c) pack electrical connection 63

Figure 4.2 Circuit schematic diagram of the battery cell equivalent circuit model 64

Figure 4.3 Circuit to demonstrate nodal analysis method 66

Figure 4.4 Resistor stamping at a time step in transient simulation 68

Figure 4.5 Current source stamping at a time step in transient simulation 68

Figure 4.6 A circuit contains a voltage source 69

Figure 4.7 Voltage source stamping at a time step in transient simulation 70

Figure 4.8 The companion model of a capacitor under the forward Euler approximation for the time step from t to $t + \Delta t$ 71

Figure 4.9 Equivalent circuit model with one time constant in (a); the corresponding Thévenin circuit in (b); and Norton circuit in (c). (note: V_{eq} and I_{eq} are equivalent voltage in Thévenin circuit and current source in Norton circuit) 73

Figure 4.10 The process in the proposed battery pack circuit simulator for WESS 74

Figure 4.11 Battery pack circuit simulator: Norton and Thévenin circuit transformation .. 75

Figure 4.12 Battery pack circuit simulator: current calculation 78

Figure 4.13 Circuit diagram for verification simulation, plotted with Simulink (using SIMSCAPE components) 79

Figure 4.14 Verification A: (a): the voltage results from the scale-up method and the cell level simulation; (b): the voltage difference between the two methods 81

Figure 4.15 Verification B: Cell current simulation result from Simulink and the proposed simulator and the difference between them (a)-(h): cell 1-8 83

Figure 4.16 Verification B: Cell voltage simulation results from Simulink and the proposed simulator and the difference between them (a): cell 1; (a): cell 3; (a): cell 5; (a): cell 7 84

Figure 5.1 Measurements showing BMS cutting of the battery due to the battery exceeding the maximum allowed cell voltage deviation, 150mV (SoC: from 72.7% to 93.8%): (a) pack voltage, (b) cell voltage deviation, (c) pack power from BMS, (d) pack current and (e) BMS SoC 89

Figure 5.2 Two repeat experiments (blue: experiment 1, red: experiment 2): (a) pack voltage, (b) pack SoC from BMS, (c) pack power from BMS, (d) pack current (charging: positive), (e) cell voltage deviation vs. time, (f) cell voltage deviation vs. BMS SoC. Note: the legend for each subfigure is identical, and hence only one legend is shown in (a) 91

Figure 5.3 Single time constant ECM 92

Figure 5.4 EIS and ECM fitting result of 4 LTO cells at 50% SoC: (a) overall result, (b) result when $Z_{im} < 0$, (c) – (f) ECM fitting result from Cell02 to Cell05 94

Figure 5.5 Parameter value and the coefficient of variation of: (a) R_0, (b) τ_1, (c) R_1, (d) C_1, (e) R_{total}, (f) OCV. Note: the legend for each subfigure is identical, and hence only one legend is shown in (b) 95

Figure 5.6 The process of generating and modelling R_0, R_1 and C_1 at full SoC range for 21,120 number of cells. Step 1: random value generating for different cell at different SoC points. Step 2: reorganise the random value, gather parameter value for the same cell at different SoC into the same group. Step 3: obtain parameter-SoC relationship for each cell by curve fitting 99

Figure 5.7 A randomly generated WESS sized battery, all cells' ECM parameters and their CoVs (red inline: CoV of generated pack; circle points: CoV from EIS experiment): (a) R_0; (b) R_1; (c) C_1; (d) OCV vs. SoC 100

Figure 5.8 The result from a single simulation. (a) battery pack voltage, (b) pack current, (c - d) cell terminal voltage and deviation, (e - f) cell terminal current and deviation, and (g - h) cell SoC and deviation in the single simulation. t_1: 600 s (t_2: 4465 s, t_3: 5060 s, t_4: 9130 s; t_a: 832 s, t_b: 1271 s, t_c: 3744 s, t_d: 5832 s, t_e: 8369 s, t_f: 8826 s) 102

Figure 5.9 Cell terminal voltage deviation of 100 times Monte Carlo simulation 104

Figure 6.1 Schematic diagram of OCV hysteresis in a battery cell, (a): an incomplete major loop; (b): a minor loop 108

Figure 6.2 OCV of a single Toshiba SCiB LTO cell: (a) OCV after charging (OCV_{ch}) and discharging (OCV_{dis}) (data source: [128]), (b) hysteresis voltage: OCV_{ch} minus OCV_{dis} 109

Figure 6.3 Schematic diagram of the low current method 110

Figure 6.4 Schematic diagram of incremental charge/discharge method 111

Figure 6.5 The impact of different relaxation lengths on an LFP cell's OCV measurement. (a): OCV incrementally measured at 5% SoC interval, (b): ΔU, the difference between the OCV measured after a certain relaxation period and the OCV measured after 3 h relaxation (positive: OCV difference after charging. negative: OCV difference after discharging). (adapted from: [133]) 112

Figure 6.6 One-side Preisach operators (adapted from: [138]) 114

Figure 6.7 Preisach triangle T..... 114

Figure 6.8 An example of the Preisach triangle partition. (a): input; (b): L(t) at t_1; (c): L(t) at t_2; (d): L(t) at t_3; L(t): the interface, plotted in solid red line..... 116

Figure 6.9 A discrete Preisach model triangle (K=5, N=15). (a): allocate (αi, βj); (b): the value of (αi, βj); (c): the operator diagram for each region 117

Figure 6.10 A Li//Si half-cell's OCV modelling using discrete Preisach model (K=100) (data collected from: [138])..... 118

Figure 6.11 Result of the major and minor cycles in OCV hysteresis experiment: the pack voltage, current and BMS SoC in (a-c): loop 1, (d-f): loop 2, (g-i): loop 3 and (j-l): loop 4. Note: t_1: 30.1 h, t_2: 36.8 h 119

Figure 6.12 Battery pack terminal voltage vs. BMS SoC (DCH: discharge, CH: charge), (a-c): loop 1-4 121

Figure 6.13 Sequential probabilistic inference..... 123

Figure 6.14 The block diagram of linear Kalman filter..... 124

Figure 6.15 Flowchart of linear Kalman filter..... 125

Figure 6.16 Flowchart of extended Kalman filter 128

Figure 6.17 Single time constant ECM 129

Figure 6.18 Battery pack voltage vs. EKF SoC (first column) and estimated OCV vs. EKF SoC (second column). (note: DCH: discharge, CH: charge)..... 131

List of Tables

Table 2.1 Theoretical and practical specific capacity of various lithium battery 13

Table 3.1 WESS's partial history data on day 1 43

Table 3.2 Coefficients of 8th polynomial equations: pseudo-OCV and SoC relationship (show 4 significant digits). 45

Table 3.3 Simulation settings and RMSE of voltage result 57

Table 4.1 Partial netlist of the circuit diagram 65

Table 4.2 Netlist of the circuit diagram 66

Table 4.3 Netlist of the circuit diagram with a voltage source 69

Table 4.4 Cell open circuit voltage model coefficients 80

Table 4.5 Cell ECM parameters setting in simulation 82

Chapter 1. Introduction

1.1 Overview of electrical energy and challenges for the grid

As civilization evolves, electronic devices and electrical machines are widely used in modern industrial and domestic activities, which cause a massive demand for electrical energy. In the UK, from 1920 to 2018, the electricity generated by major power producers was boosted from 4 TWh to 281 TWh per year [1] to meet the increasing electricity demand.

Traditionally, electricity is gained from fossil energy sources such as coal through combustion reaction and energy conversion during which a large amount of greenhouse gases (e.g., carbon dioxide) are produced. Excessive greenhouse gases lead to a global temperature rise and extreme climate events [2] which urges counties to achieve sustainable development. As suggested by the ongoing 26th Conference of the Parties (COP26), net-zero carbon emission is expected to be achieved by the year 2050 [3].

To reduce greenhouse gases emission and achieve sustainable development, renewable energy such as solar PV, wind power, etc. are displacing non-renewable forms of generation such as coal. However, some of these renewable sources are influenced by environmental conditions. For example, the output power of a wind farm is affected by wind and so it cannot be relied upon to be available all the time. The change in electricity supply and demand will cause the grid frequency fluctuation. In detail, a frequency raise will be witnessed when the electricity supply is more than the demand. On the contrary, if the electricity supply is less than the demand, the grid frequency will drop.

When penetration of renewable energy generation onto the grid was very low, stability could be easily managed through excess generation provision and ancillary services. However, in the UK, renewable energy takes a significant part in generating electricity. Taking the first quarter of 2021 as an example, renewable energy contributed 41.6% of the electricity in the UK [4]. As a result, the stability of the grid is compromised by the introduction of these variable renewable energy sources.

Replacing traditional generators with renewable energy sources also leads to another challenge for the grid inertia reduction. Traditional generators have large inertia which provides the grid with a long response time to a fault (e.g., a power station trip). However,

renewable energy such as solar PV and wind power have low inertia which makes the maintaining of a constant frequency more challenging.

Infrastructure ageing is another problem for the grid. The grid system was devised well over half a century ago since which the demand in certain geographic areas has increased and exceeded the ability of its local substation. The replacement of old infrastructure takes a large financial cost. For instance, as reported in [5], in Isle of Wight, the railway system cannot be fully supported by the local electrical infrastructure. The railway system including the infrastructure is under an upgrade that costs £26 million [6].

1.2 Opportunities for battery energy storage system

The challenges that the grid is facing, and the pursuit of sustainable development provide the energy storage systems, especially battery energy storage systems (BESSs), with a golden opportunity. Compared to other types of energy storage systems such as compressed pumped hydro energy storage systems [7], air energy storage systems [8] and flywheel energy storage systems [9], battery energy storage systems have an advantage in scalability. As will be discussed in Chapter 2, BESSs can be manufactured at small to large scales which provides a wide range of capacity from Wh level to MWh level.

BESS is a promising candidate for overcoming the challenges in the grid. Grid-tied BESSs can compensate for the instability of renewable energy [10] and help maintain a stable utility frequency by balancing the difference between electricity supply and demand. Normally, a lithium-ion battery is preferred in grid scale applications because it has high power and energy capacities and low self-discharge [11]. Besides, batteries have a fast response time (lead-acid and lithium-ion batteries response time: ~40 ms [12]) which is capable of meeting the challenge caused by inertia reduction. Moreover, BESS can also defer the upgrade of the electrical infrastructure and avoid (or at least defer) a large amount of investment. As [13] reports, two 4 MWh batteries were installed in Punkin, Arizona which saved half of the cost of upgrading the infrastructure.

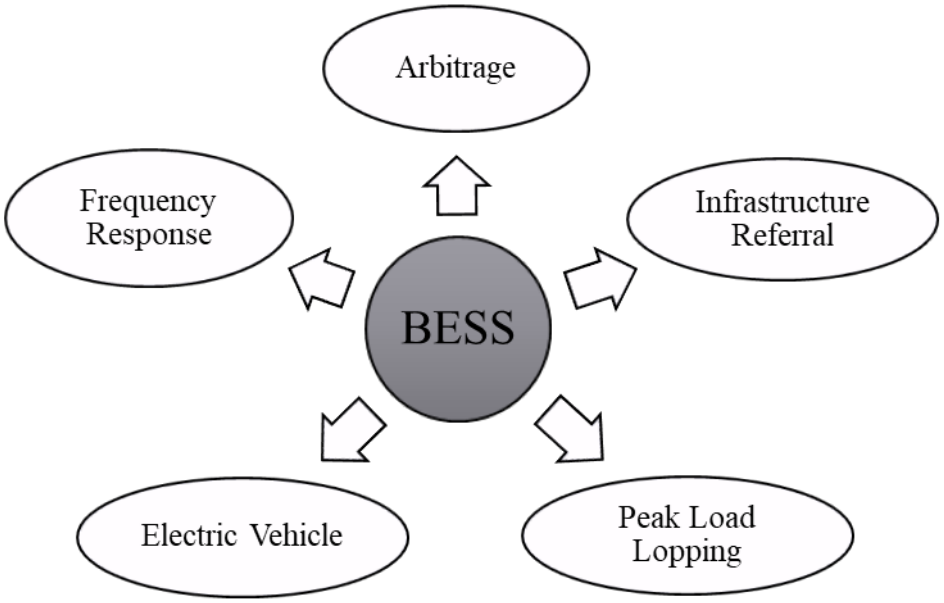

Figure 1.1 Some important applications of battery energy storage systems

Apart from frequency response services and infrastructure upgrade deferral, there are some other emerging applications of BESS including peak load lopping, electric vehicles and arbitrage as shown in Figure 1.1. To achieve sustainable development, electric vehicles are being promoted by many governments which is causing increased demand for (mostly lithium-ion) batteries. As a result, due to the demand in transportation (e.g., EVs), stationary (e.g., grid-tied BESSs), end consumer electronics (e.g., smartphones), and as Figure 1.2 shows, the global lithium-ion battery market steadily increased from about 30 GWh in 2011 to 195 GWh in 2019.

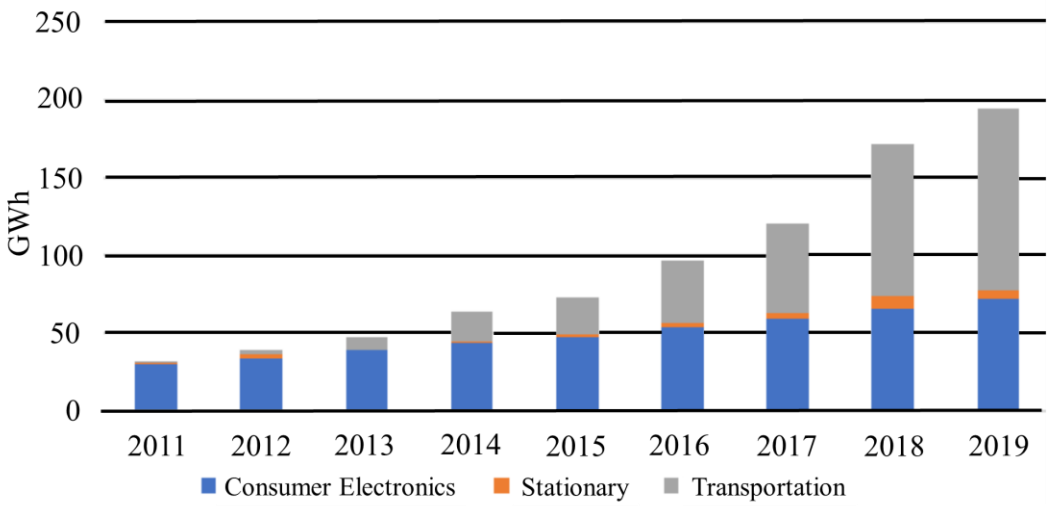

Figure 1.2 Historical global lithium-ion battery market (adapted from: [14])

1.3 Research purpose

As discussed in section 1.2, battery energy storage systems have the potential to overcome the challenges in modern grid systems and, at this time, are essential for the prosperous electric vehicle market. The batteries in grid applications normally have a large scale which requires a large investment. For example, the 1 MWh battery energy storage system in Willenhall, Willenhall Energy Storage System (WESS) as shown in Figure 1.3, cost four million pounds [15]. In this case, the simulation of large-scale battery becomes important for investment evaluation, battery energy management, control strategy development, etc.

Figure 1.3 Willenhall Energy Storage System (source: [15])

The main motivation of this research is to propose generic models for large-scale BESSs at cell level and pack level. The research demonstrated the modelling process on the WESS platform which is an LTO battery. Theoretically, the modelling techniques proposed in this research can be adopted in other types of BESSs. The modelling of other cell chemistries are not included in this thesis.

The common simulation method for a large-scale battery is scaling from a single cell model according to the electrical configuration inside the battery pack without considering the cell-to-cell variation (CtCV) that can often exist within the battery. This method is convenient but has some shortcoming. In detail, scaling up a single cell does not capture the properties of other parts in the BESS such the inverter and the battery management system. More

importantly, the cell level information cannot be obtained from a single whole battery equivalent circuit, because each cell is subtly different, which causes difficulties for further understanding the BESS's operation if it is considered a symmetrical collection of identical cells.

The first challenge to the large-scale battery modelling is the data accessibility of large-scale BESSs. The lack of experimental data restricts the direct modelling of large-scale BESS. Fortunately, the research described here uses WESS as the experiment platform which provides the users a limited but valuable data access. WESS is owned by the university as a research platform and can be used for experimental work. Secondly, cell level equivalent circuit for a large-scale BESS produces a large-order RC circuit network which is challenging to simulate. As will be discussed later in Chapter 4, modified nodal analysis method used in traditional circuit solver is not able to solve the massive RC circuit for large-scale battery in a computationally efficient manner to support extensive optimisation and Monte Carlo type analyses. To explore the battery properties at the cell level, an efficient simulator is required.

The purpose of this research is, therefore, to develop a software tool that can evaluate large-scale battery storage systems under various applications from both pack level and cell level so that the internal operations within battery and the effects of cell-to-cell variation on battery performance can be understand through simulations. At the end, the developed software tool should be able to simulate large-scale BESSs under various applications and to evaluate the economic value of the applications and to help develop energy management strategies.

1.4 Main contributions

This research mainly focuses on the simulation of large-scale battery energy storage system. To achieve that, many experiments and simulations were conducted, during which contributions were made as listed below.

• Implementation of cell-to-cell variance in large-scale BESS.

The research developed the cell-to-cell variance phenomenon in large-scale BESSs through the equivalent circuit modelling method. This research discussed the intrinsic CtCV in cell capacity, internal resistance etc but the effect of temperature and degradation on cells are not included. The study helps the researchers understand the cell voltage deviation in

BESSs, especially the changing trend of the cell voltage deviation in charging and discharging cycles. The related experiments revealed the cut-off mechanism in WESS that trigged by cell voltage deviation.

- Research and development of a novel cell level simulator for large-scale battery packs.

  The computational complexity of cell level simulation is a main challenge that limits cell level simulation for large-scale battery packs. The simulator introduced in this research is able to simulate a battery pack with over 21 thousand cells at an acceptable speed. The simulator is programmed with MATLAB language (as a MATLAB script) and run in MATLAB environment.

- A minor comparison between pack modelling and single cell scale-up method.

  The single cell scale-up method is commonly used in large-scale battery simulation with the assumption that all cells in the battery are identical. In this research, with the support of the experiment platform (WESS), the single cell scale-up method is able to be compared with the pack level modelling method.

- Exploration of the open circuit voltage (OCV) hysteresis phenomenon in large-scale BESS.

  Much prior research into OCV hysteresis has mainly focused on single cell behaviour. This research described in this thesis extends this to an OCV hysteresis study and experiment on a large-scale BESS. Hysteresis characteristics of WESS are described alongside a research investigation to accommodate hysteresis behaviour within a simulator using Preisach model. The OCV hysteresis theoretically exists in large-scale BESS. However, under the hardware and software settings in WESS, the OCV hysteresis in WESS is not experimentally verifiable.

1.5 List of publications

Conference paper:

Zeyuan Wang, Jonathan Davidson and Martin Foster, "A large-scale battery energy storage system simulation tool for studying cell variation," The 10th International Conference on Power Electronics, Machines and Drives (PEMD 2020), pp. 261-265, doi: 10.1049/icp.2021.1117.

Journal paper:

Zeyuan Wang, Zhuo Wang, Jonathan Davidson, Martin Foster and Daniel Gladwin, "A Monte Carlo simulator to investigate cell-to-cell deviation in a grid-tied battery pack", IET Power Electronics. 1– 15 (2022). https://doi.org/10.1049/pel2.12289

1.6 Thesis overview

The thesis presents the modelling of a large-scale battery energy storage system, using WESS as an example. The thesis is constructed in the following structure. A literature review is provided in Chapter 2 which includes the background of electrochemical battery cells, the basic information of battery management and modelling, popular application of BESS such as enhanced frequency response support for the grid and peak load lopping, and the basic knowledge of battery pack simulation with considering cell to cell variation. The purpose of the literature review is to provide the basic and necessary information on battery storage systems and their simulation.

Chapter 3 demonstrates a modelling process of a large-scale BESS at pack level. In this chapter, two experiments conducted on WESS will be discussed. The battery terminal current and voltage during the experiment are used to identify one-time-constant and two-time-constant equivalent circuit models for WESS. The identified models from the battery pack are compared with scaling up a single cell model to the size of a full pack (scale-up method). Some important properties of WESS and its battery management system are reported in this chapter.

Chapter 4 is a detailed discussion of the proposed cell level simulation tool for large-scale battery packs. First, the chapter explains the reason why the modified nodal analysis method in traditional circuit simulators cannot efficiently deal with the cell level simulation of large-scale battery packs. The proposed simulator using Thévenin and Norton transformations will be explained and its operation verified.

In Chapter 5, the phenomenon related to cell voltage deviation from observation taken from experiments performed using WESS is reported. The effect of cell-to-cell variation on the cell voltage deviation in WESS sized battery pack will be explored with the simulator introduced in Chapter 4. Monte Carlo simulation will be conducted with the battery pack’s

parameters generated according to specific probably distribution functions obtained from several single cell experimental characterisations.

Chapter 6 investigates the open circuit voltage (OCV) hysteresis phenomenon in the large-scale battery pack of WESS. After a discussion of the OCV hysteresis at single cell and the commonly used hysteresis model, the experiment for extracting OCV hysteresis in WESS will be introduced. The experiment result will be improved by an extended Kalman filter and will be discussed in detail in this chapter. Chapter 7 concludes and summarises this work and suggests some potential future work that would extend the research.

Chapter 2. Literature review

This chapter provides a literature review of battery technologies including aspects from the cell chemistries and properties to applications, from a single cell to large-scale energy storage systems, from cell level modelling to pack level modelling, etc. The discussion in this chapter will provide a general background information of battery technologies which it is intended will help the reader understand the later chapters.

2.1 Basics of battery chemistries

Battery is a general term referring to a type of energy storage device that stores energy in electrochemical form. Batteries are classified into the primary and secondary types where the latter one can be charged and discharged multiple times whereas the former type cannot. Secondary batteries have been widely used as energy storage device to power up modern industrial and domestic activities. Due to its advantage of rechargeability over primary batteries, secondary batteries have drawn a lot attention from researchers and manufactures.

After a long history of development, various secondary batteries with different shapes and chemistries have been invented and commercialised. Among many different types of secondary batteries, two most prevalent kinds of batteries, lead-acid batteries and lithium-ion batteries, will be introduced and compared next.

2.1.1 Lead-acid batteries

Lead-acid batteries was invented in 1859 [16]; each cell has a ~2 V terminal voltage. As one of the oldest types of secondary batteries, lead-acid batteries are still active in the battery market mainly working as starting batteries in motor vehicles for SLI (starting, lighting, ignition) [17] or standby applications. Lead-acid batteries have advantages of outstanding safety, wide working temperature range (e.g., Yuasa NPL65-12IFR: -20°C to 60°C during discharge [18]), and low price (within 20 $/kWh [19]). However, the low energy density (~50 Wh/kg [20]) and low cycle durability characterises make lead-acid batteries inappropriate for applications like electric vehicles where large energy density and high durability are expected.

Figure 2.1 illustrates the diagram of a lead-acid cell including the main parts: the negative electrode (metallic lead: Pb) also known as the anode, the positive electrode (lead-

dioxide: PbO_2) also known as the cathode, the electrolyte (sulphuric acid: H_2SO_4) and the porous separator.

The main function of the separator is to avoid the physical contact between electrodes. The separator also holds the active martial, which helps to maintain the contact between the active martial and the grid [21]. The grid collects electrons from electrodes during the chemical reaction and also named as current collector [22].

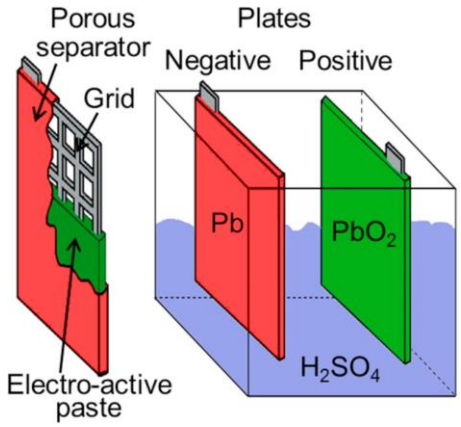

Figure 2.1 Diagram of a lead-acid battery (source: [17])

The anode and cathode materials, also known as active materials, take part in the chemical reaction during battery charging and discharging processes as equation (2.1) shows. The reactions happen at positive and negative electrodes are separately shown in (2.2) and (2.3). During the charging and discharging processes, the movement of sulphate ions SO_4^{2-} and hydrogen ions H^+ inside the battery and the flowing of electrons through the outside circuit generate a closed circuit.

Total reaction:

$$Pb + PbO_2 + 2H_2SO_4 \underset{\text{charge}}{\overset{\text{discharge}}{\rightleftharpoons}} 2PbSO_4 + 2H_2O \quad (2.1)$$

Positive electrode reaction:

$$PbO_2 + 4H^+ + SO_4^{2-} + 2e^- \underset{\text{charge}}{\overset{\text{discharge}}{\rightleftharpoons}} PbSO_4 + 2H_2O \quad (2.2)$$

Negative electrode reaction:

$$Pb + SO_4^{2-} \underset{\text{charge}}{\overset{\text{discharge}}{\rightleftharpoons}} PbSO_4 + 2e^- \quad (2.3)$$

2.1.2 Lithium-ion batteries

Lithium-ion batteries can be manufactured into different shapes such as cylindrical cells, coin cells, prismatic cells and pouch cells as Figure 2.3. However, for different shapes of lithium-ion batteries, the fundamental structure of a lithium-ion battery remains the same. Similar to the pre-described lead-acid batteries, a lithium battery also consists of five main parts that are the cathode, anode, electrolyte, separator and current collector. Figure 2.3 shows the schematic diagram of lithium-ion batteries where the separator in the electrolyte is omitted.

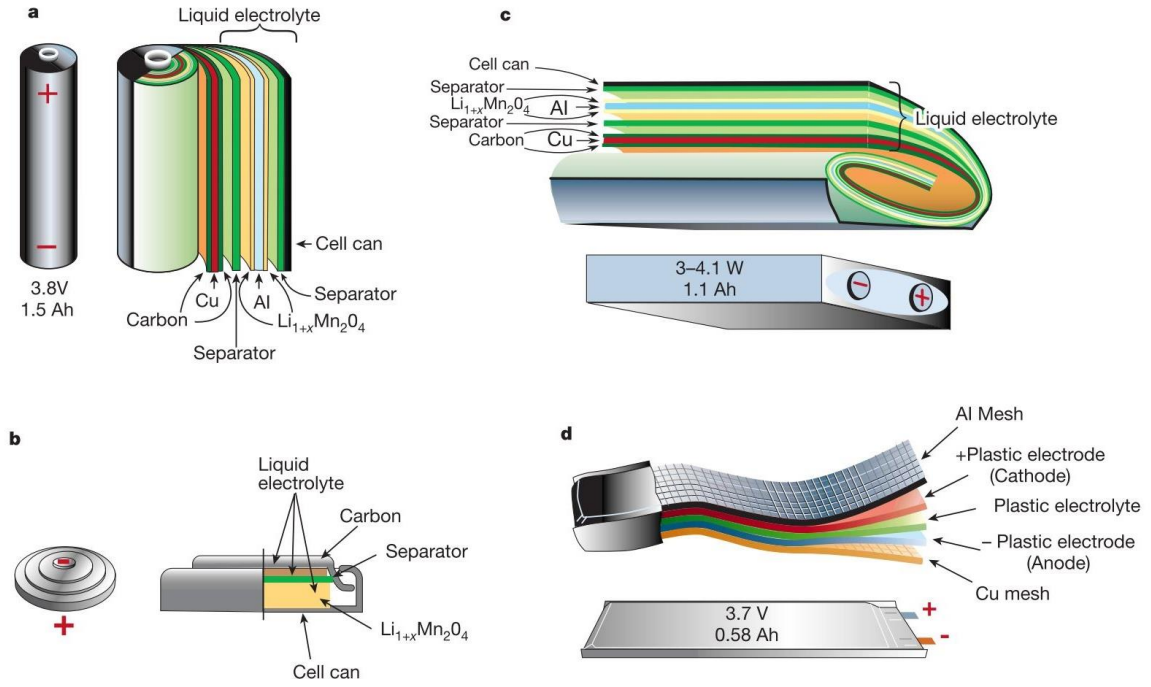

Figure 2.2 Schematic diagram of different shapes of Li-ion battery cell, (a): cylindrical, (b) coin, (c) prismatic, (d) pouch (source: [23])

The lithium-ion battery shown in Figure 2.3 has a $Li_{1-x}CoO_2$ cathode and a graphite (C_6) anode where x is a number between 0 and 1. The chemical reaction equations for a $LiCoO_2/C_6$ battery are shown in (2.4)–(2.6). During charging and discharging process, the active material in lithium-ion battery can be lithium-doped and lithium-undoped [24]. The Li^+ departs from one electrode and travels to another electrode through the electrolyte which

generates the current path inside the battery. Similar to lead-acid batteries, the electron flows through the circuit outside the battery and forms a closed circuit with the internal current path.

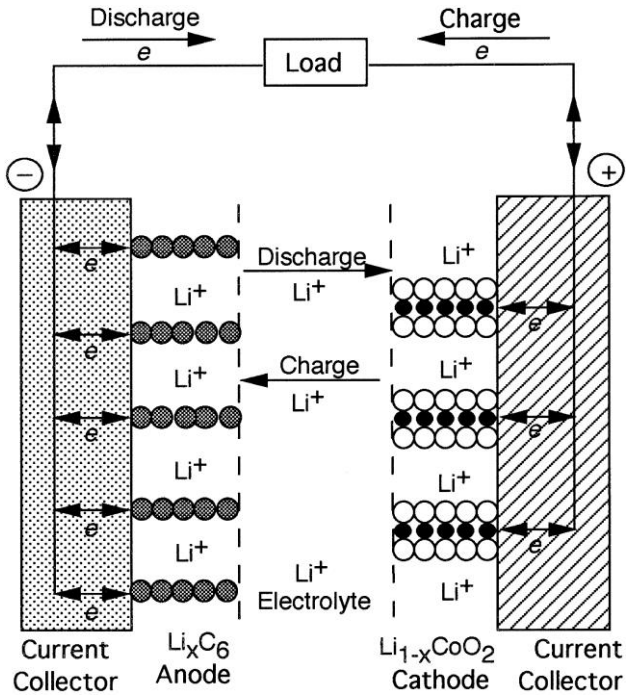

Figure 2.3 A schematic diagram of lithium-ion batteries using $LiCoO_2$ battery as example (source: [25])

Total reaction:

$$Li_{1-x}CoO_2 + Li_xC_6 \underset{\text{charge}}{\overset{\text{discharge}}{\rightleftharpoons}} C_6 + LiCoO_2 \tag{2.4}$$

Positive electrode reaction:

$$Li_xC_6 \underset{\text{charge}}{\overset{\text{discharge}}{\rightleftharpoons}} xLi^+ + xe^- + C_6 \tag{2.5}$$

Negative electrode reaction:

$$Li_{1-x}CoO_2 + xLi^+ + xe^- \underset{\text{charge}}{\overset{\text{discharge}}{\rightleftharpoons}} LiCoO_2 \tag{2.6}$$

Apart from $LiCoO_2$, various types of cathode active material for lithium-ion batteries have been developed. The other popular cathode active material includes $LiFePO_4$, $LiMn_2O_4$, $LiNiMnCoO_2$, etc. The working principle of these cells is similar to the $LiCoO_2$ which has been introduced above. A description of LMO cell chemistry can be found in reference [26].

According to Faraday's law, the theoretical specific capacity (C_{th}, often written in mAh/g, the capacity per unit mass) of an active material can be calculated as (2.7) [27], where F is Faraday constant, M_{w} is the molecular weight of the material and n is the number of moles of transferred electrons in the chemical reaction per mole of the material (For example: $n = 1$, for $LiFeO_4$).

$$C_{\mathrm{th}} = \frac{nF}{M_w} \tag{2.7}$$

Table 2.1 shows the theoretical specific capacity for different cathode materials calculated from (2.7) and the practical specific capacity from measurement. As Table 2.1 shows, the practical specific capacity is much lower than the theoretical value due to the reasons such as material purity. There are many types of $LiNiMnCoO_2$ which has different ratio between Ni Mn and Co. $LiNi_{1/3}Mn_{1/3}Co_{1/3}O_2$ is the most common NMC cells [28], and it is being gradually replaced with $LiNi_{0.8}Mn_{0.1}Co_{0.1}O_2$ [29] which has a higher practical specific capacity.

Table 2.1 Theoretical and practical specific capacity of various lithium battery
(*: data not found).

Chemistry	Theoretical specific capacity (mAh/g)	Practical specific capacity (mAh/g)
$LiCoO_2$	274	165 [30]/140 Ah [31]
$LiFePO_4$	170	120–160 [32]
$LiMnO_2$	148	~120 [33]
$LiNi_{1/3}Mn_{1/3}Co_{1/3}O_2$	278	163 [34]
$LiNi_{0.4}Mn_{0.4}Co_{0.2}O_2$	279	*
$LiNi_{0.6}Mn_{0.2}Co_{0.2}O_2$	277	*
$LiNi_{0.8}Mn_{0.1}Co_{0.1}O_2$	276	203 [34]

Compared with cathode material, the developed anode materials for lithium-ion battery normally have a much larger specific capacity. Carbon-based materials such as graphite are popular anode materials for lithium-ion batteries. The graphite has a theoretical specific capacity of 372 mAh/g [35] which can be easily approached by Polyfurfuryl alcohol derived

carbon (PFA-C) 350 mAh/g [24]; The porous carbon nanofibers (CNFs), 566 mAh/g [36], can easily exceed the theoretical specific capacity of the graphit. Another anode material, lithium titanate oxide who has a relatively low practical specific capacity (170 mAh/g [37]) shows 'extremely stable and robust' [35] properties during cycling, which is chosen by some manufactures such as Mitsubishi and Honda [38]. By contrast, the specific capacity of lead-acid battery is ~30 mAh/g [39] which is much lower than lithium ion batteries.

2.2 From cell to battery pack

The battery structure and different battery chemistries have been discussed in section 2.1. Cells should be operated under certain restrictions, which will be discussed next. After introducing the concept of state of charge (SoC), the open circuit voltage (OCV) and SoC relationship for batteries will be discussed. In the end of this section, different scales of battery will be introduced.

2.2.1 Cell operation restrictions

For a battery cell, regardless of the chemistry, it needs to be operated under the restrictions specified by the manufacture to keep the battery safe and healthy. Summarized from the datasheet of some commercial cells [40–42], these restrictions mainly includes: the maximum and minimum cut-off voltages, the operating temperature, the storage temperature, the maximum allowed continuous charging and discharge current, the maximum allowed peak charging and discharge current, ambient humidity, etc. Violating these restriction or mechanically abusing batteries could cause permanent damage to the battery such as capacity loss, gassing, fires, thermal runaway, explosions, etc [43].

Among the restrictions, the maximum and minimum cut-off voltages are especially important for defining some vital concepts in battery study. The concepts and their definitions that used in this thesis are presented as below.

- Fully charged: a battery is defined as in the fully charged state when its open circuit voltage (after relaxing) equals the specified maximum cut-off voltage.
- Fully discharged: a battery is defined as in the fully charged state when its open circuit voltage (after relaxing) equals the specified minimum cut-off voltage.

- Capacity: the amount of charge that can be extracted from a battery when discharge it from the fully charged state to the fully discharged state, normally in the unit of Ah.
- Remaining capacity: the amount of charge that can be extracted from a battery when discharge it from the present state to the fully discharged state.
- State of charge (SoC): the ratio between the remaining capacity and the capacity, normally in a percentage form.

Normally, the battery cut-off voltages provided by manufacturers are temperature-invariant; However, battery OCV and internal resistance are changing with temperature, which makes the measured battery capacity vary with temperature [44]. Ideally, defining temperature dependent cut-off voltages could maintain the battery capacity at a constant value and normalize SoC.

It should be noted that strictly fully charged and fully discharged states are difficult to achieve in reality due to the existence of battery internal resistance so that fully charge and discharged states are normally replaced by a nearly fully charged and discharged state respectively. The ampere-hour (charge) capacity is the commonly used capacity index for batteries. However, it does not totally reflect the capability of a battery and sometimes is replaced by watt-hour (energy) capacity. The nominal watt-hour capacity is equal to the battery nominal voltage multiplied the battery nominal charge capacity.

2.2.2 Cell open circuit voltage and state of charge relationship

For a given battery cell, the open circuit voltage (OCV) changes is dominated by SoC and could be influenced by temperature and ageing [45]. Besides, the OCV and SoC relationship varies between cells with different chemistry. Reference [46] measured and modelled the OCV and SoC relationship of five cells with different chemistry. As the result in Figure 2.4 shows, at the same SoC, the OCV value are different for different cells and the LMO battery has the greatest value while the LTO has the least value.

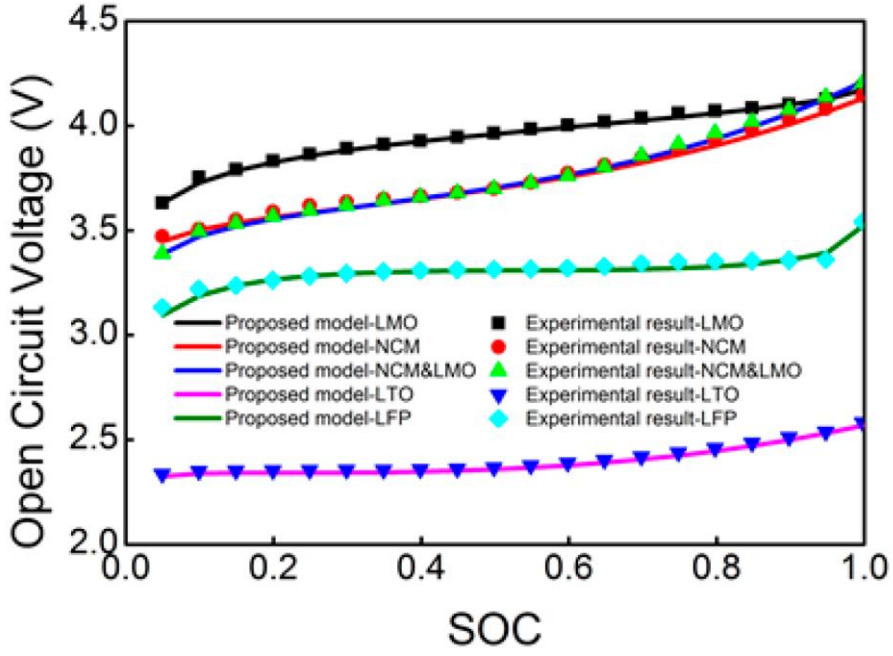

Figure 2.4 The measured and modelled OCV-SoC relationship for five cells with different chemistry. LMO: $LiMn_2O_4$, NCM: $LiNi_{1/3}Mn_{1/3}Co_{1/3}O_2$, NCM&LMO: NCM and LMO mixed, LTO: $Li_4Ti_5O_{12}$, LFP: $LiFePO_4$ (source: [46])

In general, as Figure 2.4 shows, the OCV of a battery gradually increase as the value of SoC increases. However, Lithium–Sulphur batteries have unique and unusual OCV and SoC relationship as Figure 2.5 shows. The OCV and SoC relationship are divided into two phases (Phase 1: 0-69%. Phase 2: 69%-100%). In phase 1, as SoC increases, the OCV keeps around 2.1 V and has a slight decrease. In phase 2, similar to other pre-described chemistry, the OCV increases as SoC increases. For Lead-acid batteries the trend is almost linear, as shown in Figure 2.6, which allows the battery OCV to provide a reasonable indication of SoC.

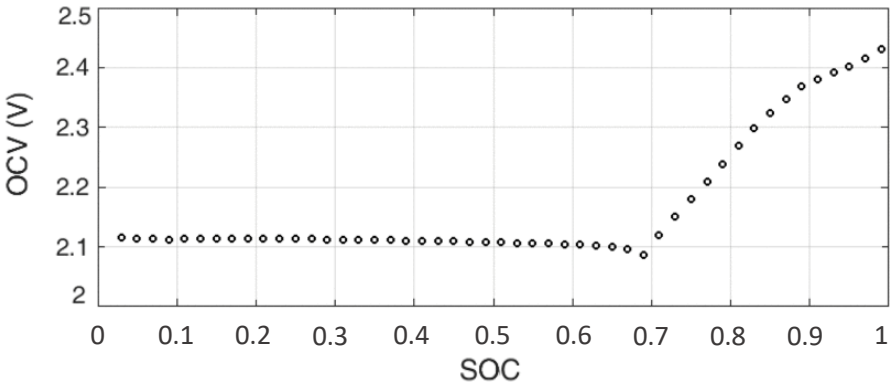

Figure 2.5 OCV and SoC relationship in a lithium–sulphur battery (adapted from [47])

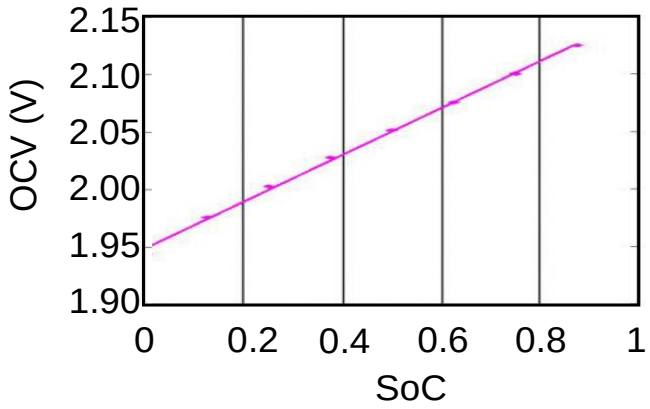

Figure 2.6 OCV and SoC relationship in a lead-acid battery (adapted from [48])

2.2.3 Small, medium and large scale batteries

As section 2.2.1 and 2.1.2 discuss, a single cell has a low voltage (about several volts) and has a limitation in maximum allowed current so that the power delivered by a single cell is limited. To meet the design requirements (such as power and energy demand) in different applications, battery cells are often connected in series and parallel which generates different scales of batteries from small to medium to large [49]. Connecting cells in parallel increases the battery capacity and the series connection boosts the battery voltage [50].

Samsung SDI, which is a well-known lithium-ion battery manufacturer, displays various applications of different battery (from small to large) on its website [51]. As the website shows, typical applications of small scale batteries are laptops, mobile phones, wearable devices, etc. A small scale battery normally contains one or several battery cells with around tens of watt-hours of capacity (e.g., Samsung PGF3183A2 cell: 11.21 Wh [52]). The batteries for electric vehicles are in medium scale and have an capacity at kWh level (e.g., the battery in Nissan Leaf: 40kWh [53], 192 cells [54]). The large scale batteries have a capacity at MWh level and the typical example of large scale batteries is grid-tied battery energy storage system (e.g. Minamisoma Substation battery (Japan): 40 MWh [55], cell number not disclosed. Willenhall Energy Storage System: 1 MWh [15], 21,120 cells).

2.3 Battery management system

As section 2.2.3 describes, the cell number varies a lot between different scales of batteries. Despite of the scales of batteries, the users commonly expect the batteries to be safe and to

have a long lifespan, which motivates the battery, manufacturers to develop specialised battery management systems.

2.3.1 Battery management system function

Battery management system (BMS) is an essential part of battery energy storage system (BESS) and the functions of a BMS is achieved through the cooperation of hardware and software. Four main functions of advanced BMSs are summarize from [50,56–61] and listed below.

1. Monitoring: the BMS measures the battery cell information including current, voltage and temperature through sensor system.
2. Safety: the BMS avoids any battery cell exceeds the allowed current, voltage and temperature boundary as specified in the datasheet.
3. Estimation: the BMS estimates the battery SoC value and the battery ageing condition.
4. Cell balancing: through the balancing circuit, BMS reduces the voltage difference among cells to achieve a larger available capacity and long battery lifespan.

Apart from the main functions, other functions such as communication with other parts of the system, providing user interface (to display information such as SoC), fault diagnosis and handling, and data recording are also generally included in a modern BMS. Achieving these BMS functions in a battery often requires extra hardware which increases the cost. For example, as it will be discussed later, the cell balancing function normally requires complex control algorithms and extra components such as resistor, capacitor, etc. Some BMSs are designed without balancing function to keep the battery price affordable. Similarly, in a large-scale battery, monitoring every cell's current, voltage and temperature requires a large number of sensors and recording these data requires large memory space which will increase the financial cost and the system size. A BMS should therefore make a balance between the functionality and the cost.

2.3.2 Cell balancing

Passive balancing and active balancing are two categories of balancing strategies where passive balancing uses resistors to consume the energy in the cells with higher voltage [62]. By contrast, in the active balancing method, the energy is transformed from the cells with higher voltage to other cells with lower voltage through capacitors and inductors [63].

2.3.2.1 Passive balancing

In passive balancing strategy, each cell is connected in parallel with a resistor. These resistors are controlled by switches as Figure 2.1 shows. During balancing, the switches connected to the cells with higher voltage will be turned-on and a discharge current will pass through the balancing resistors and the energy will be released as heat [62].

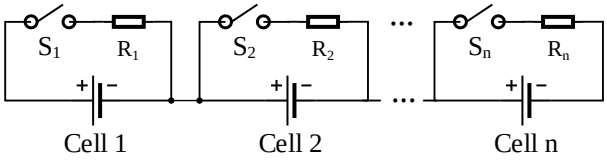

Figure 2.7 Passive balancing diagram with n number of cells in series

Passive balancing has a simple structure and control algorithm, which makes it extremely robust and reliable. More importantly, the passive balancing has a low cost [64] which means it still the preferred choice for a large-scale battery pack. However, the efficiency of passive balancing strategy is low and is suggested to work during the battery charging mode only [65]. Besides, a long balancing time is required to avoid serious thermal problems [64].

2.3.2.2 Capacitor and inductor based balancing

Figure 2.8 presents diagrams of capacitor-based and inductor based active balancing using two series connected cells as an example. The main idea for capacitor balancing [66] and inductor balancing [67] are similar. They are operated by switching the energy storage device (i.e. capacitor or inductor), which is first connected to the cell with higher voltage first and then to the cell with lower voltage. In this way, the energy from a cell with higher voltage transfers to the energy storage device first and then to the cell with a lower voltage.

Taking the capacitor based balancing in Figure 2.8(b) as an example, assuming cell 1 has a higher voltage than cell 2, the capacitor will be combined with cell 1 first by turning the switches S_1 and S_2 to left. In this process, the capacitor is charged to the same voltage with cell 1. Then cell 2 with lower voltage will be connected with the capacitor by turning the switches to right. The energy will be released by the capacitor into cell 2.

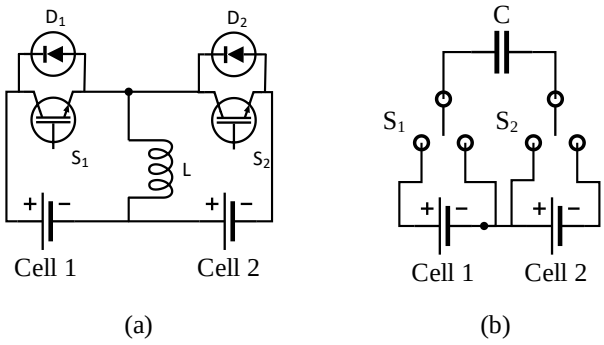

Figure 2.8 Simple examples of capacitor based balancing and inductor-based balancing

In reality, a string could contain more than two cells and the energy transfer is not limited between two adjacent cells. The design of the capacitor and inductor balancing circuits are flexible. As [68] shows, the capacitor balancing for a string can be design in a single capacitor structure with a complex switching network (shown in Figure 2.9(a)) and also a multi-capacitors structure with slower balancing speed (shown in Figure 2.9(b)). Similarly, more complex design with inductors (transformer) can also be achieved as shown in [65] where each cell is parallel connected with a inductor (secondary winding of a transformer) and the balancing can be achieved with the cooperation of a shared primary winding.

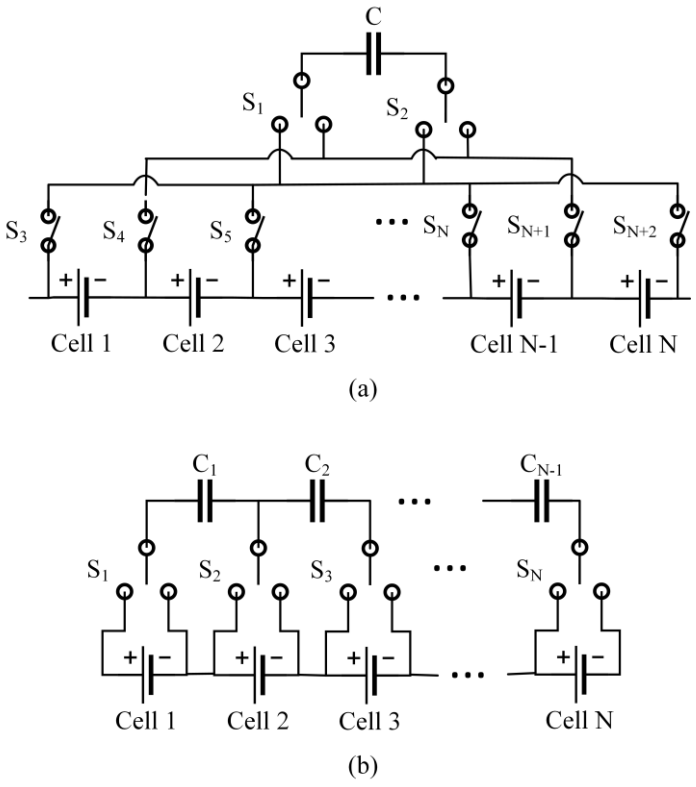

Figure 2.9 Capacitor based balancing. (a): single capacitor, (b): multi-capacitor (adapted from: [68])

2.3.3 State of charge estimation

Apart from cell balancing, SoC estimation is another main function of BMS which provides an important system status information for the user and for the energy management system to make usage decisions. The SoC estimation methods can be classified into two categories that are online and offline methods. The main difference between these two methods is that the offline methods are not suitable for real-time SoC estimation due to their restricted requirements. For example, the long resting time in the open circuit voltage method.

In this section, an offline method (open circuit voltage method) will be discussed first. Then, several online SoC estimation methods will also be introduced including the coulomb-counting method, model-based method, and data-driven method.

2.3.3.1 Offline method: open circuit voltage method

The open circuit voltage method is a typical offline SoC estimation method which is also known as the look-up method. It uses the relationship between OCV and SoC to estimate the SoC value in a battery cell. The OCV and SoC relationship is obtained from pre-experiments.

An accurate OCV and SoC relationship containing the effect of ageing, temperature, etc. is crucial to this method which requires a large number of experiments. The open circuit voltage method is a good method to estimate a start SoC value. However, it is not very appropriate for a battery with a flat OCV and SoC relationship such as the lithium–sulphur battery [47]. Moreover, a strict OCV value should be measured after a few hours (1~3 h) of relaxation which is unacceptable for most applications.

2.3.3.2 Online methods

Method 1: coulomb-counting

The coulomb-counting method is a commonly used conventional method which estimates SoC value by integration of the battery current. (2.8) provides a general expression of the coulomb-counting method in which S, S_{init}, I, and Q represents the value of SoC, initial SoC, current, and capacity respectively.

$$S(t) = S_{\text{init}} + \int_0^t I(t)dt \,/Q \tag{2.8}$$

The coulomb-counting has advantages in the low complexity of computation but the accuracy can be easily influenced by the initial SoC value and current sensor accuracy [69].

Method 2: model-based method

The extended Kalman filter is a typical example of model based SoC estimation method which is not as sensitive to the initial SoC value since the Kalman filter can 'correct' the SoC estimation through the battery model and the difference between the measured and model estimated battery voltage. The developing and deriving process of Kalman filters is based on the equivalent circuit model of batteries. A detailed discussion of the extended Kalman filter and its application of it can be found in section 6.3.

Similar algorithms include adaptive Kalman filter [70], particle filter [71], etc. These algorithms require a complex deriving process and the SoC estimation from these methods can be influenced by the battery model [72–74].

Method 3: data-driven method

The data-driven methods include three main procedures that are data collection, model training and SoC estimation [75]. In this type of method, a data-driven model is trained with collected data such as current, voltage, temperature and the corresponding SoC value. During the online operation of a battery, the SoC can be estimated through the trained model and the measured data (e.g., current, voltage and temperature).

Artificial neural network (ANN) is a popular type of data-driven model. Reference [76] introduces the back propagation (BP) ANN whose structure is shown in Figure 2.10. In the diagram, a circle represents an artificial neuron. The BP ANN has three layers including the input layer (n number of the artificial neuron), the hidden layer (m number of the artificial neuron), and the output layer (one number of the artificial neuron). x and z are the input and output information respectively, $\boldsymbol{X} = [x_1, x_2, \dots, x_n]^T$. v and w are the weight between different layers, $\boldsymbol{W} = [w_1, w_2, \dots, w_n]^T$. For the i^{th} neuron in hidden layer, $\boldsymbol{V_i} = [v_{1i}, v_{2i}, \dots, v_{ni}]^T$. For the input layer, the input and the output of a neuron are the same. For the i^{th} neuron in the hidden layer, the input $y_i = \boldsymbol{V}_i^T \boldsymbol{X}$ and the output $o_i = f(y_i)$ where the excitation function $f(y) = \frac{1}{1+e^{-y}}$. For the neuron in the output layer, the input $p = \boldsymbol{W^T O}$ where $\boldsymbol{O} = [o_1, o_2, \dots, o_m]^T$ and the output $z = f(p)$. In the case of battery SoC estimation, z is the value of SoC.

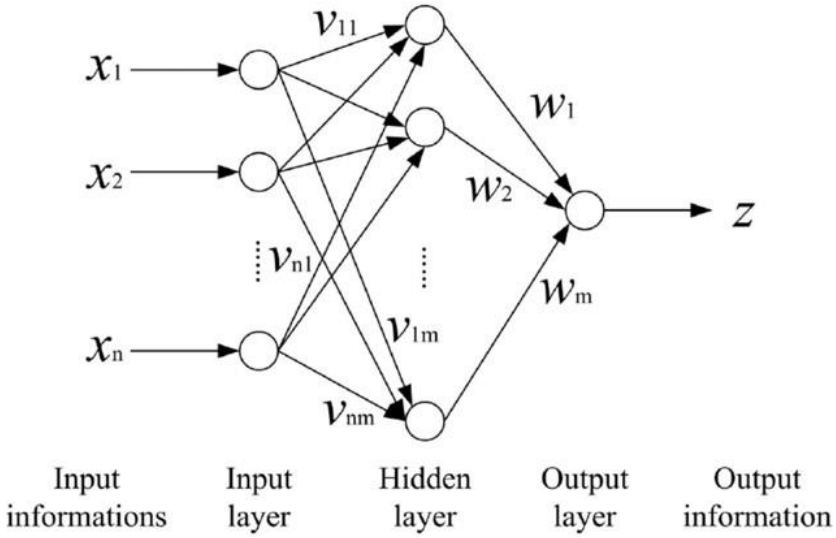

Figure 2.10 Single hidden layer ANN structure (source: [76])

Artificial neural networks become complex when more hidden layers and more input are introduced into the model as shown in [77]. A large amount of experiment data and computation are required to training the neural network in the method.

2.4 Battery Energy storage system applications

As mentioned before, a large-scale battery system could have a capacity at MWh-level which makes it a promising candidate for large-scale applications. In this section, some popular application of large-scale battery energy-storage systems will be introduced.

2.4.1 Enhanced frequency response

Frequency response services are aiming to constrain the grid frequency between 49.5 Hz and 50.5 Hz (in the EU) by reducing the difference between supply and demand. Enhanced frequency response (EFR) is a type of frequency response services. The National Grid requires the participators in this service, such as BESS operators, to respond to the frequency deviation within 1s.

In general, a grid-tied BESS is expected to release energy to the grid when the grid frequency is low and to absorb energy from the grid when the grid frequency is high. At different frequency values, the National Grid allows EFR service participator (e.g., a battery) to provide output power according to the service envelope as shown in Figure 2.11. The output power value of the battery to the grid is expected to be inside the upper and lower envelopes. Operating the energy storage system outside the envelope will incur a penalty [78].

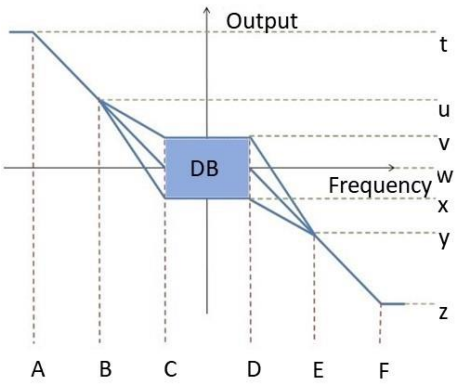

Service 1			
Reference point (Hz)		Reference point (%capacity)	
A	49.5	t	100%
B	49.75	u	44.44444%
C	49.95	v	9%
D	50.05	w	0%
E	50.25	x	-9%
F	50.5	y	-44.44444%
		z	-100%

Service 2			
Reference point (Hz)		Reference point (%capacity)	
A	49.5	t	100%
B	49.75	u	48.45361%
C	49.985	v	9%
D	50.015	w	0%
E	50.25	x	-9%
F	50.5	y	-48.45361%
		z	-100%

Figure 2.11 EFR service 2 envelop and reference point [78]

The National Grid allows participators to choose from Service 1 and Service 2 as shown in Figure 2.11. The main difference between the services is the dead band (Service 1: [49.95Hz, 50.05Hz] and Service 2 [49.985Hz, 50.015Hz]). Two EFR services with different dead band are compared and analyzed in [79]. As a result in [79], under the same frequency profile, Service 2 requires greater energy exchange between BESS and the grid.

2.4.2 Peak load lopping

Peak load lopping or peak shaving is the technique of reducing the peak power demand from the grid at peak time. BESS is an effective way to achieve peak shaving. The battery is charged during off-peak time (low power demand) and discharged during peak time.

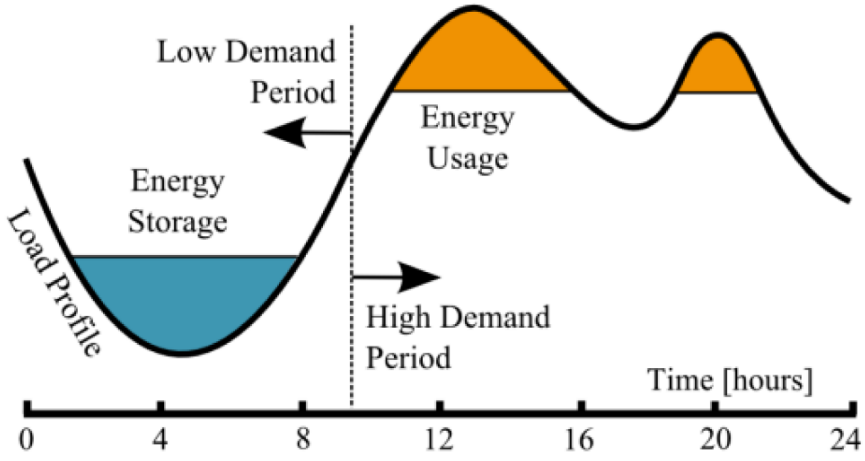

Figure 2.12 A load profile in peak shaving application (source: [80])

Peak load lopping can effectively reduce the average and peak power demand from the grid. Reference [81] introduced a peak shaving method for a grid-connected PV system in which a battery works as ESS. The result showed a 15% reduction in average peak power and 39% maximum peak power. Since the difference between peak and off-peak times electricity prices, the reduction in peak power will result in the saving in operating cost of the system.

2.5 Battery simulations

Battery modelling and simulation are important. As it has been discussed in section 2.3, a battery management system could use battery models to estimate some important battery states such as SoC. Battery modelling and simulation are also useful to predict the return on investment of a battery system which is important for the invertor.

The electrochemical model, data driven model and equivalent circuit model (ECM) are three types of battery models that are widely used in different areas. In this section, the electrochemical model and data driven model will be introduced first and then a review of the commonly used electrical equivalent battery model will be presented.

2.5.1 Electrochemical model

Electrochemical models can provide an accurate description of the physical and chemical processes inside a battery. In electrochemical models, the physical and chemical properties of battery components and electrochemical reactions are represented by a set of equations [82].

Single particle model (SPM) is the simplest electrochemical model whose mathematical expression can be found in [83]. SPM assumes that the chemical reaction in electrodes is uniform. According to Fick's law, the diffusion process of lithium inside the active material is governed by (2.9) in spherical coordinates. r_i, c_i and D_i are the radial coordinates, lithium concentration, and lithium diffusion coefficient in electrode i where i can be + (representing the cathode) or – (representing the anode).

$$\frac{\partial c_i}{\partial t} = \frac{D_i}{r_i^2}\frac{\partial}{\partial r_i}\left(r_i^2 \frac{c_i}{\partial r_i}\right) \tag{2.9}$$

The boundary conditions are $D_i \frac{\partial c_i}{\partial r_i}\Big|_{r_i=0} = 0$ and $D_i \frac{\partial c_i}{\partial r_i}\Big|_{r_i=0} = -j_i$ where j_i is molar flux and can be calculated as $j_+ = -\frac{I}{\alpha_+ \delta_+ FA}$ and $j_- = \frac{I}{\alpha_- \delta_- FA}$. I, α_i, δ_i, F and A are the battery current, the specific active surface area of the electrode i, the thickness of the electrode i, Faraday's constant, and the electrode surface area respectively.

In SPM, the battery terminal voltage V is calculated with (2.10) where U_i is the OCV of the electrode i. The relationship between U_i and the surface stoichiometry x_i^s is obtained from pre-experiments. The surface stoichiometry is the ratio of the surface lithium concentration c_i^s to the maximum lithium concentration c_i^{max}.

$$V = U_+(x_+^s) - U_-(x_-^s) + \eta_+ - \eta_- \tag{2.10}$$

η_i is the overpotential on electrode i and is governed by the Butler-Volmer equation. By setting the charge transfer coefficient equal to 0.5, the η_i is represented by (2.11) where $i_{0,i}$ is the exchange current density. $i_{0,i}$ is a function of the reaction rate constant k_i, the electrolyte concentration c_e, and the surface lithium concentration c_i^s.

$$\eta_i = \frac{2RT}{F} \sinh^{-1}\left(\frac{j_i F}{2i_{0,i}}\right) \tag{2.11}$$

$$i_{0,i} = k_i F \sqrt{c_e} \sqrt{c_i^s} \sqrt{c_i^{max} - c_i^s} \tag{2.12}$$

Using electrochemical models to simulate a battery cell requires a large number of equations to describe the battery chemical reaction and quantities such as the electrode, separator and positive thicknesses are needed. The electrochemical model benefits cell designing [84] but the complexity of the electrochemical model leads to a heavy computational burden.

2.5.2 Data driven model

Data driven models (for example, neural network model, auto-regressive model, and support vector machine model) use a large amount of experiment data to train the model and do not directly simulate the physical or chemical process inside a battery [82].

Data driven models can estimate the battery internal states based on the battery external signal. For example, section 2.3.3.2 has discussed the SoC estimation method using data driven model (neural network). Apart from SoC estimation, data driven models can also be

used for terminal voltage prediction ([85]: auto-regressive model) and state of health estimation ([86]: support vector machine model).

Although data driven models avoid the complex mathematic description in electrochemical models, it requires a large amount of data to achieve good accuracy. Besides, the model training process normally takes a long time.

2.5.3 Equivalent circuit model

Equivalent circuit models are using simple electrical components to represent the main electrical properties of a battery. Some basic electrical properties of a battery are listed below which may not be totally included in every model.

1. Open circuit voltage (OCV): section 2.2.2 describes, the OCV of a battery changes with SoC which is the main part of the battery terminal voltage.
2. Ohmic resistance: when a current flow through a battery, an instantaneous voltage change will be witnessed as a result of ohmic resistance. The ohmic resistance mainly comes from the electrolyte, current collector, and the membrane in the battery [87].
3. Transient properties or time constant: during a resting process, after the instantaneous voltage change, a gradually voltage recovering process will happen which is related to the charge transfer and diffusion processes in the battery [88]. These chemical processes also effect the battery voltage during charging and discharging.
4. Self-discharge: a battery could be discharged through the path inside the battery. Self-discharge is a slow process in batteries. The typical self-discharge rate for lithium-ion batteries is 1-3% per month [89].

2.5.3.1 Internal resistance Model

Internal resistance model, as shown in Figure 2.13, consists of an ideal voltage source and a resistor representing the internal resistance of a cell. The model is simple, but the internal resistance can reflect the transient voltage change due to the diffusion and charge transfer process.

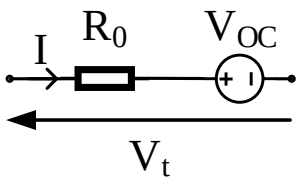

Figure 2.13 Internal resistance model (adapted from: [90])

2.5.3.2 Randles' model

Randles' model first published in [91] in 1947 to describe an electrochemical process. Since then, it has been modified or simplified for electrical circuit simulation. Reference [92] provides a Randles' model circuit for lead-acid battery simulation as shown in Figure 2.14. In the model R_0 represent the ohmic resistance of the battery, C_1 and R_1 represents the properties related to charge transfer and diffusion processes in the battery and R_d is the self-discharge resistance. In this model, the voltage on C_b represents the battery OCV which is appropriate for lead-acid batteries that has an almost linear OCV and SoC relationship as shown in Figure 2.6.

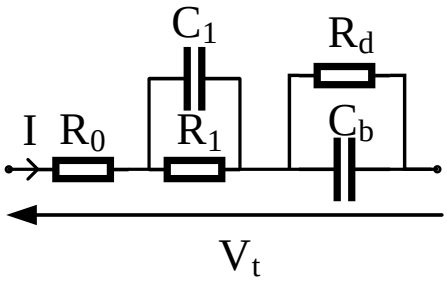

Figure 2.14 Randles' model circuit for lead-acid battery (adapted from: [92])

2.5.3.3 One-time-constant model

The one-time-constant model, as shown in Figure 2.15, uses a voltage source to replace the bulk capacitor C_b in Randles' model and the self-discharge resistance R_d is omitted while the rest part of the circuit remains the same. The value of the voltage source is SoC-dependent which makes it suitable for batteries with non-linear OCV and SoC relationship.

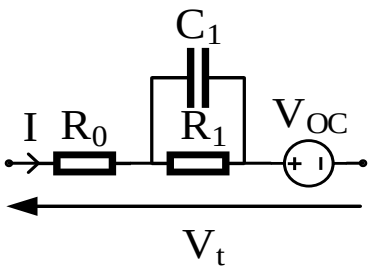

Figure 2.15 One time constant model (adapted from: [93])

2.5.3.4 Two-time-constant model

The two-time-constant model, as Figure 2.16 shows, is generated by introducing another RC branch into the one-time-constant model. In the two-time-constant model, one RC branch with a larger time constant emulates the diffusion process. The other RC branch with a smaller time constant is corresponding to charge transfer process.

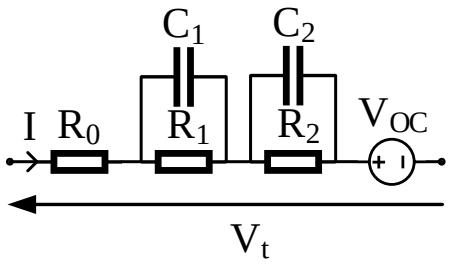

Figure 2.16 Two time constant model (adapted from: [94])

2.5.3.5 Constant and dependent parameter

In reference [95], a battery is represent with a Randles model where the component parameters of the equivalent circuit (R_0, R_1,C_1 and C_b) are constant. On the contrary, as reference [94,96,97] shows, the components value in the equivalent circuit models changes with SoC. In this case, either partially or all the parameters in the equivalent circuit models are set as SoC dependent.

Apart from the SoC, the value of the equivalent circuit parameters also vary with temperature [98], battery current value [99], ageing condition [100], etc. Introducing the dependency or nonlinearity between factors and parameters increases the model complexity. Whether or not introducing the nonlinearity of parameters should be decided by the application, simulation purpose, etc.

2.5.4 Battery pack simulation

As section 2.2.3 describes, for a large-scale battery pack, there are over tens of thousands of cells which are connected in series or parallel. If all the cells are identical, the voltage and current of a battery pack can be simulated by scaling-up a single cell's voltage and current according to the series/parallel relationship. Due to the existence of cell-to-cell variance, the battery pack simulation becomes complex. In this section, cell-to-cell variance will be introduced first which will be follow by a discussion of Monte Carlo simulation for battery.

2.5.4.1 Cell-to-cell variance

The differences between cells, namely the cell-to-cell variation (CtCV), is generally classified by whether it is brought about by intrinsic or extrinsic sources [101]. The intrinsic variations are caused by the difference in cell chemistry and electrical properties; for example, the impedance and capacity. On the other hand, factors like the unevenness of pack temperature, cooling system and external circuits are considered extrinsic sources. These variation sources also influence each other in difficult to predict ways [102].

Experiments and statistical analysis on CtCV have been widely conducted on cells with different sample sizes, from dozens to thousands [103–106]. The CtCV measurement mainly includes temperature, capacity, weight, DC resistance, AC impedances, self-discharge, calendar ageing and frequencies for typical impedance value.

The experiment results provide statistical data for variation research based on a simple electrical model [107]. In more sophisticated electrochemical models [84][108], the variation sources are considered from the other quantities such as the electrode thickness, electrode density and weight fraction of active material.

2.5.4.2 Monte Carlo simulation

After introducing parameter variance into the battery pack simulation, once simulation is not capable of representing the behaviour of the battery under the give parameter distribution. To solve this problem, the Monte Carlo method is adopted by repeating a large number of simulations.

Reference [109] provides an example of Monte Carlo analysis by considering the cell parameter variance. The author measured 50 cells to extract the parameter distributions of

equivalent circuit components and studied the influence of the parallel branches number on parallel-series structure battery pack (the battery pack contains two parallel branches and each branch consists of 108 series connected cells). For every configuration, five hundred simulations were completed. The authors used the maximum, minimum, and median values as metrics to analyse the losses in battery packs. Moreover, the mean value and standard derivation of cell capacity are used to measure cell degradation.

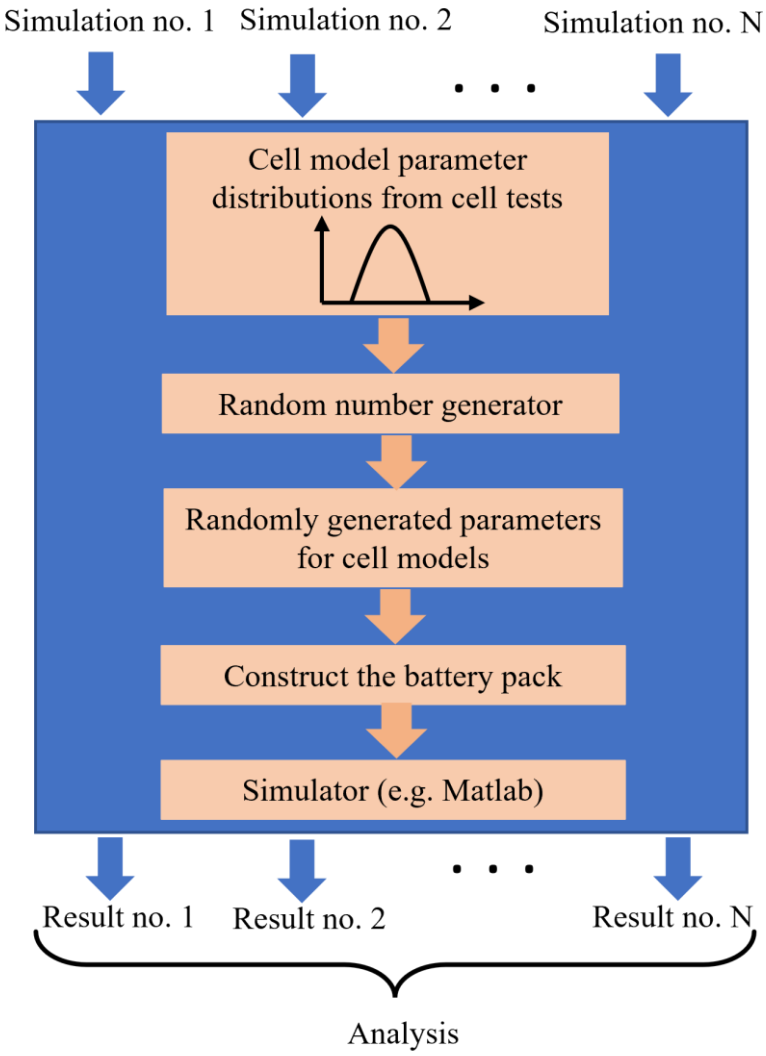

Figure 2.17 The process of Monte Carlo Analysis on battery pack simulation

In summary, the process of the Monte Carlo method on battery pack simulation is showed in Figure 2.17. Since the parameter is uncertain, the parameter distribution is used to generate the data for simulations. N times of independent simulations are carried on with the same distribution obtained from pre-measurements. The general conclusion will be made from all the N times simulation.

2.6 Summary

This chapter introduced the background information of battery energy storage systems (BESSs) which includes battery chemistries, battery properties, the battery management system (BMS), applications of battery energy storage system, battery pack simulation with cell-to-cell variation (CtCV), etc. General functions of a BMS have been discussed in this chapter and the BMS in large-scale BESS will be discussed in the following chapters. Besides, the concepts defined in this chapter such as state of charge, capacity, etc. will be frequently used in this thesis.

As has been discussed in section 2.5, equivalent circuit models (ECMs) are widely used in battery simulations. However, ECMs are normally identified from a cell. This work will present a more challenging ECM identification process on a large-scale BESS in Chapter 3. The computational complexity of battery equivalent circuit simulation increases with the cell number so that the CtCV is normally simulated within a small or medium-scale battery. This work will expand the simulations to large-scale batteries (>21k cells) with the help of an efficient simulator. The simulator will be presented in Chapter 4 and the cell level large-scale BESS simulation can be found in Chapter 5.

Chapter 3. Pack-level modelling for Willenhall Energy Storage System

Battery modelling is the study of the performance of a battery at a specific operating condition (load, temperature, history, age, etc.). Accurate modelling and simulation of battery energy storage systems are extremely important to both system builders and investors. The system builder is required to ensure satisfactory operation of the system under anticipated events and the investors undertake economic viability studies to ensure adequate return on investment. Essential to these activities is the fidelity of the battery model which should provide an accurate indication of the available capacity.

Willenhall Energy Storage System (WESS) is a grid-tied battery energy storage system which contains a 2 MW/1 MWh Toshiba lithium titanium oxide (LTO) battery pack. This chapter aims to build equivalent circuit models (ECMs) with a different number of time constants for WESS which can be used for the system simulation under specific loads, such as frequency service.

However, the traditional ECM parameter identification method for single cell cannot be directly applied on a large-scale battery energy storage system (BESS) like WESS due to hardware limitations and software restrictions in WESS. This chapter proposes a modified parameter identification method in the time domain that can be used for large-scale BESSs (e.g. WESS). During the parameter identification process, WESS was subjected to power pulse profiles from which the corresponding voltage and current waveforms were used to extract equivalent circuit parameters for RC equivalent circuit battery models.

The experiments for parameter identification reveal some properties in WESS related to the controller, state of charge calculation, battery management system, etc. The WESS has a power-controlled inverter which cannot provide convenient control of current. The SoC in WESS's BMS is estimated from the Coulomb counting method with a self-correction mechanism, which could contain a large error after a long-term charging or discharging. The WESS's BMS recorded data at a low frequency (1Hz) with frequent data missing. These issues could lead to misinterpretation of the battery system behaviour and complicate the battery modelling process. In this chapter, these phenomena will be discussed alongside some experimental profiles.

3.1 Experimental platform: Willenhall Energy Storage System

WESS is a grid-connected energy storage system research platform. The 2 MW / 1 MWh battery enclosure located at Willenhall consists of 21,120 Toshiba SCiB LTO cells. The connection of the cells is shown in Figure 3.1. Working from the pack to cell level: the pack contains 40 parallel connected racks. Within one rack, there are 22 series-connected 2P12S modules [110]. Every 2P12S module consists of 12 series of 2 parallel cells. The blue dashed lines in Figure 3.1 represent the self-balancing paths in WESS battery. Compared to the single SCiB LTO cell, WESS's voltage, maximum allowed current, Ah capacity, and power are significantly increased because of series and parallel connections. The complex internal connection provides WESS with more paths for self-balancing current and greater flexibility in maintenance and operation.

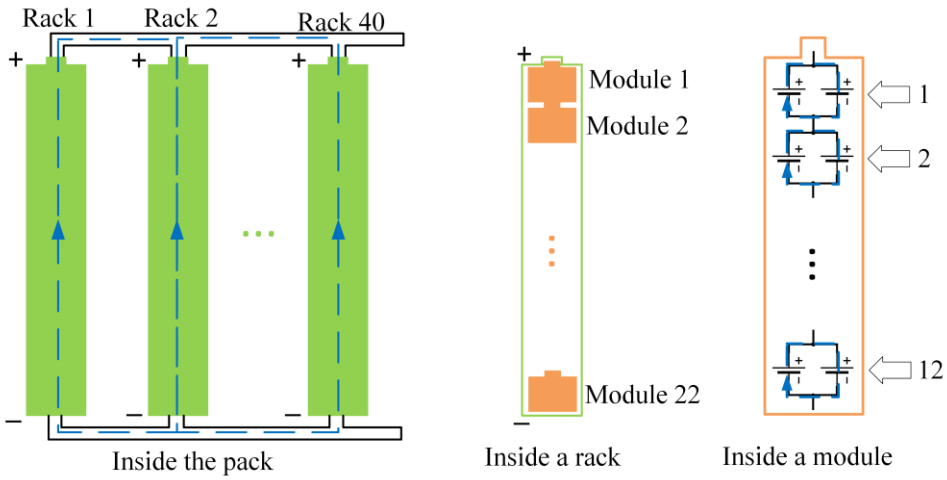

Figure 3.1 Schematic diagram of cell connection inside WESS battery

LTO cells are noted for their exceptional performance on lifetime and safety [111]. SCiB LTO cells used in WESS have a 20 Ah nominal capacity and could be operated between 1.5 V and 2.7 V. These LTO cells have a maximum rated charge and discharge current of 160 A (8 C-rate) and could work under a temperature as low as -30°C. SCiB LTO cells have been shown to survive over 1,500 cycles (decrease to 80 % capacity) and can be charged from 0% to 80% SoC in just 6 mins [111]. For lithium iron phosphate cells, the suggested continuous charging current is normally restricted to 1 C-rate or lower. Thus, constructing a BESS using LTO provides greater accessible power than a similar system built using lithium iron phosphate cells.

Toshiba provided its own BMS for WESS. The main functions of a BMS include: safety and protection for the battery and also facility and the operators; providing crucial information such as battery terminal voltage, current, SoC and temperature to the operator (software management platform) and to help optimise the overall battery performance and maintain lifetime. Under the supervision of the BMS, the operator can charge or discharge the battery within a limit of 5% to 95% SoC. The operation beyond this SoC limitation is very rare.

3.2 Equivalent circuit models and traditional parameter identification

3.2.1 Equivalent circuit models

Equivalent circuit models (ECMs) use simple electrical components to simulate the dominant behaviour of the battery/cell. Figure 3.2(a) and (b) provide two examples of battery ECMs with a different number of time constants, which will be used for modelling Willenhall Energy Storage System (WESS) later in this chapter. Commonly, three electrical behaviours are described in an ECM. First, ohmic resistance R_0 corresponding to the instantaneous voltage drop when a current flows through a battery/cell. This resistance mainly comes from electrolyte and contact resistance. Second, a parallel connected resistor and capacitor branch (or branches) are used to simulate the dynamic responses of the battery including the electrochemical diffusion process and charge transfer reaction [112]. The voltage source corresponding to the battery/cell's open circuit voltage (sometimes termed the equilibrium terminal voltage). The number of time-constants is chosen to balance model accuracy and computation cost. Generally, model accuracy increases with the number of time constants [113].

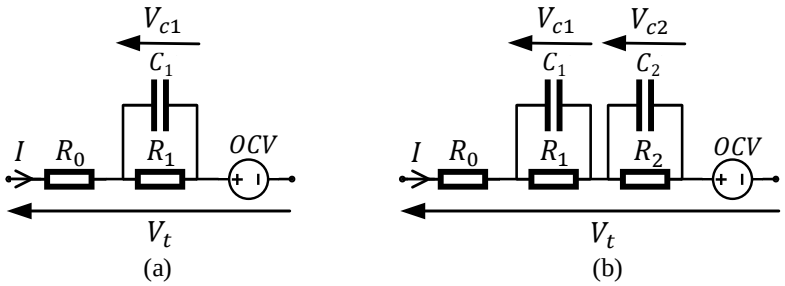

Figure 3.2 Battery equivalent circuit models (a): ECM1; (b): ECM2

Equations (3.1)-(3.3) are the mathematical expressions for the relationship between the battery current *I* (defined as flowing into battery, i.e. charging) and terminal voltage V_t in

ECM1. The state of charge (SoC) is calculated using current integration and is relative to the maximum battery capacity Q and initial SoC value S_{init}. The value of $R_0, R_i \& C_i$ and open circuit voltage (OCV) are all SoC dependent. In this thesis, in the equations S and V_{OC} are the values of SoC and OCV respectively.

$$dV_{C1}(t)/dt = -V_{C1}(t)/(R_1(S(t))C_1(S(t))) + I(t)/C_1(S(t)) \tag{3.1}$$

$$V_t(t) = V_{OC}\big(S(t)\big) + I(t)R_0(S(t)) + V_{C1}(t) \tag{3.2}$$

$$S(t) = S_{\text{init}} + \int_0^t I(t)dt\,/Q \tag{3.3}$$

The process used to simulate the battery is illustrated in Figure 3.3 where the battery current provides SoC from which the battery equivalent circuit parameters of R_0, R_i and C_i and OCV are determined from *an a priori* curve-fit. Δt is the simulation step length which is set as 1 s in this chapter. The value of resistances and capacitances are estimated through the linear interpolation method whereas a cubic spline is used to determine OCV under different SoC. During the simulation, in every time step, these values are updated according to the pre-calculated SoC. Then the battery internal state V_{C1} and terminal voltage are obtained.

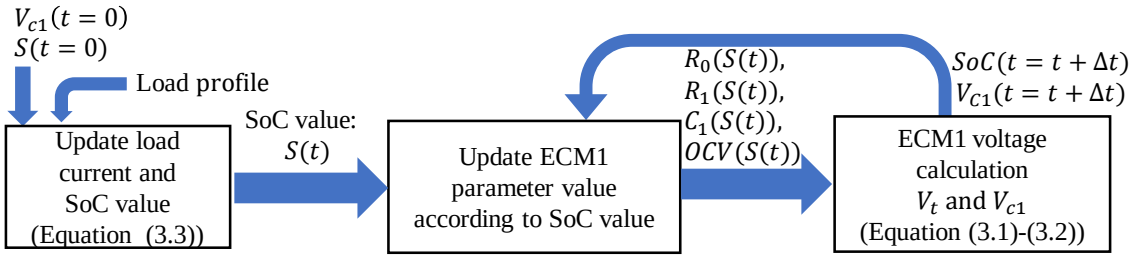

Figure 3.3 Simulation processes, using ECM1 as an example

3.2.2 Parameter identification method for a small battery

To identify the ECM parameters for single cell or small-scale battery pack, a constant pulse current experiment is normally conducted in a laboratory environment. The cell current value is accurately controlled, and experiment data is recorded in high resolution and sample rate.

Reference [114] provides a typical parameter identification method in time domain for battery equivalent circuits and the method is demonstrated with a two time constant ECM

(as shown in Figure 3.2(b)) in which a cell is discharged with a constant pulse current at every 10% SoC and the voltage response during resting is used for parameter identification.

Figure 3.4 shows the battery voltage profile after a constant current pulse discharge (PD). t_{cpe} is the time instant when discharging current pulse ends. At t_0, the current decreases to zero. There are two time windows (time window 1: from t_{11} to t_{12}, time window 2: from t_{21} to t_{22}), are chosen for identifying the RC branches with different scale of time constant in Figure 3.2(b), for example $\tau_1 = R_1C_1 \ll \tau_2 = R_2C_2$. In [114], time windows are chosen as $t_{11} = 0$ s, $t_{12} = 12$ s, $t_{21} = 240$ s and $t_{22} = 600$ s, and typically $t_{11} = t_0$.

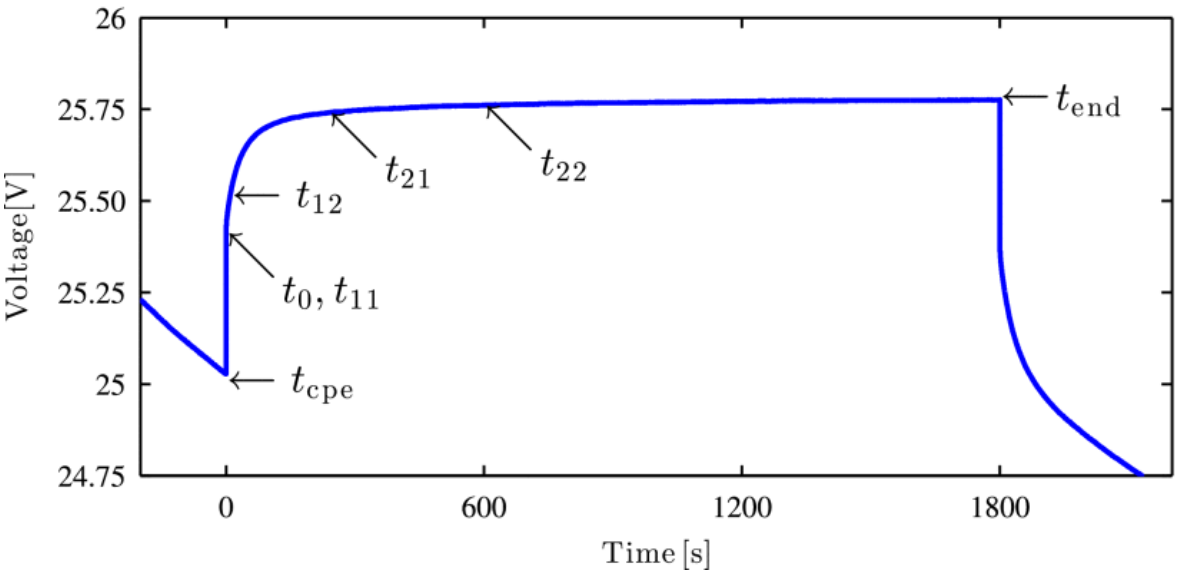

Figure 3.4 Battery terminal voltage profile during a pulse discharge (PD) test (source: [115])

The method assumes that at the end of the first window, the R_1C_1 branch with a smaller time constant is fully discharged and have zero voltage. At the end of resting t_{end}, the battery terminal voltage V_t equals the OCV (V_{OC}). For $t > t_{21}$, V_{C2} (the voltage on R_2C_2) can be written as (3.4):

$$V_{C2}(t) = V_{C2}(t_{21}) \cdot \exp\left(-\frac{t - t_{21}}{\tau_2}\right) \tag{3.4}$$

At t_{22}, terminal voltage equals $V_{\text{t}}(t_{22})$ and the larger time constant τ_2 can be estimated with (3.5) where V_{C2} at t_{21} and t_{22} can be estimated with (3.6).

$$\tau_2 = \frac{t_{22} - t_{21}}{\ln\left(\frac{V_{C2}(t_{21})}{V_{C2}(t_{22})}\right)} \tag{3.5}$$

$$V_{C2}(t) = V_t(t) - V_{OC} \tag{3.6}$$

Because the value τ_2 is obtained, the value of V_{C2} can be calculated for $t > 0$ including the time window 1. During the time window 1, V_{C1} (the voltage on the R_1C_1) can be described with the following (3.7):

$$V_{C1}(t) = V_{C1}(t_{11}) \cdot \exp\left(-\frac{t - t_{11}}{\tau_1}\right) \tag{3.7}$$

At t_{12}, terminal voltage equals $V_{\mathrm{t}}(t_{12})$ and the small time constant τ_1 can be estimated with (3.8) where V_{12} at t_{11} and t_{12} can be estimated with (3.9) and (3.4).

$$\tau_1 = \frac{t_{12} - t_{11}}{\ln\left(\frac{V_{C1}(t_{11})}{V_{C1}(t_{12})}\right)} \tag{3.8}$$

$$V_{C1}(t) = V_t(t) - V_{\mathrm{OC}} - V_{C2}(t) \tag{3.9}$$

In the method, ohmic resistance R_0 is calculated from the instant voltage change ΔV at the beginning or the end of the discharging current as (3.10) shows where I is the amplitude of the pulse current. Normally the voltage change ΔV during 0.1 s is used for R_0 estimation [116].

$$R_0 = \left|\frac{\Delta V}{I}\right| \tag{3.10}$$

In theory, the equivalent circuit parameter identification method developed on a single cell can be also applied to large-scale batteries. However, there are some obstacles in large-scale battery systems like WESS causing difficulties in applying the method. As will be discussed in section 3.3, there is a long current raising and falling process in WESS which could last for over 10 s. During this process, the voltage on R_0, R_1C_1 and even R_2C_2 are changing at the same time. The changing of battery terminal voltage is the combined result of R_0, R_1C_1 and R_2C_2. This slow current response causes a slow change in battery terminal voltage, which not only makes the ohmic resistance method invalid but also basically eliminates the

existence of the first window. Other properties like low sample rate, data missing, and low data resolution exacerbate the situation and make the R_0 calculation less reliable.

In the proposed parameter identification method in this chapter, WESS is discharged with a constant power load. R_1C_1 and R_2C_2 are identified from a voltage profile during resting using the nonlinear least square error method. The ohmic resistance R_0 is calculated as a supplementary element to complete the function of ECM. Before discussing the detail of the method, the parameter identification experiments on WESS will be introduced first.

3.3 Experiment profiles

To build ECMs for WESS, two similar pulse experiments were conducted on two different days. In the two experiments on WESS, the battery voltage and current and the real power were recorded by the battery management system (BMS). The minus sign of the current and real power indicates that the battery is being discharged.

3.3.1 Controller related phenomena: inverter and current response speed

As a grid-connected facility, the inverter of the battery pack is designed for power control rather than current control. The power control strategy is necessary for a frequency response service where the demanding output and operating criteria are normally power. However, this is at the expense of losing direct and accurate control of the battery current. Due to this restriction, in the WESS, to identify the ECM parameter value, a constant current experiment is replaced by a constant power test (500 kW, 0.5 C). C is the theoretical current required to discharge the battery at constant current in one hour. Figure 3.5(a) and (b) show the battery's real power profile on 3rd (day 1) and 4th (day 2) September 2019 respectively.

To provide a direct view of the magnitude change of the recorded data, the current and real power are plotted with a reversed vertical axis. In the following discussion, the describing words such as 'increase' and 'decrease' refer to the change of magnitude, unless otherwise specified.

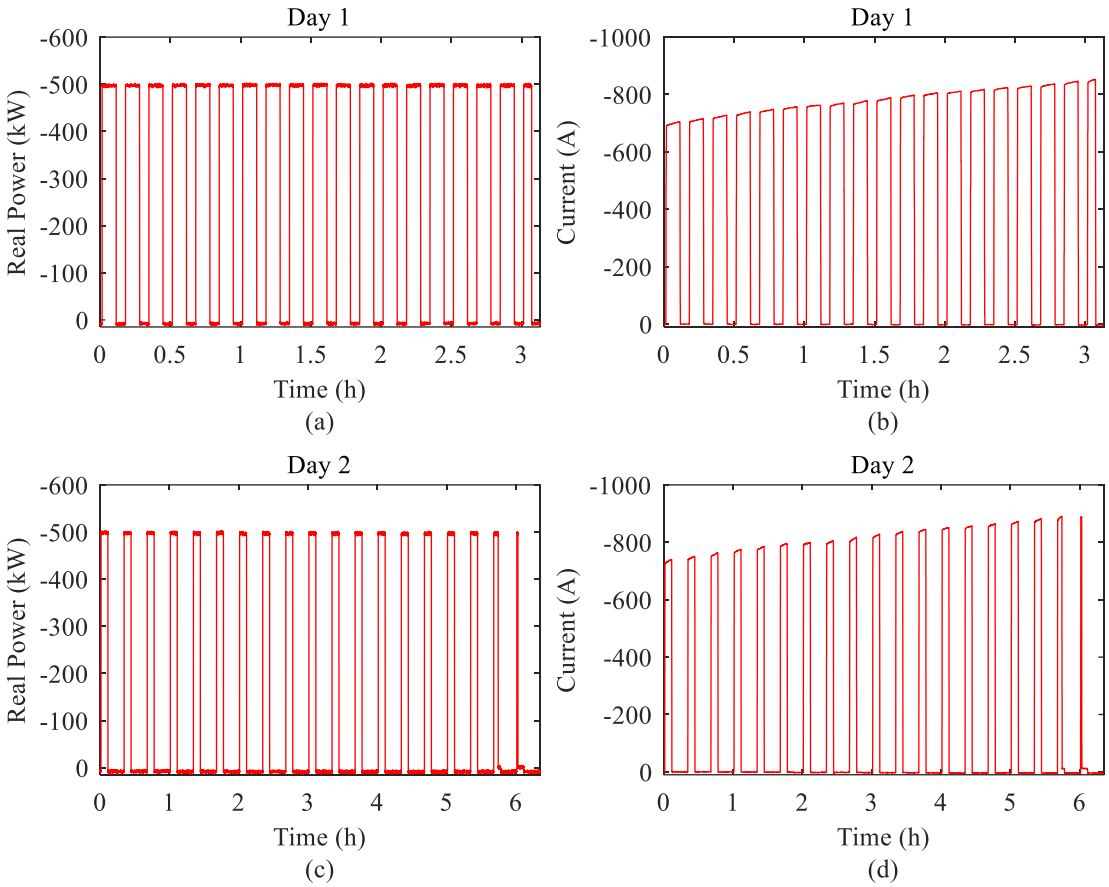

Figure 3.5 Experimental real power and battery current profiles, on day 1 and day 2. (note: 'Time' refers to the time in the experiments)

For both days, the battery was discharged from 95% SoC and expected to be discharged in 5% SoC intervals until it reached a minimum of 5% SoC. Each discharge interval is characterised by discharge and then relaxation. For the test on day 1, each discharge interval takes 10 mins including discharging (~6 mins) and resting (~4 mins) phases. For the test on day 2, each pulse takes 20 mins including discharging (~6 mins) and resting (~14 mins) phases. At the end of the tests, some discharge intervals are incomplete since the operation of the test sequence is overridden by the protection features of the BMS. The battery current, Figure 3.5(b) and (d), in constant power tests is no longer constant because the battery voltage is changing during discharging.

In addition to the varying current pulse amplitude, the fall-time of current is also not ideal. Figure 3.6(a-b) and (c-d) show the falling process of the first power pulse in the two experiments and the corresponding instantaneous battery current. Although the power level is seen to fall rather rapidly, the current takes longer to achieve the desired value. For the pulse on day 2 (Figure 3.6(c), (d)) the current lags the power profile by several seconds. The

battery power can be decreased from 500 kW to 0 kW in 1 or 2 seconds (Figure 3.6(a), (c)). However, it takes WESS more than 10 s to decrease the discharging current from ~700 A to ~0 A (Figure 3.6(c), (d)). A similar effect is also observed at the start of each power pulse discharge. This slow current change may lead to a bad performance under some applications that require fast responses, and also makes the battery voltage change due to ohmic resistance hard to be identified. It is believed that the battery power recorded by BMS is the aiming power of the inverter's control system rather than the real-time power of the battery. By contrast, the current response of batteries in laboratory tests is much faster (e.g. 0.01 s in [117]).

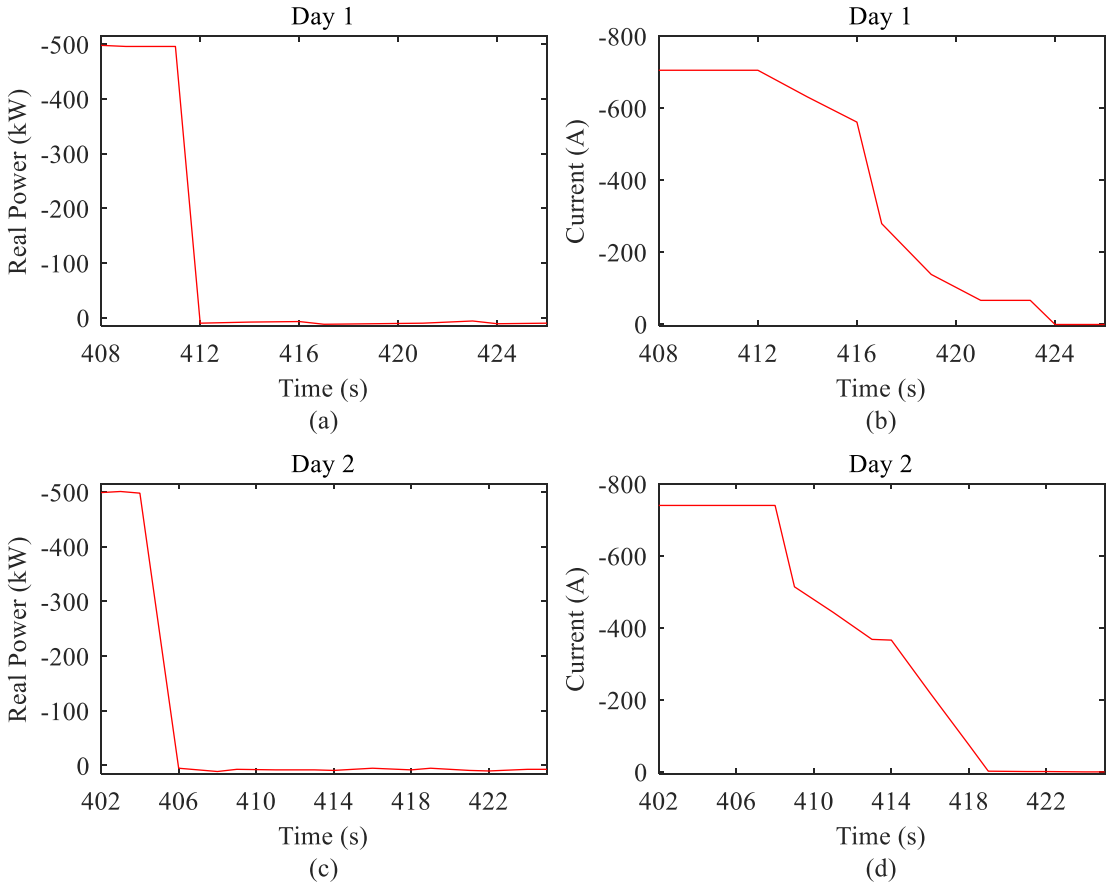

Figure 3.6 The first pulse of the experimental real power and current profiles on day 1 and day 2. (note: 'Time' refers to the time in the experiments)

Considering the WESS has an approximate 1600 Ah capacity, it is estimated that this rate-limiting is, in fact, much slower than a lithium battery's expected performance. The reason for this phenomenon is not clear but it is suspected that it is caused by a rate-limit setting within BMS or energy management system. Thus, the model of the battery which is obtained from this dataset will also include feature behaviour from the BMS and inverter.

3.3.2 State of charge related phenomena: calculation, correction and resolution

Coulomb counting (current integration) is a widely accepted technique for estimating SoC. Since current integration is known to suffer from issues associated with drift and sensor precision, the BMS often periodically corrects SoC estimations. Figure 3.7(a) and (c) show SoC as a function of time for the day 1 and day 2 tests. SoC can be seen to decrease during discharge and the relaxation intervals can be readily seen. Figure 3.7(d) show the BMS applying a correction to its estimate during quiet periods of little or no current flow. It is believed the BMS is using the OCV and SoC relationship to correct the SoC estimation value. Figure 3.7(d) shows a 0.9 percentage point SoC change, labelled at ΔSoC, which is a correction for SoC estimation. This "correction" step in SoC was observed in the data of day 2 experiment but not in the day 1 experiment (Figure 3.7(b)), which indicates that this type of correction only occurs when the quiet periods are of sufficient length (5 mins in WESS) for the terminal voltage to approximate OCV.

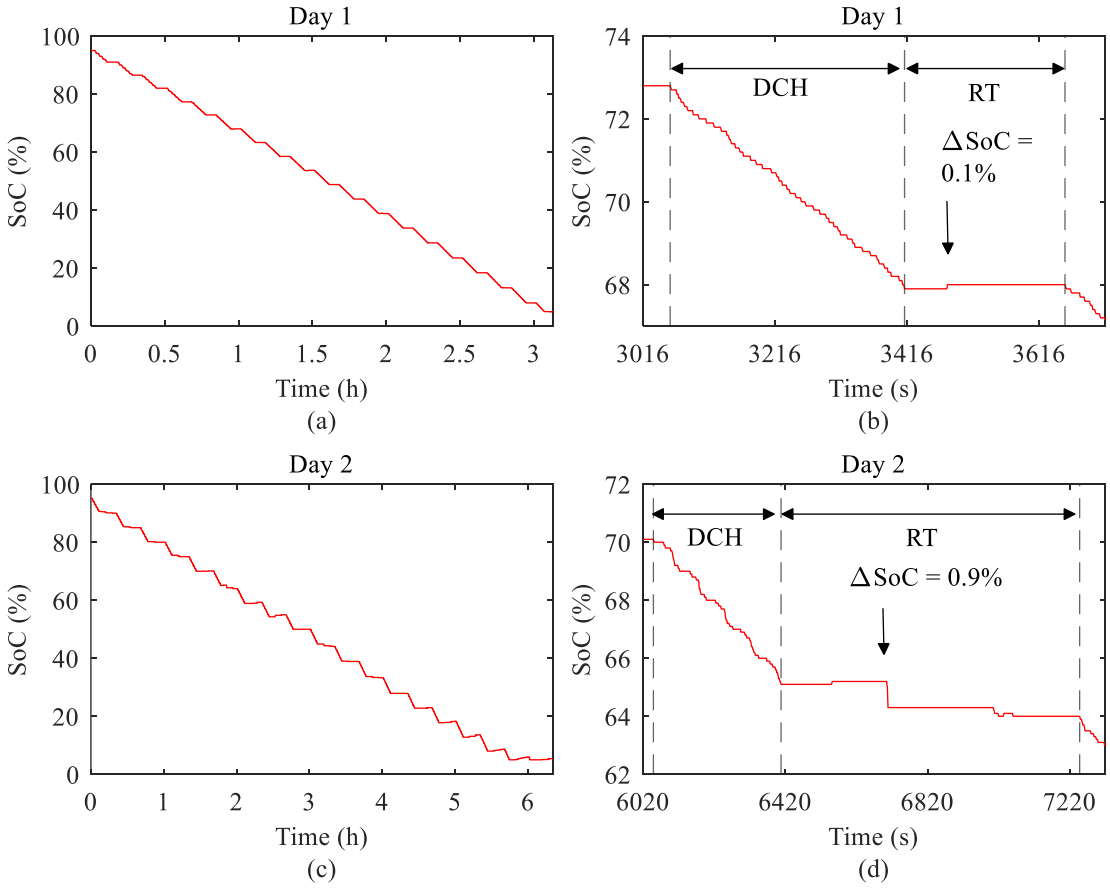

Figure 3.7 The SoC profiles and the pulse around 70% on day 1 and day 2. (note: 'Time' refers to the time in the experiments. DCH: discharge. RT: rest)

3.3.3 Battery management system data related phenomena: sample rate, resolution and accessibility

Table 3.1 shows some points from the raw dataset of day 1. As the first column in Table 3.1 suggests, the maximum data sample rate is 1 Hz and samples often go missing. By contrast, the data sample rate in single cell or small battery laboratory tests is normally much higher (e.g. 10 Hz in [113,118] and 100 Hz in [117]). The resolution of the reported battery current measurements is 1 A and 0.1 V for the voltage measurement. The quantisation of the current might lead to inaccurate SoC estimation. For example, if there is a constant 0.99 A measurement error, after 24 hours continuous operation the SoC has an error of 1.5%. Besides, the ohmic resistance of a battery is small (in milliohms) and the low resolution of current and voltage measurements introduces a large error in its calculation in the traditional method ($R_0 = \left|\frac{\Delta V}{I}\right|$).

Table 3.1 WESS's partial history data on day 1

Time (24h format)	Current (A)	Voltage (Volt)	SoC (%)	Real power (kW)
7:30:56	-718	655.5	88	-504
7:30:58	-718	655.5	88	-503
7:30:59	-719	655.3	87.9	-500
7:31:01	-719	655	87.9	-502
7:31:03	-720	654.9	87.9	-500
7:31:04	-720	654.9	87.9	-501
7:31:06	-720	654.9	87.8	-503
7:31:08	-720	654.8	87.8	-505
7:31:09	-720	654.8	87.8	-502

3.3.4 Voltage response in profiles and pseudo-OCV model

Interesting behaviour regarding the shape of the terminal voltage curve has been observed for SoC around 60%, Figure 3.8(a) and (b). The voltage response to the discharge intervals repeats a similar pattern where the voltage decreases on the application of the discharge pulse and then increases during the relaxation time. Figure 3.8(a) and (b) show the instantaneous battery voltage and the upper and lower envelopes associated with the battery voltage deviation that occurs during the discharge and rest cycles. As can be seen, the separation between the two envelopes is constant for the majority of the experiment. However, at approximately 60% SoC the pulse discharge voltage waveform is somewhat different. The voltage rising process around 60% SoC is slower than that in the other SoC zones.

Consequently, the tops of these voltage profiles during resting around 60% SoC are no longer as flat.

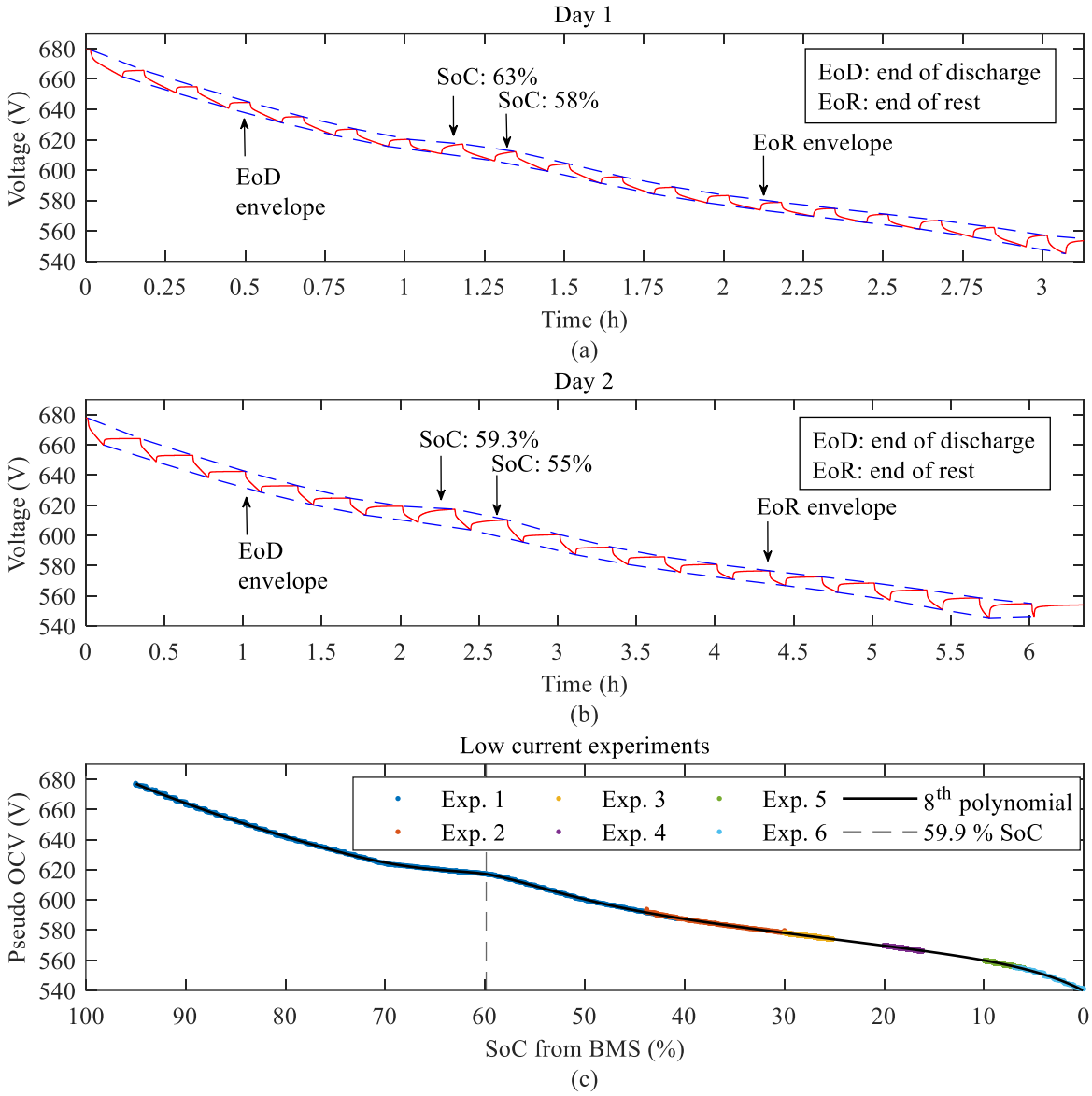

Figure 3.8 Experimental voltage profiles and pseudo-OCV. (a) and (b): battery voltage profiles from the experiments on day 1 and day 2 respectively; (c): pseudo-OCV vs. SoC from BMS obtained from six separated low current experiments (fitted with two 8th polynomial equations)

This unusual voltage behaviour around 60% SoC happened in both day 1 and day 2 experiments indicating that it is a behaviour of the battery (or the BMS) rather than the profile. As will be discussed in the following paragraph, it is believed this response is related to the battery's OCV since the end of rest terminal voltage is close to OCV. The depressed resting voltage profile located around 60% SoC requires a large time constant within the ECM.

The OCV and SoC have a stable relationship so that SoC is often used to estimate battery OCV based on an a priori characterisation of this relationship. One commonly used method to determine this relationship is by measuring OCV at least once every 10% SoC and then approximating this response using a polynomial (or other equation) to model the overall relationship [119]. Although viable, this method sometimes fails to capture the minor details between the OCV-SoC data points. In another method, a small current is used to discharge the battery and the terminal voltage is assumed to be equal to OCV under these small-signal conditions. In this method, the battery terminal voltage under the low-current is widely known as pseudo-OCV. The word "Pseudo" indicates the fact that pseudo-OCV is close but not identical to OCV.

$$V_{OC} = p_1 S^8 + p_2 S^7 + p_3 S^6 + p_4 S^5 + p_5 S^4 + p_6 S^3 + p_7 S^2 + p_8 S + p_9 \quad (3.11)$$

Table 3.2 Coefficients of 8th polynomial equations: pseudo-OCV and SoC relationship (show 4 significant digits).

Coefficients	SoC <= 59.9%	SoC > 59.9%
p_1	-1.096×10^{-11}	7.334×10^{-10}
p_2	2.413×10^{-9}	-4.458×10^{-7}
p_3	-2.323×10^{-7}	1.179×10^{-4}
p_4	1.328×10^{-5}	-1.770×10^{-2}
p_5	-5.063×10^{-4}	1.651
p_6	1.344×10^{-2}	-97.93
p_7	-0.2428	3605
p_8	3.506	-7.527×10^{4}
p_9	539.7	6.830×10^{5}

Over the 4 years that WESS has been in service, six individual low current (< 0.01 C, 16 A) discharge experiments have been performed. As can be seen in Figure 3.8(c), the six experiments cover most of the SoC zone and so can provide a good estimator for OCV. The pseudo-OCV and SoC relationship is modelled with two 8th polynomial equations (3.11) and plotted in a black line in Figure 3.8(c). In the equations S and V_{OC} are the values of SoC and OCV respectively. The coefficients of the polynomial equations are listed in Table 3.2. It should be noted that, between 55% and 70%, a change in gradient is observed and it is believed this is responsible for the characteristics observed in Figure 3.8(a) and (b). As will be discussed in section 3.4.5, the pseudo-OCV and SoC relationship is close to the embedded OCV-SoC lookup table for SoC correction which is unsuitable for the ECM simulation in this chapter.

3.4 Equivalent circuit model parameter identification

3.4.1 Capacity estimation

Both ECMs require a value for the battery capacity Q. The SoC value at the beginning and the end of an experiment (day 1 or day 2) can be obtained from BMS history data and the charge accumulation can also be estimated using Coulomb counting ($\int_0^t I(t)\mathrm{d}t$). According to (3.3), Q is estimated as 1606.2 Ah for day 1 and 1605.3 Ah for day 2 and both values are close to the nominal capacity 1600 Ah.

3.4.2 RC parameter estimation

As mentioned in section 3.2.1, the ECM parameters are observed to be a function of SoC and so must be found through an identification process which is undertaken with the following assumptions:

i) the ECM can represent the electrical behaviour of the battery pack.

ii) the voltages on the internal RC branches within the ECM have reached a maximum value before the resting period (i.e. C is fully charged).

iii) the same internal capacitors are fully discharged by the end of the resting period.

iv) the operating temperature is constant.

v) the battery response model is independent of current direction or value.

The parameter identification is demonstrated with ECM1 and it is achieved by fitting the expected voltage responses of an ECM during resting, in (3.12), to the experimental voltage data through the nonlinear least square error method. Figure 3.9 shows this process using a power pulse at 58.5% SoC from the day 1 experiment. Figure 3.9(a) and (b) are the voltage and current profiles. Between t_1 and t_2, the battery discharging current first takes 12 s to increase from 0 to 760 A and then slowly increases to 770 A until t_2, during which the effect of R_0, R_i and C_i and OCV on battery terminal voltage are simultaneously combined and this complicated the identification process as the cause-and-effect of each parameter is not easily separable from the data. On the contrary, during the resting process (t_2 - t_3), the OCV is constant, and after the current decreased to zero, the voltage change is dependent on R_i&C_i

only (where $i = 1$ for ECM1). In Figure 3.9(c) and (d), the red and the blue lines are the battery terminal voltage profile during resting before and after the battery current completely transitions to zero.

Step 1: (3.12) describes the blue section of the battery terminal voltage response,

$$V_t(t) = k_0 + k_1 \cdot \exp(-(t - t_2)/\tau_1) \tag{3.12}$$

where k_0 is battery OCV which is estimated at slightly higher than or equal with the voltage at the end of resting (t_3):

$$V_t(t_3) \leq k_0 = \text{OCV} \tag{3.13}$$

and k_1 is the voltage on capacitor C_1 at the beginning of resting interval with a value approximated to IR_1 in which I is the current value at the end of discharge:

$$k_1 = V_{C1}(t_2) = I(t_2) \cdot R_1 \tag{3.14}$$

and τ_1 is time constant:

$$\tau_1 = R_1 \cdot C_1 \tag{3.15}$$

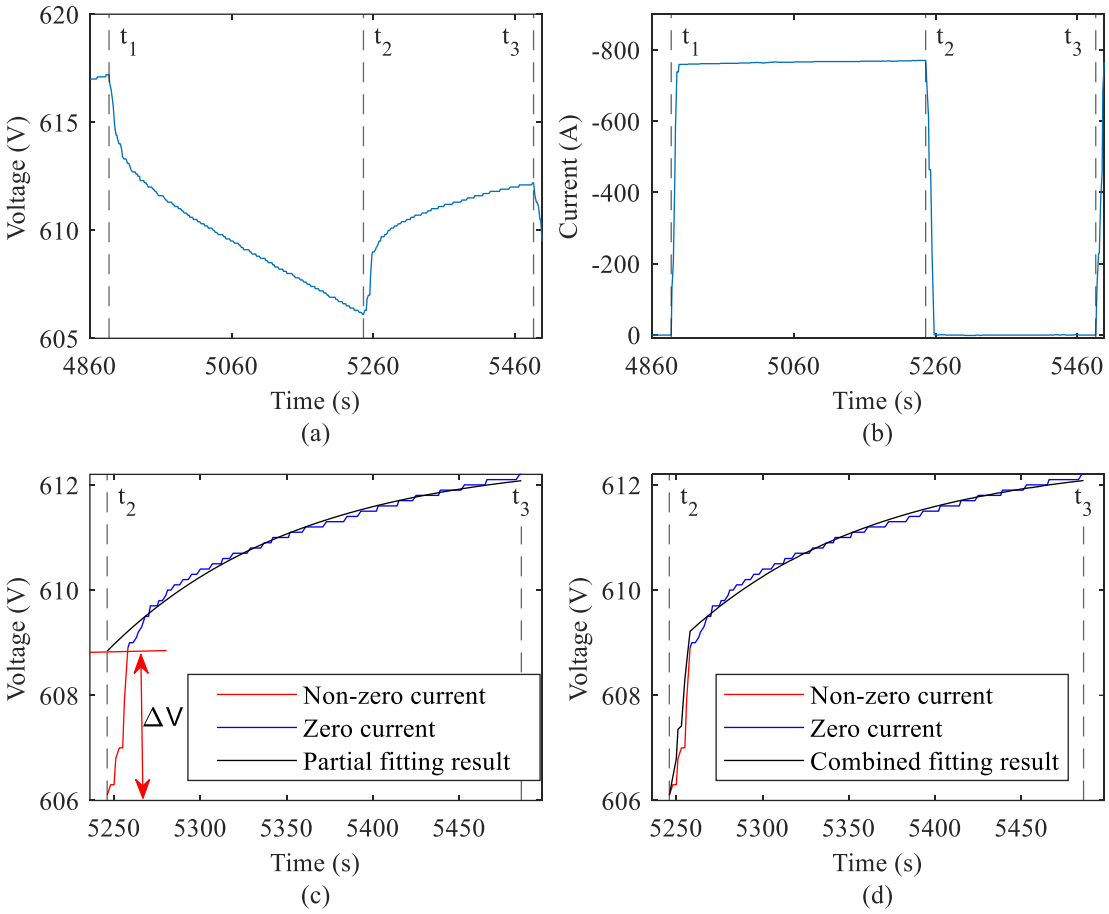

Figure 3.9 Curve fitting process for ECM parameter identification using the day 1 experiment at 58.5% SoC as an example: (a) voltage, (b) current, (c) step 1 of parameter identification, (d) step 2 of parameter identification

After the current step decreases to zero, the voltage (blue line) is assumed to only depend on the internal capacitor voltage (V_{C1}) and, hence, (3.12) can be used to estimate the value of R_1, C_1 and OCV. The black line in Figure 3.9(c) is the partial fitting result of battery voltage with the estimated value of R_1, C_1 and OCV. A significant change in voltage ΔV at t_2 is observed in the response. This change is assumed to be due to the effect of the series resistance R_0. Thus, step 2: R_0 can be estimated using $R_0 = \left|\frac{\Delta V}{I(t_2)}\right|$. The combined response (of R_1, C_1 and R_0) is shown as the black line in Figure 3.9(d). The parameter extraction process for the 2 time-constant ECM is similar.

3.4.3 Equivalent circuit model 1 (ECM1) parameters

The first column of plots in Figure 3.10 presents the ECM1 parameters as a function of SoC for both day 1 and day 2 experiments. The general trend between 90% and 70% SoC is that

the values of $R_0 + R_1$, in Figure 3.10(e), are approximately constant. However, between 70% and 50% SoC, as SoC decreases the total internal resistance has a sudden increase and then quickly restores to the previous level. After 50% SoC for day 1 (and 40% for day 2) the total internal resistance gradually increases. It can be observed that the parameters R_1 (diffusion resistance) and R_0 (ohmic resistance) have the same order of magnitude. R_1 has a similar change trend to $R_0 + R_1$ except for a difference that R_1 has a slight decrease as SoC decreases between 90% and 80% SoC. For R_0, the value fluctuates around 4.5 mΩ for day 1 and 3 mΩ for day 2 in the SoC zone 15% - 90% and then increase steeply as SoC decreases in SoC zone 5% - 15%.

For the time constant τ_1, both day 1 and day 2 have a peak value at around 60% SoC which coincides with the aforementioned unusual behaviour discussed with respect to Figure 3.8. However, for most SoC points, day 1 has a smaller time constant than day 2, Figure 3.10(g). It is believed that it is caused by the nature of the modelling process. In detail, the modelling process is a fitting process to determine the optimal solution which causes the least error for the candidate model (ECM1 in this case) and the experimental data. The time constant that the algorithm provides is the dominant time constant or the optimal time constant value that represents the overall effect of all the time constants in the battery. Compared to day 2, day 1 has a shorter resting time. Hence, the resting voltage change on day 1 is dominated by the smaller time constants. As a result, the calculated time constant is smaller than day 2's result.

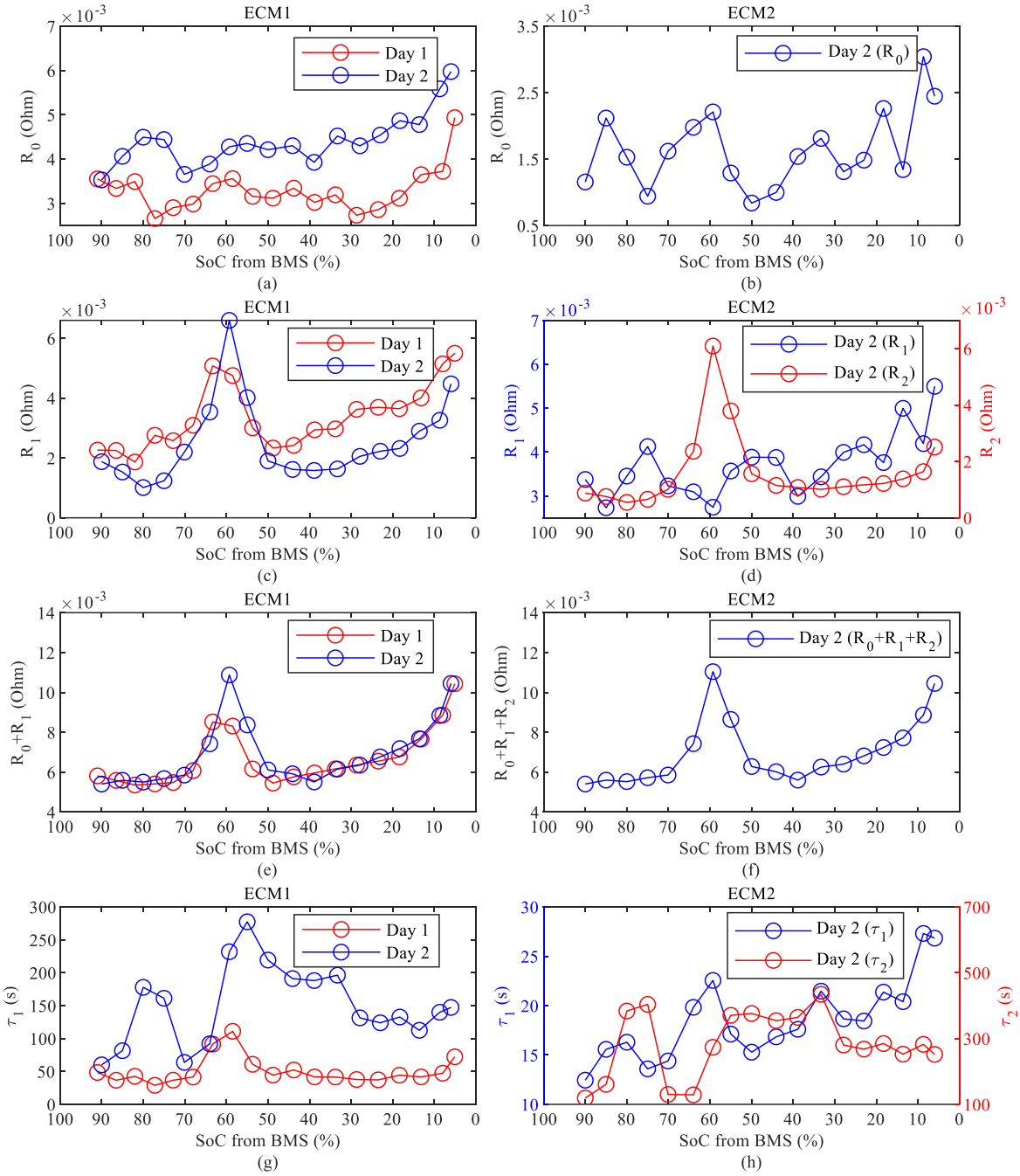

Figure 3.10 ECM1 and ECM2 resistance and time constants identified from the experiments on day 1 and day 2 with respective to SoC BMS. The first column: two sets of ECM1 identified from day 1 and day 2 experiment; the second column: ECM2 identified from day 2 experiment

3.4.4 Equivalent circuit model 2 (ECM2) parameters

The second column in Figure 3.10 shows the parameter results extracted from the day 2 experiment for a two time constant model ECM2 (Figure 3.2(b)). This result shares similarities with ECM1. It can be observed that the total internal resistance for ECM2, $R_0 + R_1 + R_2$, (Figure 3.10(f)) is almost identical to that of ECM1, $R_0 + R_1$, extracted from day

2 (Figure 3.10(e), blue). The total internal resistance is responsible for total voltage change (IR drop and polarization voltage) during the resting and so the total internal resistance for ECM1 and ECM2 identified from the same voltage profile must be identical.

R_0 and R_1 identified from day 2 experiment (Figure 3.10(b) and (d) in blue) have the same changing trend with R_0 from day 1 in Figure 3.10(a). As SoC decreases, their value fluctuates among high SoC zone and increase in lower SoC zone. As has been discussed, R_0 cannot be directly calculated from the voltage change and it is estimated after the RC time constants have been identified. Consequently, in ECM1 the small time-constant information is hidden inside the ohmic resistance R_0 and also the single RC branch. Compared with ECM1, in ECM2, the appearance of the small time-constant resistance R_1 reveals the hidden information and causes an obvious decrease in R_0 (Figure 3.10(a), blue vs. Figure 3.10(b)). For branch 1 (τ_1), Figure 3.10(h) in blue, the peak value occurs at around SoC of 60%, which is consistent with observations for ECM1. However, the peak in τ_2 (Figure 3.10(h) in red) at 75% SoC coincides with the first peak at SoC=75% for ECM1 (Figure 3.10(g), blue). It should be noted that the day 1 experiment operated with a shorter rest duration and thus contained less information to identify τ_2 and this is the reason for providing only ECM2 parameters for day 2.

3.4.5 OCV-SoC response and ECMs built with the SoC from BMS and the Coulomb-counting method

OCV-SoC relationship in a battery should be irrelevant to the number of time constants in ECM. However, due to the SoC self-correction mechanism in the BMS of WESS, the determination of OCV-SoC relationship for ECMs become complex. During the previous ECM parameter identification process, the OCV value was estimated alongside the value of R_0, R_i and τ_i ($i = 1$ or 2). The OCV-SoC relationships estimated from the day 2 experiment during ECM1 and ECM2 identification processes are presented in Figure 3.11(a) in circle and asterisk markers, respectively. As Figure 3.11(a) shows, these two sets of OCV-SoC points are extremely close to each other and are located on the pseudo-OCV line (shown in black). As discussed before, the SoC values in these OCV-SoC sets that are estimated from the day 2 experiment are corrected by BMS which indicates that BMS SoC in low current experiments is the estimated from OCV-SoC lookup table; The pseudo-OCV model obtained from the experiments is the same as the embedded lookup table.

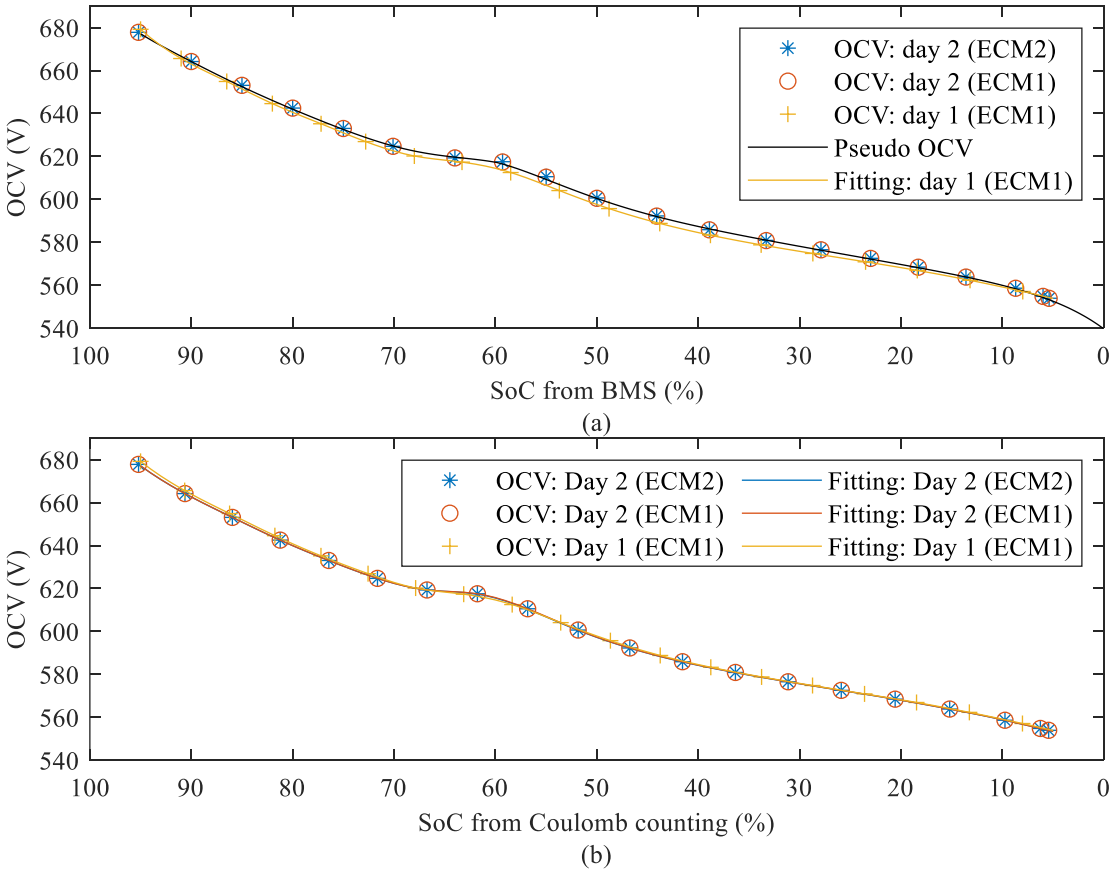

Figure 3.11 The OCV value estimated from different experiments (i.e. day 1 and day 2) and ECM models (i.e. ECM1 and ECM2) with respect to SoC from (a) BMS and (b) the Coulomb-counting method

However, in the simulations in this chapter, the SoC is calculated by the Coulomb-counting method which does not have the self-correction mechanism. In this specific case of WESS, using the SoC calculated by the Coulomb-counting method to estimate the OCV value through an OCV-SoC relationship built with the SoC value after self-correction causes an error. The same problem caused by the difference between the BMS SoC and Coulomb-counting SoC also exists in the models of parameters R_0, R_i and τ_i ($i = 1$ or 2).

The purpose of this work is to build battery energy-storage system ECMs suitable for system modelling. This modelling process is demonstrated on WESS which is a specific case, as was mentioned earlier in this section. It is preferable to build ECM with the SoC estimated by the Coulomb-counting method rather than the SoC from BMS. The value of R_0, R_i and τ_i ($i = 1$ or 2) under SoC measured using the Coulomb-counting method is presented Figure 3.12. The OCV models under the Coulomb-counting SoC from the two experiments and two ECMs are shown in Figure 3.11(b). It can be seen that these estimated OCV-SoC

relationships from day 1 and day 2 are much closer than that in Figure 3.11(a). The solid lines are the fitting results (cubic spline) of OCV under the Coulomb-counting SoC whose coefficients are provided in the appendix Table A. 1 and each of them is used in their corresponding ECM.

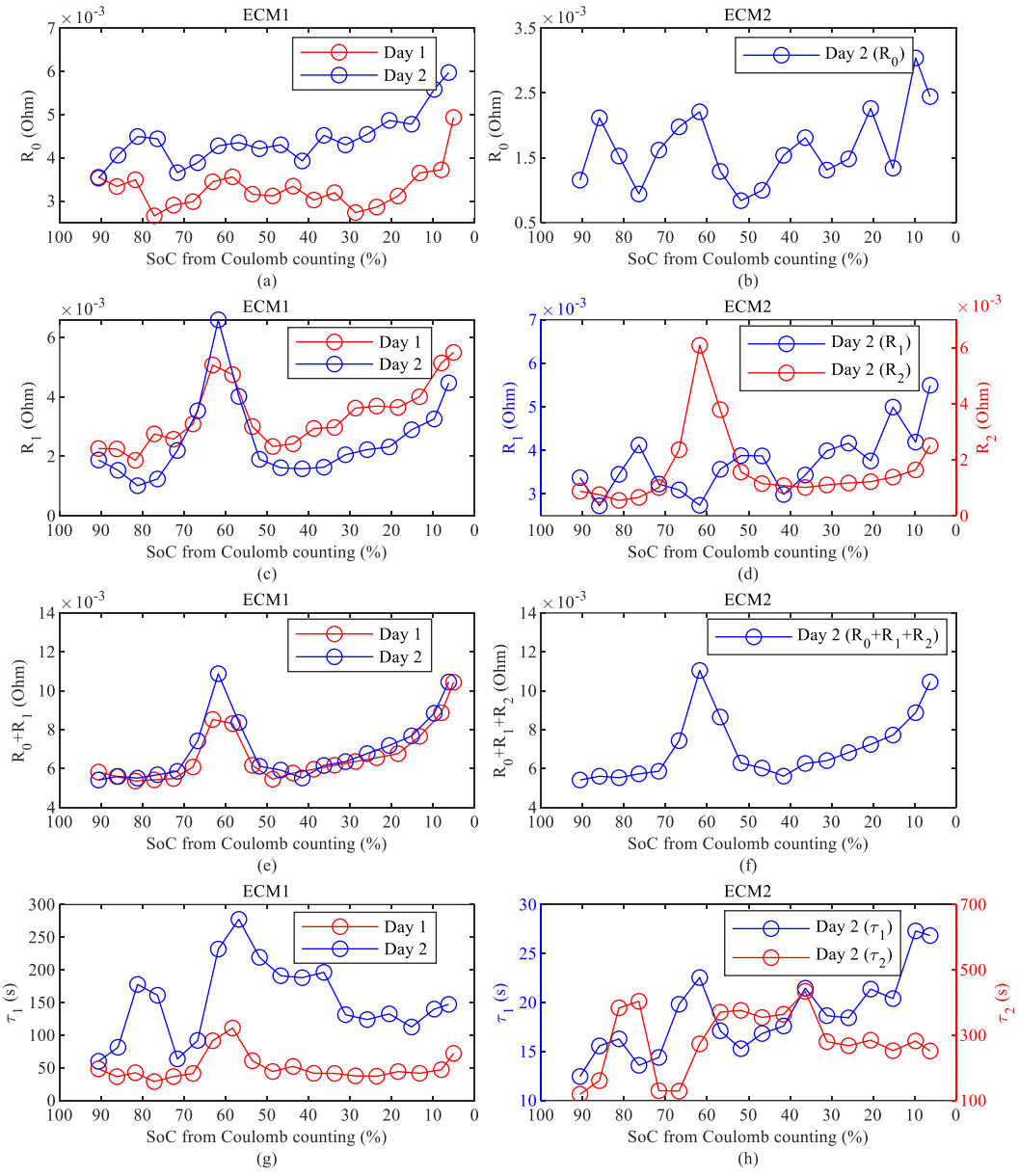

Figure 3.12 ECM1 and ECM2 resistance and time constants identified from the experiments on day 1 and day 2 with respective to SoC from the Coulomb-counting method. The first column: two sets of ECM1 identified from day 1 and day 2 experiment; the second column: ECM2 identified from day 2 experiment

Because there is no self-correction in SoC due to the BMS in the day 1 experiment, the modification of ECMs by using the Coulomb-counting SoC has less impact on the ECM parameters obtained from the day 1 experiment than that from the day 2 experiment. Figure

3.13(a) and (b) demonstrate the superiority of the ECM modelled with the Coulomb-counting SoC by comparing the voltage simulation results of it with the ECM modelled with the BMS SoC. Both ECMs used in the simulations, in Figure 3.13(a), are ECM1 identified from the day 2 data set. As Figure 3.13(b) shows, the ECM modelled with the Coulomb-counting SoC in the red line has a much smaller error (root mean square error (RMSE): 0.39 V) than the one modelled under the BMS SoC in the blue line (RMSE: 2.48 V). Hence, ECMs built with the Coulomb-counting SoC will be used in the rest of the chapter.

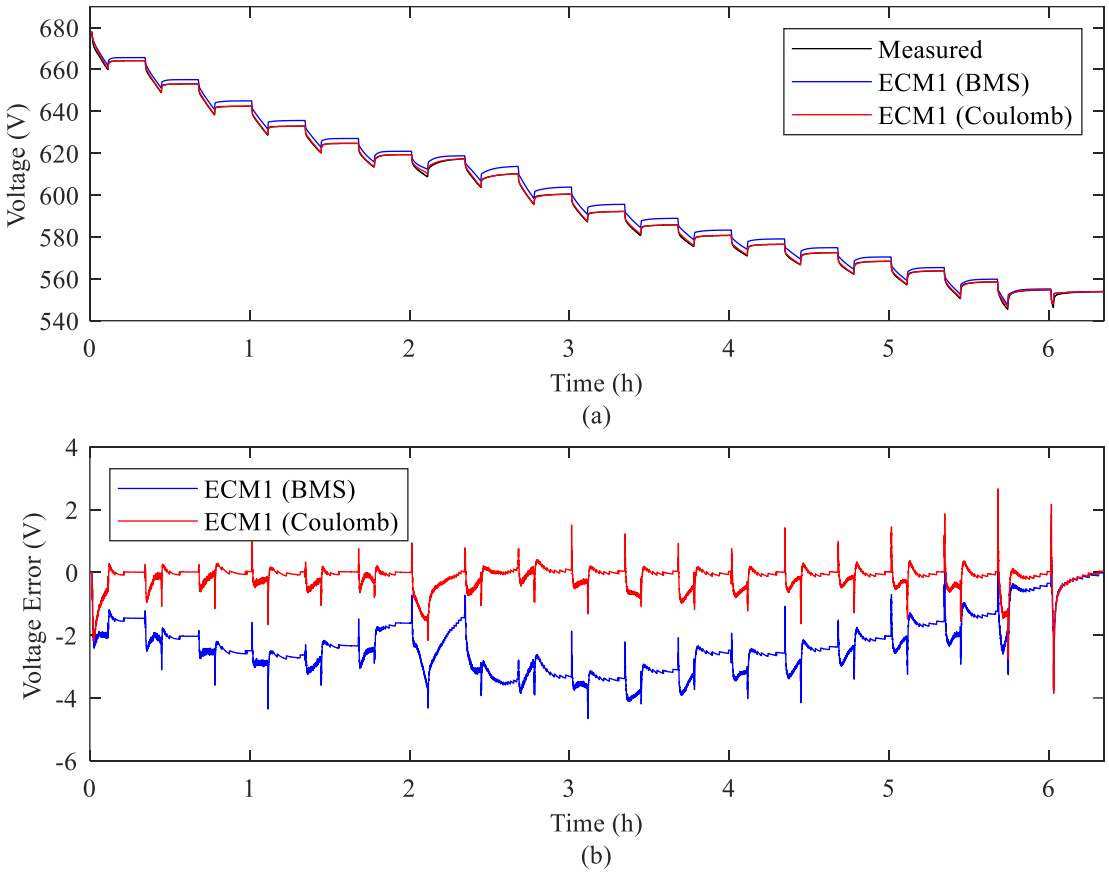

Figure 3.13 A simulation voltage (a) and error (b) comparison between ECMs modelled with the BMS SoC (ECM1 (BMS)) and Coulomb-counting SoC (ECM1 (Coulomb)): using ECM1 (identified from day 2) and day 2 input as an example

3.5 Simulation results

This section provides a detailed comparison of the estimations using ECM1 and ECM2 for the day 1 and day 2 datasets alongside scaled-up results obtained from a cell model fitted to measurements taken using EIS. Above all, the scale-up simulation approach using a single cell ECM will be introduced.

3.5.1 Single cell equivalent circuit model scale-up approach

Figure 3.14 provides the one time-constant model (ECM1) parameters obtained from EIS measurements based on a single Toshiba lithium titanium oxide (LTO) cell. The LTO cell shown in Figure 3.14 is one of the four tested LTO cells in this work. The experiment detail is not the focus of this chapter and will be described later in Chapter 5 when the four cells' equivalent circuit models are heavily used.

The single LTO cell and WESS shares similarities in ECM parameter's general change trend between 90% and 10% SoC. The ECM parameter of WESS in Figure 3.10 were extracted from the large signal-measurements and the single LTO parameter was from small-signal EIS test. The large internal resistance, time constant and special OCV change phenomena at 60% SoC in WESS also occur in the single cell's parameter characteristic which might be the unique properties of Toshiba super charge ion battery (SCib) LTO cell. Single cell ECM parameters (especially R_1 and τ_1) at extreme SoC points make the simulation voltage result deviate from the measured value and hence be removed from the ECM model. The single SCiB LTO's OCV and SoC relationship is obtained from 11 SoC-OCV points.

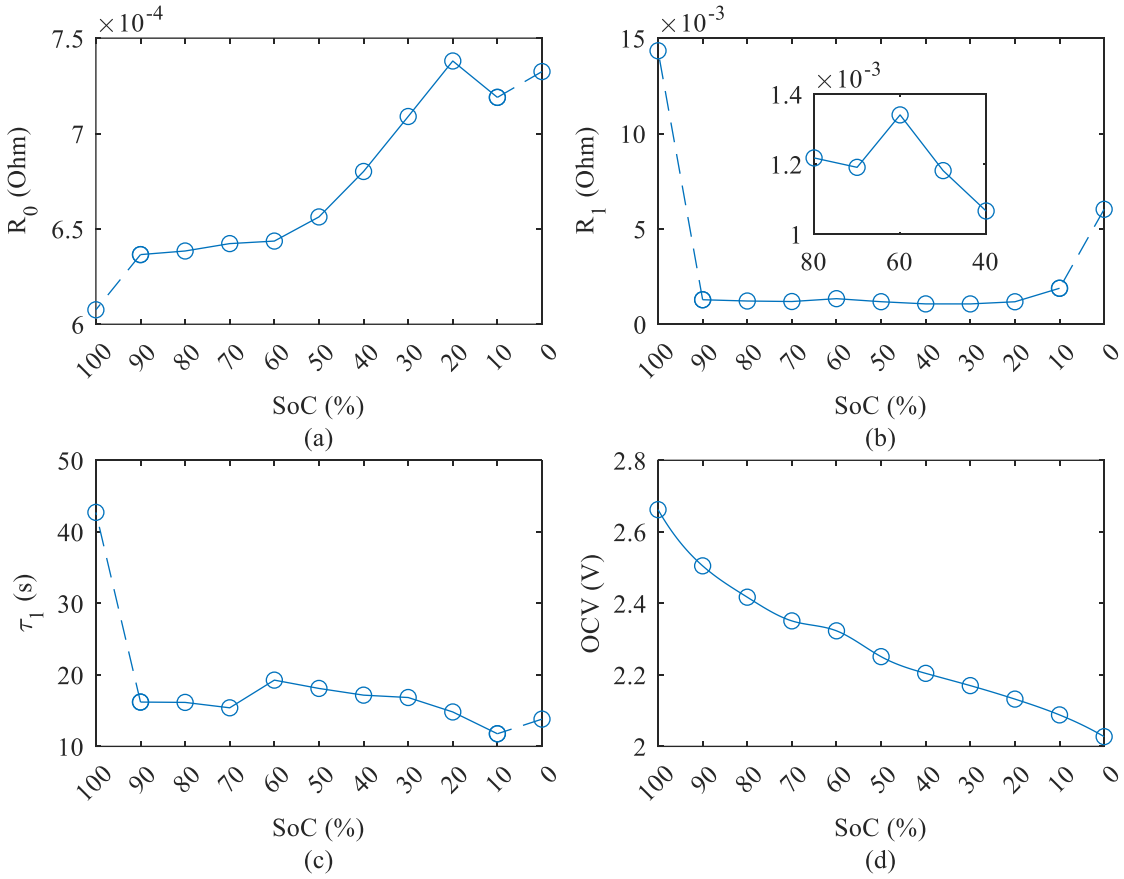

Figure 3.14 Single Toshiba SCiB LTO cell ECM1 parameters identified from EIS experiments

If all cells in a battery pack can be assumed to be identical then a large-scale battery can be simulated by scaling the parameters of a single-cell model. There are 40 parallel racks in WESS. The battery current separates into 40 equal streams and each of them flows into a rack. Furthermore, because of the parallel structure inside the 2P12S module, the cell current is half of the rack current. As a result, a single cell experiences a current that is 1/80 of the battery current. Besides, the series structure in the 2P12S module and rack increases the cell voltage by 12 times and the module voltage by 22 times, respectively. So that, the WESS can be simulated by scaling up the voltage of a single cell model (by 264 times) that has a load current that equals 1/80 of WESS current. The result of this simulation process will be shown in section 3.5.2.

3.5.2 Detailed comparison of model performance based on dataset parameter extraction

In this chapter, three ECM parameter sets have been identified based on the two datasets (day 1 & 2). In this section, the following nomenclature will be used to represent an ECM fitted to a dataset: $ECMi_{Dj}$ where i=1,2 is the different ECMs and j=1,2 is the dataset day 1

or 2, such that $ECM1_{D1}$ corresponds to ECM1 parameters identified from the day 1 dataset. Thus, the six permutations (sim. 1-6) using the proposed pack level ECMs are listed in Table 3.3. Besides, there are two more simulations (sim. 7-8) in Table 3.3 that use the single cell ECM from EIS experiment ($ECM1_{EIS}$) and scale-up approach.

Table 3.3 Simulation settings and RMSE of voltage result

Simulation No.	Model	Input	RMSE (V)
Sim. 1	$ECM1_{D1}$	Day 1	0.29
Sim. 2	$ECM1_{D2}$	Day 1	0.60
Sim. 3	$ECM2_{D2}$	Day 1	0.58
Sim. 4	$ECM1_{D1}$	Day 2	0.37
Sim. 5	$ECM1_{D2}$	Day 2	0.39
Sim. 6	$ECM2_{D2}$	Day 2	0.40
Sim. 7	$ECM1_{EIS}$	Day 1	2.22
Sim. 8	$ECM1_{EIS}$	Day 2	2.01

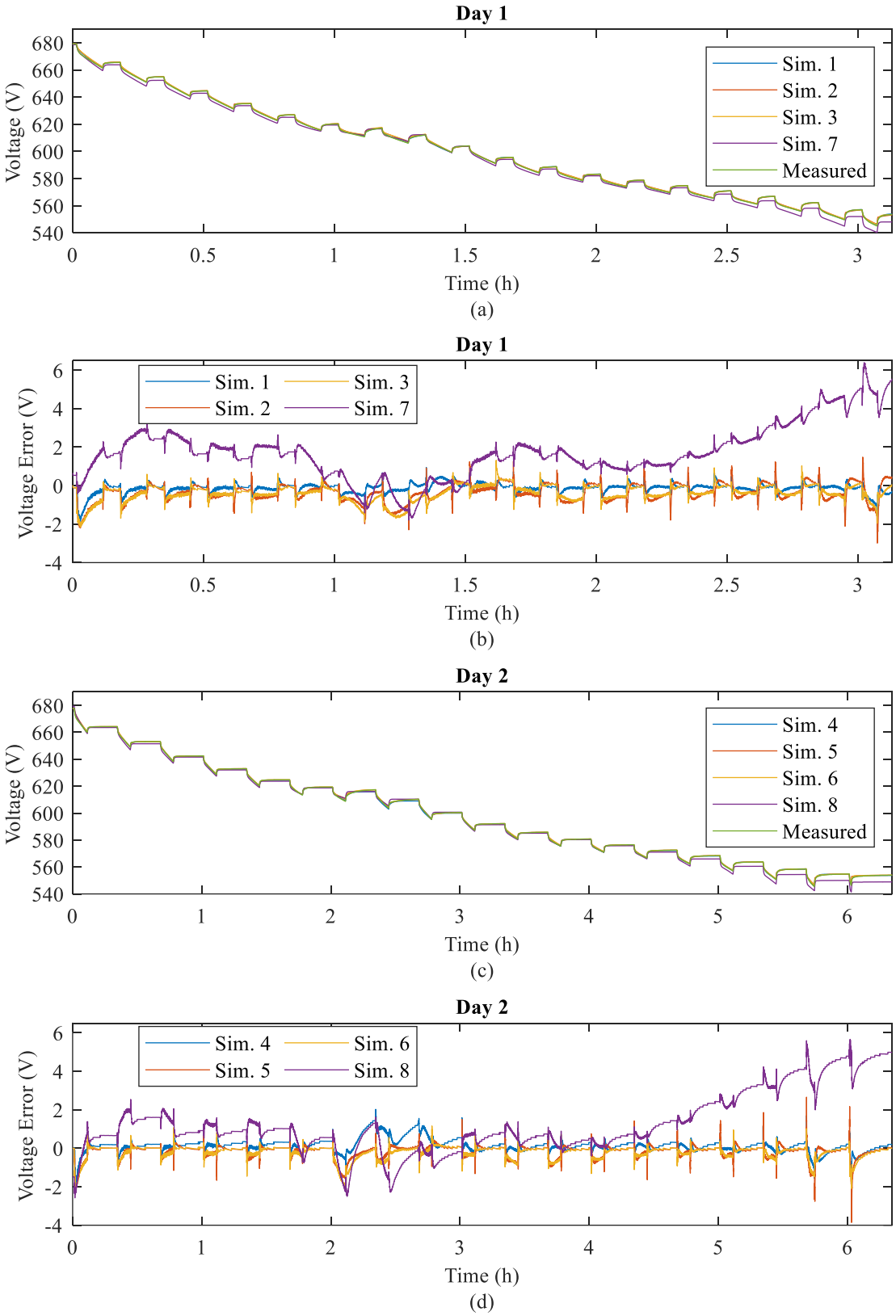

Figure 3.15 Simulation voltage and voltage error result in sim. 1 – 8. (a - b): voltage and error of sim. 1 - 3 and 7 using day 1 as input; (c - d): voltage and error of sim. 4-6 and 8 using day 2 as input. sim. 1-6 use battery pack ECMs identified from day 1 or day 2 dataset and sim. 7 - 8 use the scale-up approach and the single cell ECM from EIS test

Figure 3.15(a) shows the voltage results of sim. 1-3 and 7, which use day 1 as input; their errors are shown in (b). The voltage results and errors of simulations that use day 2 as input (sim. 4 – 6 and 8) are presented in Figure 3.15(c) and (d), respectively. In terms of the ECMs identified from the dataset day 1 and day 2, all three models have good performance with both day 1 and day 2 as input. Generally, these simulations (sim. 1-6) have a larger error at the beginning of the discharge pulses. This error decreases during resting and approaches to ~0 V at the end of rest. The error at the start of a discharge cycle indicates that the battery discharging impedance may be slightly different from the resting impedance. The much smaller error at end of rest intervals reflects the high accuracy of the OCV-SoC relationship. For the simulations using $ECM1_{EIS}$ (sim. 7 and 8), the general trend of the result is in agreement with the measured voltage. However, the maximum error (~6 V) is greater than with the models proposed in this chapter.

The root-mean-square error (RMSE) of the voltage in each simulation compared to the measured voltage is listed in Table 3.3. Among the simulations using $ECMi_{Dj}$, as battery model and day 1 as input (sim. 1-3), sim. 1 has the least RMSE 0.29 V. The model $ECM1_{D1}$ used in sim. 1 also has the best performance when simulating day 2 input (RMSE: 0.37 V). As expected, the ECMs have a smaller RMSE value when simulating the voltage profile from which they are identified. For example, $ECM1_{D2}$ has a larger RMSE in sim. 2 than sim. 5. The accuracy difference between $ECM1_{D2}$ and $ECM2_{D2}$ is not obvious. For the simulations with $ECM1_{EIS}$ model (sim. 7-8), the voltage RMSE is higher than that of simulation with $ECMi_{Dj}$ model (sim 1-6) by an order of magnitude.

3.5.3 Verification

The previous section has shown that the identified pack level ECMs in this chapter have a better performance than simply scaling up a single cell model. A history data is used to further verify the models ($ECMi_{Dj}$). The history of current data on 3rd May 2019, Figure 3.16(a), is taken as input profile for the three models described in this chapter. The BMS SoC and simulated SoC are plotted in Figure 3.16(b). The simulated SoC is calculated from the Coulomb-counting method which is incapable of achieving a self-correction. Hence, after a long rest, simulated SoC departs from the BMS SoC, for example at the rest after 0.6 h and 1.6 h. All three models have a good performance during the simulation with a peak absolute error smaller than 5 V, as Figure 3.16(d) shows. It should be noted that as time passes the SoC estimation error accumulates which makes the error in OCV and parameters

larger. Consequently, for all simulations, the voltage error in the whole process is gradually increased. In terms of the RMSE of the three simulations, their RMSE value is in the same order as Table 3.3: $ECM1_{D1}$ (1.77 V) < $ECM1_{D2}$ (2.10 V) ≈ $ECM2_{D2}$ (2.15 V).

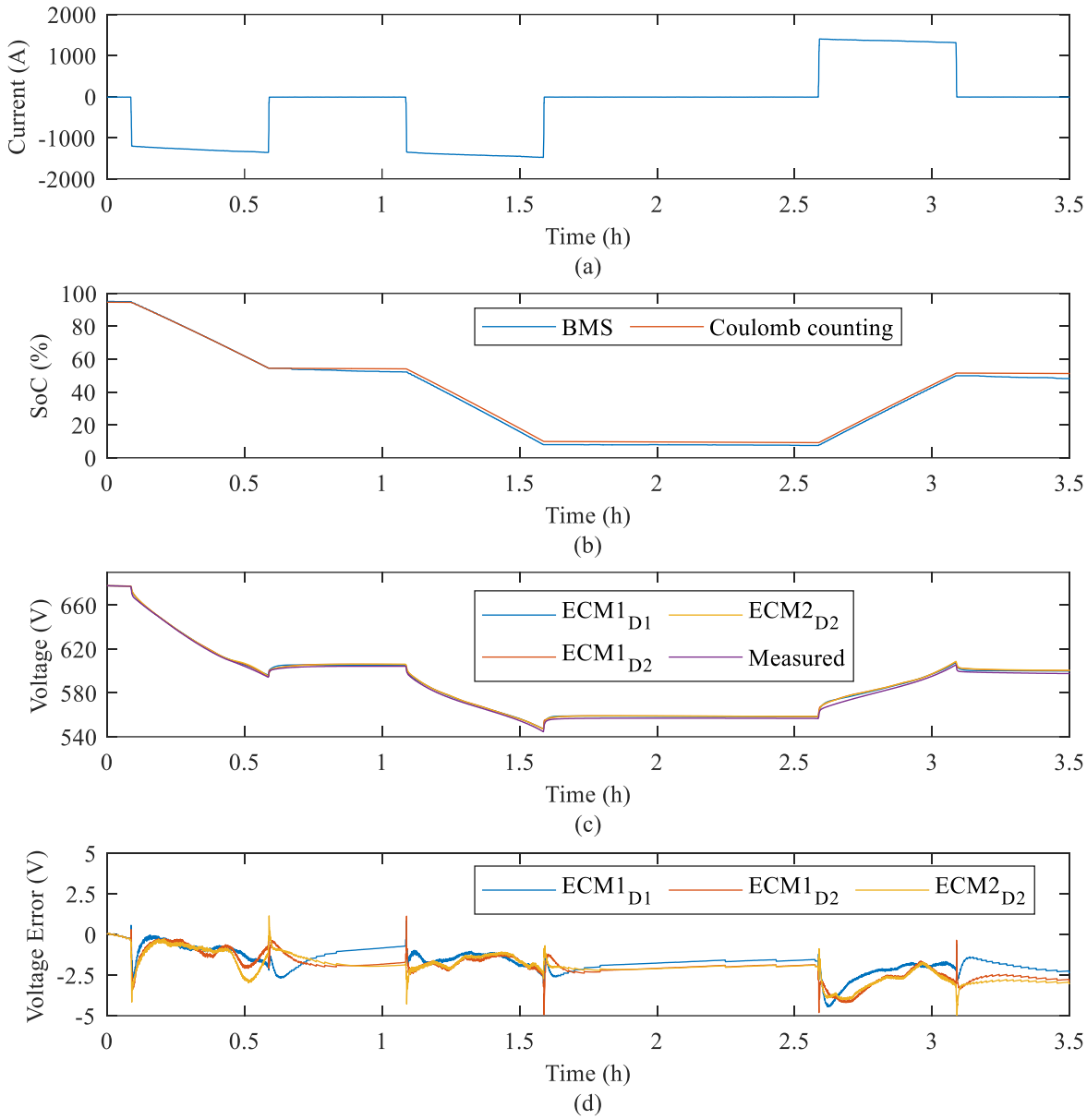

Figure 3.16 Current profile on May 3rd, 2019 and simulation results with $ECM1_{D1}$, $ECM1_{D2}$ and $ECM2_{D2}$: (a) current, (b) voltage, (c) SoC, (d) voltage error

3.6 Conclusion

This chapter demonstrates the modelling process of a 2 MW grid-tied BESS, WESS, using ECMs. It is found that some hardware and software settings in WESS could cause misunderstanding of a BESS and difficulties in building ECMs. In the proposed modelling

method, constant power experiments instead of constant current tests are used to identify ECM parameters because of the power-controlled inverter. Besides, due to the low sample rate, non-ideal measurement accuracy and slow current response speed, the ohmic resistance is calculated as a complementary component rather than from instant voltage drop. In addition, as discussed in section 3.4.5, the SoC self-correction mechanism in BMS prevents the large SoC estimation error from the Coulomb-counting method but could misguide the modelling process. For instance, the OCV-SoC relationship obtained from the resting experiment or low current pseudo-OCV experiment is the OCV-SoC lookup table stored in BMS which is not appropriate for offline simulations using empirical ECMs and the Coulomb-counting method. To build models that are suitable for offline simulations, OCV and other parameters should be modelled with respect to the Coulomb-counting SoC rather than BMS SoC after self-correction.

The identified models have excellent performance when they are used for simulating the parameter identification experiment profiles and verified with historical data. Compared to the traditional single cell scale-up approach, modelling large scale battery systems directly from its terminal information reduces the simulation voltage root mean square error by an order of magnitude.

The ECMs proposed in this chapter are for pack-level simulations that use one equivalent circuit to model over twenty-one thousand cells. These ECMs are appropriate for simulating the system performance under a specified load and for developing the battery energy management system. However, the pack level ECMs and simulations cannot provide cell level information such as the individual cell voltage and current which is important for understanding the battery management system and the characterises of WESS. To achieve a cell level simulation for WESS, a cell level battery equivalent circuit simulator will be introduced in the next chapter.

Chapter 4. Cell level battery equivalent circuit simulator

In the pack level simulation presented in Chapter 3, a multi-cell battery pack is modelled by a single equivalent circuit model (ECM) in which cell level information, such as cell voltage and current, are amalgamated into single variables. While this provides a good first-order approximation for the outward characteristics of the battery pack, it cannot account for variation between cells as a result of manufacture, ageing or temperature. This variation is important because it has implications on cell lifetime, safety and balancing which can have implications for the entire battery system. Thus cell-level information is important for the study and understanding of the characteristics of large-scale batteries.

To obtain the cell-level information, pack simulation and a circuit simulator at cell level are required. With the increase in the number of cells in the battery pack, traditional equivalent circuit simulation becomes increasingly cumbersome. The common approach, modified nodal analysis (MNA), as used in circuit simulation software such SPICE, cannot be used

Since the Willenhall Energy Storage System (WESS) consists of over 21,000 cells, the results from the modified nodal analysis produces large sparse matrices which are difficult to solve and require considerable computational resources. This chapter proposes a computationally efficient method where circuit transformation techniques are used to avoid issues with large solving large sparse matrices. Subsequently, the proposed simulator will be used to study cell-to-cell variance study in Chapter 5.

4.1 Internal cell connection within the Willenhall Energy Storage System

A cell-level equivalent circuit for a large-scale battery pack is built by representing every cell by an equivalent circuit model (ECM) and connecting them, which requires the internal connection structure of the battery pack. WESS is a grid-tied battery research facility with a 2 MW/1 MWh battery pack and consists of 21,120 Toshiba super charge ion battery (SCiB) lithium titanate oxide (LTO) cells [120]. The LTO cells inside WESS have an operating voltage window from 1.5 V to 2.7 V. A single SCiB LTO cell's diagram and electrical symbol are shown in Figure 4.1(a). Every 24 cells are connected and packed into a 2P12S module which consists of 12 series links of 2 parallel cells as shown by Figure 4.1(b).

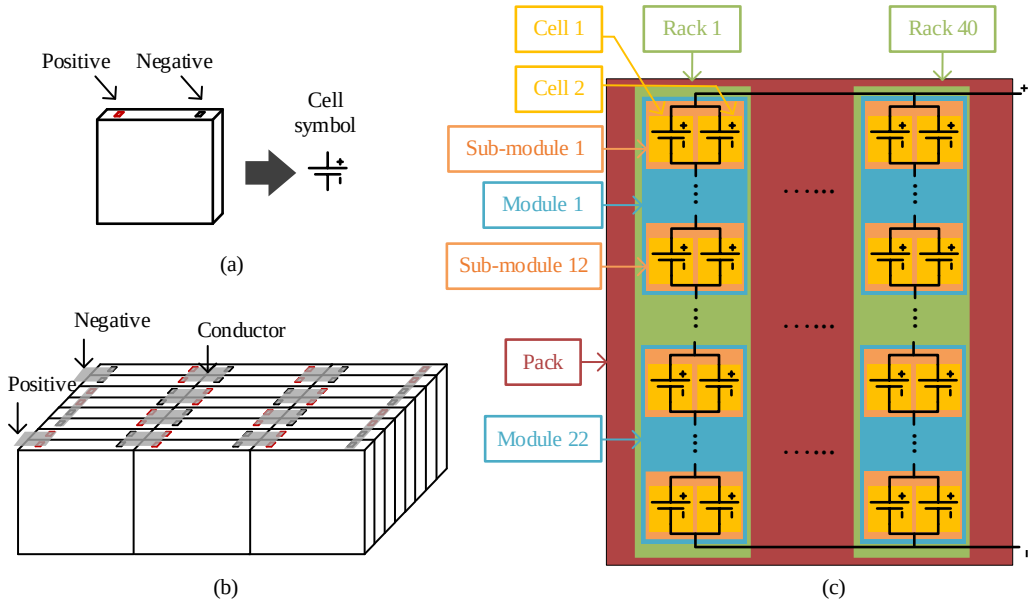

Figure 4.1 Battery connection in WESS: (a) cell diagram and electrical symbol, (b) 2P12S module diagram, (c) pack electrical connection

In WESS the battery pack has 40 parallel racks and each rack is made of 22 series-connected 2P12S modules [110]. As a result, the electrical connection at cell level has a symmetrical hierarchical structure as Figure 4.1(c) illustrates, where different hierarchical levels are shown in different background colours (pack: red, rack: green, module: blue, sub-module: orange, cell: yellow). Working from cell-level: a sub-module refers to the 2 parallel-connected cells; a module consists of 12 series-connected sub-modules; a rack consists of 22 series-connected modules and the whole pack is created from 40 parallel-connected racks. Thus, the number of cells within WESS can be determined from:

2 parallel cells × 12 series connected × 22 series connected modules × 40 parallel connected racks = 21,120 cells

Although the structure of the electrical connection varies across different applications [121], the overall aim is to guarantee similar currents are applied to all cells to achieve uniform ageing, state of charge (SoC) and temperature inside the battery. To reduce the manufacturing complexity, a pack is usually constructed using identical modules.

4.2 Traditional circuit simulator

SPICE is a commonly used circuit simulator that stands for ‘simulation program with integrated circuit emphasis’. SPICE was originally developed by the University of California

at Berkeley in the 1970s. After that, many SPICE-based circuit simulators are developed including LTSPICE, PSPICE and PartSim etc. SPICE-type software can translate a circuit schematic diagram into a netlist. According to the netlist, the SPICE simulator stamps the component voltage and current equations into a matrix equation using the modified nodal analysis technique. Stamping refers to the process of adding elements to a matrix equation. The detail of the stamping process and the form of the matrix equation will be discussed in section 4.2.2.

Once the MNA equations have been generated, they are solved in discrete time and the procedure is iterated with a variable time step until the end of the simulation. This chapter will use a battery-cell equivalent circuit with one time constant to demonstrate this circuit simulation with MNA.

4.2.1 Circuit schematic diagram and netlist in SPICE type simulators

Figure 4.2 demonstrates the circuit diagram of battery equivalent circuit model with one time constant under a constant current load which is plotted with LTSPICE. The circuit diagram contains four kinds of elements: a resistor (ohmic resistor: R0 and diffusion resistor: R1), a capacitor (diffusion capacitor: C1), a voltage source (representing open circuit voltage: Voc) and a current source (load: I). After the ground node (N0 by convention) is designated, the simulator automatically names the remaining nodes in sequence from node 1 (N1) to node 3 (N3).

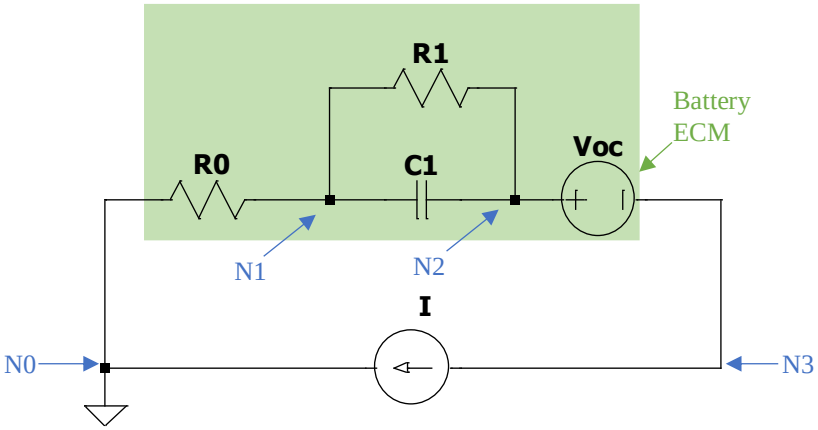

Figure 4.2 Circuit schematic diagram of the battery cell equivalent circuit model

According to the assigned node names, SPICE generates a netlist for the circuit. A netlist is a code file that contains information such as the simulation commands, the simulation file

address and all the needed information to represent the structure of a circuit. The elements of the circuit diagram in Figure 4.2 are written in the form of a netlist in Table 4.1. The information for each element is written in a single line which starts with the element name and is followed by the node names and the parameter value. I, V, R and C represent the current source, voltage source, resistor and capacitor respectively and the number or letter after the first character is used as an identifier for the element.

Table 4.1 Partial netlist of the circuit diagram

Name	Terminal Node1	Terminal Node2	Value
I	N3	N0	set by user
Voc	N2	N3	set by user
R0	N0	N1	set by user
R1	N1	N2	set by user
C1	N1	N2	set by user

4.2.2 Modified node analysis and the stamping rules

This section uses a series of circuits to demonstrate how to generate the MNA matrix equations. The MNA matrix equations are generated according to the netlists and stamping rules, which is the same as SPICE simulators. First, a simple circuit will be introduced. Then, more complex circuits including Figure 4.2 will be discussed. In a transient simulation, the MNA matrix equation is generated and solved at every time step to obtain the voltage and current information in the circuit. This information will be used to update the states in the circuit such as the voltage on capacitors which will be used in the next time step. Reference [122] comprehensively describes the stamping rules in SPICE simulator which will be described below. The stamping process happens at every time step and the following discussion the process on a time instant during a transient simulation.

4.2.2.1 Nodal analysis

Before explaining the MNA and stamping rules, traditional nodal analysis (NA) needs to be introduced first. Nodal analysis is developed based on Kirchhoff's current law which is suitable for circuit networks consisting of resistor and current source such as Figure 4.3. Compared with the circuit in Figure 4.2, the circuit in Figure 4.3 does not have the capacitor and the voltage source. The netlist of the circuit in Figure 4.3 is provided in Table 4.2. This circuit will be used for demonstrating the nodal analysis process and the stamping rules for resistors and current sources.

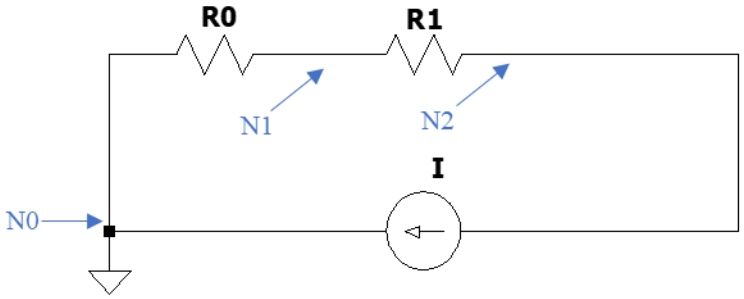

Figure 4.3 Circuit to demonstrate nodal analysis method

Table 4.2 Netlist of the circuit diagram

Name	Terminal Node1	Terminal Node2	Value
I	N2	N0	set by user
R0	N0	N1	set by user
R1	N1	N2	set by user

For the resistor R_0, it has the current and voltage relationship as (4.1) shows, where I_{R_0} is the current of R_0, G_0 is the conductance of the resistor and equals $1/R_0$, V_{N0} and V_{N1} is the voltage of the resistor's nodes (N0 and N1).

$$I_{R_0} = G_0(V_{N0} - V_{N1}) = G_0(0 - V_{N1}) = -V_{N1}G_0 \tag{4.1}$$

Similarly, for the resistor R_1, (4.2) can be obtained where I_{R_1} is the current of R_1, G_1 equals $1/R_1$ and V_{N2} is the voltage of node N2.

$$I_{R_1} = G_1(V_{N1} - V_{N2}) \tag{4.2}$$

In nodal analysis method, there are two unknown values V_{N1} and V_{N2} in the circuit (in Figure 4.3) which requires two equations to be solved. According to Kirchhoff's current law (KCL), for node N1:

$$I_{R_0} - I_{R_1} = -V_{N1}G_0 - G_1(V_{N1} - V_{N2}) = 0 \tag{4.3}$$

For node N2:

$$I_{R_1} - I = G_1(V_{N1} - V_{N2}) - I = 0 \tag{4.4}$$

As a result, V_1 and V_2 can be solve with (4.3)-(4.4). The KCL equations in nodal analysis method can be transformed into a matrix equation in the form of $\boldsymbol{Y} \cdot \boldsymbol{V} = \boldsymbol{J}$ where $\boldsymbol{V}$ is the

column vector of nodal voltages $[V_{N1}\ V_{N2}\ ...\ V_{Nn}]^T$, V_{Nn} represent the voltage potential at node Nn with respect to the grounded node $N0$, $\boldsymbol{Y}$ is the admittance matrix containing the reciprocals of resistances (and later reactances), and $\boldsymbol{J}$ is a column vector of the current source input. The matrix equation is more convenient for a computer to solve. In the case of the circuit shown in Figure 4.3, one expression of $\boldsymbol{Y}, \boldsymbol{V}$ and $\boldsymbol{J}$ are provided in (4.5).

$$\boldsymbol{Y} = \begin{bmatrix} -G_0 & 0 \\ G_1 & -G_1 \end{bmatrix};\ \boldsymbol{V} = \begin{bmatrix} V_{N1} \\ V_{N2} \end{bmatrix};\ \boldsymbol{J} = \begin{bmatrix} I \\ I \end{bmatrix} \tag{4.5}$$

There are many forms that this equation could take. The stamping method to be described results in an alternative format. This form is achieved by a two-step transformations:

Step (1): subtracting the first row in $\boldsymbol{Y} \cdot \boldsymbol{V} = \boldsymbol{J}$ with the second row.

Step (2): multiply both side of the result from step (1) with -1.

a new equivalent form of $\boldsymbol{Y}\ \boldsymbol{V}$ and $\boldsymbol{J}$ is obtain as shown in (4.6) which will be compared with the matrix equation obtained from stamping process in section 4.2.2.2.

$$\boldsymbol{Y} = \begin{bmatrix} G_0 + G_1 & -G_1 \\ -G_1 & G_1 \end{bmatrix};\ \boldsymbol{V} = \begin{bmatrix} V_{N1} \\ V_{N2} \end{bmatrix};\ \boldsymbol{J} = \begin{bmatrix} 0 \\ -I \end{bmatrix} \tag{4.6}$$

4.2.2.2 The stamping rules of resistor and current source

When the number of resistor and current source in a circuit is large, writing the KCL equation for the circuit becomes a cumbersome process. Fortunately, the matrices $\boldsymbol{Y}, \boldsymbol{V}$ and $\boldsymbol{J}$ can be constructed by stamping components value into specific location of a $n \times n$ zero matrix, a $n \times 1$ zero vector and a $n \times 1$ zero vector respectively where n is the number of nodes in the circuit (exclude the ground node N0).

The stamp rules for a resistor are shown in Figure 4.4. A resistor has two nodes so that the current of the resistor contributes to the KCL equations of two nodes. As Figure 4.4 shows, for a resistor which has a resistance of R and is connected between nodes a and b, its conductance $G = 1/R$ will be stamped (or added) into $\boldsymbol{Y}(a, a)$ and $\boldsymbol{Y}(b, b)$ while $-G = -1/R$ will be stamped into $\boldsymbol{Y}(a, b)$ and $\boldsymbol{Y}(b, a)$. $\boldsymbol{Y}(a, b)$ represents the element at row a and column b of matrix $\boldsymbol{Y}$. Row a and row b of the $\boldsymbol{Y} \cdot \boldsymbol{V} = \boldsymbol{J}$ equation represents the KCL equation for the resistor's node a and b.

For any element with a grounded node, the ground node will cause no stamp because stamping with grounded node will introduce the ground node voltage V_{N0} which is zero and does not cause any current flowing into or out of any node.

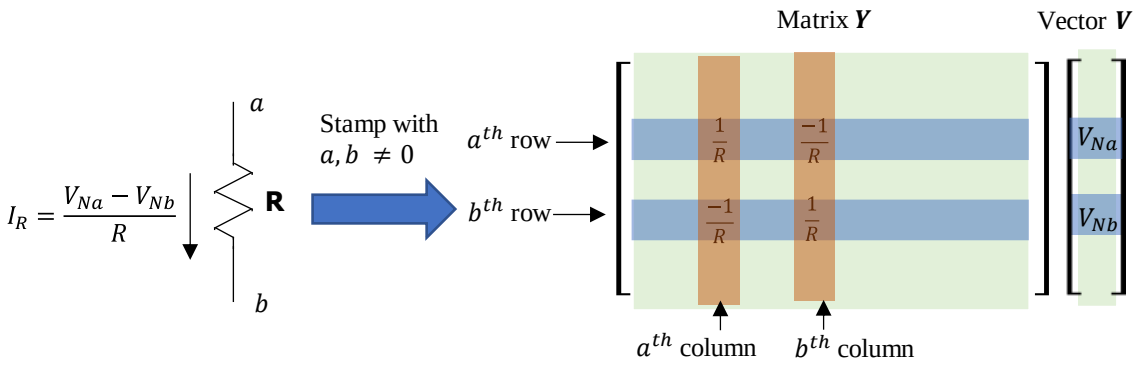

Figure 4.4 Resistor stamping at a time step in transient simulation

For a current source, the stamp changes the vector $\boldsymbol{J}$ only. If the current source, as shown in Figure 4.5, has a value of I and is connected between nodes of a and b, $-I$ and I will be added into the a^{th} and b^{th} row of vector J respectively. Stamping the current value into a row of vector $\boldsymbol{J}$ is completing the KCL equation for the corresponding node. The stamped values for a^{th} and b^{th} row have different sign because the current source causes a 'flowing out' current for node a but a 'flowing in' current for node b.

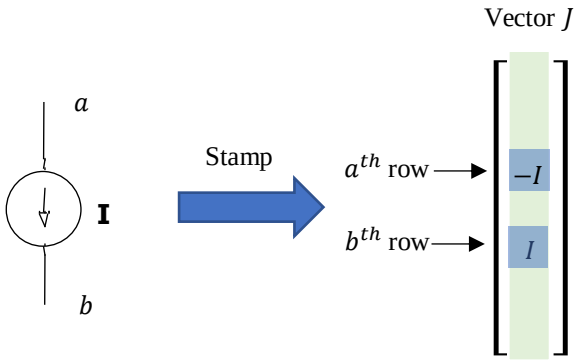

Figure 4.5 Current source stamping at a time step in transient simulation

Since the stamping location and value in the matrices are decided by the components value, node number and type which are contained in the netlist, the stamping process for a circuit can be conducted according to the netlist only. With the previously described stamping rules of resistor and current source, the stamping result of the circuit in Figure 4.3 can be obtained as (4.7) shows. The result from stamping in (4.7) is identical with that from KLC equations

in (4.6) which verifies the correctness of the stamping rules. The current source in Figure 4.3 is grounded so that only $-I$ is stamped into vector $\boldsymbol{Y}$.

$$\begin{bmatrix} G_0 + G_1 & -G_1 \\ -G_1 & G_1 \end{bmatrix} \begin{bmatrix} V_{N1} \\ V_{N2} \end{bmatrix} = \begin{bmatrix} 0 \\ -I \end{bmatrix} \tag{4.7}$$

4.2.2.3 Modified nodal analysis

When there is a voltage source in the circuit as Figure 4.6 shows, the traditional nodal analysis cannot stamp it into the $\boldsymbol{Y} \cdot \boldsymbol{V} = \boldsymbol{J}$ equation as the voltage source has an undefined admittance and the previous stamping rules for resistor does not apply to it. Hence, the traditional nodal analysis needs to be modified to deal with the stamping of voltage sources, as modified nodal analysis. The circuit in Figure 4.6 will be used to describe the MNA method and the stamping rules for voltage sources. The netlist of the circuit is given in Table 4.3.

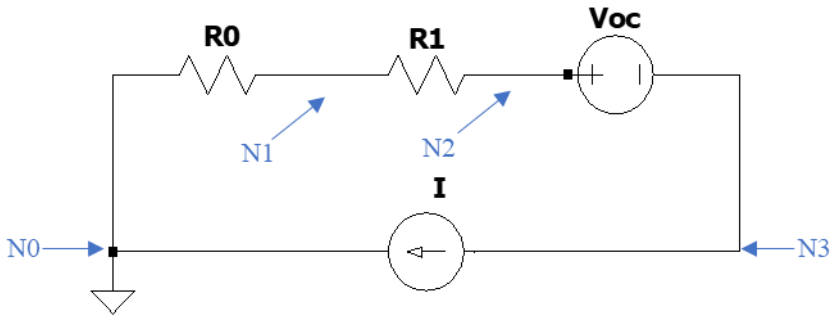

Figure 4.6 A circuit contains a voltage source

Table 4.3 Netlist of the circuit diagram with a voltage source

Name	Terminal Node1	Terminal Node2	Value
I	N3	N0	set by user
Voc	N2	N3	set by user
R0	N0	N1	set by user
R1	N1	N2	set by user

If there is a voltage source(s) in the circuit, the matrix equation $\boldsymbol{Y} \cdot \boldsymbol{V} = \boldsymbol{J}$ should be written according to the stamping processes described in section 4.2.2.2. Then the equation is augmented to include the voltage source which creates a new matrix equation $\boldsymbol{A} \cdot \boldsymbol{X} = \boldsymbol{Z}$ by introducing extra row(s) and column(s) into $\boldsymbol{Y}$, and extra row(s) into $\boldsymbol{V}$ and $\boldsymbol{J}$. Essentially,

the matrix formulation $\boldsymbol{A} \cdot \boldsymbol{X} = \boldsymbol{Z}$ is a group of equations based on Kirchhoff's current law (KCL) and Kirchhoff's voltage law (KVL).

In detail, as Figure 4.7 shows, in the MNA method, each voltage source introduces an extra row and column into $\boldsymbol{Y}$. The a^{th} element of the newly added row and column is set to 1; Meanwhile, the b^{th} element of the newly added row and column is set as -1. The current of the voltage source I_{ab} is combined with vector $\boldsymbol{V}$ as the last row in the newly constructed vector $\boldsymbol{X}$. Similarly, the voltage value V is combined with $\boldsymbol{J}$ to form the vector $\boldsymbol{Z}$.

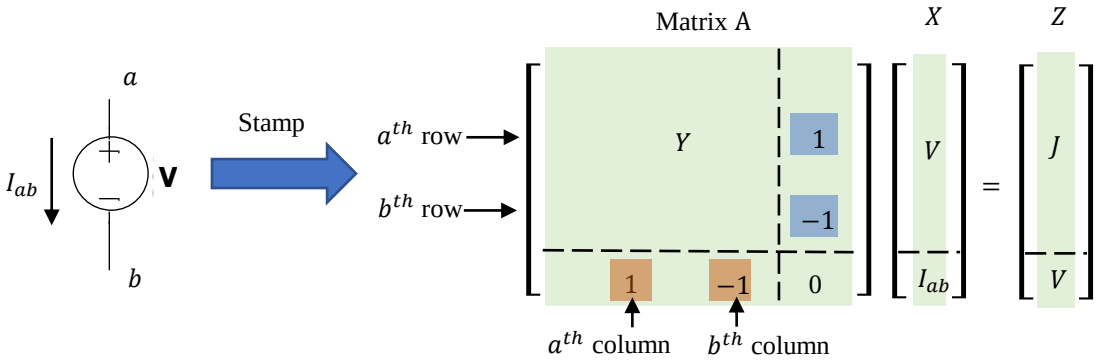

Figure 4.7 Voltage source stamping at a time step in transient simulation

4.2.2.4 Stamping rules for capacitors

For a capacitor, the relationship between its terminal voltage and current is shown in (4.8). As mentioned before, in transient simulations with SPICE type simulator, the MNA equation updates at every time step and so does the voltage on capacitors. From a step at time t to the next time step $t + \Delta t$, the voltage on the capacitor can be calculated with (4.9). The current i in (4.9) is time varying but when Δt is small, the current can be considered as constant ($\int_t^{t+\Delta t} i(\tau) d\tau \approx \Delta t \cdot i(\mathrm{t})$) and the capacitor voltage is approximated as (4.10). This approximation is known as the forward Euler method. In this case, at every time step during a transient simulation, a capacitor can be seen to be equivalent to a voltage source whose voltage is calculated with (4.10). The equivalent voltage source is the companion model of the capacitor under the forward Euler approximation. Consequently, at each time-step the capacitor is replaced by a new voltage source whose stamping rules will be introduced next.

$$I = C \frac{dv}{dt} \tag{4.8}$$

$$v(t+\Delta t) = v(t) + \frac{1}{C}\int_{t}^{t+\Delta t} i(\tau)d\tau \tag{4.9}$$

$$v(t+\Delta t) \approx v(t) + \frac{\Delta t}{C} i(t) \tag{4.10}$$

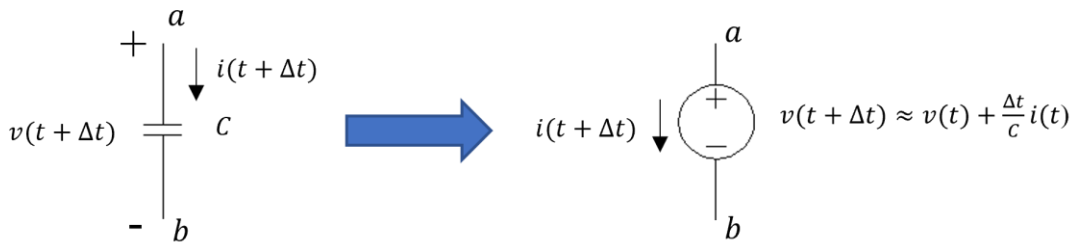

Figure 4.8 The companion model of a capacitor under the forward Euler approximation for the time step from t to $t + \Delta t$

Because the capacitor in the circuit is replaced by its companion model at every time step, the stamping of the capacitor turns to the stamping of its companion model, a voltage source, which has been described in section 4.2.2.3. In this application, a constant time step Δt is chosen heuristically to ensure acceptable accuracy without incurring significant computational expense.

4.2.2.5 Generating the modified nodal analysis equation with stamping rules

According to the described stamping rules and the circuit netlist in Table 4.1, the MNA equation of the battery equivalent circuit with a single time constant can be written. First, according to the stamping rules in section 4.2.2.2, the matrix equation $\boldsymbol{Y} \cdot \boldsymbol{V} = \boldsymbol{J}$ is generated as (4.11) shows. V_{N1}, V_{N2} and V_{N3} are the node voltages at nodes 1, 2 and 3 respectively. I is the current of load. R_0 and R_1 is the value of resistor R0 and R1 in Figure 4.2.

$$\boldsymbol{Y} \cdot \boldsymbol{V} = \boldsymbol{J}$$

$$\begin{bmatrix} \frac{1}{R_0} + \frac{1}{R_1} & -\frac{1}{R_1} & 0 \\ -\frac{1}{R_1} & \frac{1}{R_1} & 0 \\ 0 & 0 & 0 \end{bmatrix} \begin{bmatrix} V_{N1} \\ V_{N2} \\ V_{N3} \end{bmatrix} = \begin{bmatrix} 0 \\ 0 \\ -I \end{bmatrix} \tag{4.11}$$

Then, the equation (4.11) is augmented in to $\boldsymbol{A} \cdot \boldsymbol{X} = \boldsymbol{Z}$ according to the stamping rules for voltage sources and capacitors in section 4.2.2.3 and 4.2.2.4 respectively. The final result of

$\boldsymbol{A} \cdot \boldsymbol{X} = \boldsymbol{Z}$ is shown in (4.12). I_{C1} and I_{oc} are the current of capacitor $C1$ and the current of voltage source V_{oc}. At every time step in a transient simulation, the unknown vector $\boldsymbol{X}$ is solved and the known vector $\boldsymbol{Z}$ is updated for next step according to their profiles or the companion model.

$$\boldsymbol{A} \cdot \boldsymbol{X} = \boldsymbol{Z}$$

$$\begin{bmatrix} \frac{1}{R_0}+\frac{1}{R_1} & -\frac{1}{R_1} & 0 & 1 & 0 \\ -\frac{1}{R_1} & \frac{1}{R_1} & 0 & -1 & 1 \\ 0 & 0 & 0 & 0 & -1 \\ 1 & -1 & 0 & 0 & 0 \\ 0 & 1 & -1 & 0 & 0 \end{bmatrix} \begin{bmatrix} V_{N1} \\ V_{N2} \\ V_{N3} \\ I_{C1} \\ I_{oc} \end{bmatrix} = \begin{bmatrix} 0 \\ 0 \\ -I \\ V_{C1} \\ V_{oc} \end{bmatrix} \tag{4.12}$$

Matrix $\boldsymbol{A}$ is in (4.12) a sparse matrix that has 13 zeros out of 25 elements. Equation (4.12) is for one cell's equivalent circuit and can be easily solved by computer. This method works well for a pack with a low number of cells, but it is not appropriate for large-scale battery pack simulation due to the sparsity of the matrices.

For example, in WESS there are 21,120 cells in WESS. If every cell were represented by an equivalent circuit model with one time constant, the overall circuit would contain over fifty thousand nodes and over forty thousand voltage sources and capacitors. As a result, in the $\boldsymbol{A} \cdot \boldsymbol{X} = \boldsymbol{Z}$ formulation generated by MNA method, the matrix **A** is not only sparse but also large (about 95 thousand by 95 thousand) which cannot be directly and efficiently inverted. As a result, SPICE type simulator and MNA cannot be used for the simulation of a large-scale battery pack like WESS.

4.3 Novel battery pack circuit simulator for the Willenhall Energy Storage System

4.3.1 The overall structure of the proposed simulator

The equivalent circuit of the entire battery pack can be generated by connecting the cells' equivalent circuits in the electrical structure shown in Figure 4.1(c). The difficulty of solving the cell-level battery-pack equivalent circuits for WESS is obtaining the current of every cell at every time step. Instead of using MNA method, the proposed novel simulator uses Thévenin and Norton transformations to reduce the number of computations to determine the cell level currents.

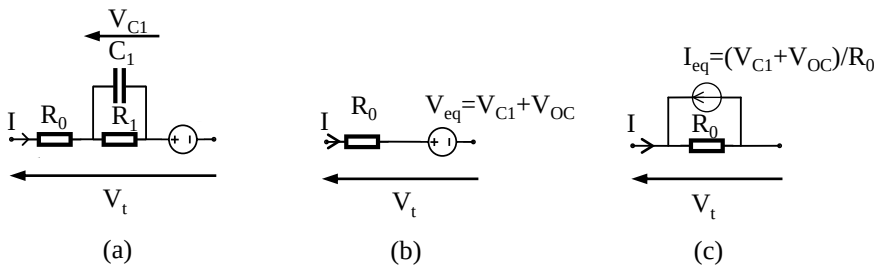

Figure 4.9 Equivalent circuit model with one time constant in (a); the corresponding Thévenin circuit in (b); and Norton circuit in (c). (note: V_{eq} and I_{eq} are equivalent voltage in Thévenin circuit and current source in Norton circuit)

In order to demonstrate the modelling process, this section uses cell equivalent circuit model (ECM) with a single time constant, shown in Figure 4.9(a). However, the battery simulator can operate with an arbitrary-order ECM. For the single time-constant ECM, the ohmic resistance R_0, diffusion resistance R_1, capacitance C_1, time constant τ_1 and open circuit voltage (OCV) V_{oc} are state of charge (SoC)-dependent. The discretised mathematical description of the cell ECM is given in (4.13)-(4.16) where Q is maximum available cell capacity in ampere seconds and Δt is time step length ($\Delta t = 1$ s), k represent for the time step and V_{t} is battery terminal voltage. The Thévenin and Norton transformations of the ECM is shown in Figure 4.9(b) and (c).

$$V_{\mathrm{t}}[k] = I[k] \cdot R_0[k] + V_{\mathrm{C1}}[k] + V_{\mathrm{oc}}[k] \tag{4.13}$$

$$\tau_1[k] = R_1[k] \cdot C_1[k] \tag{4.14}$$

$$V_{\mathrm{C1}}[k+1] = V_{\mathrm{C1}}[k] \cdot \exp\left(\frac{-\Delta t}{\tau_1[k]}\right) + R_1[k] \cdot I[k] \cdot \left(1 - \exp\left(\frac{-\Delta t}{\tau_1[k]}\right)\right) \tag{4.15}$$

$$\mathrm{SoC}[k+1] = \mathrm{SoC}[k] + \frac{I[k] \cdot \Delta t}{Q} \tag{4.16}$$

Figure 4.10 illustrates the main processes that occur within the battery pack simulator. At every step, cell parameters in the ECM are updated according to the cell's SoC. The values of current for the 21,120 cells are calculated in two stages: ECM circuit transformation and cell current calculation (which will be discussed in section 4.3.2 and section 4.3.3 respectively). The calculated value of cell current is used to update cell SoC and V_{C1} (according to (4.15) and (4.16)) that will be used in the next time step. Elementwise and dimensional matrix operation and graphics processing unit (GPU) calculation were adopted

to boost the simulator's speed. Compared with the calculation with central processing unit (CPU), GPU could deal with a much larger number of parallel calculations at the same time.

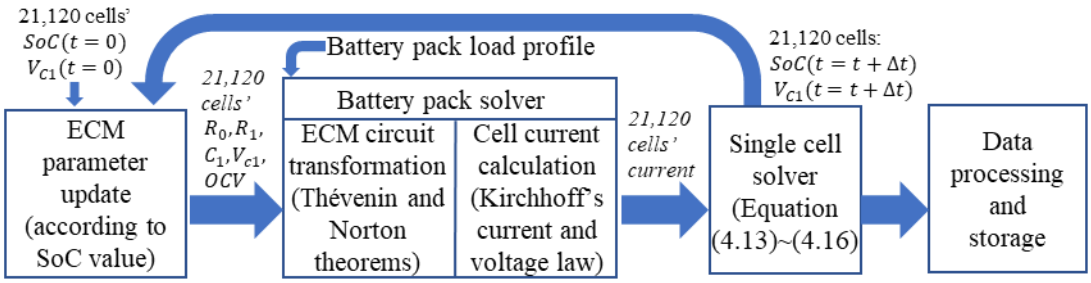

Figure 4.10 The process in the proposed battery pack circuit simulator for WESS

4.3.2 Equivalent circuit transformation

Figure 4.11 demonstrates the process of equivalent circuit transformation that simplifies the overall battery pack circuit using Thévenin or Norton circuit transformations. To explain the process, the nomenclature needs to be explained first. Symbols I, V, and R are the current source, voltage source and resistor in Thévenin or Norton equivalent circuit. Lowercase subscript 'c', 'sm', 'r' and 'p' represents cell, sub-module, rack and pack respectively. The number in the subscript is used to distinguish between the different cells in the same sub-module, sub-modules in the same rack, or racks in the pack. For example, V_{c1} represents the voltage source of Thévenin circuit for cell 1 in the first sub-module of the first rack in the pack, as circuit C1.1 in Figure 4.11 shows. Circuit C1.1 is obtained by replacing the cell ECMs (show in Figure 4.9(a)) with their Thévenin circuits (shown in Figure 4.9(b)). As Figure 4.9 shows, V_{c1}, the value of the voltage source in Thévenin equivalent circuit for cell c1, is equal to the sum of the open circuit voltage V_{oc} and the voltage on capacitor C_1 (noted as V_{C1} which is labelled with a capital 'C' in the subscript).

Cx.y (x∈(1, 2, 3, 4), y∈(1,2)) names different equivalent circuits where x is from 1 to 4 representing circuit at cell level, sub-module level, rack level and pack level respectively and y is used to distinguish the Thévenin or Norton circuit in the same level. For instance, C1.1 represents the battery equivalent circuit at cell level with Thévenin form. a, b, …, h are the nodes in the first rack of the battery as shown in Figure 4.11 (for example in circuit C1.1). T1 and T2 are the battery terminal nodes.

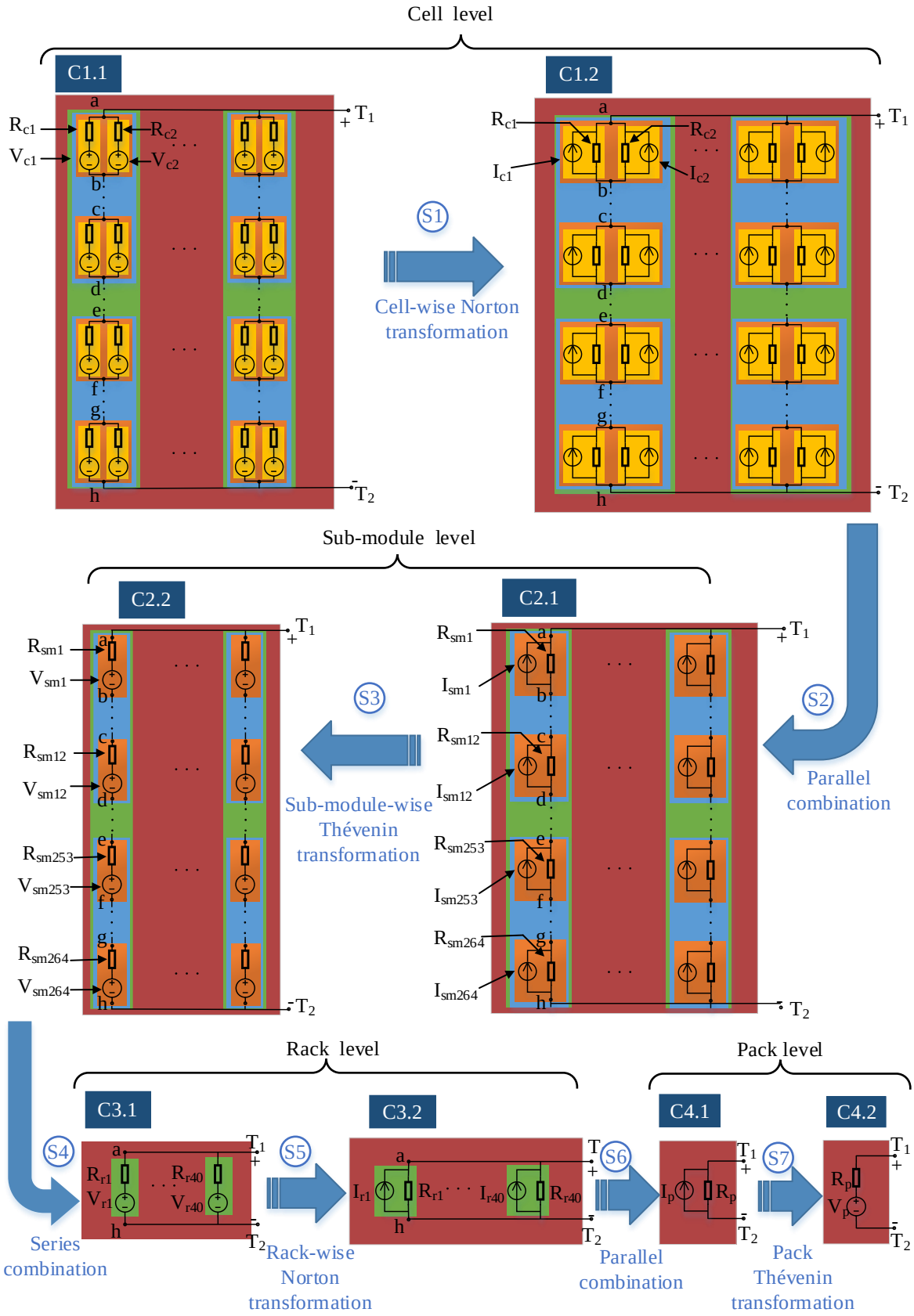

Figure 4.11 Battery pack circuit simulator: Norton and Thévenin circuit transformation

As Figure 4.11 show, series and parallel connections of cells are combined using Thévenin and Norton theorems. Working up the pack hierarchy from single cell to sub-module, and so on, until the pack is finally represented by a single equivalent resistor and voltage source. There are seven steps in Figure 4.11 which can be divided into two kinds of operation. The first kind of operation is circuit transform according to Thévenin and Norton theorems which includes steps S1, S3, S5, and S7. The second kind of operation is combining electrical components such as parallel current sources, series voltage sources and parallel/series resistors which includes steps S2, S4, and S6. The representative calculation equation for steps S1 to S7 are listed in (4.17)-(4.23) in order. These equations are repeated on all units with the same structure in the circuit. For example, (4.17) takes cell c1 as an example but the same calculation should be applied to all cells in C1.1.

S1 cell-wise Norton transformation:

$$I_{c1} = \frac{V_{c1}}{R_{c1}} \tag{4.17}$$

S2 parallel combination:

$$\begin{cases} I_{sm1} = I_{c1} + I_{c2} \\ R_{sm1} = \dfrac{1}{1/R_{c1} + 1/R_{c2}} \end{cases} \tag{4.18}$$

S3 sub-module-wise Thévenin transformation:

$$V_{sm1} = I_{sm1} \cdot R_{sm1} \tag{4.19}$$

S4 series combination:

$$\begin{cases} V_{r1} = V_{sm1} + V_{sm2+} \ldots + V_{sm264} \\ R_{r1} = R_{sm1} + R_{sm2+} \ldots + R_{sm264} \end{cases} \tag{4.20}$$

S5 rack-wise Norton transformation:

$$I_{r1} = \frac{V_{r1}}{R_{r1}} \tag{4.21}$$

S6 parallel combination:

$$\begin{cases} I_p = I_{r1} + I_{r2} + \cdots + I_{r40} \\ R_p = \dfrac{1}{1/R_{r1} + 1/R_{r2} + \cdots + 1/R_{r40}} \end{cases} \tag{4.22}$$

S7 pack Thévenin transformation:

$$V_p = I_p \cdot R_p \tag{4.23}$$

4.3.3 Cell current calculation

At the end of the process in Figure 4.11, the battery pack is simplified into a Thévenin equivalent circuit C4.2. Figure 4.12 illustrates the following process that solving the voltage and current information inside the battery pack from pack level to cell level. In Figure 4.12, the prime symbol (′) represents the true current or voltage corresponding to the load which is different from that estimated by the Thévenin equivalent voltage and Norton equivalent current. For example, I_p' is the current that flows into the battery pack. As Figure 4.12 shows, the internal currents and voltages inside the pack are determined in the sequence of racks, sub-modules, and cells through Kirchhoff's current and voltage laws.

There are three steps in Figure 4.12 from step S1′ to S4′. In step S1′, the pack current I_p' and the battery pack voltage V_{T1T2} are calculated according to the load type (type 1: voltage load, type 2: current load, type 3: power load) as (4.24) shows. After replacing C4.2 with C3.1, the pack voltage V_{T1T2} and the pack current I_p' remain the same. Hence, the rack current value can be calculated according to (4.25), taking rack 1 as example. In step S2′, the rack-level equivalent circuit C3.1 is replaced by the sub-module level equivalent circuit C2.2 so that the voltages across sub-modules can be calculated by (4.26). In step S3′, C2.2 is substituted by C1.1 and the sub-modules voltage value keeps the same. Finally, in the circuit C1.1, the cell current can be calculated according to (4.27). By now, the current for every cell is calculated and as it has been discussed in section 4.3.1 the battery pack can be simulated step by step.

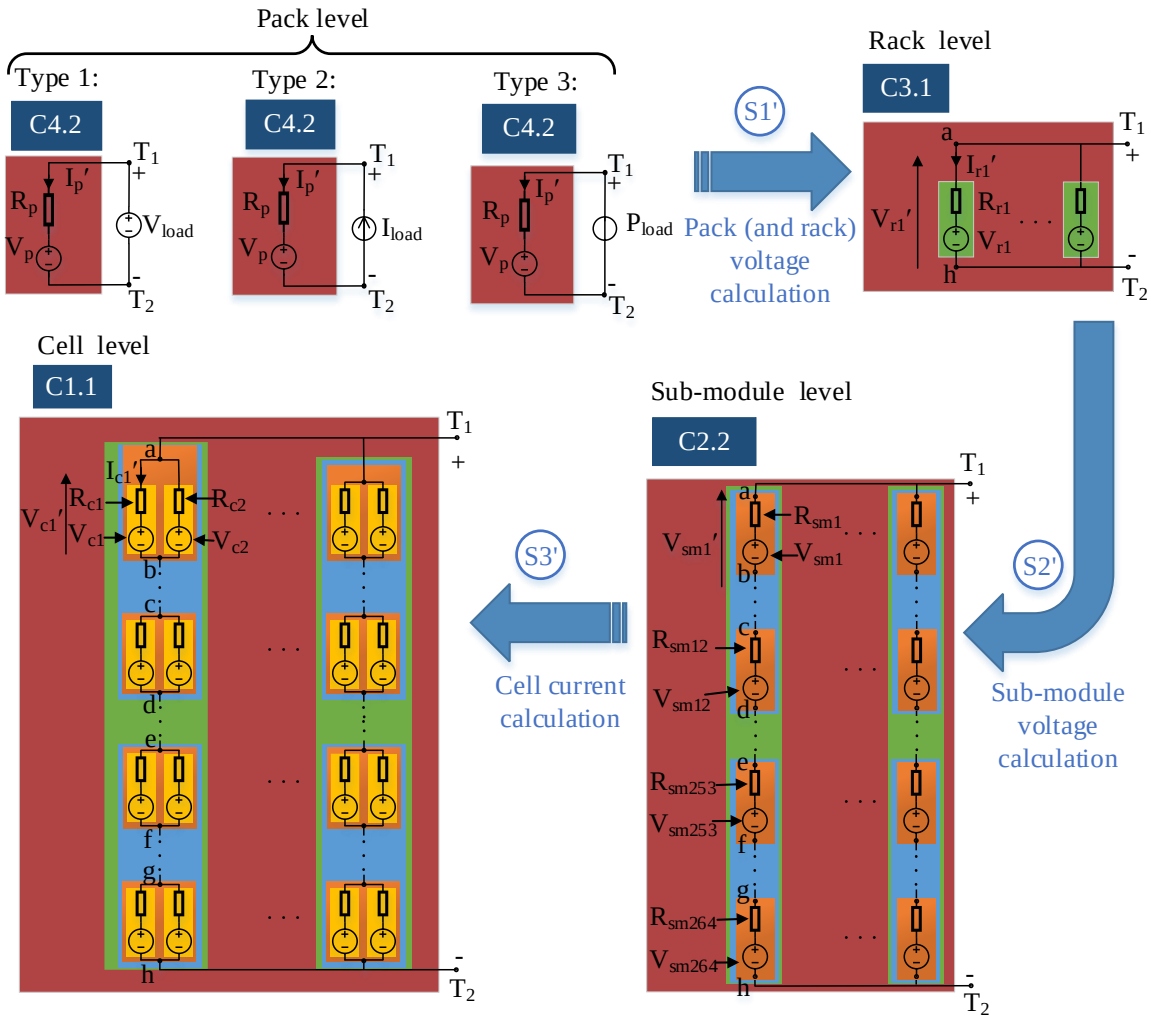

Figure 4.12 Battery pack circuit simulator: current calculation

S1′ pack (and rack) voltage and current calculation:

$$\begin{cases} V_{T1T2} = V_{\text{load}};\ I'_p = (V_{T1T2} - V_p)/R_p & \text{(type 1)} \\ I'_p = I_{\text{load}};\ V_{T1T2} = I'_p \cdot R_p + V_p & \text{(type 2)} \\ I'_p = (-V_p + \sqrt{{V_p}^2 - 4R_p \cdot (-P_{\text{load}})})/2R_p;\ V_{T1T2} = I'_p \cdot R_p + V_p & \text{(type 3)} \end{cases} \tag{4.24}$$

$$I'_{r1} = (V_{T1T2} - V_{r1})/R_{r1} \tag{4.25}$$

S2′ sub-module voltage calculation:

$$V'_{sm1} = I'_{r1} \cdot R_{sm1} + V_{sm1} \tag{4.26}$$

S3′ cell current calculation:

$$I'_{c1} = (V'_{sm1} - V_{c1})/R_{c1} \tag{4.27}$$

4.4 The validation of the proposed battery simulator

This section verifies the operation proposed battery simulator programmed in MATLAB with RC model scale-up method and with a commercial simulator, Simulink (in MATLAB 2021a). Both the proposed simulator and Simulink were executed on the same computer featuring an Intel i5-10500 processor and 8 GB random-access memory.

Unfortunately, due to model complexity, Simulink cannot draw and simulate the cell level schematic circuit diagram for WESS on the simulation platform. The purpose of the comparison is to verify the simulation method in the proposed simulation, so the battery pack used in the simulation is designed with a small number of cells (eight) whose circuit diagram can be drawn by Simulink is shown in Figure 4.13.

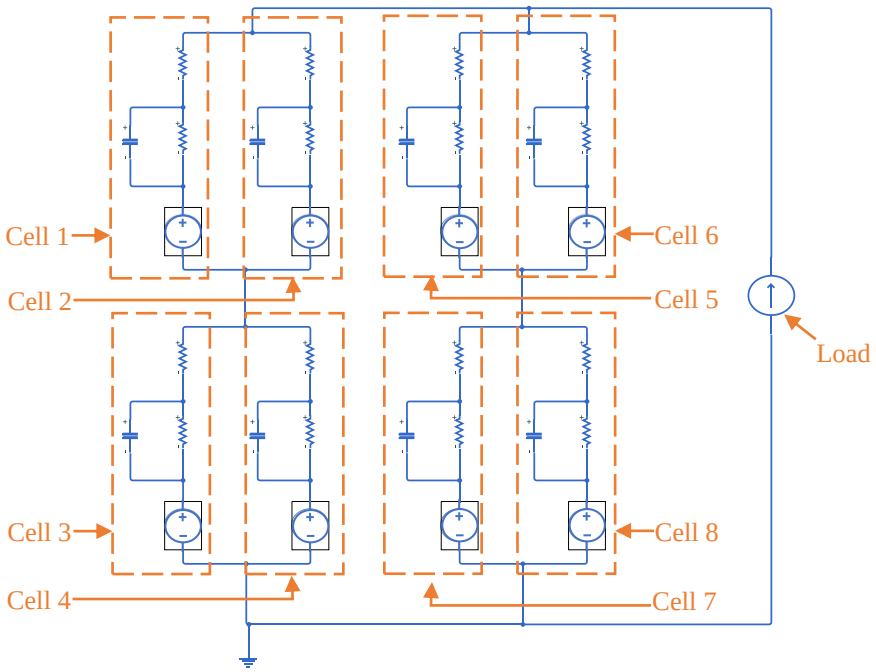

Figure 4.13 Circuit diagram for verification simulation, plotted with Simulink (using SIMSCAPE components)

To simplify the simulation circuit, the value of resistors and capacitors in the equivalent circuit are set as constant values which do not change with SoC. Chapter 3 provides the ECM parameter for WESS in pack level at different SoC points. The parameter value from the day 2 experiment at 50% SoC ($R_0 = 4.2$ mΩ, $R_1 = 1.9$ mΩ and $C_1 = 115.3$ kF) is used to estimate the single cell's ECM parameter.

Assuming all cells in WESS are identical, the theoretical value of a cell ECM parameter can be estimated by scaling the pack ECM parameter according to the electrical connection shown in Figure 4.1(c). For a single cell's ECM, the capacity Q is set as 20 Ah which is the nominal capacity. $R_0 = 1.2727$ mΩ and $R_1 = 0.5758$ mΩ which are $^{80}/_{264}$ of that in the WESS ECM. $C_1 = 380.49$ kF which is $^{264}/_{80}$ times of that in the WESS ECM. At the same SoC, the single cell's OCV value is supposed to be $^{1}/_{264}$ of the WESS's OCV. The cell OCV-SoC relationship as given by the polynomial equation of (4.28) shows where S is the value of SoC and coefficients p_1 to p_{10} are listed in Table 4.4. Number 80 and 264 are the scale factors caused by the parallel and series relationship in WESS's internal connection respectively.

$$V_{oc} = p_1 S^9 + p_2 S^8 + p_3 S^7 + p_4 S^6 + p_5 S^5 + p_6 S^4 + p_7 S^3 + p_8 S^2 + p_9 S + p_{10} \quad (4.28)$$

Table 4.4 Cell open circuit voltage model coefficients

p_1	p_2	p_3	p_4	p_5	p_6	p_7	p_8	p_9	p_{10}
1.47e-15	6.6e-13	1.25e-10	1.28e-08	7.8e-07	2.88e-05	6.37e-4	8.02e-3	5.5e-2	1.95

4.4.1 Verification A: scale-up method and cell level simulation

If the cells in a battery pack are identical, the simulated pack voltage calculated from the scale-up method should be identical to that from cell level simulation. For the battery pack shown in Figure 4.13, if all cells are identical, the cell current will be 1/4 of the battery current and the pack voltage will be 4 times of the cell voltage. In verification A, the proposed simulator will first simulate the pack at cell level using the proposed method, noted as simulation A1. Then the same simulation will be repeated with the scale-up method, noted as simulation A2. The proposed model will be verified if the battery pack voltage results from the two methods are identical.

In this verification, all the cells in Figure 4.13 are identical and have the same OCV-SoC relationship and the same parameter value: $R_0 = 1.27$ mΩ and $R_1 = 0.58$ mΩ $C_1 = 380$ kF and $Q = 20$ Ah. For each cell, the SoC and the initial condition on capacitor $C1$ are set as zero. The battery pack is charged under an 80 A (1 C-rate) current load until any of the eight cells reaches the maximum allowed voltage (2.7 V).

The blue and red lines in Figure 4.14(a) are the voltage results from simulations A1 and A2. As it can be seen in Figure 4.14(a), the voltage result from the proposed simulator (A1) are identical to that from the scale-up method (A2). In both simulations, the battery is charged for 3557s which represents a 79.04 Ah charging capacity. The difference between the voltage results from the two methods, as Figure 4.14(b) shows, is zero throughout. This demonstrates the equivalence of the scale up method with the operation of the proposed battery simulator for an identical cell battery pack.

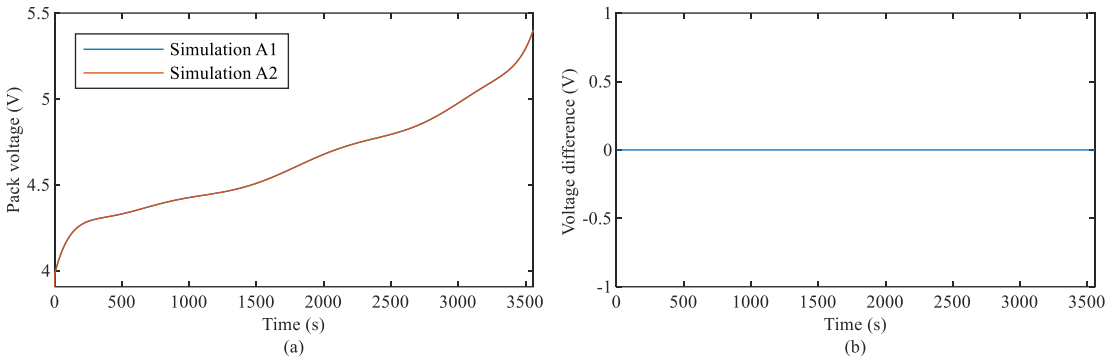

Figure 4.14 Verification A: (a): the voltage results from the scale-up method and the cell level simulation; (b): the voltage difference between the two methods

4.4.2 Verification B: Simulink vs. proposed simulator

If the cells in a battery pack are different from each other, each cell's current and voltage will be unique. In verification B, all the cells in Figure 4.13 are set to be different from one another. The ECM parameters for each cell are provided in Table 4.5 which are close to the estimated value. Cells with larger identity number have large internal resistance, large time constant and smaller capacity which is indicative of a more severe level of degradation.

Similar to verification A, the battery pack in verification B is charged under an 80 A (1 C-rate) current load until any of the eight cells reaches the maximum allowed voltage (2.7 V). The simulation is first conducted with the proposed simulator, noted as simulation B1 and then repeated with Simulink (MATLAB), noted as simulation B2.

Table 4.5 Cell ECM parameters setting in simulation

Cell number	R_0 (mΩ)	R_1 (mΩ)	C_1 (kF)	Q (Ah)
1	1.27	0.58	380	20.0
2	1.29	0.60	390	19.9
3	1.31	0.62	400	19.8
4	1.33	0.64	410	19.7
5	1.35	0.66	420	19.6
6	1.37	0.68	430	19.5
7	1.39	0.70	440	19.4
8	1.41	0.72	450	19.3

The battery pack in both simulation B1 and B2 is charged for 3474s (charging capacity: 77.2 Ah). The current of cell 1 to 8 is plotted in Figure 4.15 (a)-(h). As Figure 4.15 shows, the current results from B1 are identical to B2 and the difference between them is zero. Because the cells are connected in parallel, they have identical voltages so that only the voltage of cells 1, 3, 5 and 7 are shown in Figure 4.16. The results from the proposed simulator are identical to those from Simulink. The proposed simulator is verified by observing the same result with a reliable commercial software Simulink (MATLAB).

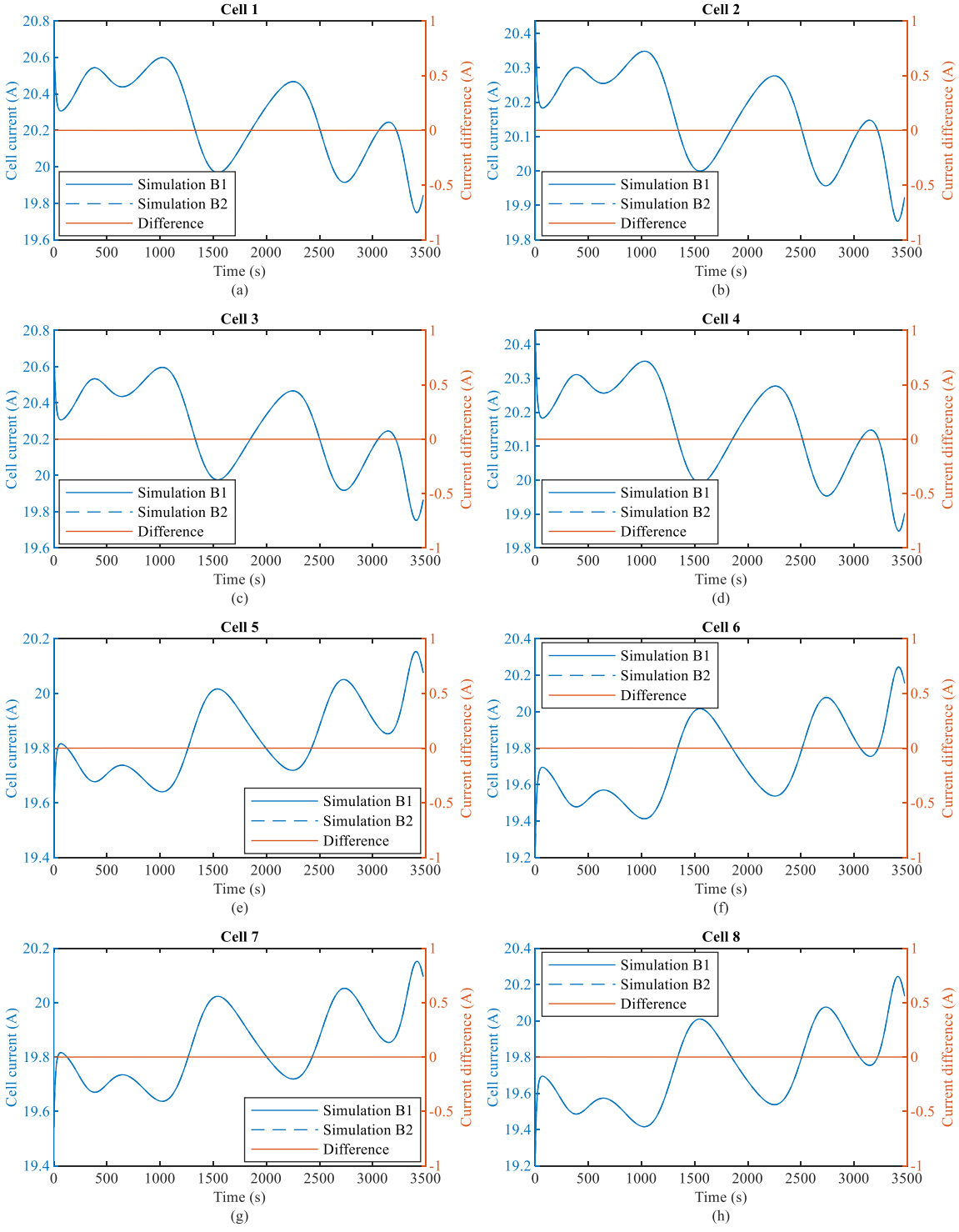

Figure 4.15 Verification B: Cell current simulation result from Simulink and the proposed simulator and the difference between them (a)-(h): cell 1-8

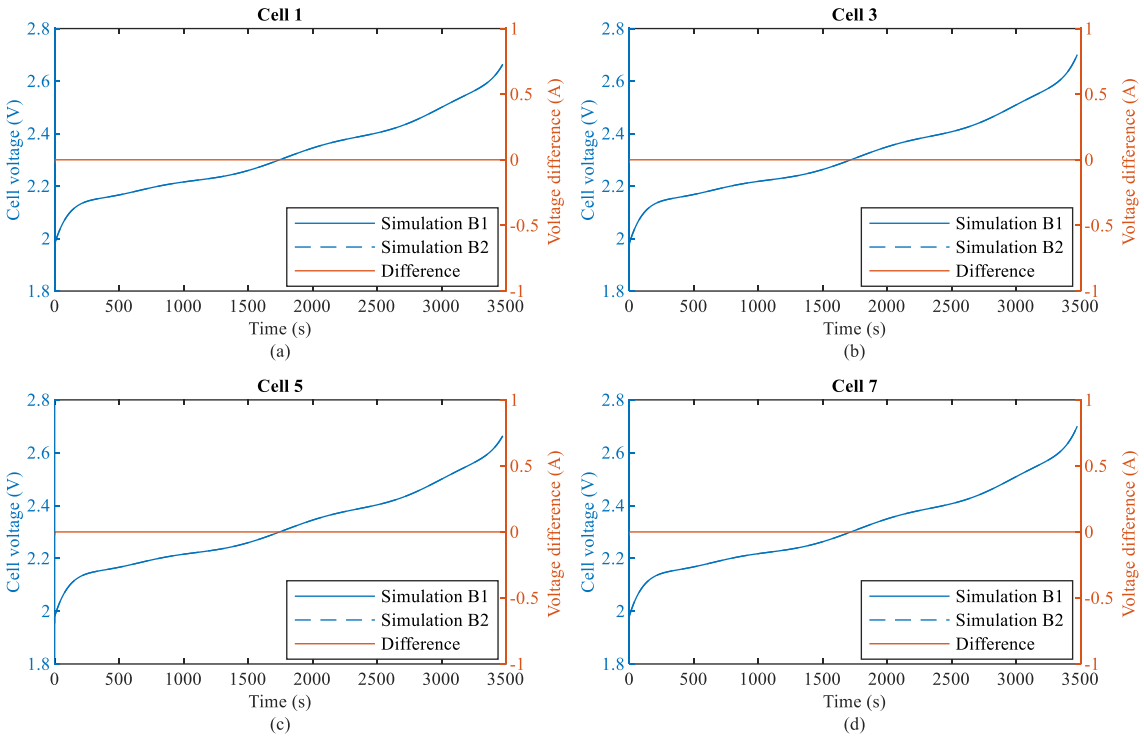

Figure 4.16 Verification B: Cell voltage simulation results from Simulink and the proposed simulator and the difference between them (a): cell 1; (a): cell 3; (a): cell 5; (a): cell 7

Comparisons between proposed battery simulator with a scaled RC model and a multicell battery validate the operation of the simulator for both terminal voltage, cell voltage and cell current.

4.5 Conclusion

The cell level simulation for a large-scale battery pack is meaningful for understanding the battery management system and the battery properties. The traditional circuit simulation method (SPICE type simulator, modified nodal analysis) is not easily able to handle calculation for the cell level equivalent circuit for a large-scale battery pack because of the difficulty in inverting a large-sparse matrix. It is worth mentioning that the author did not conduct simulations on all the SPICE simulators. Hence, a general conclusion on the capability of SPICE simulators cannot be made. This chapter proposed a circuit simulator for large-scale battery pack cell level equivalent circuit simulation using Thévenin or Norton circuit transformation. The proposed simulator is verified by another simulation method (scale-up method) and another commercial simulator (Simulink, MATLAB).

The simulations in verification A and B raise the phenomenon of cell-to-cell variance. Compared with the battery pack in verification A, verification B has different cell parameters. The differences between the cells, known as cell-to-cell variance, leads to the cell voltage and current deviation. Also, a decrease in the available pack capacity is witnessed in verification A and B (from 79.04 Ah in verification A to 77.2 Ah in verification B). In a large-scale battery pack like WESS, cell-to-cell variance could cause serious consequences such as discontinuous power delivery. In the next chapter, the proposed simulator will be used to study cell-to-cell variance in the large-scale battery pack WESS.

Chapter 5. Cell level modelling for Willenhall Energy Storage System

In Chapter 3, pack level models have been developed for Willenhall Energy Storage System (WESS). Then, a cell-level simulator for large-scale battery pack was described in Chapter 4. As the simulations conducted with the proposed simulator in Chapter 4 show, the cell-to-cell voltage deviation exists in multi-cell battery packs which could cause problems such as capacity loss in reality. In this chapter, the cell-level simulator provided in Chapter 4 will be adopted to simulate Willenhall sized battery packs and the results will be used to analyse the cell-to-cell deviation in battery packs.

In a multi-cell battery pack, all cells are restrained to operate inside a certain voltage range by the battery management system (BMS) to prevent cell damage from undesired physical and chemical changes such as collector dissolution, and lithium dendrites [123]. There is variation in manufacturing tolerance, impurities etc, which eventually leads to differences between cells, which can be observed in terminal voltage. The overall pack performance is limited by the 'worst' cell [124], which reduces the energy utility of other cells. Inside a large battery energy storage system, this energy loss becomes considerable due to its scale.

As it has been discussed in Chapter 2, for the cells with the same chemistry, manufacture and factory, cell-to-cell variation (CtCV) still generally exists. Different cells can be represented by the same equivalent circuit models (ECM) with different electrical component values. For the cells from the same factory and batch, their ECM electrical component values usually follow a statistical distribution which can be identified by sampling experiments. With knowledge of the ECM electrical component value distributions, cells can be randomly generated. Then an ECM for multi-cell battery pack considering CtCV can be constructed by connecting these individual cell ECMs.

This chapter presents an investigation of the voltage deviation related phenomena observed during the operation of WESS research platform (which was described in detail in Chapter 3), including the voltage deviation value change during full state of charge (SoC) range and the immediate cut-off mechanism caused by a large voltage deviation.

After that, cell voltage deviation in WESS sized battery pack (>21k cells) will be studied using Monte Carlo simulation through the cell level battery simulator proposed in Chapter

4. To obtain cell equivalent circuit parameter distributions (the standard deviation and mean value), electroimpedance spectroscopy measurements (EIS) and equivalent circuit modelling were conducted on the same type of cell as that be used in WESS. The obtained distribution was used to randomly generate cells for constructing WESS sized battery pack. The dependency between SoC and the parameters distribution is considered in the model.

The simulation in this chapter focuses on the impact of the intrinsic variation sources on a LTO battery pack in a limited time event (a charging and discharging cycle) and the intrinsic CtCV is represented by the difference in ECM components value. Both experiments and simulations reveal that high cell voltage deviation emerges at the low and high state of charge zones where the cell internal resistance has a large value and large extent of deviation.

5.1 Cell voltage deviation phenomena observed during the operation of Willenhall Energy Storage System

5.1.1 Maximum allowed cell voltage deviation

During the operation of Willenhall Energy Storage System (WESS), some occasional unexpected cut-off events happened during which the battery is instantly disconnected from the load regardless of the demand. This battery disconnection causes the discontinuity in delivering or absorbing energy and could lead to a penalty in the service it provides (e.g. frequency service). The history data shows that some of these events are caused by voltage deviation in the battery. It was found that instead of eliminating the voltage deviation, the battery management system (BMS) in the WESS maintains the voltage deviation at a low level (~10 mV) through relaxation and passive balancing circuit. In this case, the cell imbalance is so severe that the BMS disconnects the battery in order to protect it. Under these circumstances, it may be necessary to balance the cells manually. Figure 5.1 shows a constant charging experiment where the charging process is repeatedly interrupted by the BMS due to the 150 mV maximum voltage deviation restriction. 150 mV is the manufacturer-specified maximum allowed cell voltage deviation which is 12.5% of the difference between the LTO cell's higher and lower cut-off voltages (higher: 2.7 V and lower: 1.5 V).

In this chapter, as (5.1) (5.2) and (5.4) define, cell voltage deviation $V_{\mathrm{t,dev}}$ refers to the difference between $V_{\mathrm{t,max}}$ and $V_{\mathrm{t,min}}$ which are the maximum and minimum cell terminal

voltage in a pack. $V_{\mathrm{t,i}}$ is the terminal voltage for cell with identity number i (for WESS i is an integer between 1 and 21,120). $[N_{\mathrm{R}}, N_{\mathrm{M}}, N_{\mathrm{S}}, N_{\mathrm{C}}]$ is used to represent the location of a cell where $N_{\mathrm{R}} \in [1,40], N_{\mathrm{M}} \in [1,22], N_{\mathrm{S}} \in [1,12]$ and $N_{\mathrm{C}} \in [1,2]$ are the identity of the racks, modules, sub-modules and cells respectively as Figure 4.1(c) shows. The cell identity can be calculated as $i = 528(N_{\mathrm{R}} - 1) + 24(N_{\mathrm{M}} - 1) + 2(N_{\mathrm{S}} - 1) + N_{\mathrm{C}}$. Besides, average cell terminal voltage $V_{\mathrm{t,avg}}$ is defined in (5.3). Similar terms such as cell state of charge (SoC) deviation SoC_{dev} and cell current deviation I_{dev} are defined in the same way.

$$V_{\mathrm{t,max}}(t) = \max\left(V_{\mathrm{t},1}(t), V_{\mathrm{t},2}(t), \dots, V_{\mathrm{t},21120}(t)\right) \tag{5.1}$$

$$V_{\mathrm{t,min}}(t) = \min\ \left(V_{\mathrm{t},1}(t), V_{\mathrm{t},2}(t), \dots, V_{\mathrm{t},21120}(t)\right) \tag{5.2}$$

$$V_{\mathrm{t,avg}}(t) = \mathrm{mean}\left(V_{\mathrm{t},1}(t), V_{\mathrm{t},2}(t), \dots, V_{\mathrm{t},21120}(t)\right) \tag{5.3}$$

$$V_{\mathrm{t,dev}}(t) = V_{\mathrm{t,max}}(t) - V_{\mathrm{t,min}}(t) \tag{5.4}$$

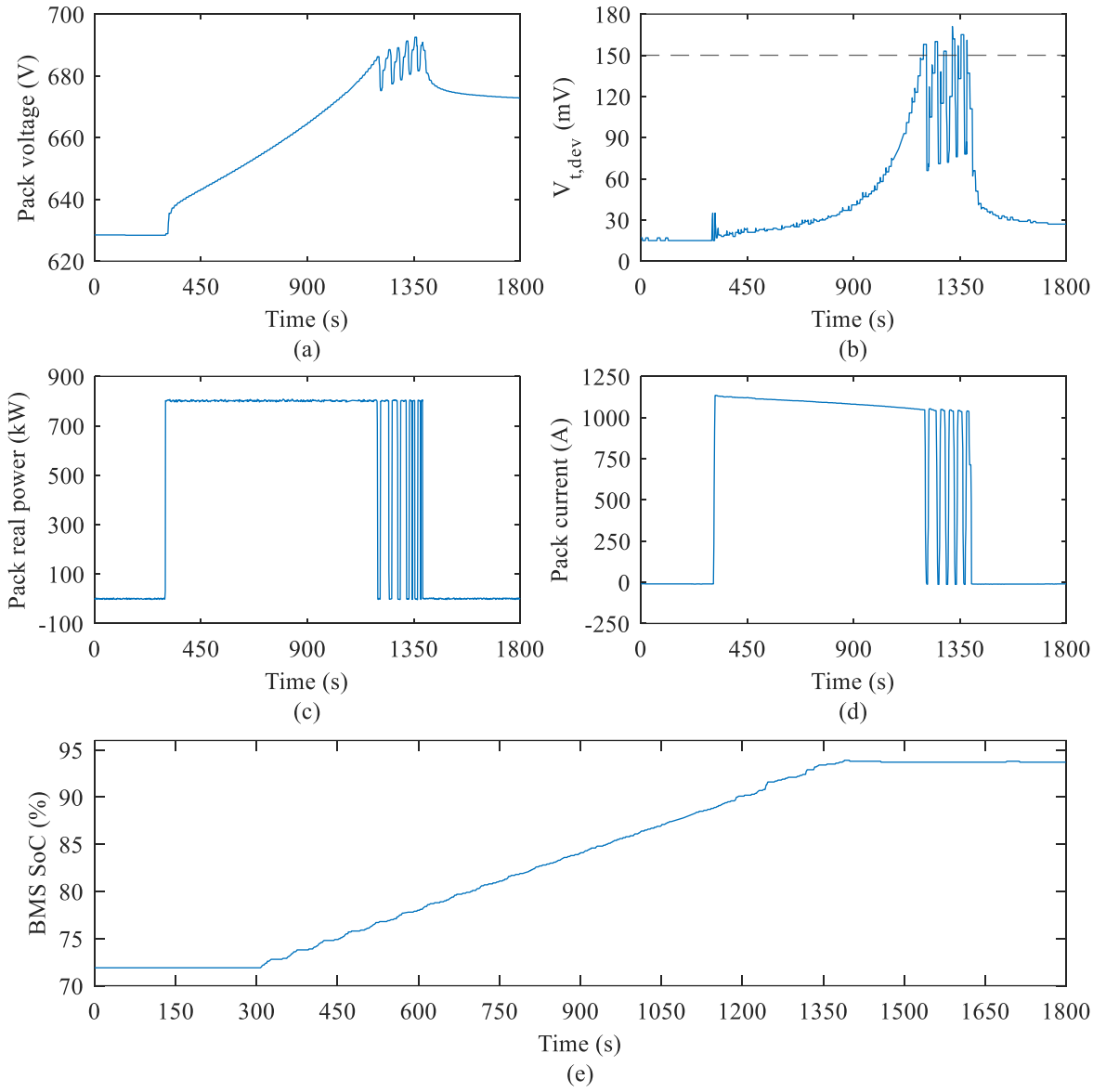

Figure 5.1 Measurements showing BMS cutting of the battery due to the battery exceeding the maximum allowed cell voltage deviation, 150mV (SoC: from 72.7% to 93.8%): (a) pack voltage, (b) cell voltage deviation, (c) pack power from BMS, (d) pack current and (e) BMS SoC

Figure 5.1 shows the BMS-recorded performance of WESS during a constant power charge with part (a) showing the pack voltage, (b) the maximum cell voltage deviation, (c) the power provided by the BMS, (d) the pack current and (e) SoC estimated by BMS. The worst voltage deviation scenario in the WESS is in the high SoC zone. When the cell voltage deviation reached the maximum allowed value of 150 mV, as shown Figure 5.1(b), the battery was cut off from the load. After a brief rest, the voltage deviation value dropped below 150mV and then the battery was brought back online by the BMS. With the reapplication of the charging current (~1000 A), the voltage deviation quickly restored to 150 mV in more than 10 s

(normally 10 s – 40 s) and triggered another cut-off. This process repeatedly occurred at the end of charge causing the discontinuity in energy delivery. The first cut-off in Figure 5.1 happens at around 90% SoC, and the rest 10% battery capacity cannot be used effectively. Under this circumstance, in frequency service applications, the battery will be failed on absorbing the extra energy from the grid network even the battery is not fully charged.

5.1.2 Cell voltage deviation in repeated experiments

To explore the changing trend of cell voltage deviation in WESS at the 'full' SoC range, constant load experiments were conducted on the WESS. Figure 5.2 presents two repeated constant power experiments (855 kW) on WESS. In both experiments, the battery was discharged from 95% SoC to ~5%; After a one-hour resting, the battery was charged to 90% as Figure 5.2(b) shows. The battery pack is in a heating, ventilating and air conditioning controlled environment which minimises the influence of the ambient environment on the experiments. At the end of discharge, there is a slight SoC difference between two experiments (Exp. 1: 5%, Exp. 2: 7%), as Figure 5.2(b) shows. Also, the internal cell balancing circuit incorporated within the Toshiba battery pack works under the instruction of a propriety BMS which operates outside the user’s control.

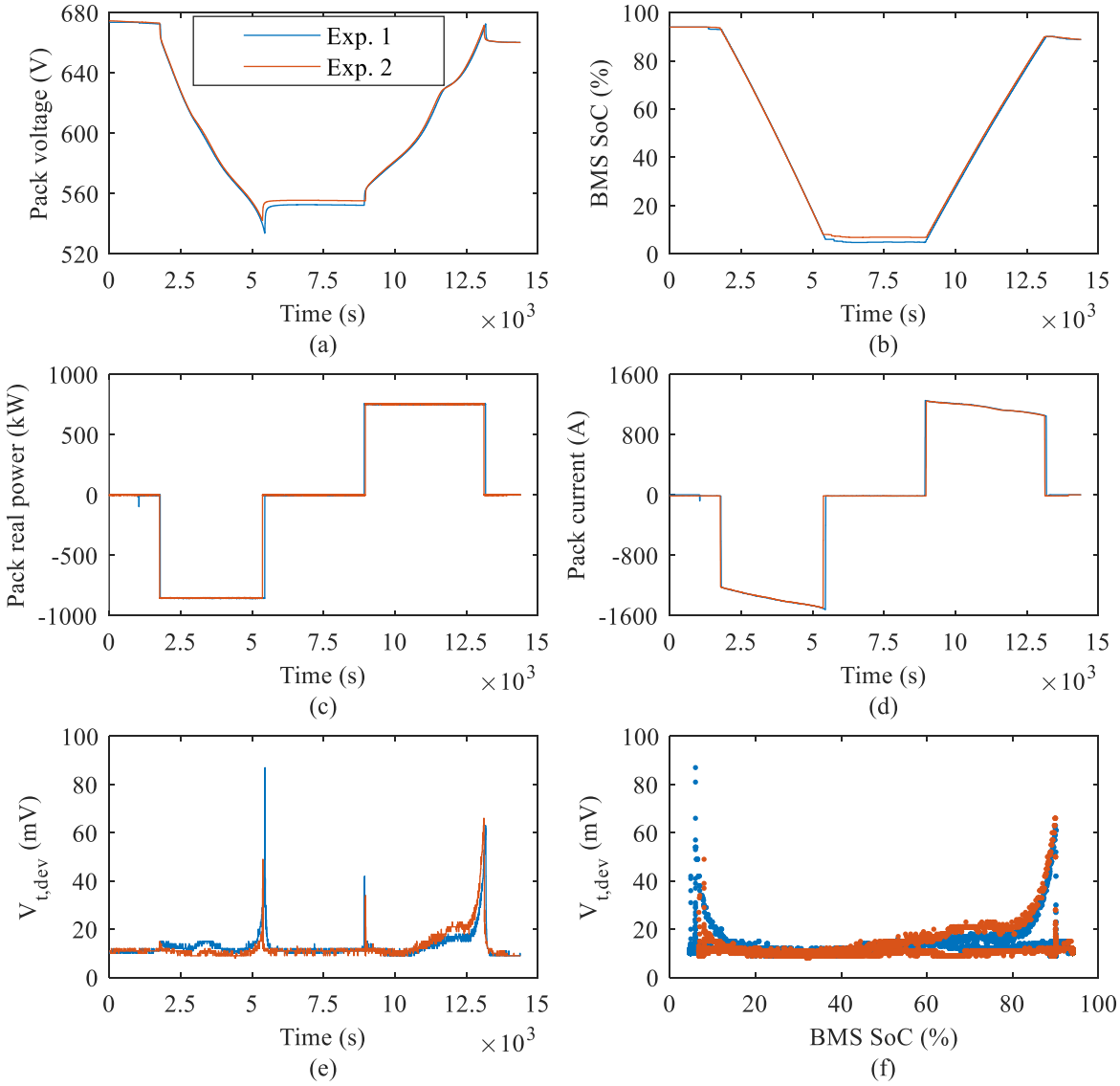

Figure 5.2 Two repeat experiments (blue: experiment 1, red: experiment 2): (a) pack voltage, (b) pack SoC from BMS, (c) pack power from BMS, (d) pack current (charging: positive), (e) cell voltage deviation vs. time, (f) cell voltage deviation vs. BMS SoC. Note: the legend for each subfigure is identical, and hence only one legend is shown in (a)

As Figure 5.2(e) and (f) show, the two cell voltage deviation results share similarities in shape and value. At the beginning of both experiments, the battery had the same and stable voltage deviation of about 10mV. The voltage deviation had a slight step increase at the beginning of discharge (~1800 s) and then experienced a long period of fluctuation during further discharge. At the end of discharge (~5500 s), the deviation value had a rapid increase but ended with different values (Exp. 1: 87 mV, Exp. 2: 49 mV). SoC difference is believed to be a reason for this value difference.

During the resting processes, the voltage deviation quickly decayed and restored to 10 mV within a few minutes. At the beginning of charge (~9000 s), there was a smaller peak of voltage deviation. After a period of relative stability, the voltage deviation increased to a large value (Exp. 1: 63 mV, Exp. 2: 66 mV) at a high charging rate. The similar phenomenon was found in another experiment in WESS and reported in [125]. From the view of the SoC domain, Figure 5.2(f), at the same SoC, the voltage deviation in the two experiments is close to each other. The peak value of voltage deviation appeared at low (~5%) and high (~90%) SoC zone.

5.2 Preparation for cell level battery pack simulation

A cell level battery pack equivalent circuit simulator has been developed and verified in Chapter 4. This simulator will be used to study the impact of the cell voltage deviation phenomenon in this chapter. In the simulator, each cell is represented by an equivalent circuit from which the entire battery pack is constructed according to its internal hierarchy. Every single cell's ECM parameter information is essential for the battery pack simulator.

In the case of the WESS, it is impractical to disassemble the WESS facility and identify the ECM parameter value for each of the 21,120 cells. Instead, all the cells' ECM parameters are assumed as following normal distributions and randomly generated from their mean values and standard deviation which are obtained from pre-experiments (electroimpedance spectroscopy measurements (EIS) tests) on four representative cells. The details and partial results of EIS test will be shown in section 5.2.1.

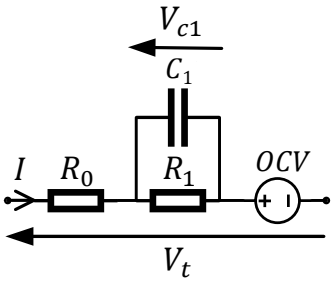

Figure 5.3 Single time constant ECM

The single time constant ECM, as shown in Figure 5.3, is chosen for fitting EIS tests and consequently the randomly generated cells in this chapter are represented by the same type of ECM (with single time constant). The single time constant ECM consists of an ohmic resistance (R_0), a RC branch (R_1C_1) and a voltage source representing open circuit voltage

(OCV) which has been used in Chapter 3 for modelling WESS in pack level and in Chapter 4 for developing cell level simulator. V_t and I are the cell terminal voltage and the cell current (defined as charging). The processes related to ECM parameter generation will be explained which mainly consists of three parts: parameter value and distribution identification (in section 5.2.1), generating parameter value (in section 5.2.2), and constructing ECM models for individual cells (in section 5.2.3).

5.2.1 Equivalent circuit model parameter value identification and the extend of parameter variation

ECM parameters used in the battery pack simulator are randomly generated according to the parameter's value and distribution from pre-experiments on sample cells. To obtain ECM parameters value at different SoC points, EIS tests were conducted on four super charge ion battery (SCiB) lithium titanium oxide (LTO) cells with the same cycle count (400 cycles). The four cells have a slight difference in cycling current value: two of the cells were cycled with 1 C-rate current and 2 C-rate for the other two. This is caused by the cells' usage history. However, the cycle counts for different cells are the same. Besides, the cycle count is small for LTO cells and not enough to cause dramatic cell degradation. So that the impact caused by the cycling current value difference is neglected in this chapter. These cells were labelled from Cell02 to Cell05 and tested at 25°C from 100% to 0% SoC in 10% intervals. In the EIS measurement, the frequency range was set from 5 kHz to 5 mHz.

Figure 5.4 illustrates the EIS impedance results of the 4 cells at 50% SoC where Z_{re} and Z_{im} are the real and imaginary parts of the impedance. When Z_{im} is positive, the test results are distorted (Figure 5.4(a)). Fortunately, the model in Figure 5.3 can never have an impedance with a positive imaginary part. Hence, only the EIS result with negative imaginary parts (Figure 5.4(b)) were used to identify the parameter's value. An example of ECM fitting results are shown in Figure 5.4(c) - (f) (fitting software: [126]). The EIS impedance results and ECM fitting results at other SoC points can be found in Appendix B.

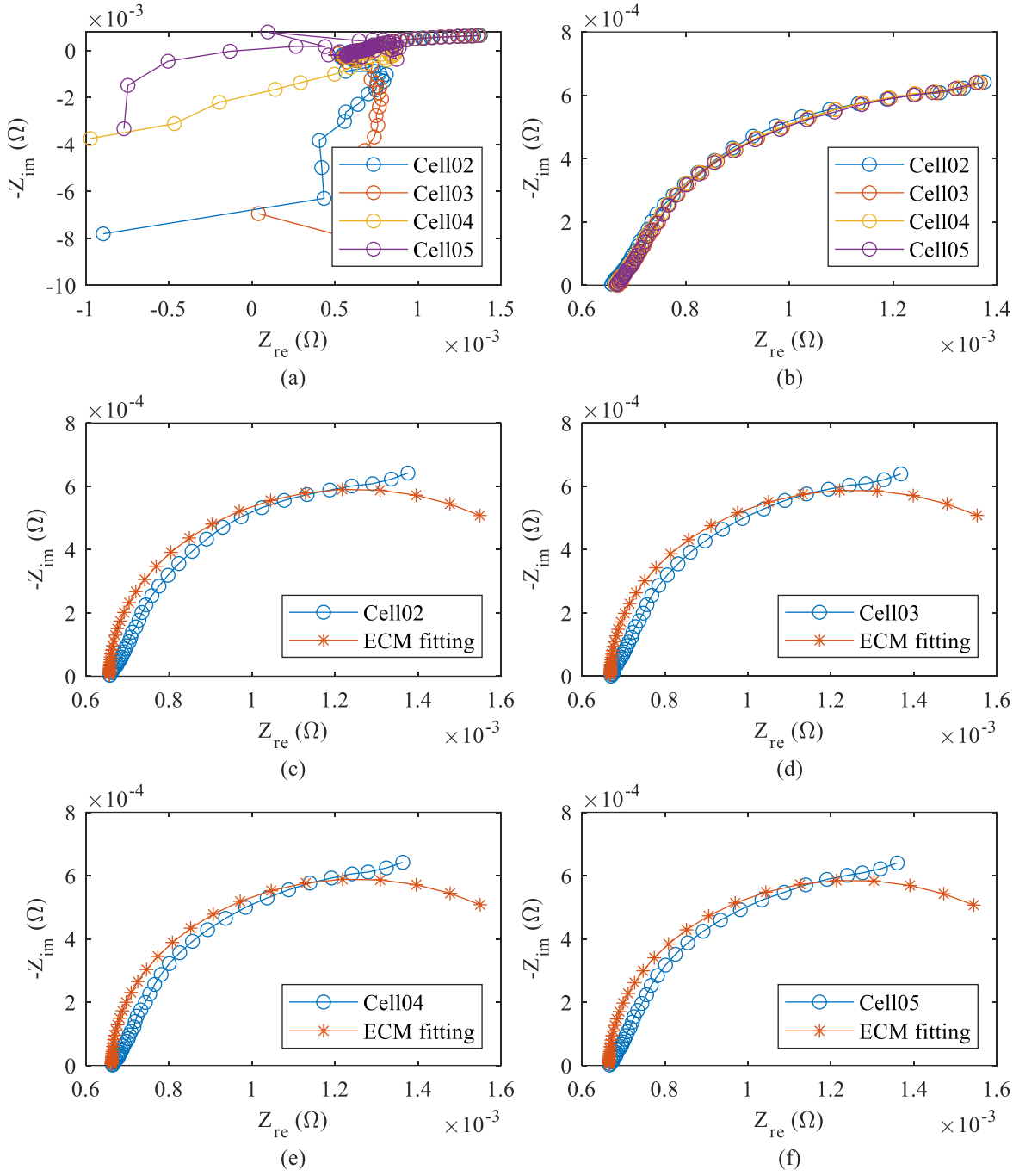

Figure 5.4 EIS and ECM fitting result of 4 LTO cells at 50% SoC: (a) overall result, (b) result when $Z_{im} < 0$, (c) – (f) ECM fitting result from Cell02 to Cell05

The overall fitting results of ECM parameters are presented in Figure 5.5 (in the left vertical axis). In general, as Figure 5.5(a) shows R_0 has a stable value (~ 0.7 mΩ) which slightly decreases as SoC increases. R_1 takes most part of the total resistance R_{total} and dominates the change of it. R_{total} is the total resistance which is equal to sum of R_0 and R_1. Both R_1 and R_{total} have the highest value at 100% SoC and second-highest value at 0% SoC. Time constant τ_1 in Figure 5.5(b) has the highest value at 100% SoC and a peak value at 60% SoC.

The results shown in Figure 5.5 provides ECM parameters of four cells and, more importantly, the distribution (the standard deviation σ to the mean μ) of each ECM parameter can be obtained from it.

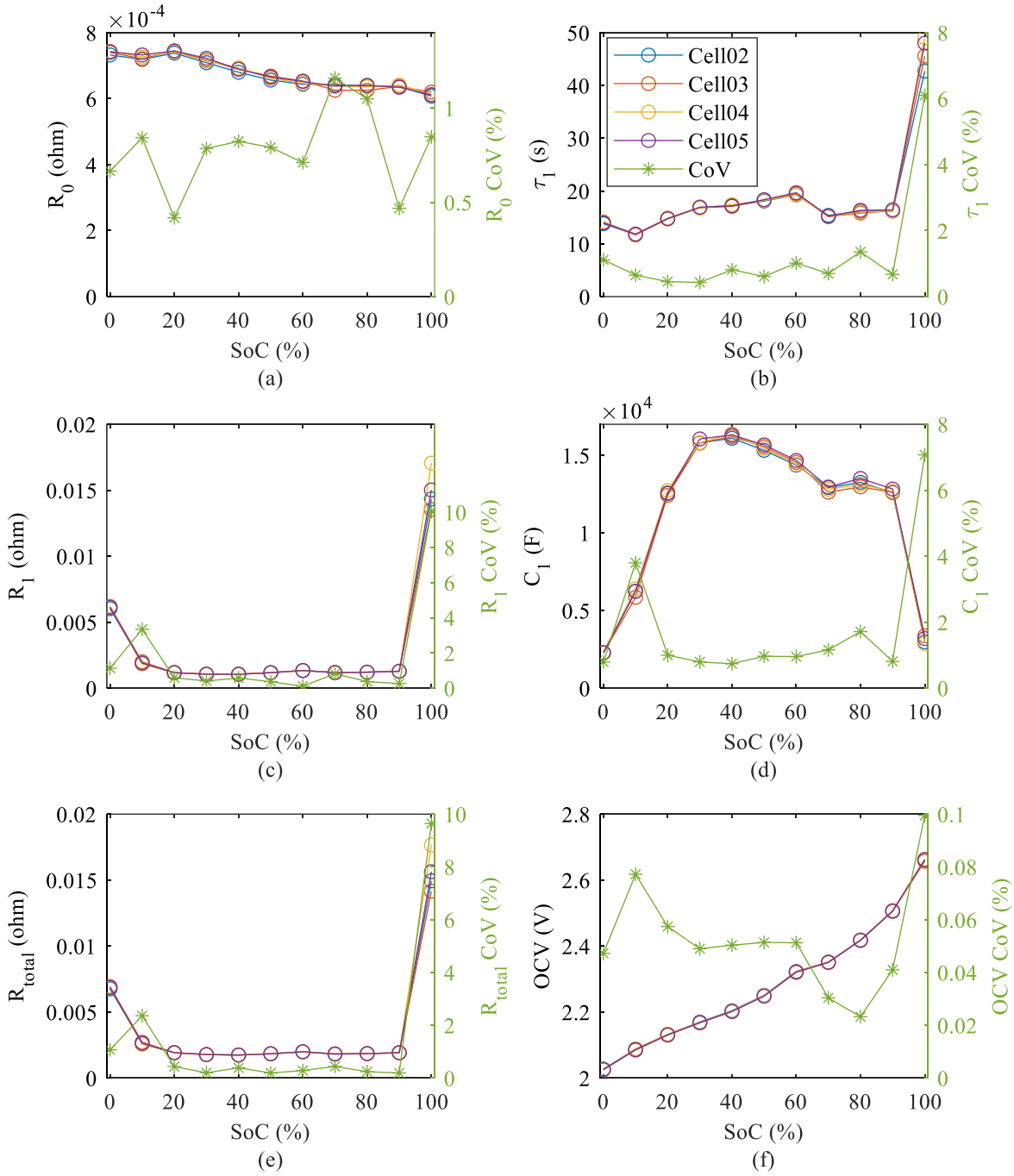

Figure 5.5 Parameter value and the coefficient of variation of: (a) R_0, (b) τ_1, (c) R_1, (d) C_1, (e) R_{total}, (f) OCV. Note: the legend for each subfigure is identical, and hence only one legend is shown in (b)

The previous experiments on WESS in Figure 5.2 shows the cell voltage deviation changes a lot during charging and discharging which indicates that the extent of cell variation in

WESS might be different at different SoC. The coefficient of variation (CoV) is used in this chapter to describe the extent of parameter variability through which the relationship between the extent of cell variation and SoC will be explored. For a data set with N elements $A_1, A_2, \ldots A_{\mathrm{N}}$, the CoV is defined by the ratio of the standard deviation σ to the mean μ as (5.5)-(5.7) show.

$$\sigma = \sqrt{\frac{1}{N-1}\sum_{\mathrm{i}=1}^{N} |A_{\mathrm{i}} - \mu|^2} \tag{5.5}$$

$$\mu = \frac{1}{N}\sum_{i=1}^{N} A_{\mathrm{i}} \tag{5.6}$$

$$CoV = \frac{\sigma}{\mu} \tag{5.7}$$

The CoV of different parameters at different SoC is also shown in Figure 5.5 (in the right vertical axis). Among all the parameters, OCV in Figure 5.5(f) has the least CoV around 0.06% (±0.04%) and the largest value of it appears at 100% SoC as 0.1%. As Figure 5.5(a) shows, R_0 has a small CoV concentrated at 0.8% (±0.4%). The CoVs of R_1 and C_1 do not have rapid change between 20% and 90% SoC and both have large values at 10% and 100% SoC. R_1 and C_1 are parameters related to the diffusion process. The large CoV indicates more distinct differences in electrical or chemical properties among tested cells, such as the reaction rate. In terms of τ_1, the large CoV only shows up at 100% SoC. The cells capacities were estimated by the Coulomb counting method (μ=20.73 Ah, σ=0.03 Ah).

As can be observed in the cell SoC experimental data, at the extremities of the SoC curve, the voltage deviation becomes greater. Battery energy storage system manufacturers recognise this issue and therefore restrict the operating range of their systems to avoid issues associated with voltage deviation at extreme SoC. The parameters' large value of CoV at these SoC regions is believed as an important reason for the high voltage deviation observed in Figure 5.1 and Figure 5.2.

5.2.2 Generating equivalent circuit model parameters value

With the ECM parameters result of EIS tests, ECM parameters used in the battery pack circuit solver can be generated to fit a measured statistical distribution. Before random

numbers are generated, the type of distribution must be chosen. Experiment results in the literature reflect that cell parameters reasonably fit normal distributions. In papers [105][127][128], a large number of lithium-ion cells were tested and the results show that cell parameters such as resistance, capacity reasonably fit normal distributions. So that, in the Monte Carlo simulation that follows, all the parameters are assumed to follow normal distributions. The standard deviation σ to the mean μ of each parameter at different SoC were estimated from the EIS results in Figure 5.5.

ECM parameters among tested cells are not independent of each other. To include the correlation among parameters, in this chapter R_0, R_1 and C_1 at every 10% SoC are set as following a joint normal distributed whose probability density function (PDF) $f(R_0, R_1, C_1)$ is shown in (5.8). μ_{R0}, μ_{R1} and μ_{C1} are the mean of random variable R_0, R_1 and C_1 respectively. $\boldsymbol{\Sigma}$ is the covariance matrix and shown in (5.9) where $\mathrm{cov}(.,.)$ represents the covariance. From 0% SoC at every 10% SoC, R_0, R_1 and C_1 are generated according to their σ, μ, and $\boldsymbol{\Sigma}$ obtained from cells EIS tests results in Figure 5.5 and the PDF in (5.8).

$$f(R_0, R_1, C_1) = \frac{1}{(2\pi)^{\frac{3}{2}} \cdot |\Sigma|^{\frac{1}{2}}} \exp\left(-\frac{1}{2}\left(\begin{bmatrix} R_0 \\ R_1 \\ C_1 \end{bmatrix} - \begin{bmatrix} \mu_{R0} \\ \mu_{R1} \\ \mu_{C1} \end{bmatrix}\right)^T \cdot \Sigma^{-1} \cdot \left(\begin{bmatrix} R_0 \\ R_1 \\ C_1 \end{bmatrix} - \begin{bmatrix} \mu_{R0} \\ \mu_{R1} \\ \mu_{C1} \end{bmatrix}\right)\right) \tag{5.8}$$

$$\boldsymbol{\Sigma} = \begin{bmatrix} \mathrm{cov}(R_0, R_0) & \mathrm{cov}(R_0, R_1) & \mathrm{cov}(R_0, C_1) \\ \mathrm{cov}(R_1, R_0) & \mathrm{cov}(R_1, R_1) & \mathrm{cov}(R_1, C_1) \\ \mathrm{cov}(C_1, R_0) & \mathrm{cov}(C_1, R_1) & \mathrm{cov}(C_1, C_1) \end{bmatrix} \tag{5.9}$$

In terms of capacity and open circuit voltage, due to the limited sample size from the experiment, it is challenging to identify the most correlated parameters and SoC point to cell capacity Q. As a compromise, Q is set as an independent normal distributed variable in this chapter and can be straightforwardly generated for different cells.

R_0, R_1 and C_1 are the parameters related to cell's dynamic properties. However, OCV is the cell terminal voltage at an equilibrium state, and it is decided by cell chemistry rather than the cell's dynamic properties (R_0, R_1 and C_1). Therefore, OCV is set as an independent variable which is irrelevant to R_0, R_1 and C_1. The coulombic efficiency for all cells is set as

100% so that the effect of coulombic efficiency variation among cells is not included in this chapter.

5.2.3 Constructing models for individual cells

Building the model of R_0, R_1 and C_1 is the most complex part of constructing ECMs for individual cells which are divided into three steps. Step 1: the value of R_0, R_1 and C_1 at different SoC (0%, 10%, … 100%) for all 21,120 cells are randomly generated as section 5.2.2 describes. Step 2: the randomly generated parameter in step 1 is regrouped according to their cell identity. Step 3: the parameter and SoC relationship is modelled using polynomial equations cell by cell. A diagram demonstrating this process is provided in Figure 5.6. The method of generating OCV-SoC model for each cell is similar.

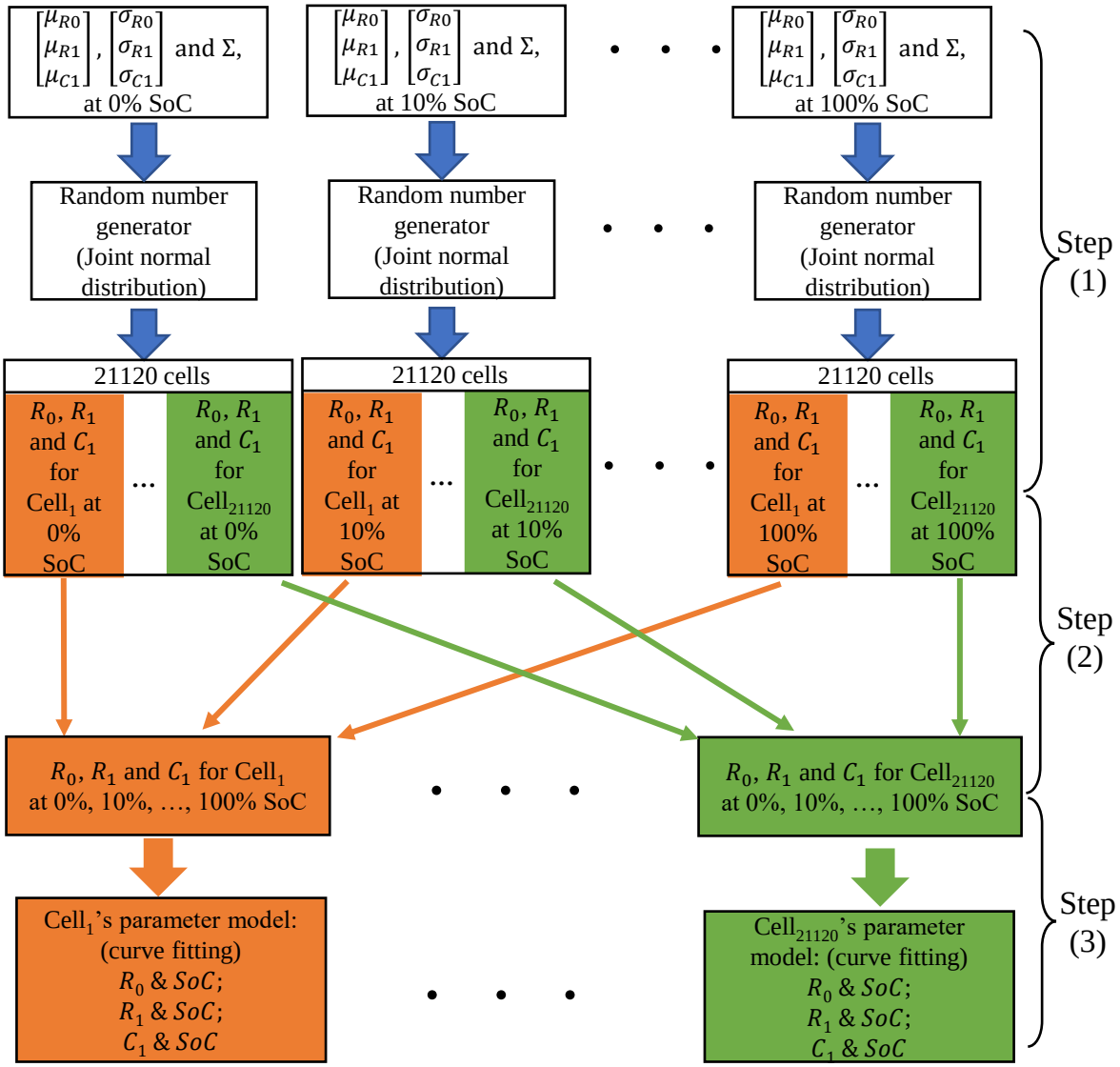

Figure 5.6 The process of generating and modelling R_0, R_1 and C_1 at full SoC range for 21,120 number of cells. Step 1: random value generating for different cell at different SoC points. Step 2: reorganise the random value, gather parameter value for the same cell at different SoC into the same group. Step 3: obtain parameter-SoC relationship for each cell by curve fitting

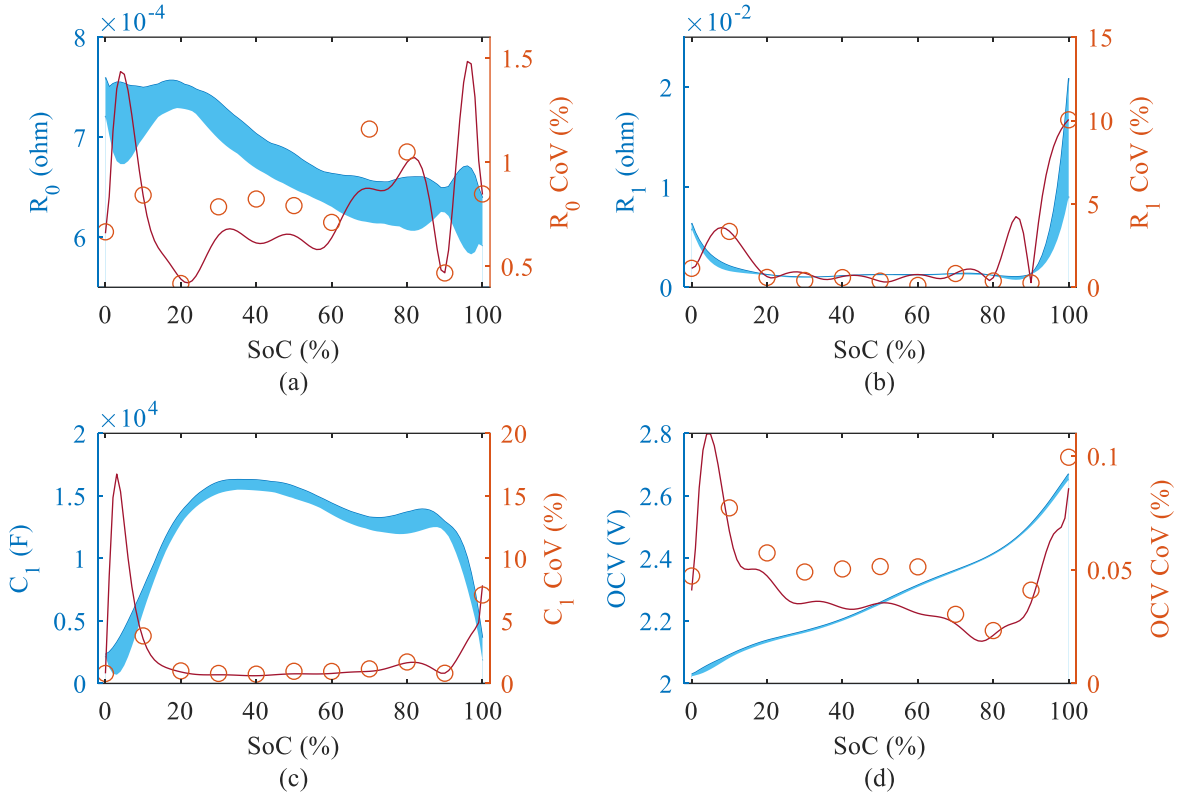

Figure 5.7 A randomly generated WESS sized battery, all cells' ECM parameters and their CoVs (red inline: CoV of generated pack; circle points: CoV from EIS experiment): (a) R_0; (b) R_1; (c) C_1; (d) OCV vs. SoC

An example of a generated battery is illustrated in Figure 5.7 in which the cyan areas contain all 21,120 cells' parameter-SoC relationship. In another word, for a cell in the generated pack, its parameter-SoC relationship is located inside the cyan regions. The red line in Figure 5.7 represents the parameter CoV of all 21,120 cells in the generated pack and the red circles are parameter CoV from the previous cells EIS experiment shown in Figure 5.5. In general, the parameters value and CoV in the generated pack are consistent with the experiment results in Figure 5.5. So far, the essential preparation for battery pack simulation has been done which includes building a battery pack simulator and generating random battery packs.

5.3 Monte Carlo simulation: constant power load

In this section, 100 randomly-generated WESS-sized battery packs are simulated under a constant power load (855 kW). The simulation results provide a general changing trend of variables such as battery voltage, current and cell voltage deviation, under the specified load and predetermined parameter uncertainty. In each simulation, all the 21,120 cells are set as 95% SoC. The cells are connected into a pack according to the electrical connection which

has been described in Chapter 4. Because of the variation in cell OCV-SoC relationship, cells have slightly different terminal voltages. This terminal voltage difference is decreased by a 10-minute rest through self-balancing during which the terminal voltage difference among cells causes an internal cell current through the internal electrical connection in the pack. After resting, the maximum cell self-balancing current decreases to a small value (~0.005 C-rate). A small (or zero) self-balancing current indicates that the battery pack cannot be further effectively balanced by itself. Then, the pack is discharged with constant power until it meets cut-off requirements. After another 10-minute rest, the battery is charged until cut-off. In this simulation, a battery pack is cut-off when any cell voltage reaches cut-off voltages or any cell SoC is outside the range of 0 to 100% or the maximum cell voltage deviation exceeds 150 mV. Compared with the experiments in Figure 5.2, the simulation explored a wider SoC range and conducted a shorter rest period.

5.3.1 Results from a single simulation: at the pack and cell level

The Monte Carlo simulation provides 100 similar simulation results with slightly different timelines. For example, because of CtCV, battery packs have different parameters (e.g., capacity, internal resistance) so that batteries were cut-off at different time instants in different simulations. To clearly describe the simulation process, one of the Monte Carlo simulations using the parameter set in Figure 5.7 is chosen to be discussed first.

Figure 5.8(a)–(b) shows the pack level simulation result of the chosen simulation. Time instants from t_1 to t_4 in the figure represent the start or end of the discharging or charging. It is interesting to note that in a constant load simulation, the magnitude of battery current, shown in Figure 5.8(b), is increasing during the discharging process and decreasing during charging because of the decreasing and increasing battery voltage, respectively. This current change is also observed during the constant load experiment in Figure 5.2.

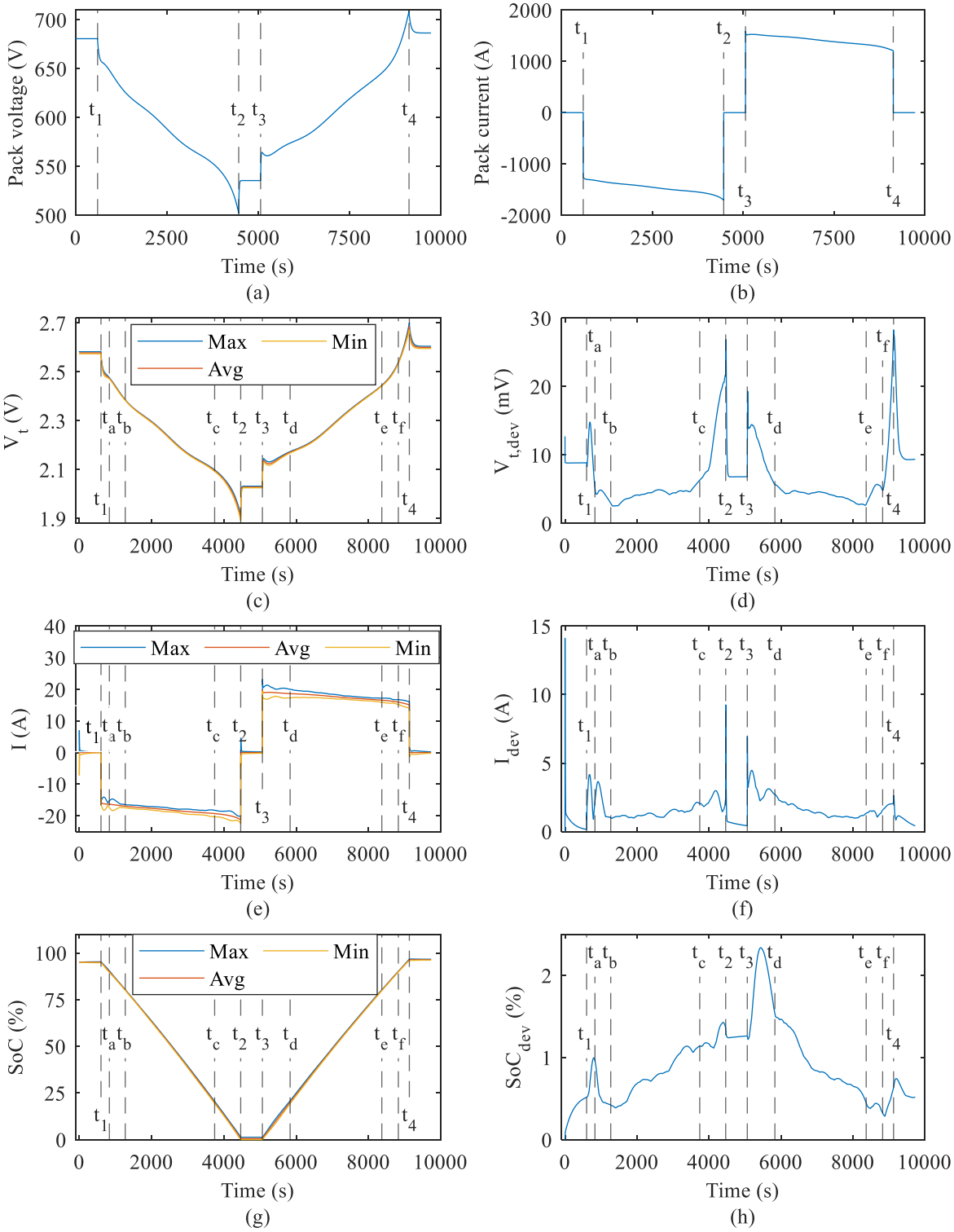

Figure 5.8 The result from a single simulation. (a) battery pack voltage, (b) pack current, (c - d) cell terminal voltage and deviation, (e - f) cell terminal current and deviation, and (g - h) cell SoC and deviation in the single simulation. t_1: 600 s (t_2: 4465 s, t_3: 5060 s, t_4: 9130 s; t_a: 832 s, t_b: 1271 s, t_c: 3744 s, t_d: 5832 s, t_e: 8369 s, t_f: 8826 s)

The cell level simulation results of the single simulation are shown in Figure 5.8(c) – (h). Apart from t_1 - t_4, six more time instants, t_a - t_f, are labelled in the figure at which cell

average SoC reaches some critical values (t_a and t_f: 90%, t_b and t_e: 80%, t_c and t_d: 20%). The most important finding in the single constant power simulation result is the relationship between the ECM parameter variation and the different kinds of cell voltage deviations that a large parameter variation causes a large deviation in the pack. Between SoC zones of 0% - 20% and 90% - 100%, all cell ECM parameters have a large CoV, as Figure 5.7 shows. Correspondingly, during t_1 - t_a, t_c - t_2, t_3 - t_d and t_f - t_4 when the battery pack is being discharged or charged in these two SoC zones, the battery pack is more unbalanced and shows a large value of $V_{t,dev}$, and I_{dev}.

It is worth mentioning the result during t_a - t_b and t_e - t_f when the cells are in the 80% - 90% SoC range. According to Figure 5.7, in this SoC range, R_1 who dominates the total internal resistance also has a large CoV. However, $V_{t,dev}$ is small during t_a - t_b and t_e - t_f for two possible reasons. First, between 80% - 90% SoC, the other parameters such as OCV and C_1 have a smaller CoV compared with 0% - 20% and 90% - 100% SoC as Figure 5.7. Second, the value of R_1 is small between 80% - 90% SoC which is unable to induce a large V_{over} and voltage difference. Consequently, a small $V_{t,dev}$ is witnessed in this SoC zone.

5.3.2 Results from Monte Carlo simulation

To obtain an overall view of the cell deviation inside WESS sized pack with the given parameter distribution under constant power load, 100 Monte Carlo simulations were conducted, and the results are presented in Figure 5.9. There are 100 lines in Figure 5.9 and each of them represents the $V_{t,dev}$ result from one of the 100 Monte Carlo simulations. As Figure 5.9 shows, all simulations have a similar changing trend in terminal voltage but with slightly different values. The finding in the previous single simulation example (in Figure 5.8) is still valid in the Monte Carlo simulation result that a large cell voltage deviation shows up at the beginning and end of charging and discharging where the cells have a large ECM parameter CoV and large internal resistance.

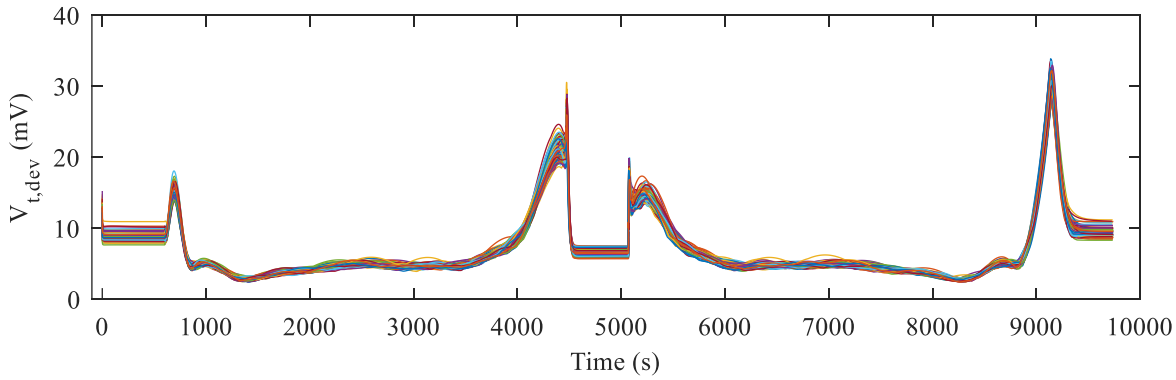

Figure 5.9 Cell terminal voltage deviation of 100 times Monte Carlo simulation

The $V_{\mathrm{t,dev}}$ results in simulations shares similarities with that in WESS experiments (Figure 5.2). In terms of the changing trend, both simulation and experiment witnessed a high $V_{\mathrm{t,dev}}$ at high and low SoC zone and also relatively small $V_{\mathrm{t,dev}}$ in between. However, in WESS experiments the $V_{\mathrm{t,dev}}$ in the beginning of discharging is not as obvious as that in simulation for unknown reasons. A possible reason is that before the experiments, cells in WESS were well balanced through the passive balancing circuit. The states (e.g., voltage, impedance) of different cells are close to each other so that cell voltage deviation is not obvious when a current pass through the battery. However, the passive balancing circuit is not included in the simulation model which causes a difference between simulation and experiments. In terms of value, $V_{\mathrm{t,dev}}$ in simulation is smaller than Exp.1 and Exp.2 in Figure 5.2. The cell balancing circuit in WESS and the error in ECM parameters' CoV are the possible reasons for it.

5.4 Conclusion

This chapter raises the awareness of the maximum allowed cell voltage deviation and the impact of SoC on cell variance which help the design of a BESS and the cell balancing technique. As it has been found in the chapter, the BMS may have an intense reaction when the voltage deviation exceeds the threshold value, for example, the battery cut-off in WESS. In most cases, the settings in a BMS cannot be changed by users. The cut-off reaction benefits the safety of the battery but may not be acceptable in some applications like electric vehicles where human life is involved.

Some multi-cell batteries contain balancing circuits to keep the cell voltage or SoC deviation under control. Normally, the balancing circuit is triggered when the voltage deviation value

reaches a setting value regardless of the SoC value. However, the simulations for WESS LTO battery packs in this chapter show that it is more likely that a high cell voltage deviation shows up at certain SoC regions (the end of charge or discharge) than others. More importantly, the cell voltage deviation decreases when the battery moves out of these SoC regions. So that, the balancing circuit could be designed with considering the impact of SoC on CtCV, for example, setting different threshold values for balancing circuit for different SoC regions.

Chapter 6. Open circuit voltage hysteresis in Willenhall Energy Storage System

6.1 Introduction

Chapter 3 and Chapter 5 successfully modelled Willenhall Energy Storage System (WESS) at pack level and cell level respectively with equivalent circuits. However, neither chapter discusses the open circuit voltage (OCV) hysteresis effect, which is a common phenomenon in a battery. An accurate OCV model is important not only for battery simulation but also state of charge (SoC) estimation.

As has been discussed in Chapter 3, because the relationship between OCV and SoC is repeatable, the OCV in battery equivalent circuit models (ECMs) is normally estimated through the OCV-SoC relationship. Because the OCV is the most significant part of the cell terminal voltage whose accuracy could significantly influence the fidelity of the ECMs.

In terms of SoC estimation, as discussed, in the WESS battery management system (BMS), the SoC estimation is corrected according to OCV-SoC relationship (implemented as a look-up table) when the battery has been rested for a long time. However, because of the hysteresis phenomenon, the same value of OCV is witnessed under different SoC with different SoC history. Consequently, without hysteresis information in the OCV-SoC relationship, an error can occur in the SoC estimation especially in the plateau OCV region.

This chapter discusses OCV hysteresis in the large-scale battery pack WESS. A low power (50 kW, 0.05C-rate) experiment was conducted on WESS, consisting of hysteresis loops of differing ranges. The OCV-SoC relationship during charging and discharging, and hence the OCV hysteresis, might be expected to be obtained from a straightforward experiment. However, the experimental data obtained does not fully agree with theoretical expectation and, at times, appears to be contrary to theory. Compensating for the effects of hysteresis on OCV therefore remains an open research topic. As will be shown, at the same SoC, the measured battery voltage during discharging can be measured higher than that during charging which cannot be a true reflection of the underlying physics.

The extended Kalman filter (EKF) is used to improve the SoC estimation during the continuous charging-discharging experiment. Under the SoC calculated from EKF, the OCV

hysteresis profile is improved insofar as, at all SoC points, the measured battery voltage during discharging lower than during charging. While this avoids the impossible scenario described above, the EKF is a model-based method and the EKF SoC can be influenced by the battery model and algorithm. This means that the SoC used for the hysteresis study should be determined using measurements from a high precision current sensor directly. Unfortunately, the studied platform does not have this capability and thus the findings of this chapter are not fully verified. It is believed that high precision current sensor and voltage sensor are needed in WESS to obtain the required data on this topic.

6.2 Open circuit voltage hysteresis and experiment on Willenhall Energy Storage System

6.2.1 Background of open circuit voltage hysteresis

The OCV of a battery cell is not only dependent on the state of charge (SoC) but also on SoC history which results in a hysteresis phenomenon in the open circuit votlage (OCV) and SoC relationship. Hysteresis can be measured by applying a balanced charge and discharge cycle. Figure 6.1 shows a schematic diagram of the OCV-SoC hysteresis phenomenon in a battery cell. There are a few terms that show up in Figure 6.1 including major loop, minor loop, hysteresis voltage and maximum hysteresis voltage. In a OCV-SoC hysteresis loop, SoC changes from a starting SoC point to a return SoC point and then back to the starting point. In a major loop, the battery starts at either 100% or 0 SoC, is fully charged or discharged (to 0 or 100%), and then discharged or charged (as the case may be) to its starting SoC. In a minor loop, at least one of the starting and turning SoC points are not 100% or 0%. In both cases, the SoC moves from A to B to A again where A is the starting point and B is the turning point. The OCV obtained from discharging and charging processes are noted as OCV_{dis} and OCV_{ch} respectively. The difference between OCV_{ch} and OCV_{dis} in a cycle is named the hysteresis voltage. The hysteresis voltage in the major cycle is larger than that in minor cycles so that it is named as the maximum hysteresis voltage. Hysteresis voltage varies with SoC, as well as the starting and turning points.

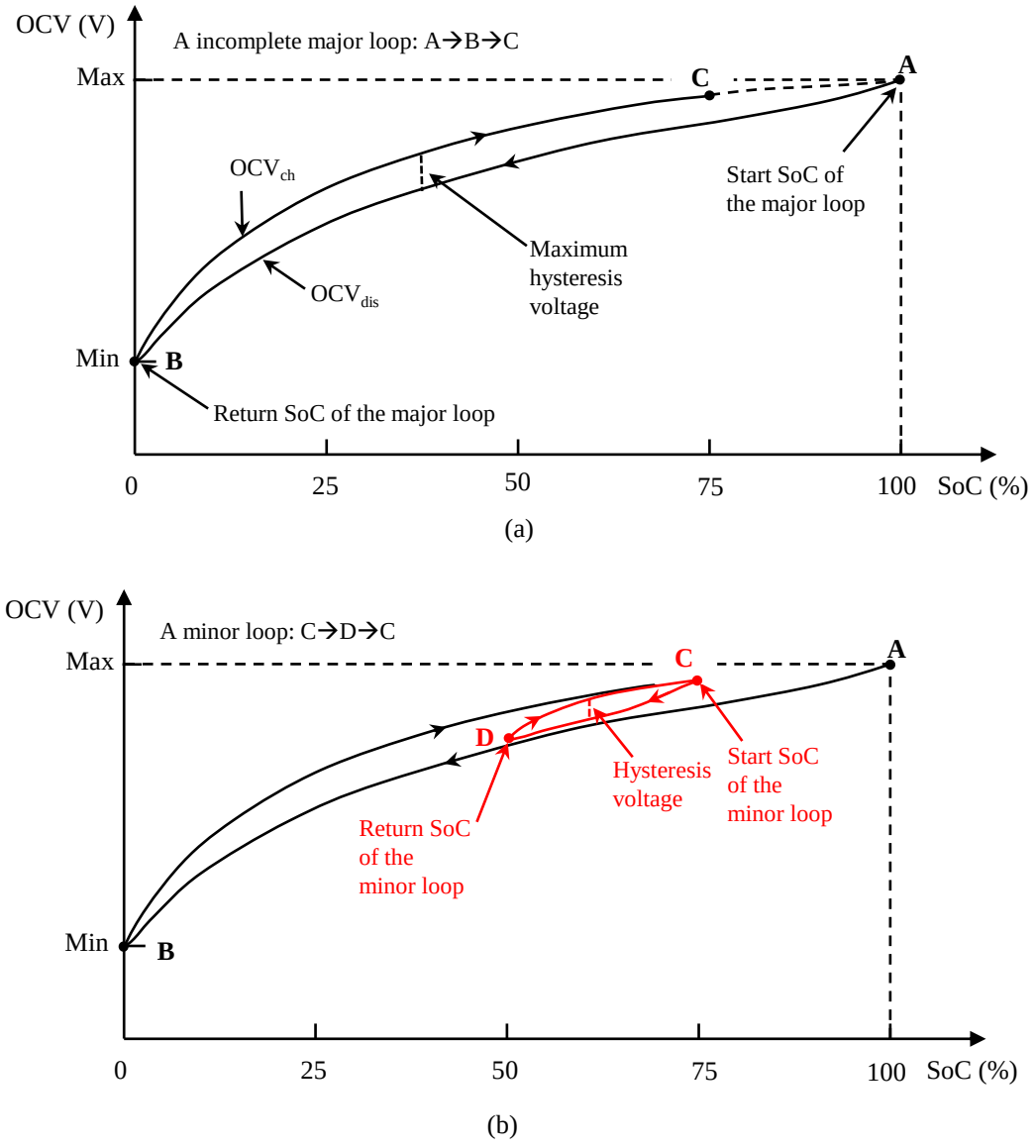

Figure 6.1 Schematic diagram of OCV hysteresis in a battery cell, (a): an incomplete major loop; (b): a minor loop

Figure 6.1(a) shows a schematic OCV-SoC relationship in a process in which the battery is discharged from 100% SoC (point A) to 0% (point B) and then charged to 75% (point C), which makes an incomplete major loop. The arrows on the OCV-SoC result represents the SoC movement changing direction in the process. As Figure 6.1(b) shows, at point C the battery cell is discharged to 50% SoC (point D) then charged back to 75% (point C) which makes a minor loop which is plotted in the red line in Figure 6.1(b). Again, the arrow on the minor loop indicates the SoC change direction.

During phase A→B, the battery cell is being discharged and has a history of decreasing SoC. By contrast, the battery has an increasing history of SoC during phase B→C. At the same

SoC, the OCV during the decreasing process (A→B) is smaller than that during the charging process (B→C). At point C, the direction change of battery SoC movement is reversed. The OCV is gradually decreasing with SoC and approaching line AB.

The hysteresis phenomenon in Figure 6.1 is expected to be seen in a large-scale battery but with a larger voltage value. Take Willenhall Energy Storage System (WESS) as an example, WESS is built with Toshiba Super Charge ion Battery (SCiB) cells that have lithium titanium oxide (LTO) anode. Compared with a single LTO cell, the pack voltage in WESS is increased by 264 times due to the internal series structure among cells. As a result, the hysteresis voltage, the difference between OCV during charging and discharging, should also be increased by a factor of 264.

Reference [129] measured the OCV of a SCiB LTO cell during charging (OCV_{ch}) and discharging (OCV_{dis}) at 25°C at every 10% SoC after a 30 min relaxation period. The result is shown in Figure 6.2(a). As can be seen in Figure 6.2(b), the hysteresis voltage of a single SCiB LTO cell is about 10 mV. As mentioned before, in theory, a 264 times larger hysteresis voltage (~2.6 V) would be witnessed in the WESS battery.

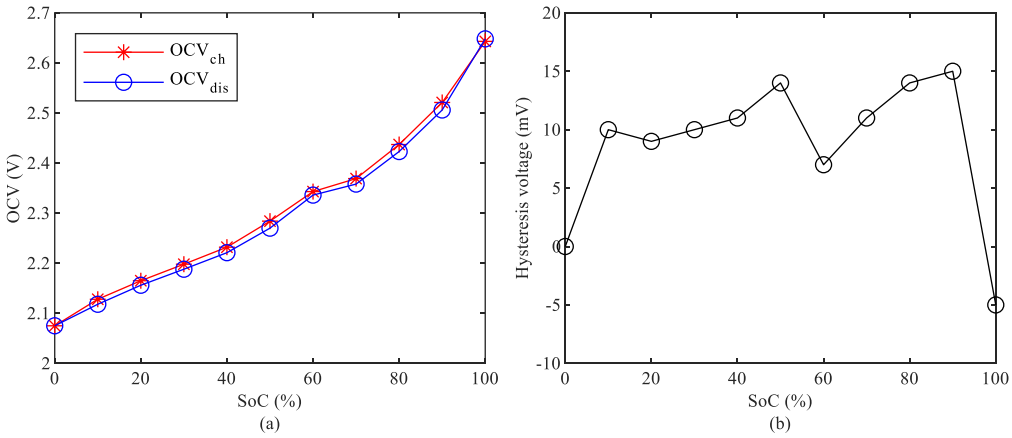

Figure 6.2 OCV of a single Toshiba SCiB LTO cell: (a) OCV after charging (OCV_{ch}) and discharging (OCV_{dis}) (data source: [129]), (b) hysteresis voltage: OCV_{ch} minus OCV_{dis}

6.2.2 The effect of cell chemistry on hysteresis

This OCV hysteresis effect is observed in various batteries with different cell chemistry, such as lead-acid cells, lithium iron phosphate (LFP) cells and lithium nickel manganese cobalt oxide (NMC) cells. The value of hysteresis voltage is different for these cells. Reference [130] systematically measures the maximum hysteresis voltage of three cells with

different chemistry LFP, NMC and LTO between 0 and 100% SoC. The maximum hysteresis voltage in a major loop is a function of SoC. The largest value of the maximum hysteresis voltage between 0 and 100% SoC is used to compare the hysteresis phenomenon in difference chemistry: LFP (38 mV) > NMC (27 mV) > LTO (16 mV). Compared with these lithium-ion cells tested in [130], lead-acid has a higher maximum hysteresis voltage (60 mV [131]). However, the hysteresis voltage in an LTO cell is so small that paper [132] postulated that it does not exist in the LTO cell.

6.2.3 The effect of experiment procedure on hysteresis

Two methods are widely used in terms of measuring OCV and hysteresis voltage: low current and incremental charge/discharge [130]. In the low current method, a battery is continuously charged or discharged by a small current as Figure 6.3 shows. In this case, the battery voltage approximately equals OCV and is known as pseudo-OCV. The error is caused by the voltage drop on the cell's internal resistance which is positively related to the amplitude of the current and the value of internal resistance.

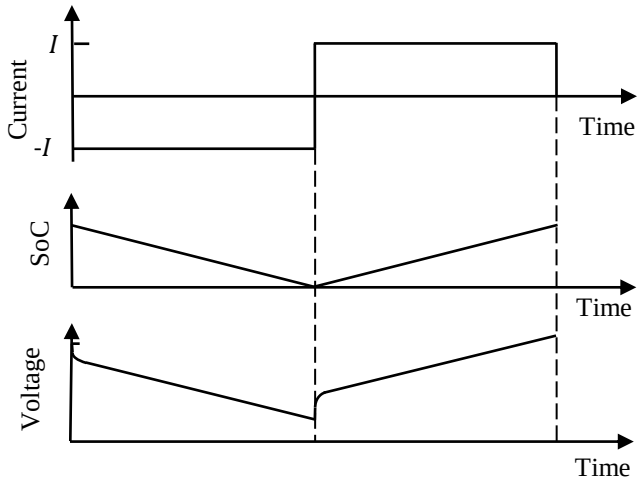

Figure 6.3 Schematic diagram of the low current method

In the incremental charge/discharge method, the battery is charged or discharged by a constant pulse current as Figure 6.4 shows. The OCV is measured at every certain SoC (e.g. at every 10% SoC) at the end of relaxation. The relaxation time is not strict and varies between 0.5 and 4 hours ([129]: 0.5 h, [132]: 2 h, [133]: 3 h, [130]: 4 h).

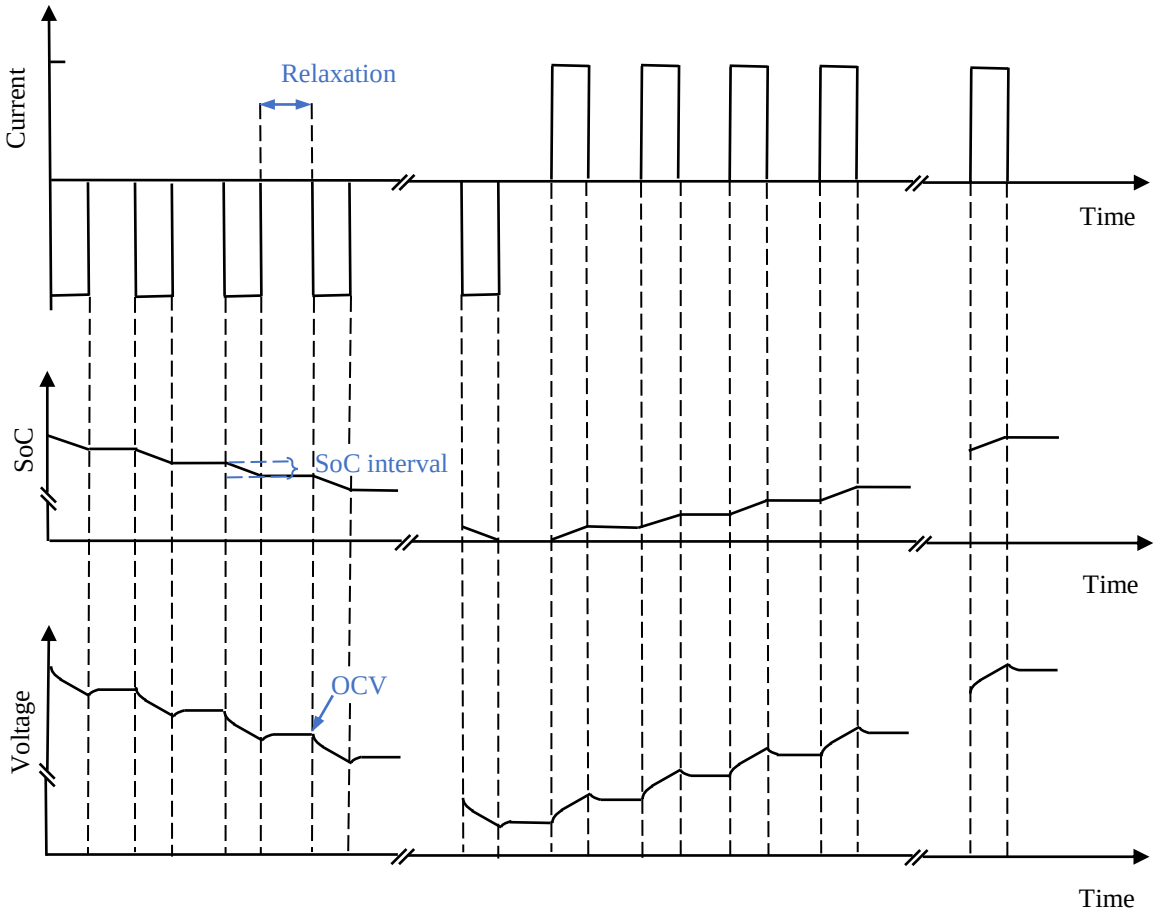

Figure 6.4 Schematic diagram of incremental charge/discharge method

The duration of relaxation can significantly influence the measured OCV value. Reference [134] explored the impact of different relaxation times (1 min, 5 mins, 30 mins and 3 h) on an LFP cell's OCV measurement value and the result is shown in Figure 6.5. In general, with the increase of the relaxation time, the measured OCV after charging becomes smaller and the measured OCV after discharging becomes greater. Consequently, a smaller hysteresis voltage will be obtained after a longer relaxation. After 3 hours of relaxation, the OCV value basically keeps constant [134].

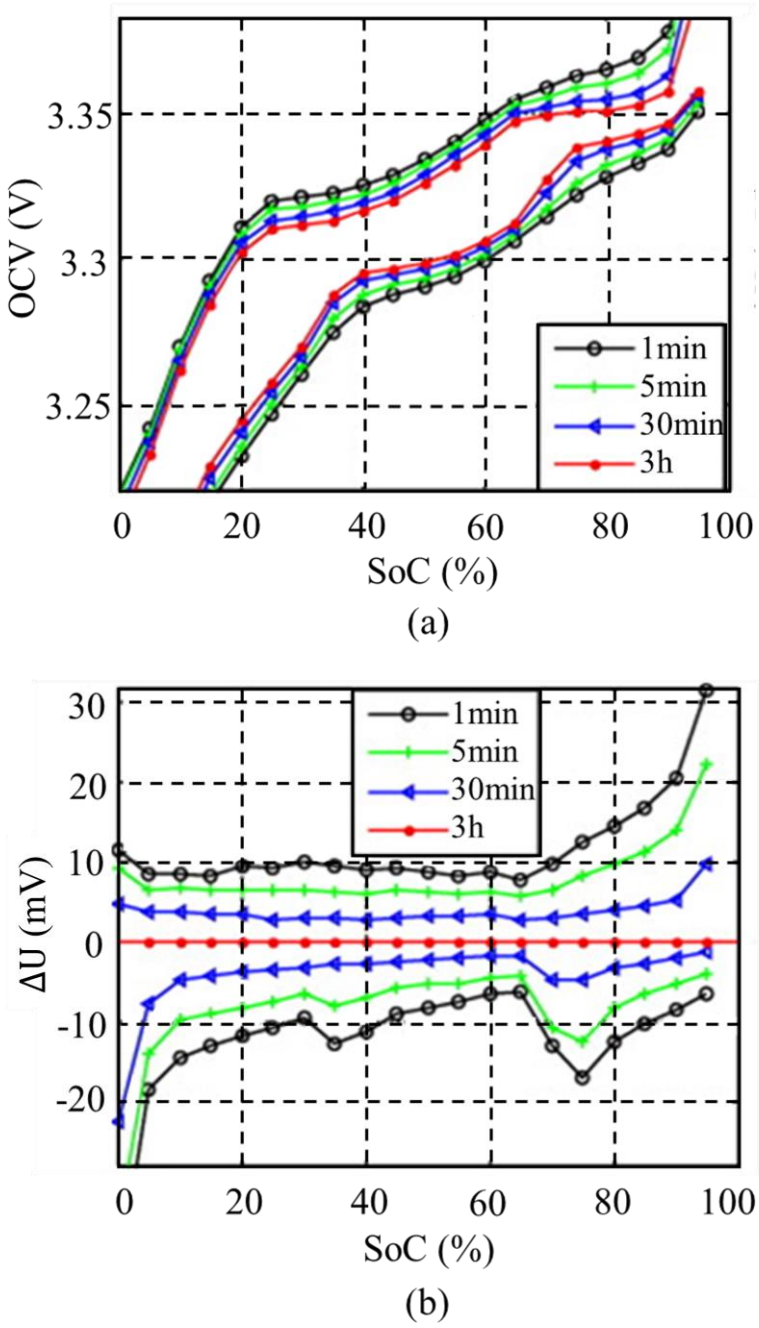

Figure 6.5 The impact of different relaxation lengths on an LFP cell's OCV measurement. (a): OCV incrementally measured at 5% SoC interval, (b): ΔU, the difference between the OCV measured after a certain relaxation period and the OCV measured after 3 h relaxation (positive: OCV difference after charging. negative: OCV difference after discharging). (adapted from: [134])

Both methods are time-consuming. The incremental method provides accurate OCVs at intermittent SoC points whereas the low current method provides continuous OCV measurements in a range. Besides, the hysteresis voltage for a cell is tens of millivolts which

is so small that can be easily influenced by experiment settings in both methods (e.g. relaxation time, current).

6.2.4 Open circuit voltage hysteresis measurement on Willenhall Energy Storage System and Preisach hysteresis model

To explore the OCV hysteresis phenomenon in a large-scale battery system, a low power (50 kW) experiment was conducted in WESS since the low current method cannot be directly applied on WESS due to the power-controlled inverter. 50 kW is chosen based on the time cost, the OCV accuracy and the properties of battery management system (BMS) in WESS. A full charging-discharging cycle in WESS (1 MWh) with 50kW load takes 40 h, which means two day during which WESS is unavailable. However, WESS is contractually demanded to provide frequency service. A lower power (<50 kW) hysteresis experiments will take a longer time (> 40 h per cycle) and could cause a financial loss.

A 50 kW (0.05C-rate) load does not generate a big difference between terminal voltage and OCV. At the same time, the experiment time is acceptable (from 100% to 0%: ~20 h). More importantly, as it has been discussed in Chapter 3, an extremely low power (~0.01 C-rate) will trigger the OCV correction mechanism in WESS's BMS. In this case, the BMS believes the battery terminal voltage is equal to the OCV and the SoC is estimated by searching the embedded OCV-SoC look-up table. Since experimental data in this work relies of the reports from the BMS, it is influenced by this property. Consequently, when the experiment power is extremely low (~0.01 C-rate), the collected OCV-SoC relationship will be identical with the embedded OCV-SoC loop-up table in the BMS. A power of 50kW should avoid nuances with the BMS SoC correction mechanism.

The purpose of the experiment is to obtain the OCV-SoC relationship in multiple hysteresis loops so that an OCV hysteresis model (the discrete Preisach model) can be built for WESS. The classical Preisach model was proposed by F. Preisach in 1935 for magnetic materials and is considered as one of the most important hysteresis models [135]. With the wide use of batteries, the Preisach model has been applied to lithium batteries for OCV modelling [136][137] and SoC estimation [138].

The Preisach model can be represented by (6.1)where $y(t)$ and $x(t)$ are the output and input of the model respectively. T is the Preisach triangle shown in Figure 6.7. $\gamma_{\alpha\beta}$ is the one-side Preisach operator as shown in Figure 6.6 which can be used in the case of a nonnegative

observation $y(t)$ such as the OCV of a battery. $\mu_{\alpha\beta}$ is the weighting function for the corresponding operator $\gamma_{\alpha\beta}$ and decides the shape of the hysteresis model [136] and is obtained from experiments. The operators can be expressed in mathematical equations (6.2).

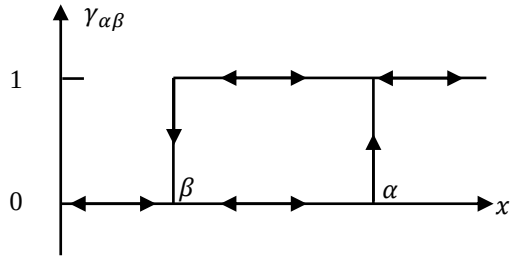

Figure 6.6 One-side Preisach operators (adapted from: [139])

$$y(t) = \iint_T \mu_{\alpha\beta}\gamma_{\alpha\beta}\big(x(t)\big)d\alpha d\beta \tag{6.1}$$

Every single point on the Preisach triangle T in Figure 6.7 represents for a one-side Preisach operators $\gamma_{\alpha\beta}$ with unique value of α and β and the output of the Preisach operator $\gamma_{\alpha\beta}$ is decided by the history of input $x(t)$. The history of input $x(t)$ decides the value of every Preisach operator $\gamma_{\alpha\beta}$ on T through an interface line $L(t)$ which will be introduced next.

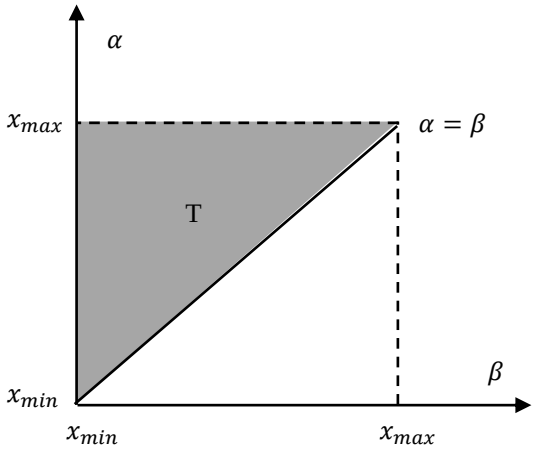

Figure 6.7 Preisach triangle T

$$\gamma_{\alpha\beta}(t) = \begin{cases} 1, & x(t) > \alpha \\ 0, & x(t) < \beta \\ \text{unchanged}, & \beta \le x(t) \le \alpha \end{cases} \tag{6.2}$$

The Preisach triangle is divided into two regions by the interface line $L(t)$ [140]. For all the Preisach operators $\gamma_{\alpha\beta}$ in the region below $L(t)$, the value of $\gamma_{\alpha\beta}$ is set as 1. On the other hand, for all the Preisach operators $\gamma_{\alpha\beta}$ in the region above $L(t)$, $\gamma_{\alpha\beta} = 0$.

Figure 6.8 demonstrates the process of generating the interface line $L(t)$, plotted with a solid red line, according to the history of the given input $x(t)$ in Figure 6.8(a). Figure 6.8(b) (c) and (d) are the snapshot of $L(t)$ in Preisach triangle T at time t_1 t_2 and t_3 respectively. The red arrow indicates the changing direction of the interface line $L(t)$.

As Figure 6.8 shows, when $x(t)$ is increasing: $t_0 \rightarrow t_1$ and $t_2 \rightarrow t_3$, the horizontal line $\alpha = x(t)$ (moving up) redefines the bottom of $L(t)$ and the rest of $L(t)$ remains constant. When $u(t)$ is decreasing: $t_1 \rightarrow t_2$, the vertical line $\beta = x(t)$ (moving towards left) redefines the right edge of $L(t)$ while the rest of $L(t)$ keep unchanged. As a result, in the Preisach model, as (6.1)

shows, the history of input $x(t)$ is remembered by the shape of the interface line $L(t)$ which changes the value of $\gamma_{\alpha\beta}$ and then controls the value of output $y(t)$.

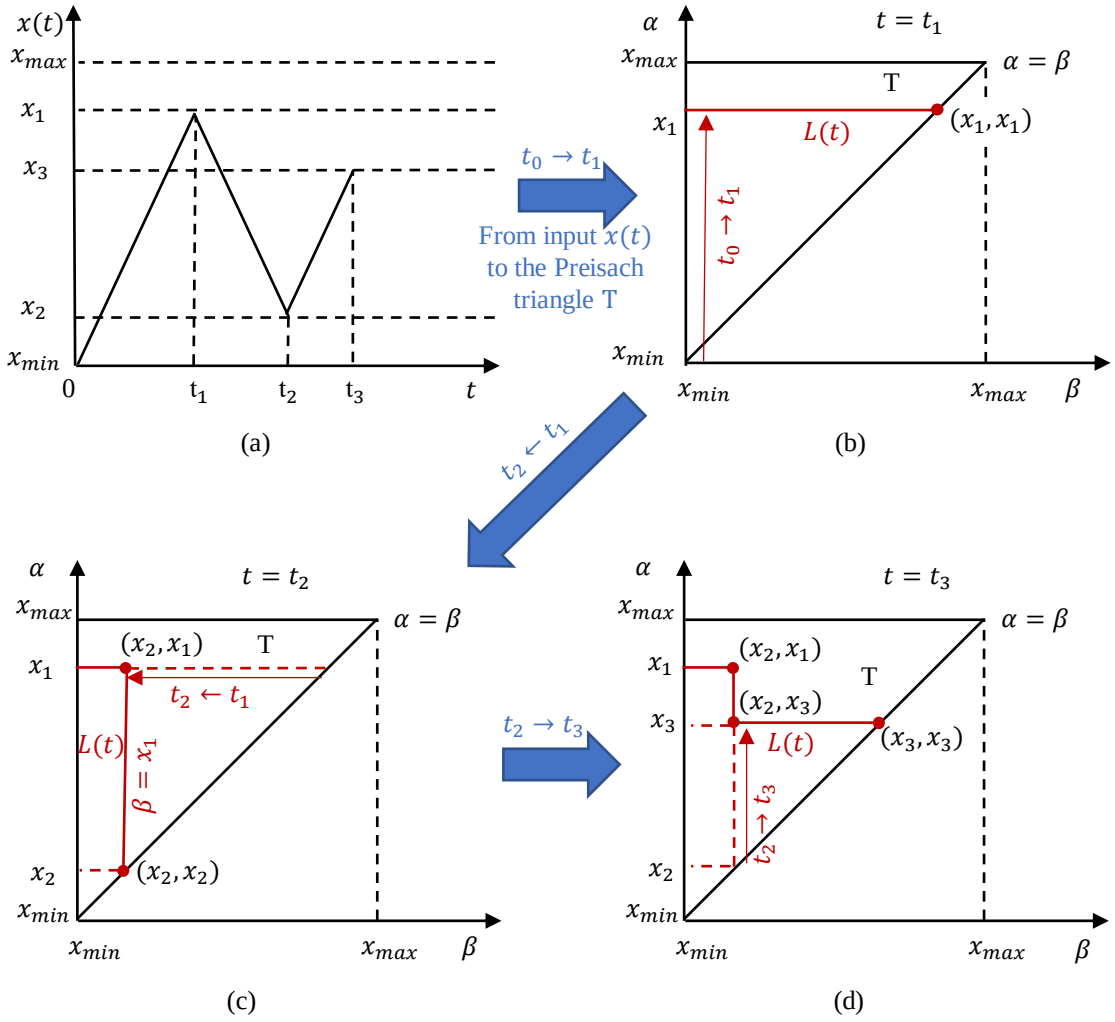

Figure 6.8 An example of the Preisach triangle partition. (a): input; (b): $L(t)$ at t_1; (c): $L(t)$ at t_2; (d): $L(t)$ at t_3; $L(t)$: the interface, plotted in solid red line

Preisach model can be discretised by dividing the α and β axis into K parts and generates N number of regions in the Preisach triangle, $N = K(K+1)/2$ [139]. Each region corresponds to one Preisach operator $\gamma_{\alpha\beta}$ with unique numbers of α and β. Figure 6.9 shows an example of the Preisach triangle T of a discrete Preisach model with $K = 5$ and the Preisach triangle T is divided into 15 regions. In Figure 6.9(a), The Preisach operators $\gamma_{\alpha_i\beta_j}$ for each region is represented by (α_i, β_j), i and $j \in [1,2,\ldots,5]$. The corresponding value of (α_i, β_j) and the corresponding operator diagrams are shown in Figure 6.9(b) and (c) respectively where $X = x_{\max} - x_{\min}$.

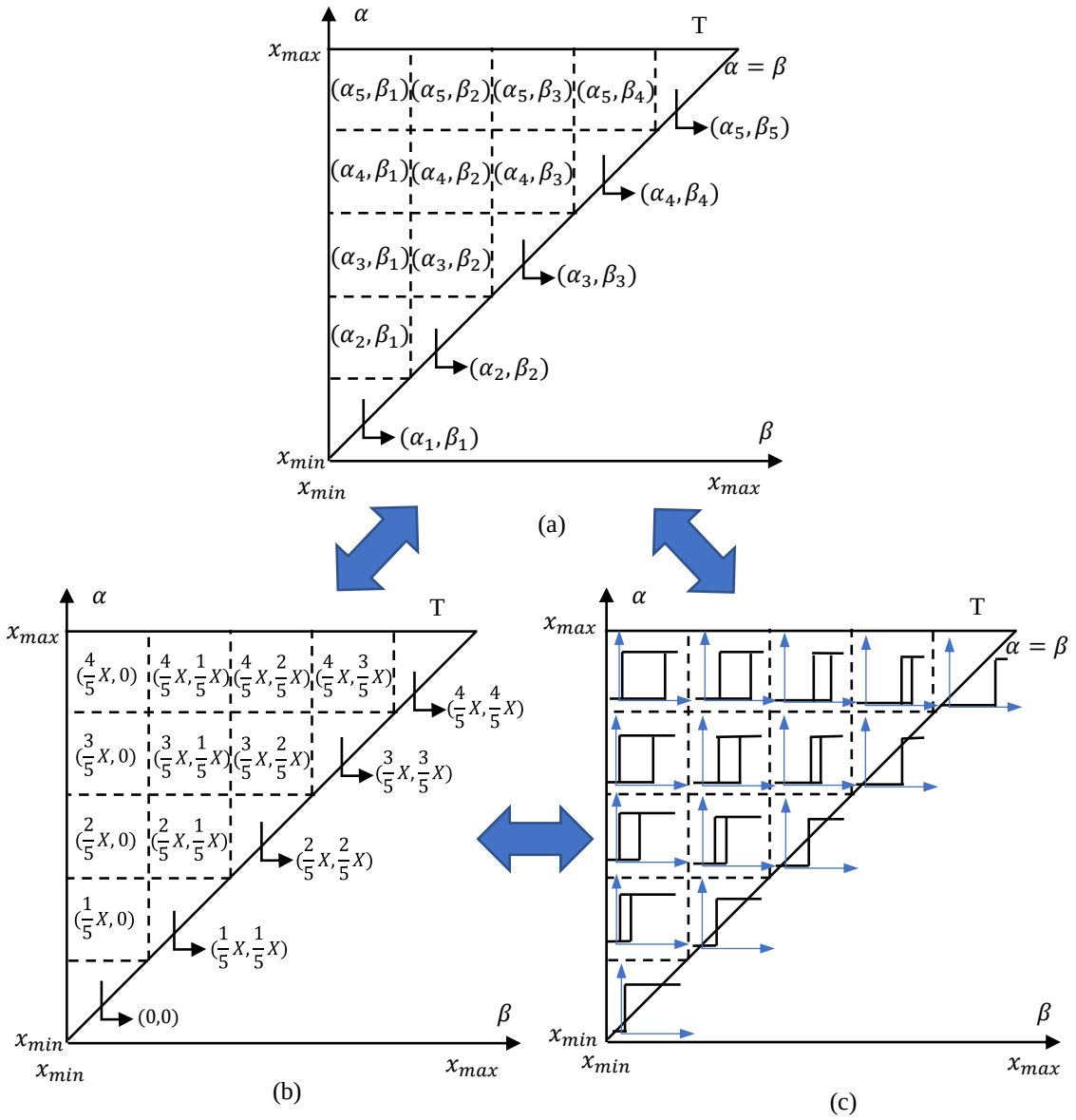

Figure 6.9 A discrete Preisach model triangle (*K*=5, *N*=15). (a): allocate (α_i, β_j); (b): the value of (α_i, β_j); (c): the operator diagram for each region

The output in the discrete Preisach model is represented by (6.3). Similar to the classical Preisach model, in the discrete Preisach model $\gamma_{\alpha_i\beta_j}$ is the Preisach operators and $\mu_{\alpha_i\beta_j}$ is the corresponding the weighting function where i and $j \in [1, 2, \ldots K]$. The value of $\gamma_{\alpha_i\beta_j}$ is decided by the history of input $x(t)$ through the interface $L(t)$ in the same way as Figure 6.8 shows. $\mu_{\alpha_i\beta_j}$ is determined through experiment and (6.3). In detail, the output $y(t)$ can be obtained from measurement and $\gamma_{\alpha_i\beta_j}$ is known from the input $x(t)$ history and $\mu_{\alpha_i\beta_j}$ can be estimated from least square error method.

$$y(t) = \sum_{i=1}^{K} \sum_{j=1}^{i} \mu_{\alpha_i \beta_j} [\gamma_{\alpha_i \beta_j}(x(t))] \tag{6.3}$$

Figure 6.10 provides an example of using the discrete Preisach model to estimate the OCV of a lithium-silicon (Li//Si) half-cell (lithium metal vs. 30% Si/55% graphite half-cell). The model normally requires a large number of N (e.g., 100) to achieve a satisfactory result. In terms of WESS, the OCV hysteresis loops are required to obtain $\mu_{\alpha_i \beta_j}$ for Preisach model which demands experiments.

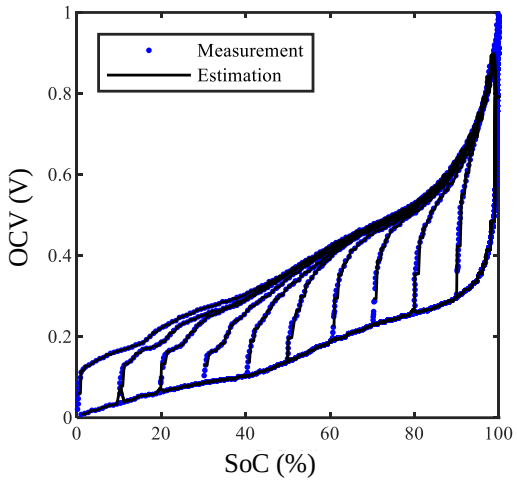

Figure 6.10 A Li//Si half-cell's OCV modelling using discrete Preisach model (K=100) (data collected from: [139])

6.2.5 Open circuit voltage hysteresis experiment: results

To build a Preisach hysteresis model and determine the value of weighting function $\mu(\alpha_i, \beta_j)$, OCV hysteresis experiment that contains 4 loops (loop 1 - 4) were conducted on Willenhall Energy Storage System. In each loop, WESS is discharged from 90% SoC to different return SoC points (loop 1: 10%, loop 2: 30%, loop 3: 50%, loop 4: 70%) and then charged to 90%.

Figure 6.11 shows the experiment result of the four loops which was recorded by the BMS, including (a) battery pack voltage, (b) current, and (c) BMS SoC. As the first row in Figure 6.11 shows, during loop 1, when the battery was charged to 78% SoC at t_1, the battery was disconnected from the grid for 6 hours and 45 minutes for an unknown reason and there was no data recorded by BMS.

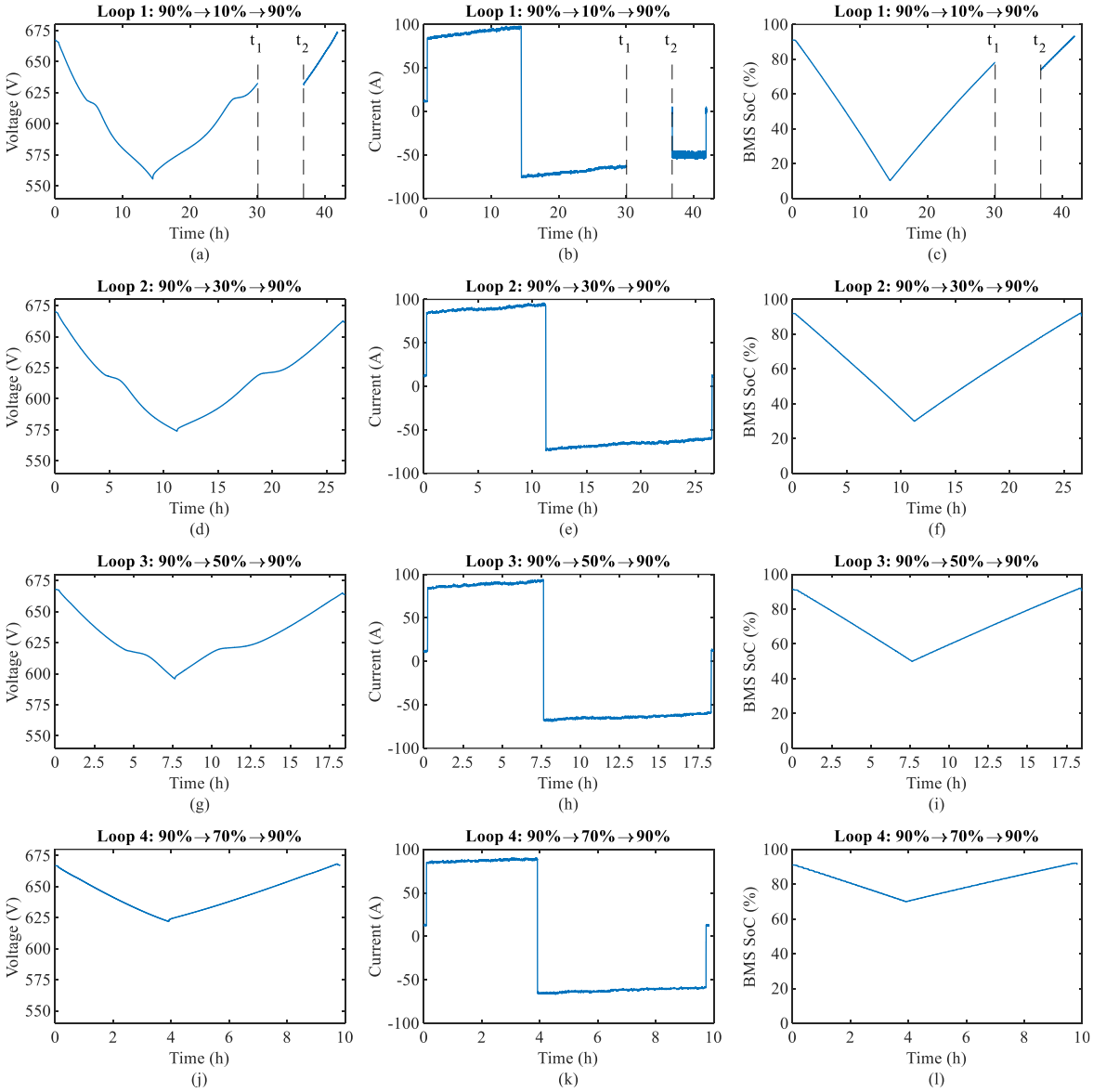

Figure 6.11 Result of the major and minor cycles in OCV hysteresis experiment: the pack voltage, current and BMS SoC in (a-c): loop 1, (d-f): loop 2, (g-i): loop 3 and (j-l): loop 4. Note: t_1: 30.1 h, t_2: 36.8 h

The pack voltage results of the four cycles are plotted with respect to their corresponding BMS SoC in Figure 6.12. In Figure 6.12(a), a pseudo-OCV model is shown in black line. This pseudo-OCV model was first introduced in Chapter 3 and obtained from a series of extremely low power discharging experiments. As it has been discussed in Chapter 3, this pseudo-OCV model is the same as the embedded OCV-SoC look-up table inside the BMS.

As can be seen in Figure 6.12, in all four cycles, at some SoC points the battery voltage during charging is smaller than that under discharging which is against the nature of a battery for two reasons. First, due to the internal resistance, the battery terminal voltage is higher

than its OCV under a charging current and lower than OCV under a discharging current. Second, in a charging-discharging loop, at the same SoC, the OCV with a charging SoC history is higher than OCV with a discharging SoC history. These two properties of batteries make the battery voltage during charging greater than that under discharging at the same SoC.

The SoC estimation method in the BMS is believed to be the main reason that causes this unusual situation. In WESS, BMS uses the Coulomb-counting method to estimate SoC during charging and discharging and correct the SoC estimation according to an embedded lookup table when the battery is relaxed. The Coulomb-counting method introduces integration error due to measurement error in battery current. The SoC error in the Coulomb-counting method accumulates with time which matches with the fact that loop 4 who consumed the least time compared with other loops has far fewer unusual result points. The voltage sensor error could be another reason for the unusual result in Figure 6.12.

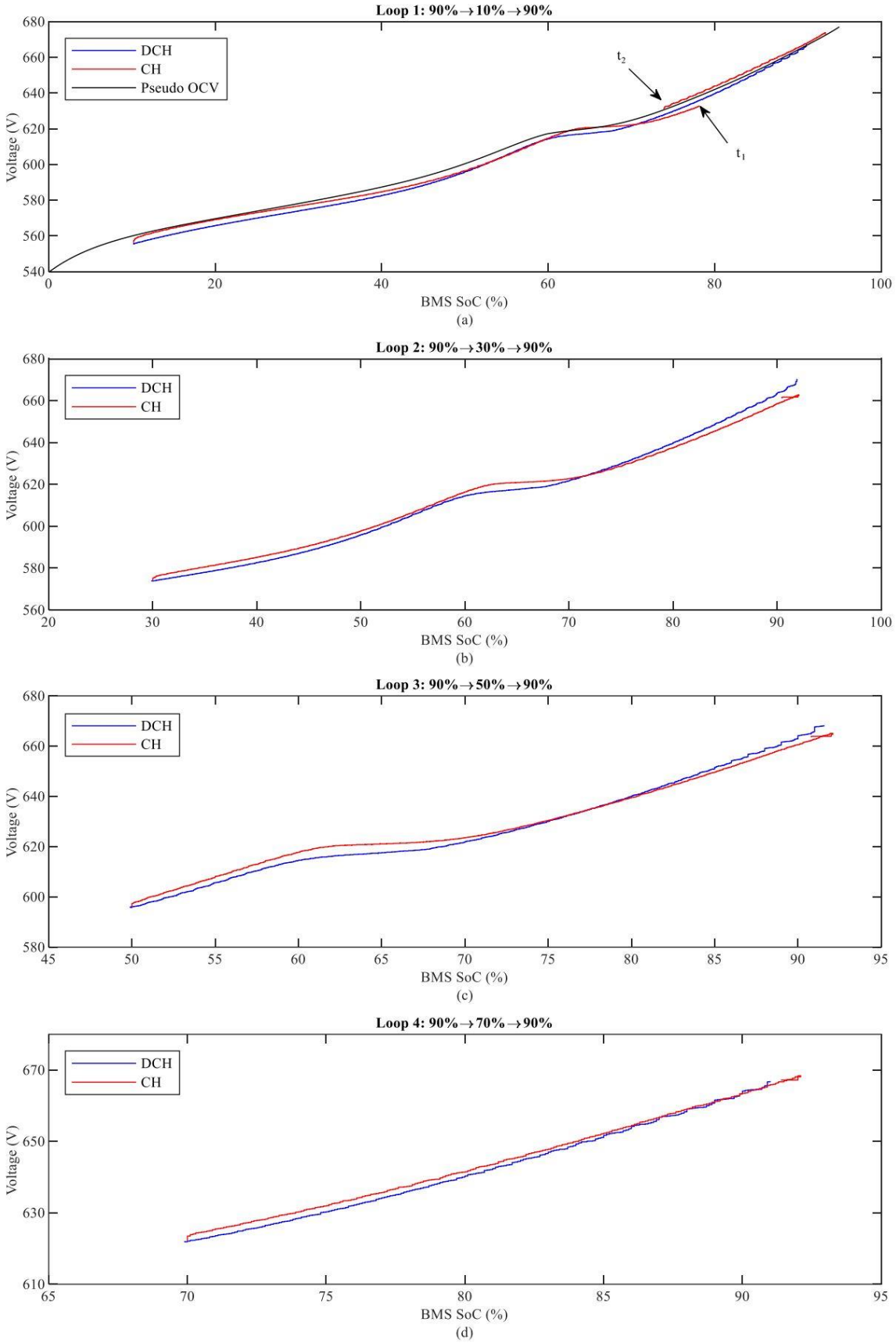

Figure 6.12 Battery pack terminal voltage vs. BMS SoC (DCH: discharge, CH: charge), (a-c): loop 1-4

As it has been mentioned, in loop 1 WESS is disconnected from the grid at t_1 and reconnected at t_2 (see $t_1 \rightarrow t_2$ in Figure 6.11(a) - (c) and Figure 6.12(a)) during which some properties of the BMS are revealed. The BMS has a SoC correction mechanism to minimise the SoC error of the Coulomb-counting method. As mentioned in Chapter 3, this mechanism only works after resting or under extremely low load current (<0.01 C-rate). The correction mechanism is triggered in cycle 1 between t_1 and t_2.

At t_2, the SoC has a charging history and is corrected according to the embedded OCV-SoC loop-up table. Assuming the loop-up table in WESS contains the hysteresis information, the (SoC, voltage) point at t_2 is supposed to be located above the pseudo-OCV model that has discharging SoC history. However, the (SoC, voltage) point at t_2 is located exactly on the pseudo-OCV model as shown in Figure 6.12(a) so that the assumption does not hold which means that the embedded OCV-SoC loop-up table in WESS does not capture hysteresis behaviour.

6.3 Improvements to the SoC estimation

The previous section shows that the battery pack hysteresis voltage in WESS cannot be identified with the measured voltage and BMS SoC due to the error in the Coulomb-counting method. The relationship between hysteresis voltage and SoC cannot be determined without an accurate SoC estimation. The BMS SoC estimation error is mainly caused by the inaccurate current measurement. Kalman filter based method can provide an optimized recursive SoC estimation in a system that contains process and measurement noise. Extended Kalman filter (EKF) can be used on a non-linear system such as a battery. In theory, the SoC error caused by current sensor accuracy can be reduced by EKF. Therefore, the EKF method is adopted in this section to improve SoC estimation.

6.3.1 Sequential probabilistic inference and Kalman filter

The Kalman filter (KF) is a recursive algorithm designed by R.E. Kalman in 1960 for the optimal estimation problem in linear systems [141][142]. KF is a special case (the linear Gaussian case) of sequential probabilistic inference (SPI).

In general, a (non-linear) dynamic system can be represented by a dynamic state space model written in (6.4)-(6.5) where $\boldsymbol{x}_k$ is the hidden state in the system and $\boldsymbol{y}_k$ is the output (or

observation) of the system. f and g are the state transition function and observation (or output) function respectively. $\boldsymbol{w}_{\mathrm{k}}$ is process noise and $\boldsymbol{v}_{\mathrm{k}}$ is observation noise.

$$\boldsymbol{x}_{\mathrm{k+1}} = f(\boldsymbol{x}_{\mathrm{k}}, \boldsymbol{u}_{\mathrm{k}}, \boldsymbol{w}_{\mathrm{k}}) \tag{6.4}$$

$$\boldsymbol{y}_{\mathrm{k}} = g(\boldsymbol{x}_{\mathrm{k}}, \boldsymbol{u}_{\mathrm{k}}, \boldsymbol{v}_{\mathrm{k}}) \tag{6.5}$$

The sequential probabilistic inference calculates the optimal value of hidden system states $\boldsymbol{x}_{\mathrm{k}}$ given all the observations with noise. Mathematically, the optimal state estimation is calculated as a conditional expectation $\hat{\boldsymbol{x}}_{\mathrm{k}} = E[\boldsymbol{x}_{\mathrm{k}}|\boldsymbol{Y}_{\mathrm{k}}] = \int \boldsymbol{x}_{\mathrm{k}}\, p(\boldsymbol{x}_{\mathrm{k}}|\boldsymbol{Y}_{\mathrm{k}}) d\boldsymbol{x}_{\mathrm{k}}$ given all the observations $\boldsymbol{Y}_{\mathrm{k}} = \{\boldsymbol{y}_1, \boldsymbol{y}_2, \dots, \boldsymbol{y}_{\mathrm{k}}\}$. Figure 6.13 shows the concept of sequential probabilistic inference. In a system, the hidden state $\boldsymbol{x}_{\mathrm{k}}$ has a conditional probability density $p(\boldsymbol{x}_{\mathrm{k}}|\boldsymbol{x}_{\mathrm{k-1}})$ and an initial probability density $p(\boldsymbol{x}_0)$. The value of $p(\boldsymbol{x}_{\mathrm{k}}|\boldsymbol{x}_{\mathrm{k-1}})$ is decided by the state transition function f, input $\boldsymbol{u}_{\mathrm{k}}$, and process noise $\boldsymbol{w}_{\mathrm{k}}$. The conditional probability density for output $p(\boldsymbol{y}_{\mathrm{k}}|\boldsymbol{x}_{\mathrm{k}})$ is specified by output function g, input $\boldsymbol{u}_{\mathrm{k}}$,and measurement noise $\boldsymbol{v}_{\mathrm{k}}$.

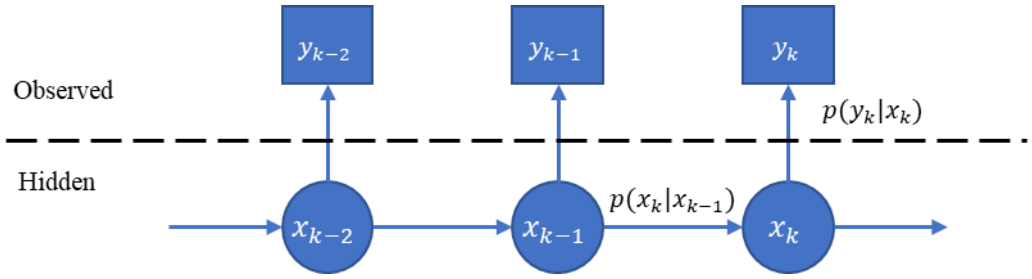

Figure 6.13 Sequential probabilistic inference

The value of $\hat{\boldsymbol{x}}_{\mathrm{k}}$ and the state conditional probability density $p(\boldsymbol{x}_{\mathrm{k}}|\boldsymbol{Y}_{\mathrm{k}})$ can be updated recursively as reference [143] shows. When all the distributions are assumed to be Gaussian and the system is linear, the sequential probabilistic inference becomes the linear Kalman filter as reference [144] demonstrates. The process of the linear Kalman filter will be introduced in the next section.

6.3.2 Linear Kalman filter

Figure 6.14 shows the block diagram of the linear Kalman filter which uses the difference between the noisy measurement from a real system and the output estimation from the model to refine the estimation of system states. The model of linear discrete systems is shown in (6.6)-(6.7) where $\boldsymbol{x}_{\mathrm{k}}$ and $\boldsymbol{y}_{\mathrm{k}}$ are the state and output vectors respectively; $\boldsymbol{A}$, $\boldsymbol{B}$, $\boldsymbol{C}$, and $\boldsymbol{D}$ are system matrix, input matrix, output matrix and feedforward matrix; System noise

$\boldsymbol{w}_{\mathrm{k}} \sim N(0, \boldsymbol{Q})$ and measurement noise $\boldsymbol{v}_{\mathrm{k}} \sim N(0, \boldsymbol{R})$ are zero mean independent Gaussian noises. $\boldsymbol{Q}$ and $\boldsymbol{R}$ are the system and measurement noise covariance. Symbol '~' (a connection symbol) connects a variable and its distribution and N represent a Gaussian distribution.

$$\boldsymbol{x}_{\mathrm{k+1}} = \boldsymbol{A}\boldsymbol{x}_{\mathrm{k}} + \boldsymbol{B}\boldsymbol{u}_{\mathbf{k}} + \boldsymbol{w}_{\mathrm{k}} \tag{6.6}$$

$$\boldsymbol{y}_{\mathrm{k}} = \boldsymbol{C}\boldsymbol{x}_{\mathrm{k}} + \boldsymbol{D}\boldsymbol{u}_{\mathbf{k}} + \boldsymbol{v}_{\mathbf{k}} \tag{6.7}$$

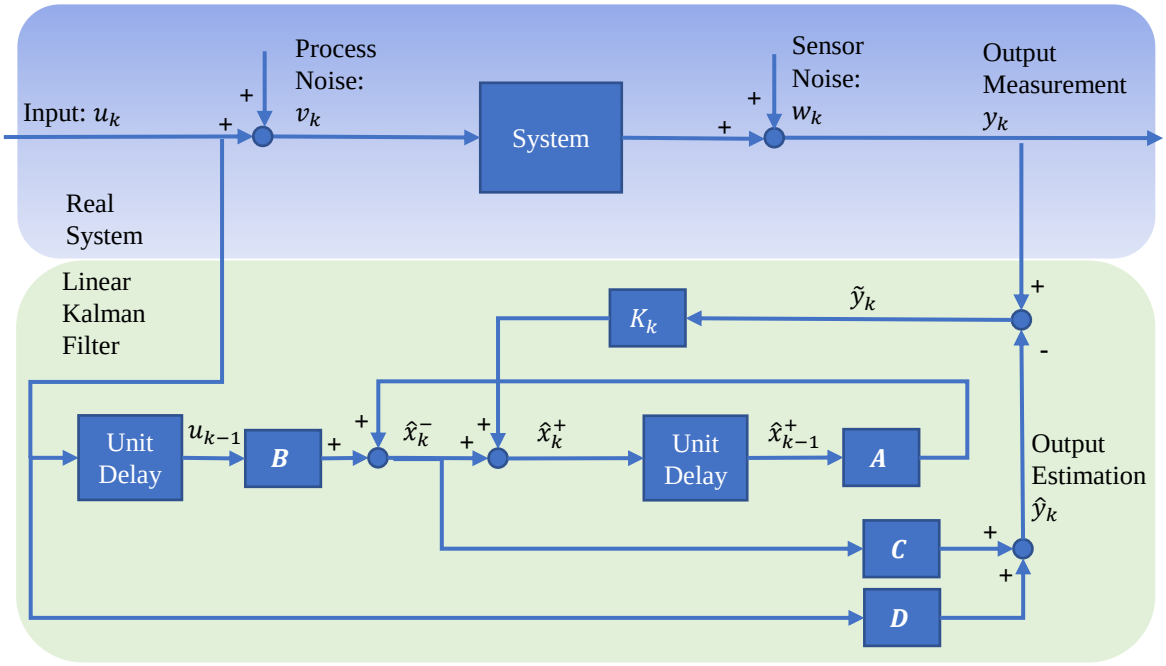

Figure 6.14 The block diagram of linear Kalman filter

The following notations are used in KF where k is time instant, T is matrix transpose operation, tilde '~' (an accent symbol) indicates the error between the actual value and the estimated value and subscripts '-' and '+' indicate *a priori* and *a posteriori* estimation respectively:

$\hat{\boldsymbol{x}}_k^-$ is the *a priori* state estimate of the state $\boldsymbol{x}_{\mathrm{k}}$, given observation $\boldsymbol{Y}_{k-1} = \{\boldsymbol{y}_1, \boldsymbol{y}_2, \ldots, \boldsymbol{y}_{k-1}\}$.

$\hat{\boldsymbol{x}}_k^+$ is the *a posterior* state estimate of the state $\boldsymbol{x}_{\mathrm{k}}$, given observation $\boldsymbol{Y}_k = \{\boldsymbol{y}_1, \boldsymbol{y}_2, \ldots, \boldsymbol{y}_k\}$.

$\tilde{\boldsymbol{x}}_k^-$ is the *a priori* state estimate error and equals $\boldsymbol{x}_k - \hat{\boldsymbol{x}}_k^-$.

$\tilde{\boldsymbol{x}}_k^+$ is the *a posterior* state estimate error and equals $\boldsymbol{x}_k - \hat{\boldsymbol{x}}_k^+$.

$\boldsymbol{P}_{\mathrm{k}}^{-}$ is the *a priori* state estimation error covariance and equals $E[(\tilde{\boldsymbol{x}}_k^-)(\tilde{\boldsymbol{x}}_k^-)^{\mathrm{T}}] = E[(\boldsymbol{x}_k - \hat{\boldsymbol{x}}_k^-)(\boldsymbol{x}_k - \hat{\boldsymbol{x}}_k^-)^{\mathrm{T}}]$.

$\boldsymbol{P}_{\mathrm{k}}^{+}$ is the *a posterior* state estimation error covariance and equals $E[(\tilde{\boldsymbol{x}}_k^+)(\tilde{\boldsymbol{x}}_k^+)^{\mathrm{T}}] = E[(\boldsymbol{x}_k - \hat{\boldsymbol{x}}_k^+)(\boldsymbol{x}_k - \hat{\boldsymbol{x}}_k^+)^{\mathrm{T}}]$.

$\tilde{\boldsymbol{y}}_k$ is the innovation (or estimation error) of output and equals $\boldsymbol{y}_k - \hat{\boldsymbol{y}}_k$.

The KF algorithm in Figure 6.14 can be divided into two parts called prediction (or "time update") and correction (or "measurement update") as Figure 6.15 shows. The KF algorithm is summarised in the following steps [145]:

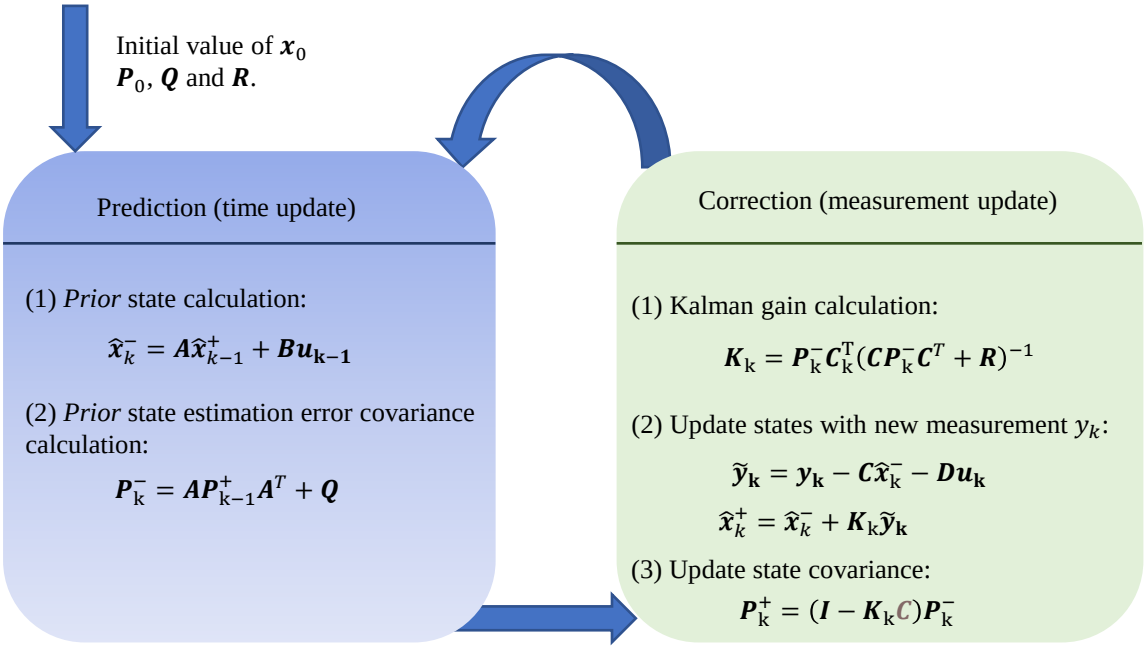

Figure 6.15 Flowchart of linear Kalman filter

At the first step k=0, the initial value of the states $\boldsymbol{x}_0$, system noise $\boldsymbol{Q}$, measurement noise covariance $\boldsymbol{R}$ and state estimation error covariance $\boldsymbol{P}_0^+$ are set by users. At every time step, because $\boldsymbol{w}_{\mathrm{k}}$ has zero mean ($E[\boldsymbol{w}_{\mathrm{k-1}}|\boldsymbol{Y}_{k-1}] = 0$), with (6.6) the state can be updated (time update):

$$\begin{aligned}\hat{\boldsymbol{x}}_k^- &= E[\boldsymbol{A}\boldsymbol{x}_{\mathrm{k-1}} + \boldsymbol{B}\boldsymbol{u}_{\mathbf{k-1}} + \boldsymbol{w}_{\mathrm{k-1}}|\boldsymbol{Y}_{k-1}] \\ &= E[\boldsymbol{A}\boldsymbol{x}_{\mathrm{k-1}}|\boldsymbol{Y}_{k-1}] + E[\boldsymbol{B}\boldsymbol{u}_{\mathbf{k-1}}|\boldsymbol{Y}_{k-1}] + E[\boldsymbol{w}_{\mathrm{k-1}}|\boldsymbol{Y}_{k-1}] \\ &= \boldsymbol{A}\hat{\boldsymbol{x}}_{k-1}^+ + \boldsymbol{B}\boldsymbol{u}_{\mathbf{k-1}}\end{aligned} \tag{6.8}$$

Substituting (6.8) into the mathematical expression of *priori* state estimate error $\tilde{\boldsymbol{x}}_k^- = \boldsymbol{x}_k - \hat{\boldsymbol{x}}_k^-$, $\tilde{\boldsymbol{x}}_k^-$ can be written as:

$$\begin{aligned}\tilde{\boldsymbol{x}}_k^- &= (\boldsymbol{A}\boldsymbol{x}_{\mathrm{k}-1} + \boldsymbol{B}\boldsymbol{u}_{\mathbf{k-1}} + \boldsymbol{w}_{\mathrm{k}-1}) - (\boldsymbol{A}\hat{\boldsymbol{x}}_{k-1}^+ + \boldsymbol{B}\boldsymbol{u}_{\mathbf{k-1}}) \\ &= \boldsymbol{A}\tilde{\boldsymbol{x}}_{k-1}^+ + \boldsymbol{w}_{\mathrm{k}-1}\end{aligned} \tag{6.9}$$

Because $\boldsymbol{w}_{\mathrm{k}-1}$ is zero mean independent Gaussian noises, $E[\tilde{\boldsymbol{x}}_k^+(\boldsymbol{w}_{\mathrm{k}-1})^{\mathrm{T}}]$ and $E[\boldsymbol{w}_{\mathrm{k}-1}(\tilde{\boldsymbol{x}}_k^+)^{\mathrm{T}}]$ are zero. Substituting (6.9) into the definition of the *priori* state estimation error covariance $\boldsymbol{P}_{\mathrm{k}}^-$, $\boldsymbol{P}_{\mathrm{k}}^-$ can be updated as (time update):

$$\begin{aligned}\boldsymbol{P}_{\mathrm{k}}^- &= E[(\tilde{\boldsymbol{x}}_k^-)(\tilde{\boldsymbol{x}}_k^-)^{\mathrm{T}}] \\ &= E[(\boldsymbol{A}\tilde{\boldsymbol{x}}_k^+ + \boldsymbol{w}_{\mathrm{k}-1})(\boldsymbol{A}\tilde{\boldsymbol{x}}_k^+ + \boldsymbol{w}_{\mathrm{k}-1})^{\mathrm{T}}] \\ &= E[(\boldsymbol{A}\tilde{\boldsymbol{x}}_k^+ + \boldsymbol{w}_{\mathrm{k}-1})((\tilde{\boldsymbol{x}}_k^+)^{\mathrm{T}}\boldsymbol{A}^{\mathrm{T}} + \boldsymbol{w}_{\mathrm{k}-1}{}^{\mathrm{T}})] \\ &= E[\boldsymbol{A}\tilde{\boldsymbol{x}}_k^+(\tilde{\boldsymbol{x}}_k^+)^{\mathrm{T}}\boldsymbol{A}^{\mathrm{T}} + \boldsymbol{w}_{\mathrm{k}-1}(\tilde{\boldsymbol{x}}_k^+)^{\mathrm{T}}\boldsymbol{A}^{\mathrm{T}} + \boldsymbol{A}\tilde{\boldsymbol{x}}_k^+(\boldsymbol{w}_{\mathrm{k}-1})^{\mathrm{T}} \\ &\quad + \boldsymbol{w}_{\mathrm{k}-1}(\boldsymbol{w}_{\mathrm{k}-1})^{\mathrm{T}}] \\ &= \boldsymbol{A}\boldsymbol{P}_{\mathrm{k}-1}^+\boldsymbol{A}^{\mathrm{T}} + \boldsymbol{Q}\end{aligned} \tag{6.10}$$

When the new output information $\boldsymbol{y}_{\mathbf{k}}$ is obtained, Kalman filter uses the output innovation $\tilde{\boldsymbol{y}}_k$ to update the *a priori* state estimation to the *a posterior* state estimation as (6.11) shows, where the Kalman gain and the output innovation is calculated according to equation (6.12) and (6.13).

$$\hat{\boldsymbol{x}}_k^+ = \hat{\boldsymbol{x}}_k^- + \boldsymbol{K}_{\mathrm{k}}\tilde{\boldsymbol{y}}_k \tag{6.11}$$

$$\boldsymbol{K}_{\mathrm{k}} = \boldsymbol{P}_{\mathrm{k}}^-\boldsymbol{C}^{\mathrm{T}}(\boldsymbol{C}\boldsymbol{P}_{\mathrm{k}}^-\boldsymbol{C}^{\mathrm{T}} + \boldsymbol{R})^{-1} \tag{6.12}$$

$$\tilde{\boldsymbol{y}}_k = \boldsymbol{y}_{\mathbf{k}} - \boldsymbol{C}\hat{\boldsymbol{x}}_{\mathrm{k}}^- - \boldsymbol{D}\boldsymbol{u}_{\mathbf{k}} \tag{6.13}$$

After the *a posterior* state estimation $\hat{\boldsymbol{x}}_k^+$ is calculated, the *a posterior* state estimation error covariance can be updated with equation (6.14):

$$\begin{aligned}\boldsymbol{P}_{\mathrm{k}}^+ &= E[(\tilde{\boldsymbol{x}}_k^+)(\tilde{\boldsymbol{x}}_k^+)^{\mathrm{T}}] \\ &= E[(\tilde{\boldsymbol{x}}_k^- - \boldsymbol{K}_{\mathrm{k}}\tilde{\boldsymbol{y}}_k)(\tilde{\boldsymbol{x}}_k^- - \boldsymbol{K}_{\mathrm{k}}\tilde{\boldsymbol{y}}_k)^{\mathrm{T}}] \\ &= \boldsymbol{P}_{\mathrm{k}}^- - \boldsymbol{K}_{\mathrm{k}}E[\tilde{\boldsymbol{y}}_k(\tilde{\boldsymbol{y}}_k)^{\mathrm{T}}]\boldsymbol{K}_{\mathrm{k}}{}^{\mathrm{T}} \\ &= (\boldsymbol{I} - \boldsymbol{K}_{\mathrm{k}}\boldsymbol{C})\boldsymbol{P}_{\mathrm{k}}^-\end{aligned} \tag{6.14}$$

The KF is suitable for only linear systems because it is derived with the linear model equation shown in (6.6)-(6.7). Since the model of nonlinear systems cannot be written in the same form, the KF cannot be directly applied to a nonlinear system.

6.3.3 Extended Kalman filter

Equation (6.15)-(6.17) shows the state space model of nonlinear systems in which $\boldsymbol{x}_{\mathrm{k}}$ and $\boldsymbol{y}_{\mathrm{k}}$ are the state and output vectors and k is time instant. f and g are the state transition function and the output function. $\boldsymbol{w}_{\mathrm{k}}$ and $\boldsymbol{v}_{\mathrm{k}}$ are process noise and measurement noise which are independent Gaussian noises. The KF is designed for linear systems and cannot be used on a non-linear system like a battery model. To apply KF on a non-linear system, the first order Taylor series approximation is applied to the system model as a form of linearisation to allow the KF to be applied. The first order Taylor series approximation of the state transition function f and the output function g are shown in (6.18) and (6.19). $\frac{\partial f(\boldsymbol{x}_{\mathrm{k}},\boldsymbol{u}_{\mathrm{k}})}{\partial \boldsymbol{x}_{\mathrm{k}}}$ and $\frac{\partial g(\boldsymbol{x}_{\mathrm{k}},\boldsymbol{u}_{\mathrm{k}})}{\partial \boldsymbol{x}_{\mathrm{k}}}$ are the Jacobian matrices of f and g. Assuming input $\boldsymbol{x}_{\mathrm{k}}$ is a $N \times 1$ vector, the expression of the Jacobian matrices of f is given in as (6.20) an example. The notations '~', '+' and '-' in EKF have the same meaning as that in EK which represent an error, a *a priori* and a *a posteriori* estimation respectively.

$$\boldsymbol{x}_{\mathrm{k+1}} = f(\boldsymbol{x}_{\mathrm{k}}, \boldsymbol{u}_{\mathrm{k}}) + \boldsymbol{w}_{\mathrm{k}} \tag{6.15}$$

$$\boldsymbol{y}_{\mathrm{k}} = g(\boldsymbol{x}_{\mathrm{k}}, \boldsymbol{u}_{\mathrm{k}}) + \boldsymbol{v}_{\mathrm{k}} \tag{6.16}$$

$$\boldsymbol{w}_{\mathrm{k}} \sim N(0, \boldsymbol{Q}), \boldsymbol{v}_{\mathrm{k}} \sim N(0, \boldsymbol{R}) \tag{6.17}$$

$$f(\boldsymbol{x}_{\mathrm{k}}, \boldsymbol{u}_{\mathrm{k}}) \approx f(\hat{\boldsymbol{x}}_{\mathrm{k}}, \boldsymbol{u}_{\mathrm{k}}) + \left.\frac{\partial f(\boldsymbol{x}_{\mathrm{k}}, \boldsymbol{u}_{\mathrm{k}})}{\partial \boldsymbol{x}_{\mathrm{k}}}\right|_{x_{\mathrm{k}}=\hat{x}_{\mathrm{k}}} (\boldsymbol{x}_{\mathrm{k}} - \hat{\boldsymbol{x}}_{\mathrm{k}}) \tag{6.18}$$

$$g(\boldsymbol{x}_{\mathrm{k}}, \boldsymbol{u}_{\mathrm{k}}) \approx g(\hat{\boldsymbol{x}}_{\mathrm{k}}, \boldsymbol{u}_{\mathrm{k}}) + \left.\frac{\partial g(\boldsymbol{x}_{\mathrm{k}}, \boldsymbol{u}_{\mathrm{k}})}{\partial \boldsymbol{x}_{\mathrm{k}}}\right|_{x_{\mathrm{k}}=\hat{x}_{\mathrm{k}}} (\boldsymbol{x}_{\mathrm{k}} - \hat{\boldsymbol{x}}_{\mathrm{k}}) \tag{6.19}$$

$$\frac{\partial f(\boldsymbol{x}_{\mathrm{k}}, \boldsymbol{u}_{\mathrm{k}})}{\partial \boldsymbol{x}_{\mathrm{k}}} = \begin{bmatrix} \frac{\partial f_1}{\partial \boldsymbol{x}_1} & \cdots & \frac{\partial f_1}{\partial \boldsymbol{x}_N} \\ \vdots & \ddots & \vdots \\ \frac{\partial f_N}{\partial \boldsymbol{x}_1} & \cdots & \frac{\partial f_N}{\partial \boldsymbol{x}_N} \end{bmatrix} \tag{6.20}$$

Let $\widehat{\boldsymbol{A}}_{\mathrm{k}} = \frac{\partial f(\boldsymbol{x}_{\mathrm{k}}, \boldsymbol{u}_{\mathrm{k}})}{\partial \boldsymbol{x}_{\mathrm{k}}}$ and $\widehat{\boldsymbol{C}}_{\mathrm{k}} = \frac{\partial g(\boldsymbol{x}_{\mathrm{k}}, \boldsymbol{u}_{\mathrm{k}})}{\partial \boldsymbol{x}_{\mathrm{k}}}$, substituting (6.18)-(6.19) into (6.15)-(6.17), the nonlinear system can be linearised and the system state space model can be written as (6.21)-(6.22) which are similar to (6.6)-(6.7). In (6.21)-(6.22), since the input $\boldsymbol{u}_{\mathrm{k}}$ and the estimation of state $\widehat{\boldsymbol{x}}_{\mathrm{k}}$ are known so that value of the second and third items of both equations are known. Consequently, there is no nonlinear items in (6.21)-(6.22) and the process of deriving KF can be 'extended' and applied to the linearized system. The algorithm is named as then extended Kalman filter.

$$\boldsymbol{x}_{\mathrm{k+1}} \approx \widehat{\boldsymbol{A}}_{\mathrm{k}} \boldsymbol{x}_{\mathrm{k}} + f(\widehat{\boldsymbol{x}}_{\mathrm{k}}, \boldsymbol{u}_{\mathrm{k}}) - \widehat{\boldsymbol{A}}_{\mathrm{k}} \widehat{\boldsymbol{x}}_{\mathrm{k}} + \boldsymbol{w}_{\mathrm{k}} \tag{6.21}$$

$$y_{\mathrm{k}} \approx \widehat{\boldsymbol{C}}_{\mathrm{k}} \boldsymbol{x}_{\mathrm{k}} + g(\widehat{\boldsymbol{x}}_{\mathrm{k}}, \boldsymbol{u}_{\mathrm{k}}) - \widehat{\boldsymbol{C}}_{\mathrm{k}} \widehat{\boldsymbol{x}}_{\mathrm{k}} + \boldsymbol{v}_{\mathrm{k}} \tag{6.22}$$

The steps for EKF is summarized in reference [95][146] and shown in Figure 6.16 as a flow chart. The process of extended Kalman filter is similar to that of linear Kalman filter except for that system matrix $\boldsymbol{A}$ and output matrix $\boldsymbol{C}$ used in linear Kalman filter is replaced with $\widehat{\boldsymbol{A}}_{\mathrm{k}}$ and $\widehat{\boldsymbol{C}}_{\mathrm{k}}$ [145].

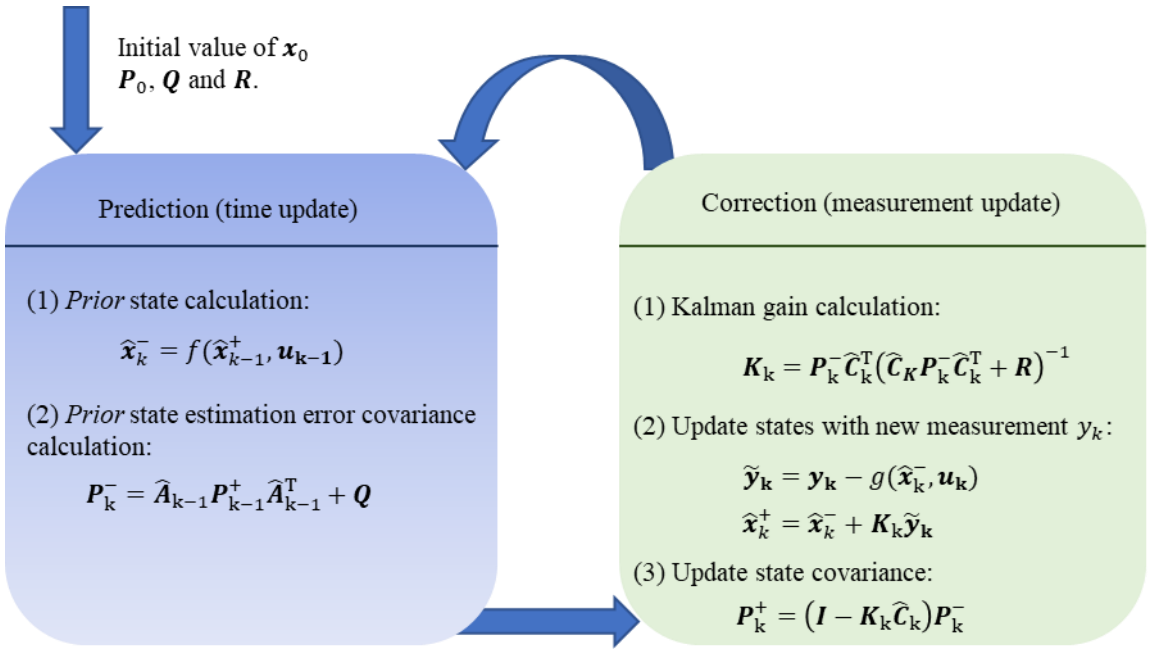

Figure 6.16 Flowchart of extended Kalman filter

6.3.4 State of charge estimation with extended Kalman filter

The EKF method is expected to produce a better SoC estimation for the hysteresis experiment (shown in Figure 6.11) than the BMS SoC. To estimate SoC with EKF, the single

time constant equivalent circuit model (ECM) identified from the day 2 experiment ($ECM1_{D2}$) in Chapter 3 is chosen. The electrical diagram of $ECM1_{D2}$ and its parameter value are shown in Figure 6.17 and Figure 3.10 respectively. The one time constant is used for simplicity. Day 2 is chosen because BMS SoC self-correction happened during the (day 2) experiment which prevented a large SoC error from the Coulomb-counting method. A discussion about the Coulomb-counting method in WESS can be found in section 3.3.2.

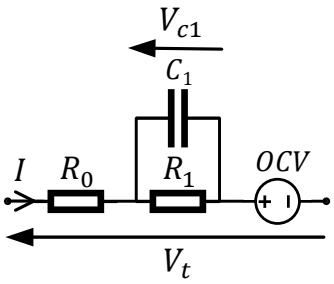

Figure 6.17 Single time constant ECM

For EKF with $ECM1_{D2}$, SoC and the voltage on capacitor C_1 in the equivalent circuit are chosen as the internal states $\boldsymbol{x}_{\mathrm{k}} = [SoC_{\mathrm{k}} \quad V_{\mathrm{C1,k}}]^{\mathrm{T}}$. The discretised model of the circuit is shown in (6.23) and (6.24) where I_{k} is the battery current, $V_{\mathrm{t,k}}$ is the battery terminal voltage, Q is the battery capacity, τ_1 is the time constant which equals R_1C_1 and Δt is the step length (1 s) in the simulation.

$$\begin{aligned}\begin{bmatrix} SoC_{\mathrm{k+1}} \\ V_{\mathrm{C1,k+1}} \end{bmatrix} &= f(\boldsymbol{x}_{\mathrm{k}}, \boldsymbol{u}_{\mathrm{k}}) + \boldsymbol{w}_{\mathrm{k}} \\ &= \begin{bmatrix} 1 & 0 \\ 0 & \exp\left(-\dfrac{\Delta t}{\tau_1(SoC_{\mathrm{k}})}\right) \end{bmatrix} \begin{bmatrix} SoC_{\mathrm{k}} \\ V_{\mathrm{C1,k}} \end{bmatrix} \\ &\quad + \begin{bmatrix} \dfrac{\Delta t}{3600Q} \\ R_1\left(1 - \exp\left(-\dfrac{\Delta t}{\tau_1(SoC_{\mathrm{k}})}\right)\right) \end{bmatrix} I_{\mathrm{k}} + \begin{bmatrix} w_{1,\mathrm{k}} \\ w_{2,\mathrm{k}} \end{bmatrix}\end{aligned} \tag{6.23}$$

$$\begin{aligned} V_{\mathrm{t,k}} &= g(\boldsymbol{x}_{\mathrm{k}}, \boldsymbol{u}_{\mathrm{k}}) + v_{\mathrm{k}} \\ &= OCV(S_k) + V_{\mathrm{C1,k}} + R_0 I_{\mathrm{k}} + v_{\mathrm{k}} \end{aligned} \tag{6.24}$$

The Jacobian matrices of the state transition function f and the output function g are calculated according to the definition during which the relationships between parameters R_0, R_1 and τ_1 and SoC are ignored, $\widehat{\boldsymbol{A}}_{\mathrm{k}} = \frac{\partial f(\boldsymbol{x}_{\mathrm{k}}, \boldsymbol{u}_{\mathrm{k}})}{\partial \boldsymbol{x}_{\mathrm{k}}} = \mathrm{diag}\left[1 \quad \exp(-\frac{\Delta t}{R_1 C_1})\right]$ and $\boldsymbol{C}_{\mathrm{k}} =$

$\frac{\partial g(\boldsymbol{x}_k,\boldsymbol{u}_k)}{\partial \boldsymbol{x}_k} = \left[\frac{\partial V_{OC}}{\partial SoC} \quad 1\right]$. In this way, the Jacobian matrices keep in a simple form which keeps the battery EKF robust and reliable. The relationships between parameters and SoC are adopted for the time update of state $\boldsymbol{x}_k$ for a better *a priori* state estimation. The value of $\boldsymbol{Q}$, $\boldsymbol{R}$ and $\boldsymbol{P}_0^+$ in EKF are set as $[10^{-6}, 0;\ 0, 10^{-10}]$, 1 and diag$[1 \quad 10^{-10}]$, respectively. The SoC in the four hysteresis experiment cycles are calculated through EKF and the voltage vs. EKF SoC is presented in the first column of Figure 6.18.

In the new relationship shown in the first column of Figure 6.18, at the same SoC, the battery charging voltage is larger than discharging voltage. Because the hysteresis voltage is small, the voltage caused by the battery current (~80 A) on the battery internal resistor (~7 mΩ) in WESS is not negligible. The total internal resistance of WESS ($R_0 + R_1$, shown in Figure 3.10(e)) and the battery current I in each cycle (shown in the second column of Figure 6.11) are known. The OCV can be estimated as the measured pack voltage (shown in the first column of Figure 6.11) minus the voltage on the total internal resistance ($\approx I(R_0 + R_1)$).

The second column of Figure 6.18 shows the estimated OCV result in each cycle after subtracting the voltage on the total internal resistance ($\approx I(R_0 + R_1)$). In terms of the hysteresis voltage amplitude, the estimated OCV hysteresis voltage of WESS is less than 1 V and it is lower than 0.1 V when SoC is around 40% and smaller than 70% which is much less than the theoretical value (~2.6 V). The hysteresis voltage has a peak value at around 60% SoC and decreases with SoC between 10% and 40% SoC.

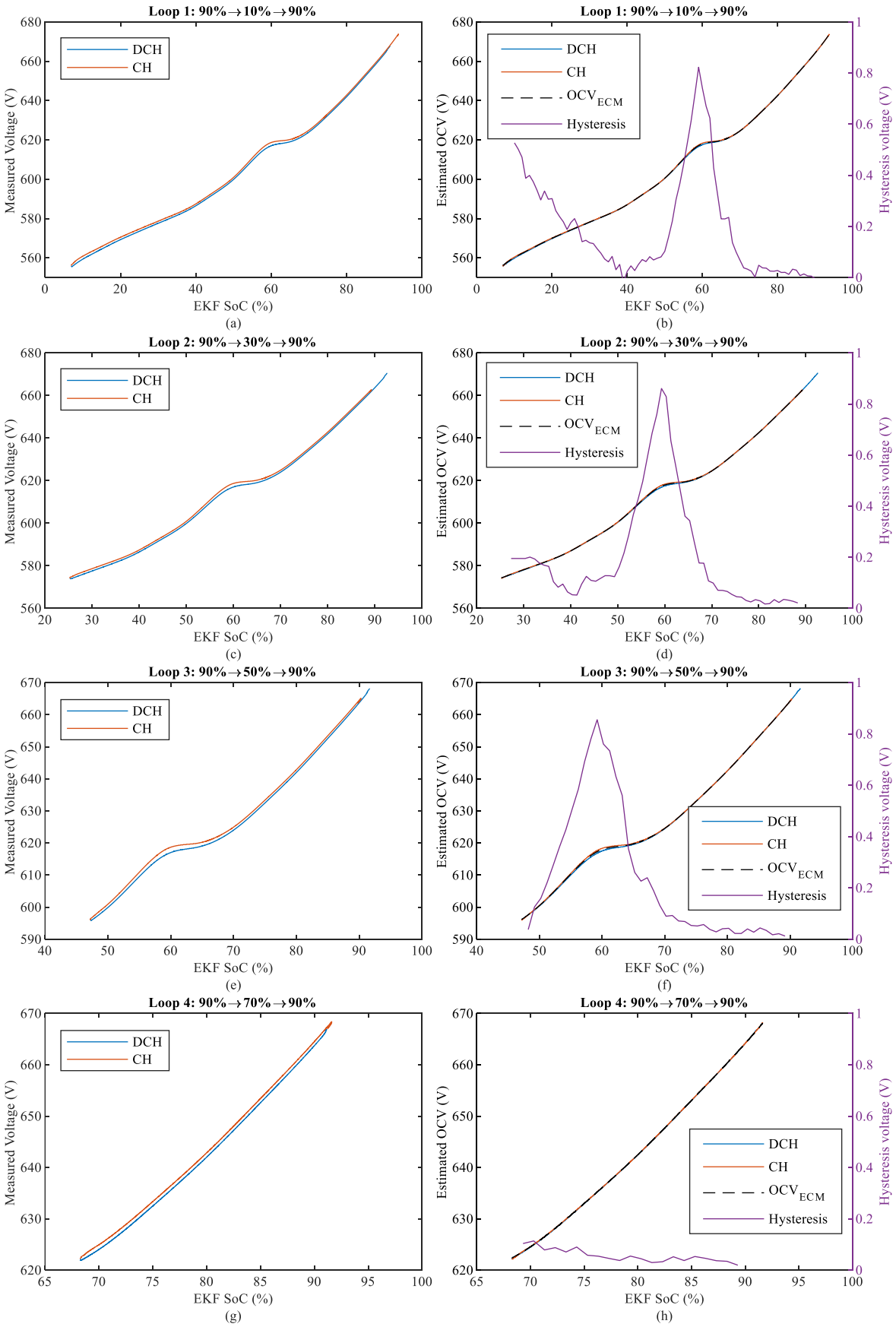

Figure 6.18 Battery pack voltage vs. EKF SoC (first column) and estimated OCV vs. EKF SoC (second column). (note: DCH: discharge, CH: charge)

To obtain the OCV-SoC hysteresis relationship (or hysteresis loops) in a battery, an accurate measurement for the SoC and terminal voltage are required which should be estimated or measured with high-precision equipment (i.e. current sensor and voltage sensor). In hysteresis experiments, the BMS SoC estimation error grows with time, which is caused by the low data sample rate and the low current sensor accuracy in the WESS. The present equipment and setting in WESS are not adequate to directly measure the hysteresis voltage.

The EKF largely improved the SoC estimation. Compared with the hysteresis loops plotted under BMS SoC in Figure 6.12, the hysteresis loops plotted under EKF SoC Figure 6.18 are closer to reality. In detail, EKF eliminated the crossover points in hysteresis loops plotted under BMS SoC. The EKF ensured a basic rule in the OCV hysteresis phenomenon: that, at the same SoC, the measured battery voltage during charging is greater than that during discharging.

However, the EKF in this chapter is not capable of adjusting the battery OCV model inside the equivalent circuit. This is because the OCV and SoC relationship obtained from the EKF is approximately the OCV model inside the ECM. As it can be seen in the second column of Figure 6.18, the OCV profiles obtained from the charging process (plotted in orange) and discharging process (plotted in blue) are close to the OCV model in ECM (plotted in black dash line).

Further work is clearly needed to obtain the direct current and voltage measurements of a large battery pack in order to generate an accurate hysteresis model independent of that stored within the BMS. Unfortunately, such a system is not immediately available. Nonetheless, this chapter has demonstrated that the OCV hysteresis can be modelled with the discrete Preisach model. However, the hysteresis voltage of LTO cell is small which requires high accuracy measurements. To improve the SoC estimation, the EKF can be applied (as it was on WESS) to provide a better hysteresis model.

6.4 Conclusion

This chapter using Willenhall Energy Storage System (WESS) as an example explored the topic of the open circuit voltage (OCV) hysteresis phenomenon in a large-scale battery energy storage system (BESS) built with lithium titanium oxide (LTO) cells. The experiment and simulation results leave it as an open research topic and further study requires more in-

depth knowledge of cell characterisation, improved measurement accuracy and sensors with high dynamic range.

The battery management system (BMS) in WESS does not capture the hysteresis properly. WESS is a commercial BESS that functions as an energy storage system first and then a research platform. Such platforms do not allow access to their internal data. The hardware and software setting in WESS cannot achieve measurements with high precision. However, the results have shown the viability of the Presaich model for the estimation of hysteresis in a large battery back, particularly when combined with the extended Kalman filter.

Chapter 7. Conclusion and future work

7.1 Conclusion

As has been stressed in Chapter 1 and Chapter 2, the large-scale battery energy storage systems (BESSs) play a more and more important role in the grid systems. Large-scale BESSs are used to provide services such as peak load lopping, frequency response, amongst others. Meanwhile, the further understanding of the properties of large-scale BESSs has become meaningful for battery management and economic investment validation. Besides, more accurate battery models in both cell level and pack level are needed for battery system behaviour prediction and analysis.

This work was motivated by the practical need for large-scale BESS models and used Willenhall Energy Storage System (WESS) as the research platform to conduct a series of modelling work. Chapter 3 demonstrated the pack level modelling of WESS in which equivalent circuit models (ECMs) were extracted from the terminal information of the battery pack. As experiments in Chapter 3 have shown, WESS displayed some properties which cause difficulties in modelling. The properties include the slow current responses, low data resolution, low sample frequency, unsatisfactory sensor (current and voltage) accuracy, etc. The inherited properties of WESS causes difficulties in the ECM parameter identification, especially for the ohmic resistance. As shown in Chapter 3, by setting the ohmic resistance as a complementary component, the ECM can be identified. The identified ECMs has higher accuracy than scaling up a single cell but the latter method does have a reasonable performance during simulations.

The pack level battery model is not able to reflect the battery internal (cell level) conditions. To obtain the cell level information, each cell in the pack is represented by an ECM. However, as shown in Chapter 4, the massive circuit generated when cell-level equivalent circuits and combined into a pack of over 21000 cells caused failure in traditional simulators due to the difficulties in solving equations that contain large sparse matrices. Chapter 4 shows that systematically applying Thévenin and Norton transformations provide a more efficient method to solve the high order sparse matrices resulting from high-order RC network constructed from cell ECMs. This simulation tool was used for the study of cell-to-cell variation (CtCV) in this thesis, but the application of the tool can be expanded to other areas such as exploring the impacts of aged cells in a battery pack.

CtCV is known to have a significant impact on the operation of large-scale BESSs. As Chapter 5 has discussed, the voltage deviation which is a result of CtCV can trigger the cut-off mechanism in BESS when the manufacturer's recommended limits are exceeded. In Chapter 5, electroimpedance spectroscopy measurements (EIS) on cells show that the cells have a dramatic property change at operating conditions close to fully charged and close to fully discharge zones which are the extreme state of charge (SoC) characteristic. The obvious change in cell chemistry properties leads to a large change in the ECM parameter value and causes large parameter variation. In the Monte Carlo simulations, the randomly generated battery pack (obeying specific probably distributions) also showed a large deviation at low and high SoC zones. The findings in the experiments and simulations provided a possible explanation for the voltage deviation change observed in the two discharge-charge experiments on WESS. In detail, the large cell to cell differences at high and low SoC zone leads to the variation on cell electrical properties which caused a higher voltage deviation at the low and high SoC zones. Operating battery pack in these regions is more likely to cause the voltage of some of the cells within a pack exceed manufacturers limits.

Chapter 6 explored the open circuit voltage hysteresis phenomenon in a large-scale BESS. A low power charge-discharge experiment was designed for WESS according to the properties of the battery management system (BMS) in WESS. The BMS recorded result of the hysteresis experiments were still influenced by the BMS and caused some unusual phenomenon. In detail, sometimes at the same SoC, the battery voltage during the discharging process is larger than that during the charging process. This obvious error in the experiment is believed to be due to how the BMS calculates SoC. The BMS uses the Coulomb counting method to estimate the SoC value when there is a current flow through the battery and uses an OCV-SoC look-up table to current the estimation when the battery is under a zero or extreme low current for a long period of time. An error can be introduced by the Coulomb counting method because of the sensor accuracy. This error is accumulating over time until an SoC correction happens.

The SoC estimation can be largely improved by an extended Kalman filter (EKF) and the improved hysteresis experimental result shows a more satisfactory profile. However, as discussed in Chapter 6, the EKF is a model-based method and the hysteresis voltage extracted from this method is close to the OCV-SoC relationship used in the EKF algorithm.

Further experiments or more advanced algorithms are required to accurately identify the hysteresis voltage profile in a large-scale BESS.

A large-scale BESS is normally designed for a particular application or service. For example, WESS was designed for the grid application and frequency response services. The hardware and software in a large-scale BESS are usually chosen to adapt the application requirements and the economic purpose. However, the hardware and software may not be appropriate for a scientific study. Hence, when an experiment is designed for a large-scale BESS, one should consider the hardware and software properties of the facility and carefully assess the feasibility of the experiments.

7.2 Potential future work

The research provided three valuable pack level ECMs for a real large-scale BESS and also proposed an efficient cell level simulator for large-scale BESS. Based on the provided data and simulator, a few further research ideas are suggested below.

1) Economic evaluation of applications

With the pack-level ECMs provided in Chapter 3, the response of a large-scale BESS can be simulated under different applications such as frequency response. The economic value of the battery in the applications can be estimated.

2) Impact of different applications on cell voltage deviation

Using the simulator proposed in Chapter 4, the cell voltage deviation under different load profiles can be simulated which can be used to evaluate the impact of different applications on the cell voltage deviation.

3) Further hysteresis voltage study on large-scale battery packs

The study of hysteresis voltage in large-scale BESS could help increase the model accuracy which is worth further research. Based on the hysteresis experiment result from this work, more accurate current and voltage sensors are recommended to use in further experiments. These are not likely to be provided by the battery management system on a commercial battery energy storage system.

4) Introducing the cell thermal model into the proposed simulator

The CtCV on cell internal resistance is small. It is believed that the temperature variation among cells caused by cell resistance variation is small so the temperature factor is not involved in this thesis. However, the accurate impact of temperature on BESS requires further experiments and simulations to be decided.

The cell level battery simulator proposed in this work uses electrical equivalent circuit models to simulate individual cells in a pack. Thermal model can be introduced into the simulator to account for changes in ambient temperature around and within the pack. The thermal models can also be translated into a massive RC circuit which might be solvable with a similar approach as shown in Chapter 4.

5) Coupling the effects of cell-to-cell variation and ageing

Because of cell-to-cell variation, the current flowing through each cell in a pack will not be the same. After a long term of operation, the current difference among cells could lead to a variation in ageing. This topic can be explored by adding cell ageing models into the proposed cell level simulator.

References

[1] Historical electricity data: 1920 to 2019, (2020). https://www.gov.uk/government/statistical-data-sets/historical-electricity-data (accessed December 9, 2020).

[2] T.S. Ledley, E.T. Sundquist, S.E. Schwartz, D.K. Hall, J.D. Fellows, T.L. Killeen, Climate change and greenhouse gases, Eos, Trans. Am. Geophys. Union. 80 (1999) 453–458. https://doi.org/https://doi.org/10.1029/99EO00325.

[3] COP26 Goals - UN Climate Change Conference (COP26) at the Scottish Event Campus – Glasgow 2021, (n.d.). https://ukcop26.org/cop26-goals/ (accessed November 1, 2021).

[4] Kevin Harris, Chris Michaels, Stephen Rose, A. Gower, V. Martin, W. Spry, Energy Trends: UK electricity, 2021. https://www.gov.uk/government/statistics/energy-trends-section-6-renewables.

[5] C. Garnett, The future of Island Line - Options Report The future of Island Line - Options Report, 2016. https://www.iow.gov.uk/documentlibrary/download/island-line-report-by-christopher-garnett.

[6] Island Line Upgrade | Island Line | South Western Railway, (n.d.). https://www.southwesternrailway.com/destinations-and-offers/island-line/island-line-upgrade (accessed November 2, 2021).

[7] S. Rehman, L.M. Al-Hadhrami, M.M. Alam, Pumped hydro energy storage system: A technological review, Renew. Sustain. Energy Rev. 44 (2015) 586–598. https://doi.org/10.1016/j.rser.2014.12.040.

[8] M. Ragheb, Compressed Air Energy Storage, (2016) 101–112. https://doi.org/10.5772/52221.

[9] R. Arghandeh, M. Pipattanasomporn, S. Rahman, Flywheel Energy Storage Systems for Ride-through Applications in a Facility Microgrid, IEEE Trans. Smart Grid. 3 (2012) 1955–1962. https://doi.org/10.1109/TSG.2012.2212468.

[10] B. Yildirim, M. Elgendy, A. Smith, V. Pickert, Evaluation and Comparison of

Battery Cell Balancing Methods, in: 2019 IEEE PES Innov. Smart Grid Technol. Eur., 2019: pp. 1–5. https://doi.org/10.1109/ISGTEurope.2019.8905588.

[11] R. Duarte, L. Moreira, L.A.M. Barros, V. Monteiro, J.L. Afonso, J.G. Pinto, Power Converters for a Small Islanded Microgrid Based on a Micro Wind Turbine and an Battery Energy Storage System, in: ECOS 2018 - Proc. 31st Int. Conf. Effic. Cost, Optim. Simul. Environ. Impact Energy Syst., Guimarães, Portugal, 2018: pp. 1–12.

[12] L. Meng, J. Zafar, S.K. Khadem, A. Collinson, K.C. Murchie, F. Coffele, G.M. Burt, Fast Frequency Response From Energy Storage Systems—A Review of Grid Standards, Projects and Technical Issues, IEEE Trans. Smart Grid. 11 (2020) 1566–1581. https://doi.org/10.1109/TSG.2019.2940173.

[13] ENERGY STORAGE IN MARYLAND-Policy and regulatory options for promoting energy storage and its benefits 2018, 2018. https://dnr.maryland.gov/pprp/Documents/Energy-Storage-In-Maryland.pdf.

[14] U.S. Department of Energy, Energy Storage Grand Challenge Energy Storage Market Report 2020, 2020. https://www.energy.gov/sites/default/files/2020/12/f81/Energy Storage Market Report 2020_0.pdf.

[15] Willenhall: 2MW Battery Energy Storage Demonstrator | CREESA | The University of Sheffield, (n.d.). https://www.sheffield.ac.uk/creesa/facilities/willenhall (accessed October 30, 2021).

[16] J.A. Sanguesa, V. Torres-Sanz, P. Garrido, F.J. Martinez, J.M. Marquez-Barja, A Review on Electric Vehicles: Technologies and Challenges, Smart Cities. 4 (2021). https://doi.org/10.3390/smartcities4010022.

[17] J.O.G. Posada, A.J.R. Rennie, S.P. Villar, V.L. Martins, J. Marinaccio, A. Barnes, C.F. Glover, D.A. Worsley, P.J. Hall, Aqueous batteries as grid scale energy storage solutions, Renew. Sustain. Energy Rev. 68 (2017) 1174–1182. https://doi.org/https://doi.org/10.1016/j.rser.2016.02.024.

[18] Yuasa, Yuasa Technical Data Sheet: Yuasa NPL65-12IFR Industrial VRLA Battery, Yuasa. (2021). https://www.yuasa.co.uk/batteries/industrial/npl-vrla-general-

use/npl65-12ifr.html.

[19] L. Pietro P., S.V. R., Past, present, and future of lead–acid batteries, Science (80-.). 369 (2020) 923–924. https://doi.org/10.1126/science.abd3352.

[20] S.K. Martha, B. Hariprakash, S.A. Gaffoor, D.C. Trivedi, A.K. Shukla, A low-cost lead-acid battery with high specific-energy, J. Chem. Sci. 118 (2006) 93–98. https://doi.org/10.1007/BF02708770.

[21] J.W. Reitz, Separator technology for lead/acid batteries, J. Power Sources. 19 (1987) 181–188. https://doi.org/https://doi.org/10.1016/0378-7753(87)80028-9.

[22] T. İşler, M. Mazman, New Design and Analysis of Lead Acid Battery Grid, in: Comsol Conf. Cambridge/UK, 2019. https://www.comsol.com/paper/new-design-and-analysis-of-lead-acid-battery-grid-82881.

[23] J.-M. Tarascon, M. Armand, Issues and challenges facing rechargeable lithium batteries, Nature. 414 (2001) 359–367. https://doi.org/10.1038/35104644.

[24] K. Ozawa, Lithium-ion rechargeable batteries with LiCoO2 and carbon electrodes: the LiCoO2/C system, Solid State Ionics. 69 (1994) 212–221. https://doi.org/https://doi.org/10.1016/0167-2738(94)90411-1.

[25] A. Manthiram, J. Kim, Low Temperature Synthesis of Insertion Oxides for Lithium Batteries, Chem. Mater. 10 (1998) 2895–2909. https://doi.org/10.1021/cm980241u.

[26] Y. Mekonnen, A. Sundararajan, A.I. Sarwat, A review of cathode and anode materials for lithium-ion batteries, in: SoutheastCon 2016, 2016: pp. 1–6. https://doi.org/10.1109/SECON.2016.7506639.

[27] Y. Son, H. Cha, C. Jo, A.S. Groombridge, T. Lee, A. Boies, J. Cho, M. De Volder, Reliable protocols for calculating the specific energy and energy density of Li-Ion batteries, Mater. Today Energy. 21 (2021) 100838. https://doi.org/10.1016/J.MTENER.2021.100838.

[28] R. Jung, M. Metzger, F. Maglia, C. Stinner, H.A. Gasteiger, Oxygen Release and Its Effect on the Cycling Stability of LiNixMnyCozO2(NMC) Cathode Materials for Li-Ion Batteries, J. Electrochem. Soc. 164 (2017) A1361–A1377.

https://doi.org/10.1149/2.0021707jes.

[29] M. Greenwood, M. Wentker, J. Leker, A region-specific raw material and lithium-ion battery criticality methodology with an assessment of NMC cathode technology, Appl. Energy. 302 (2021) 117512. https://doi.org/10.1016/J.APENERGY.2021.117512.

[30] Q. Liu, X. Su, D. Lei, Y. Qin, J. Wen, F. Guo, Y.A. Wu, Y. Rong, R. Kou, X. Xiao, F. Aguesse, J. Bareño, Y. Ren, W. Lu, Y. Li, Approaching the capacity limit of lithium cobalt oxide in lithium ion batteries via lanthanum and aluminium doping, Nat. Energy. 3 (2018) 936–943. https://doi.org/10.1038/s41560-018-0180-6.

[31] Y. Miao, P. Hynan, A. von Jouanne, A. Yokochi, Current Li-Ion Battery Technologies in Electric Vehicles and Opportunities for Advancements, Energies. 12 (2019). https://doi.org/10.3390/en12061074.

[32] B. Lung-Hao Hu, F.-Y. Wu, C.-T. Lin, A.N. Khlobystov, L.-J. Li, Graphene-modified LiFePO4 cathode for lithium ion battery beyond theoretical capacity, Nat. Commun. 4 (2013) 1687. https://doi.org/10.1038/ncomms2705.

[33] Y. Zhang, H. Xie, H. Jin, Q. Zhang, Y. Li, X. Li, K. Li, C. Bao, Research Status of Spinel LiMn2O4 Cathode Materials for Lithium Ion Batteries, IOP Conf. Ser. Earth Environ. Sci. 603 (2020) 12051. https://doi.org/10.1088/1755-1315/603/1/012051.

[34] H.-J. Noh, S. Youn, C.S. Yoon, Y.-K. Sun, Comparison of the structural and electrochemical properties of layered Li[NixCoyMnz]O2 (x = 1/3, 0.5, 0.6, 0.7, 0.8 and 0.85) cathode material for lithium-ion batteries, J. Power Sources. 233 (2013) 121–130. https://doi.org/https://doi.org/10.1016/j.jpowsour.2013.01.063.

[35] M. Li, J. Lu, Z. Chen, K. Amine, 30 Years of Lithium-Ion Batteries, Adv. Mater. 30 (2018) 1800561. https://doi.org/https://doi.org/10.1002/adma.201800561.

[36] L. Ji, X. Zhang, Fabrication of porous carbon nanofibers and their application as anode materials for rechargeable lithium-ion batteries, Nanotechnology. 20 (2009) 155705. https://doi.org/10.1088/0957-4484/20/15/155705.

[37] A. Zhou, X. Dai, Y. Lu, Q. Wang, M. Fu, J. Li, Enhanced Interfacial Kinetics and

High-Voltage/High-Rate Performance of LiCoO2 Cathode by Controlled Sputter-Coating with a Nanoscale Li4Ti5O12 Ionic Conductor, ACS Appl. Mater. Interfaces. 8 (2016) 34123–34131. https://doi.org/10.1021/acsami.6b11630.

[38] G.E. Blomgren, The Development and Future of Lithium Ion Batteries, J. Electrochem. Soc. 164 (2017) A5019–A5025. https://doi.org/10.1149/2.0251701jes.

[39] R. Inguanta, S. Randazzo, A. Moncada, M.C. Mistretta, S. Piazza, C. Sunseri, Growth and electrochemical performance of lead and lead oxide nanowire arrays as electrodes for lead-acid batteries, Chem. Eng. Trans. 32 (2013) 2227–2232. https://doi.org/10.3303/CET1332372.

[40] Specification of product for Lithium-ion Rechargeable Cell Model: INR18650-25R, (2009) 0–15. http://www.datasheet-pdf.com/datasheet/Samsung/799163/INR18650-20R.pdf.html.

[41] Superior Lithium ion Battery Pioneer of Lithium ion Battery Technology, (n.d.). https://kokam.com/data/filebox/cell_brochure.pdf.

[42] Industrial Lithium-ion Battery ToshibaRechargeableBattery SCiB ™, (n.d.). https://www.global.toshiba/content/dam/toshiba/ww/products-solutions/battery/scib/pdf/ToshibaRechargeableBattery-en.pdf.

[43] Y. Chen, Y. Kang, Y. Zhao, L. Wang, J. Liu, Y. Li, Z. Liang, X. He, X. Li, N. Tavajohi, B. Li, A review of lithium-ion battery safety concerns: The issues, strategies, and testing standards, J. Energy Chem. 59 (2021) 83–99. https://doi.org/https://doi.org/10.1016/j.jechem.2020.10.017.

[44] S. Lv, X. Wang, W. Lu, J. Zhang, H. Ni, The Influence of Temperature on the Capacity of Lithium Ion Batteries with Different Anodes, Energies 2022, Vol. 15, Page 60. 15 (2021) 60. https://doi.org/10.3390/EN15010060.

[45] A. Farmann, D.U. Sauer, A study on the dependency of the open-circuit voltage on temperature and actual aging state of lithium-ion batteries, J. Power Sources. 347 (2017) 1–13. https://doi.org/https://doi.org/10.1016/j.jpowsour.2017.01.098.

[46] C. Zhang, J. Jiang, L. Zhang, S. Liu, L. Wang, P.C. Loh, A Generalized SOC-OCV

Model for Lithium-Ion Batteries and the SOC Estimation for LNMCO Battery, Energies. 9 (2016). https://doi.org/10.3390/en9110900.

[47] A. Fotouhi, D.J. Auger, K. Propp, S. Longo, Lithium–Sulfur Battery State-of-Charge Observability Analysis and Estimation, IEEE Trans. Power Electron. 33 (2018) 5847–5859. https://doi.org/10.1109/TPEL.2017.2740223.

[48] C.S. Moo, K.S. Ng, Y.P. Chen, Y.C. Hsieh, State-of-Charge Estimation with Open-Circuit-Voltage for Lead-Acid Batteries, in: 2007 Power Convers. Conf. - Nagoya, 2007: pp. 758–762. https://doi.org/10.1109/PCCON.2007.373052.

[49] X. Wang, Q. Fang, H. Dai, Q. Chen, X. Wei, Investigation on Cell Performance and Inconsistency Evolution of Series and Parallel Lithium-Ion Battery Modules, Energy Technol. 9 (2021) 2100072. https://doi.org/https://doi.org/10.1002/ente.202100072.

[50] H. Ren, Y. Zhao, S. Chen, T. Wang, Design and implementation of a battery management system with active charge balance based on the SOC and SOH online estimation, Energy. 166 (2019) 908–917. https://doi.org/https://doi.org/10.1016/j.energy.2018.10.133.

[51] Samsung Li-Ion Battery & Renewable Energy | Samsung SDI Official Site, (n.d.). https://www.samsungsdi.com/index.html (accessed October 30, 2021).

[52] Samsung Tablet Li-ion(Lithium ion) Battery Cell | Samsung SDI, (n.d.). https://www.samsungsdi.com/lithium-ion-battery/it-devices/tablet.html (accessed October 30, 2021).

[53] Nissan Leaf | Electric Cars | Nissan UK, (n.d.). https://www.nissan.co.uk/vehicles/new-vehicles/leaf.html (accessed October 30, 2021).

[54] Electric vehicle lithium-ion battery | NISSAN | TECHNOLOGICAL DEVELOPMENT ACTIVITIES, (n.d.). https://www.nissan-global.com/EN/TECHNOLOGY/OVERVIEW/li_ion_ev.html (accessed January 14, 2021).

[55] Electrical power & energy | SCiB^{TM} Rechargeable battery | Toshiba, (n.d.).

https://www.global.toshiba/ww/products-solutions/battery/scib/cases/energy.html#case1-1 (accessed October 30, 2021).

[56] M.A. Hannan, M.S.H. Lipu, A. Hussain, A. Mohamed, A review of lithium-ion battery state of charge estimation and management system in electric vehicle applications: Challenges and recommendations, Renew. Sustain. Energy Rev. 78 (2017) 834–854. https://doi.org/https://doi.org/10.1016/j.rser.2017.05.001.

[57] M.S. Hossain Lipu, M.A. Hannan, T.F. Karim, A. Hussain, M.H.M. Saad, A. Ayob, M.S. Miah, T.M. Indra Mahlia, Intelligent algorithms and control strategies for battery management system in electric vehicles: Progress, challenges and future outlook, J. Clean. Prod. 292 (2021). https://doi.org/10.1016/j.jclepro.2021.126044.

[58] S. Buller, E. Karden, A. Lohner, R.W. De Doncker, LabView-based universal battery monitoring and management system, in: INTELEC - Twent. Int. Telecommun. Energy Conf. (Cat. No.98CH36263), 1998: pp. 630–635. https://doi.org/10.1109/INTLEC.1998.793612.

[59] M. Lelie, T. Braun, M. Knips, H. Nordmann, F. Ringbeck, H. Zappen, D.U. Sauer, Battery Management System Hardware Concepts: An Overview, Appl. Sci. 8 (2018). https://doi.org/10.3390/app8040534.

[60] Y. Wang, J. Tian, Z. Sun, L. Wang, R. Xu, M. Li, Z. Chen, A comprehensive review of battery modeling and state estimation approaches for advanced battery management systems, Renew. Sustain. Energy Rev. 131 (2020) 110015. https://doi.org/https://doi.org/10.1016/j.rser.2020.110015.

[61] H. Qian, J. Zhang, J.S. Lai, W. Yu, A high-efficiency grid-tie battery energy storage system, IEEE Trans. Power Electron. 26 (2011) 886–896. https://doi.org/10.1109/TPEL.2010.2096562.

[62] M. Daowd, N. Omar, P. Van Den Bossche, J. Van Mierlo, Passive and active battery balancing comparison based on MATLAB simulation, in: 2011 IEEE Veh. Power Propuls. Conf. VPPC 2011, 2011: pp. 2974–2989. https://doi.org/10.1109/VPPC.2011.6043010.

[63] D. V Cadar, D.M. Petreus, T.M. Patarau, An energy converter method for battery

cell balancing, in: ISSE 2010 - 33rd Int. Spring Semin. Electron. Technol. Polym. Electron. Nanotechnologies Towar. Syst. Integr. - Conf. Proc., 2010: pp. 290–293. https://doi.org/10.1109/ISSE.2010.5547305.

[64] S. Ci, N. Lin, D. Wu, Reconfigurable Battery Techniques and Systems: A Survey, IEEE Access. 4 (2016) 1175–1189. https://doi.org/10.1109/ACCESS.2016.2545338.

[65] C. Bonfiglio, W. Roessler, A cost optimized battery management system with active cell balancing for lithium ion battery stacks, in: 2009 IEEE Veh. Power Propuls. Conf., IEEE, 2009: pp. 304–309. https://doi.org/10.1109/VPPC.2009.5289837.

[66] Y. Barsukov, Battery cell balancing: what to balance and how, Texas Instruments. (2005) 1–8. http://focus.ti.com/download/trng/docs/seminar/Topic 2 - Battery Cell Balancing - What to Balance and How.pdf.

[67] C.-H. Lin, H.-Y. Chao, C.-M. Wang, M.-H. Hung, Battery management system with dual-balancing mechanism for LiFePO<inf>4</inf> battery module, in: TENCON 2011 - 2011 IEEE Reg. 10 Conf., 2011: pp. 863–867. https://doi.org/10.1109/TENCON.2011.6129233.

[68] Y. Lee, S. Jeon, H. Lee, S. Bae, Comparison on cell balancing methods for energy storage applications, Indian J. Sci. Technol. 9 (2016). https://doi.org/10.17485/ijst/2016/v9i17/92316.

[69] J. Meng, G. Luo, M. Ricco, M. Swierczynski, D.-I. Stroe, R. Teodorescu, Overview of Lithium-Ion Battery Modeling Methods for State-of-Charge Estimation in Electrical Vehicles, Appl. Sci. 8 (2018). https://doi.org/10.3390/app8050659.

[70] V. Sircoulomb, N. Langlois, A New Adaptive Kalman Filter for Single-State Integrator Systems: Application to Battery State-of-Charge Estimation, in: 2015 IEEE Veh. Power Propuls. Conf., 2015: pp. 1–6. https://doi.org/10.1109/VPPC.2015.7352879.

[71] M. Gao, Y. Liu, Z. He, Battery state of charge online estimation based on particle filter, in: 2011 4th Int. Congr. Image Signal Process., 2011: pp. 2233–2236. https://doi.org/10.1109/CISP.2011.6100603.

[72] T. Wu, L. Liu, Q. Xiao, Q. Cao, X. Wang, Research on SOC estimation based on second-order RC model, TELKOMNIKA Indones. J. Electr. Eng. 10 (2012) 1667–1672.

[73] P. Spagnol, S. Rossi, S.M. Savaresi, Kalman Filter SoC estimation for Li-Ion batteries, Proc. IEEE Int. Conf. Control Appl. (2011) 587–592. https://doi.org/10.1109/CCA.2011.6044480.

[74] S. Park, J. Ahn, T. Kang, S. Park, Y. Kim, I. Cho, J. Kim, Review of state-of-the-art battery state estimation technologies for battery management systems of stationary energy storage systems, J. Power Electron. 20 (2020) 1526–1540. https://doi.org/10.1007/s43236-020-00122-7.

[75] Z. Wang, G. Feng, D. Zhen, F. Gu, A. Ball, A review on online state of charge and state of health estimation for lithium-ion batteries in electric vehicles, Energy Reports. 7 (2021) 5141–5161. https://doi.org/https://doi.org/10.1016/j.egyr.2021.08.113.

[76] Q. Wang, P. Wu, J. Lian, SOC estimation algorithm of power lithium battery based on AFSA-BP neural network, J. Eng. 2020 (2020) 535–539. https://doi.org/https://doi.org/10.1049/joe.2019.1214.

[77] E. Chemali, P.J. Kollmeyer, M. Preindl, A. Emadi, State-of-charge estimation of Li-ion batteries using deep neural networks: A machine learning approach, J. Power Sources. 400 (2018) 242–255. https://doi.org/https://doi.org/10.1016/j.jpowsour.2018.06.104.

[78] ENHANCED FREQUENCY RESPONSE Invitation to tender for pre-qualified parties, (2016).

[79] D.M. Greenwood, K.Y. Lim, C. Patsios, P.F. Lyons, Y.S. Lim, P.C. Taylor, Frequency response services designed for energy storage, Appl. Energy. 203 (2017) 115–127. https://doi.org/10.1016/j.apenergy.2017.06.046.

[80] S. Sabihuddin, A.E. Kiprakis, M. Mueller, A Numerical and Graphical Review of Energy Storage Technologies, Energies . 8 (2015). https://doi.org/10.3390/en8010172.

[81] N. Boyouk, N. Munzke, M. Hiller, Peak Shaving of a Grid connected-Photovoltaic Battery System at Helmholtz Institute Ulm (HIU), in: Proc. - 2018 IEEE PES Innov. Smart Grid Technol. Conf. Eur. ISGT-Europe 2018, 2018: pp. 1–5. https://doi.org/10.1109/ISGTEurope.2018.8571616.

[82] W. Zhou, Y. Zheng, Z. Pan, Q. Lu, Review on the battery model and SOC estimation method, Processes. 9 (2021). https://doi.org/10.3390/pr9091685.

[83] A.M. Bizeray, J.H. Kim, S.R. Duncan, D.A. Howey, Identifiability and Parameter Estimation of the Single Particle Lithium-Ion Battery Model, IEEE Trans. Control Syst. Technol. (2018) 1–16. https://doi.org/10.1109/TCST.2018.2838097.

[84] B. Kenney, K. Darcovich, D.D. MacNeil, I.J. Davidson, Modelling the impact of variations in electrode manufacturing on lithium-ion battery modules, J. Power Sources. 213 (2012) 391–401. https://doi.org/10.1016/j.jpowsour.2012.03.065.

[85] S.B. Vilsen, D.-I. Stroe, An auto-regressive model for battery voltage prediction, in: 2021 IEEE Appl. Power Electron. Conf. Expo., 2021: pp. 2673–2680. https://doi.org/10.1109/APEC42165.2021.9487060.

[86] V. Klass, M. Behm, G. Lindbergh, A support vector machine-based state-of-health estimation method for lithium-ion batteries under electric vehicle operation, J. Power Sources. 270 (2014) 262–272. https://doi.org/10.1016/J.JPOWSOUR.2014.07.116.

[87] A. Berrueta, A. Urtasun, A. Ursúa, P. Sanchis, A comprehensive model for lithium-ion batteries: From the physical principles to an electrical model, Energy. 144 (2018) 286–300. https://doi.org/https://doi.org/10.1016/j.energy.2017.11.154.

[88] S. Skoog, S. David, Parameterization of linear equivalent circuit models over wide temperature and SOC spans for automotive lithium-ion cells using electrochemical impedance spectroscopy, J. Energy Storage. 14 (2017) 39–48. https://doi.org/https://doi.org/10.1016/j.est.2017.08.004.

[89] M. Swierczynski, D. Stroe, A. Stan, R. Teodorescu, S.K. Kær, Investigation on the Self-discharge of the LiFePO<inf>4</inf>/C nanophosphate battery chemistry at different conditions, in: 2014 IEEE Conf. Expo Transp. Electrif. Asia-Pacific (ITEC

Asia-Pacific), 2014: pp. 1–6. https://doi.org/10.1109/ITEC-AP.2014.6940762.

[90] F. Odeim, J. Roes, A. Heinzel, Power Management Optimization of an Experimental Fuel Cell/Battery/Supercapacitor Hybrid System, Energies . 8 (2015). https://doi.org/10.3390/en8076302.

[91] J.E.B. Randles, KINETICS OF RAPID ELECTRODE REACTIONS., (1947).

[92] C.R. Gould, C.M. Bingham, D.A. Stone, P. Bentley, New battery model and state-of-health determination through subspace parameter estimation and state-observer techniques, IEEE Trans. Veh. Technol. 58 (2009) 3905–3916. https://doi.org/10.1109/TVT.2009.2028348.

[93] H. He, R. Xiong, J. Fan, Evaluation of Lithium-Ion Battery Equivalent Circuit Models for State of Charge Estimation by an Experimental Approach, Energies . 4 (2011). https://doi.org/10.3390/en4040582.

[94] F. Codeca, S.M. Savaresi, G. Rizzoni, On battery State of Charge estimation: A new mixed algorithm, Control Appl. 2008. CCA 2008. IEEE Int. Conf. (2008) 102–107. https://doi.org/10.1109/CCA.2008.4629635.

[95] F. Zhang, G. Liu, L. Fang, A battery State of Charge estimation method with extended Kalman filter, in: 2008 IEEE/ASME Int. Conf. Adv. Intell. Mechatronics, 2008: pp. 1008–1013. https://doi.org/10.1109/AIM.2008.4601799.

[96] B. Dawoud, E. Amer, D. Gross, Experimental investigation of an adsorptive thermal energy storage, Int. J. Energy Res. 31 (2007) 135–147. https://doi.org/10.1002/er.

[97] L. Yao, A. Aziz, P. Kong, N. Idrus, Modeling of lithium-ion battery using MATLAB/simulink, IECON Proc. (Industrial Electron. Conf. (2013) 1729–1734. https://doi.org/10.1109/IECON.2013.6699393.

[98] Z. Gao, C.S. Chin, W.L. Woo, J. Jia, Integrated Equivalent Circuit and Thermal Model for Simulation of Temperature-Dependent LiFePO4 Battery in Actual Embedded Application, Energies. 10 (2017). https://doi.org/10.3390/en10010085.

[99] S.S. Madani, E. Schaltz, S. Knudsen Kær, An Electrical Equivalent Circuit Model of a Lithium Titanate Oxide Battery, Batteries. 5 (2019).

https://doi.org/10.3390/batteries5010031.

[100] L. Bodenes, R. Dedryvère, H. Martinez, F. Fischer, C. Tessier, J.-P. Pérès, Lithium-Ion Batteries Working at 85°C: Aging Phenomena and Electrode/Electrolyte Interfaces Studied by XPS, J. Electrochem. Soc. 159 (2012) A1739–A1746. https://doi.org/10.1149/2.061210jes.

[101] M. Dubarry, N. Vuillaume, B.Y. Liaw, Origins and accommodation of cell variations in Li-ion battery pack modeling, Int. J. Energy Res. 34 (2010) 216–231. https://doi.org/10.1002/er.1668.

[102] L. Zhou, Y. Zheng, M. Ouyang, L. Lu, A study on parameter variation effects on battery packs for electric vehicles, J. Power Sources. 364 (2017) 242–252. https://doi.org/10.1016/j.jpowsour.2017.08.033.

[103] I. Zilberman, S. Ludwig, A. Jossen, Cell-to-cell variation of calendar aging and reversible self-discharge in 18650 nickel-rich, silicon–graphite lithium-ion cells, J. Energy Storage. 26 (2019) 100900. https://doi.org/10.1016/j.est.2019.100900.

[104] J.V. Barreras, T. Raj, D.A. Howey, E. Schaltz, Results of Screening over 200 Pristine Lithium-Ion Cells, in: 2017 IEEE Veh. Power Propuls. Conf., Institute of Electrical and Electronics Engineers (IEEE), 2018: pp. 1–6. https://doi.org/10.1109/vppc.2017.8331060.

[105] K. Rumpf, M. Naumann, A. Jossen, Experimental investigation of parametric cell-to-cell variation and correlation based on 1100 commercial lithium-ion cells, J. Energy Storage. 14 (2017) 224–243. https://doi.org/10.1016/j.est.2017.09.010.

[106] F. An, L. Chen, J. Huang, J. Zhang, P. Li, Rate dependence of cell-to-cell variations of lithium-ion cells, Sci. Rep. 6 (2016) 1–7. https://doi.org/10.1038/srep35051.

[107] I. Zilberman, J. Schmitt, S. Ludwig, M. Naumann, A. Jossen, Simulation of voltage imbalance in large lithium-ion battery packs influenced by cell-to-cell variations and balancing systems, J. Energy Storage. 32 (2020) 101828. https://doi.org/10.1016/j.est.2020.101828.

[108] D. Shin, M. Poncino, E. Macii, N. Chang, A statistical model-based cell-to-cell

variability management of Li-ion battery pack, IEEE Trans. Comput. Des. Integr. Circuits Syst. 34 (2015) 252–265. https://doi.org/10.1109/TCAD.2014.2384506.

[109] F. Chang, F. Roemer, M. Baumann, M. Lienkamp, Modelling and Evaluation of Battery Packs with Different Numbers of Paralleled Cells, World Electr. Veh. J. 9 (2018) 8. https://doi.org/10.3390/wevj9010008.

[110] B.M. Gundogdu, S. Nejad, D.T. Gladwin, M.P. Foster, D.A. Stone, A Battery Energy Management Strategy for U.K. Enhanced Frequency Response and Triad Avoidance, IEEE Trans. Ind. Electron. 65 (2018) 9509–9517. https://doi.org/10.1109/TIE.2018.2818642.

[111] Industrial Lithium-ion Battery SCiB^{TM} Industrial Pack series | TOSHIBA Rechargeable battery SCiB^{TM}, (n.d.). https://www.scib.jp/en/product/sip/index.htm#sipspec (accessed December 9, 2020).

[112] K.S. Hariharan, V.S. Kumar, A nonlinear equivalent circuit model for lithium ion cells, J. Power Sources. 222 (2013) 210–217. https://doi.org/10.1016/j.jpowsour.2012.08.090.

[113] X. Hu, S. Li, H. Peng, A comparative study of equivalent circuit models for Li-ion batteries, J. Power Sources. 198 (2012) 359–367. https://doi.org/10.1016/j.jpowsour.2011.10.013.

[114] X. Lin, H.E. Perez, S. Mohan, J.B. Siegel, A.G. Stefanopoulou, Y. Ding, M.P. Castanier, A lumped-parameter electro-thermal model for cylindrical batteries, J. Power Sources. 257 (2014) 1–11. https://doi.org/https://doi.org/10.1016/j.jpowsour.2014.01.097.

[115] A. Hentunen, T. Lehmuspelto, J. Suomela, Time-Domain Parameter Extraction Method for Thévenin-Equivalent Circuit Battery Models, IEEE Trans. Energy Convers. 29 (2014) 558–566. https://doi.org/10.1109/TEC.2014.2318205.

[116] A. Stroe, D. Stroe, M. Swierczynski, R. Teodorescu, S.K. Kær, Lithium-ion battery dynamic model for wide range of operating conditions, in: 2017 Int. Conf. Optim. Electr. Electron. Equip. 2017 Intl Aegean Conf. Electr. Mach. Power Electron., 2017: pp. 660–666. https://doi.org/10.1109/OPTIM.2017.7975044.

[117] T. Hu, B. Zanchi, J. Zhao, Simple analytical method for determining parameters of discharging batteries, IEEE Trans. Energy Convers. 26 (2011) 787–798. https://doi.org/10.1109/TEC.2011.2129594.

[118] Y. Hu, S. Yurkovich, Y. Guezennec, B.J. Yurkovich, Electro-thermal battery model identification for automotive applications, J. Power Sources. 196 (2011) 449–457. https://doi.org/10.1016/j.jpowsour.2010.06.037.

[119] R. Zhang, B. Xia, B. Li, L. Cao, Y. Lai, W. Zheng, H. Wang, W. Wang, M. Wang, A study on the open circuit voltage and state of charge characterization of high capacity lithium-ion battery under different temperature, Energies. 11 (2018). https://doi.org/10.3390/en11092408.

[120] D. Rogers, D. Gladwin, D. Stone, D. Strickland, M. Foster, Willenhall Energy Storage System: Europe's largest research-led lithium titanate battery, Eng. Technol. Ref. 4 (2017) 1–6. https://doi.org/10.1049/etr.2016.0121.

[121] M.F.R. Zwicker, M. Moghadam, W. Zhang, C.V. Nielsen, Automotive battery pack manufacturing – a review of battery to tab joining, J. Adv. Join. Process. 1 (2020) 100017. https://doi.org/10.1016/j.jajp.2020.100017.

[122] L.T. Pillage, R.A. Rohrer, C. Visweswariah, Electronic circuit and system simulation methods, McGraw-Hill, 1995.

[123] L. Lu, X. Han, J. Li, J. Hua, M. Ouyang, A review on the key issues for lithium-ion battery management in electric vehicles, J. Power Sources. 226 (2013) 272–288. https://doi.org/10.1016/j.jpowsour.2012.10.060.

[124] X. Gong, R. Xiong, C.C. Mi, Study of the characteristics of battery packs in electric vehicles with parallel-connected lithium-ion battery cells, in: Conf. Proc. - IEEE Appl. Power Electron. Conf. Expo. - APEC, Institute of Electrical and Electronics Engineers Inc., 2014: pp. 3218–3224. https://doi.org/10.1109/APEC.2014.6803766.

[125] T.L. Fantham, D.T. Gladwin, Impact of cell balance on grid scale battery energy storage systems, in: Energy Reports, Elsevier Ltd, 2020: pp. 209–216. https://doi.org/10.1016/j.egyr.2020.03.026.

[126] D. Jean-Luc, Zfit - File Exchange - MATLAB Central, (2021). https://uk.mathworks.com/matlabcentral/fileexchange/19460-zfit (accessed January 28, 2021).

[127] M.J. Brand, M.H. Hofmann, M. Steinhardt, S.F. Schuster, A. Jossen, Current distribution within parallel-connected battery cells, J. Power Sources. 334 (2016) 202–212. https://doi.org/10.1016/j.jpowsour.2016.10.010.

[128] S. Paul, C. Diegelmann, H. Kabza, W. Tillmetz, Analysis of ageing inhomogeneities in lithium-ion battery systems, J. Power Sources. 239 (2013) 642–650. https://doi.org/10.1016/j.jpowsour.2013.01.068.

[129] S. Nejad, D.T. Gladwin, M.P. Foster, D.A. Stone, Parameterisation and online states estimation of high-energy lithium-titanate cells, in: IECON 2017 - 43rd Annu. Conf. IEEE Ind. Electron. Soc., 2017: pp. 7660–7665. https://doi.org/10.1109/IECON.2017.8217342.

[130] A. Barai, W.D. Widanage, J. Marco, A. Mcgordon, P. Jennings, A study of the open circuit voltage characterization technique and hysteresis assessment of lithium-ion cells, J. Power Sources. 295 (2015) 99–107. https://doi.org/10.1016/J.JPOWSOUR.2015.06.140.

[131] A.I. Stan, M. Swierczynski, D.I. Stroe, R. Teodorescu, S.J. Andreasen, K. Moth, A comparative study of lithium ion to lead acid batteries for use in UPS applications, INTELEC, Int. Telecommun. Energy Conf. 2014-January (2014). https://doi.org/10.1109/INTLEC.2014.6972152.

[132] A.I. Stroe, M. Swierczynski, D.I. Stroe, R. Teodorescu, Performance model for high-power lithium titanate oxide batteries based on extended characterization tests, 2015 IEEE Energy Convers. Congr. Expo. ECCE 2015. (2015) 6191–6198. https://doi.org/10.1109/ECCE.2015.7310528.

[133] M.A. Roscher, O. Bohlen, J. Vetter, OCV Hysteresis in Li-Ion Batteries including Two-Phase Transition Materials, Int. J. Electrochem. 2011 (2011) 1–6. https://doi.org/10.4061/2011/984320.

[134] M.A. Roscher, D.U. Sauer, Dynamic electric behavior and open-circuit-voltage

modeling of LiFePO4-based lithium ion secondary batteries, J. Power Sources. 196 (2011) 331–336. https://doi.org/https://doi.org/10.1016/j.jpowsour.2010.06.098.

[135] D. Carnevale, S. Nicosia, L. Zaccarian, A DIFFERENTIAL HYSTERESIS MODEL, IFAC Proc. Vol. 38 (2005) 301–306. https://doi.org/10.3182/20050703-6-CZ-1902.02165.

[136] J. Eichler, M. Novak, Modeling of lithium-ion battery charging and discharging using the preisach hysteresis model, Int. Conf. Electical Drives Power Electron. 2019-Septe (2019) 221–224. https://doi.org/10.1109/EDPE.2019.8883931.

[137] F. Baronti, N. Femia, R. Saletti, C. Visone, W. Zamboni, Preisach modelling of lithium-iron-phosphate battery hysteresis, J. Energy Storage. 4 (2015) 51–61. https://doi.org/10.1016/J.EST.2015.09.004.

[138] X. Tang, X. Zhang, B. Koch, D. Frisch, Modeling and estimation of Nickel Metal Hydride battery hysteresis for SOC estimation, in: 2008 Int. Conf. Progn. Heal. Manag., 2008: pp. 1–12. https://doi.org/10.1109/PHM.2008.4711432.

[139] P. Chayratsami, G.L. Plett, Hysteresis Modeling of Lithium-Silicon Half Cells Using Discrete Preisach Model, in: 2018 8th IEEE Int. Conf. Control Syst. Comput. Eng., 2018: pp. 31–36. https://doi.org/10.1109/ICCSCE.2018.8685026.

[140] I. Mayergoyz, Mathematical models of hysteresis, IEEE Trans. Magn. 22 (1986) 603–608. https://doi.org/10.1109/TMAG.1986.1064347.

[141] X. Dong, C. Zhang, J. Jiang, Evaluation of SOC Estimation Method Based on EKF/AEKF under Noise Interference, Energy Procedia. 152 (2018) 520–525. https://doi.org/10.1016/J.EGYPRO.2018.09.204.

[142] A. Kavash, Estimation SOC for Li-Ion Batteries in EVs Using EKF, Int. J. Sci. Basic Appl. Res. 22 (2015) 225–234.

[143] R. van der Merwe, E. Wan, Gaussian mixture sigma-point particle filters for sequential probabilistic inference in dynamic state-space models, in: 2003 IEEE Int. Conf. Acoust. Speech, Signal Process. 2003. Proceedings. (ICASSP ’03)., 2003: pp. VI–701. https://doi.org/10.1109/ICASSP.2003.1201778.

[144] G.L. Plett, Sigma-point Kalman filtering for battery management systems of LiPB-based HEV battery packs: Part 1: Introduction and state estimation, J. Power Sources. 161 (2006) 1356–1368. https://doi.org/https://doi.org/10.1016/j.jpowsour.2006.06.003.

[145] G.L. Plett, Extended Kalman filtering for battery management systems of LiPB-based HEV battery packs: Part 1. Background, J. Power Sources. 134 (2004) 252–261. https://doi.org/10.1016/J.JPOWSOUR.2004.02.031.

[146] Z. Li, P. Zhang, Z. Wang, Q. Song, Y. Rong, State of Charge Estimation for Li-ion Battery Based on Extended Kalman Filter, Energy Procedia. 105 (2017) 3515–3520. https://doi.org/10.1016/J.EGYPRO.2017.03.806.

Appendix A:

Table A. 1. The cubic spline coefficients of different OCV-SoC models from different ECMs and datasets. OCV-SoC polynomial model on the SoC interval [S_1, S_2] is $V_{OC} = a(S - S_1)^3 + b(S - S_1)^2 + c(S - S_1) + d$.

ECM1 from day 1						ECM1 from day 2						ECM2 from day 2					
SoC interval		Coefficients				SoC interval		Coefficients				SoC interval		Coefficients			
S_1	S_2	a	b	c	d	S_1	S_2	a	b	c	d	S_1	S_2	a	b	c	d
8.029	13.265	-0.0001	-0.0089	1.0426	557.1	5.447	6.264	-0.0024	0.0095	1.0954	553.9	5.447	6.264	-0.0045	0.0324	1.0324	553.937
13.265	18.474	-0.0001	-0.0105	0.9408	562.3	6.264	9.753	-0.0024	0.0036	1.1061	554.8	6.264	9.753	-0.0045	0.0213	1.0763	554.800
18.474	23.603	0.0008	-0.0122	0.8225	566.9	9.753	15.207	0.0010	-0.0218	1.0426	558.6	9.753	15.207	0.0013	-0.0261	1.0595	558.622
23.603	28.732	0.0002	-0.0006	0.7570	570.9	15.207	20.583	-0.0003	-0.0055	0.8939	563.8	15.207	20.583	-0.0004	-0.0045	0.8926	563.838
28.732	33.756	0.0004	0.0031	0.7699	574.8	20.583	25.900	0.0006	-0.0104	0.8084	568.4	20.583	25.900	0.0007	-0.0109	0.8101	568.446
33.756	38.764	0.0007	0.0095	0.8333	578.8	25.900	31.141	0.0004	-0.0002	0.7520	572.5	25.900	31.141	0.0006	-0.0005	0.7498	572.544
38.764	43.753	0.0008	0.0201	0.9815	583.3	31.141	36.337	0.0002	0.0067	0.7865	576.5	31.141	36.337	0.0000	0.0085	0.7921	576.543
43.753	48.666	0.0000	0.0325	1.2437	588.8	36.337	41.555	0.0011	0.0102	0.8747	580.8	36.337	41.555	0.0013	0.0082	0.8791	580.886
48.666	53.568	-0.0006	0.0332	1.5663	595.7	41.555	46.750	0.0006	0.0276	1.0719	585.8	41.555	46.750	0.0006	0.0283	1.0696	585.879
53.568	58.351	-0.0089	0.0238	1.8457	604.1	46.750	51.846	0.0012	0.0373	1.4088	592.2	46.750	51.846	0.0012	0.0379	1.4136	592.286
58.351	63.132	0.0020	-0.1038	1.4633	612.5	51.846	56.827	-0.0071	0.0549	1.8787	600.5	51.846	56.827	-0.0077	0.0570	1.8974	600.640
63.132	67.874	0.0156	-0.0752	0.6078	617.3	56.827	61.782	-0.0086	-0.0519	1.8940	610.3	56.827	61.782	-0.0083	-0.0574	1.8955	610.559
67.874	72.566	-0.0096	0.1471	0.9489	620.2	61.782	66.750	0.0215	-0.180	0.7451	617.4	61.782	66.750	0.0218	-0.1807	0.7157	617.533
72.566	77.210	0.0016	0.0121	1.6959	626.9	66.750	71.638	-0.0057	0.1410	0.5514	619.3	66.750	71.638	-0.0059	0.1448	0.5373	619.306
77.210	81.753	-0.0001	0.0347	1.9135	635.2	71.638	76.434	-0.0030	0.0577	1.5223	624.7	71.638	76.434	-0.0032	0.0583	1.5301	624.703
81.753	86.219	-0.0032	0.0333	2.2225	644.6	76.434	81.228	0.0017	0.0150	1.8706	633.0	76.434	81.228	0.0019	0.0130	1.8719	633.035
86.219	90.649	0.0069	-0.0102	2.3253	654.9	81.228	85.945	-0.0032	0.0395	2.1319	642.5	81.228	85.945	-0.0033	0.0403	2.1273	642.516
90.649	95.000	0.0069	0.0814	2.6407	665.6	85.945	90.620	0.0050	-0.0057	2.2913	653.1	85.945	90.620	0.0050	-0.0058	2.2902	653.106
-	-	-	-	-	-	90.620	95.200	0.0050	0.0648	2.5673	664.2	90.620	95.200	0.0050	0.0649	2.5664	664.201

Appendix B:

This appendix provides the EIS and ECM curve fitting results of four LTO cells at different SoC. Each figure shows the results at a different SoC. In each figure, subfigure (a) shows the complete EIS result of four cells. Subfigure (b) shows the partial EIS result (Z_{im}>0). Subfigure (c) – (f) are the ECM curve fitting results for cell 02 – 05.

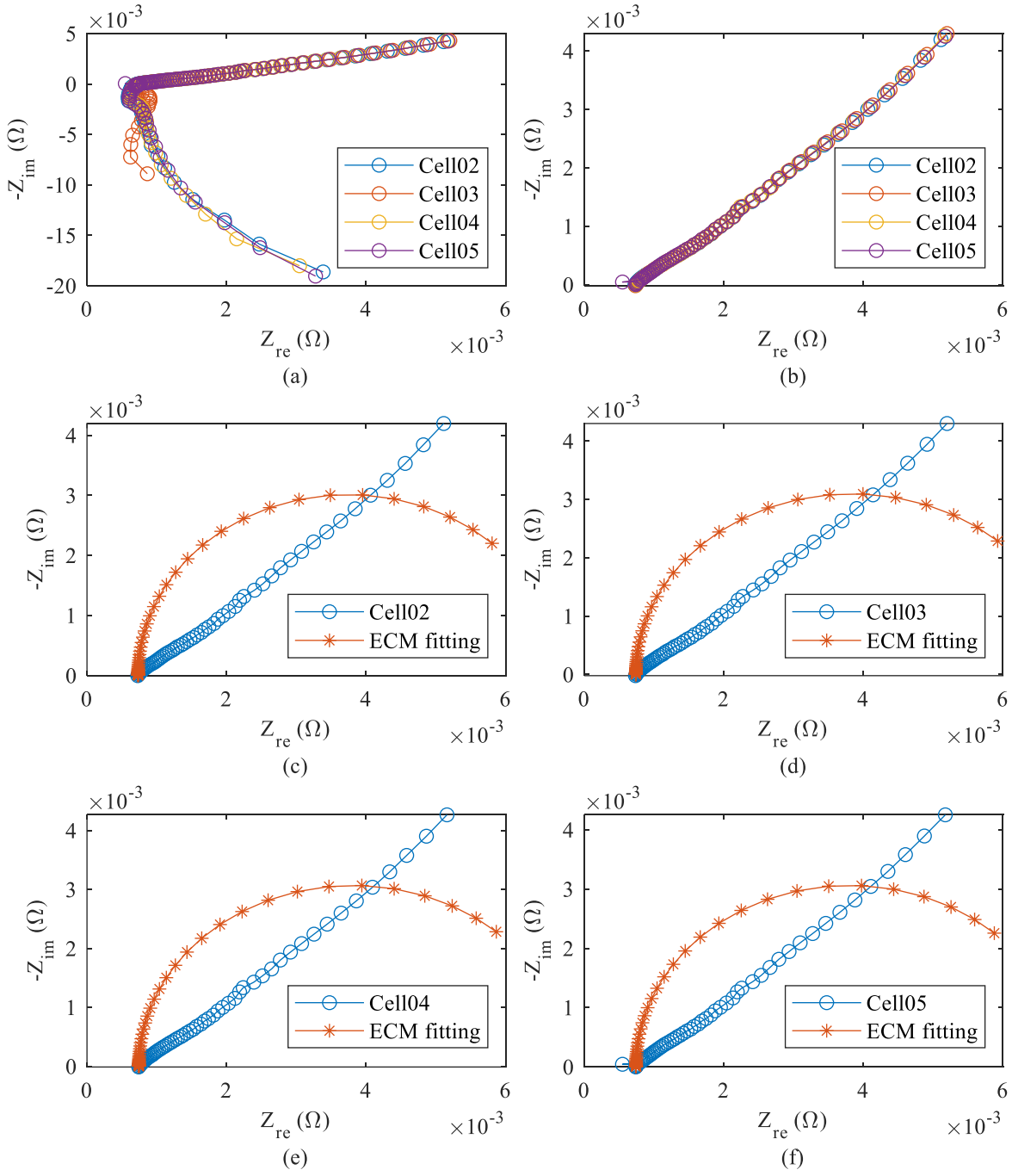

Figure B. 1 EIS and ECM fitting result of 4 LTO cells at 0% SoC: (a) overall result, (b) result when Z_{im} < 0, (c) – (f) ECM fitting result from Cell02 to Cell05

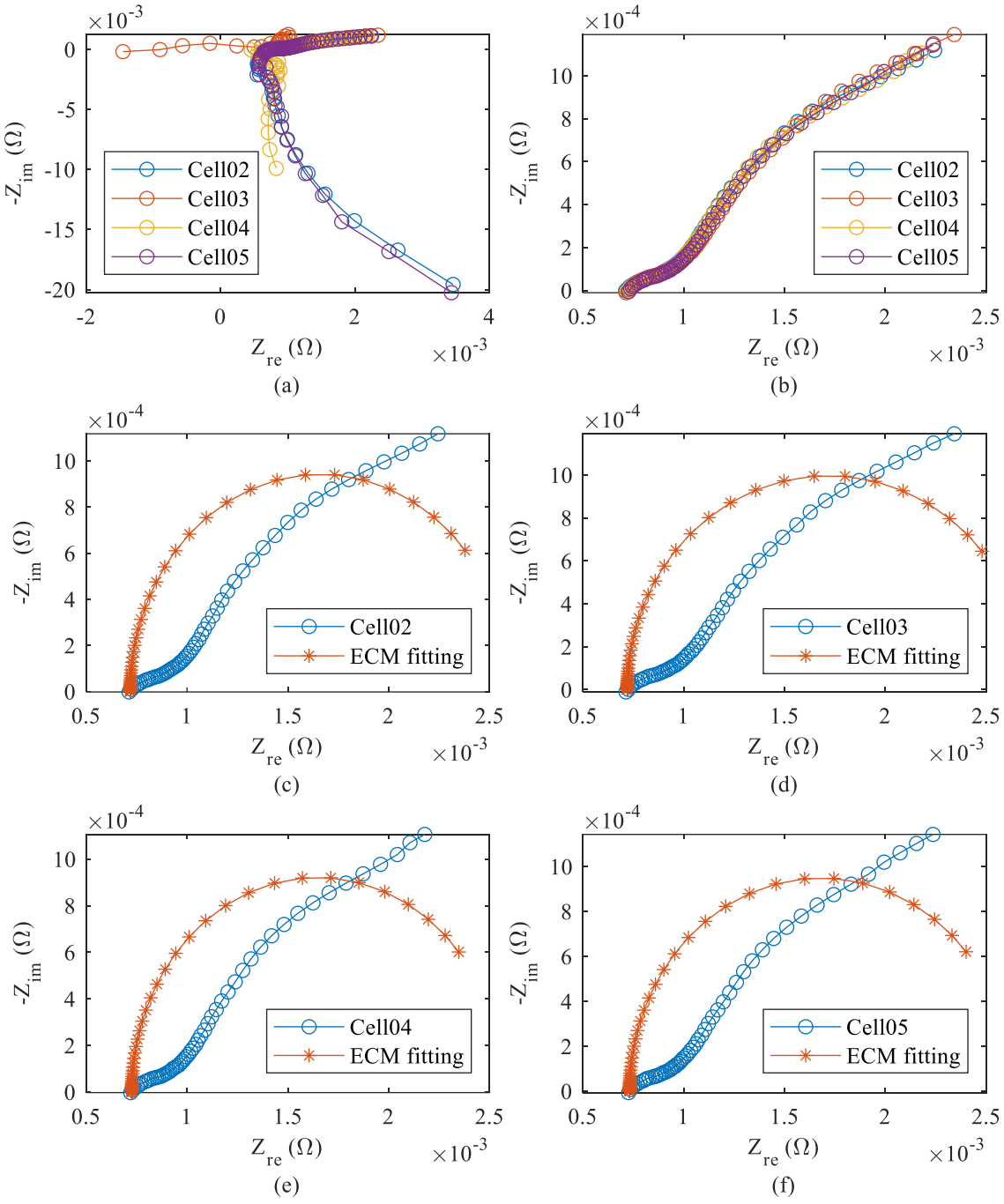

Figure B. 2 EIS and ECM fitting result of 4 LTO cells at 10% SoC: (a) overall result, (b) result when Zim < 0, (c) – (f) ECM fitting result from Cell02 to Cell05

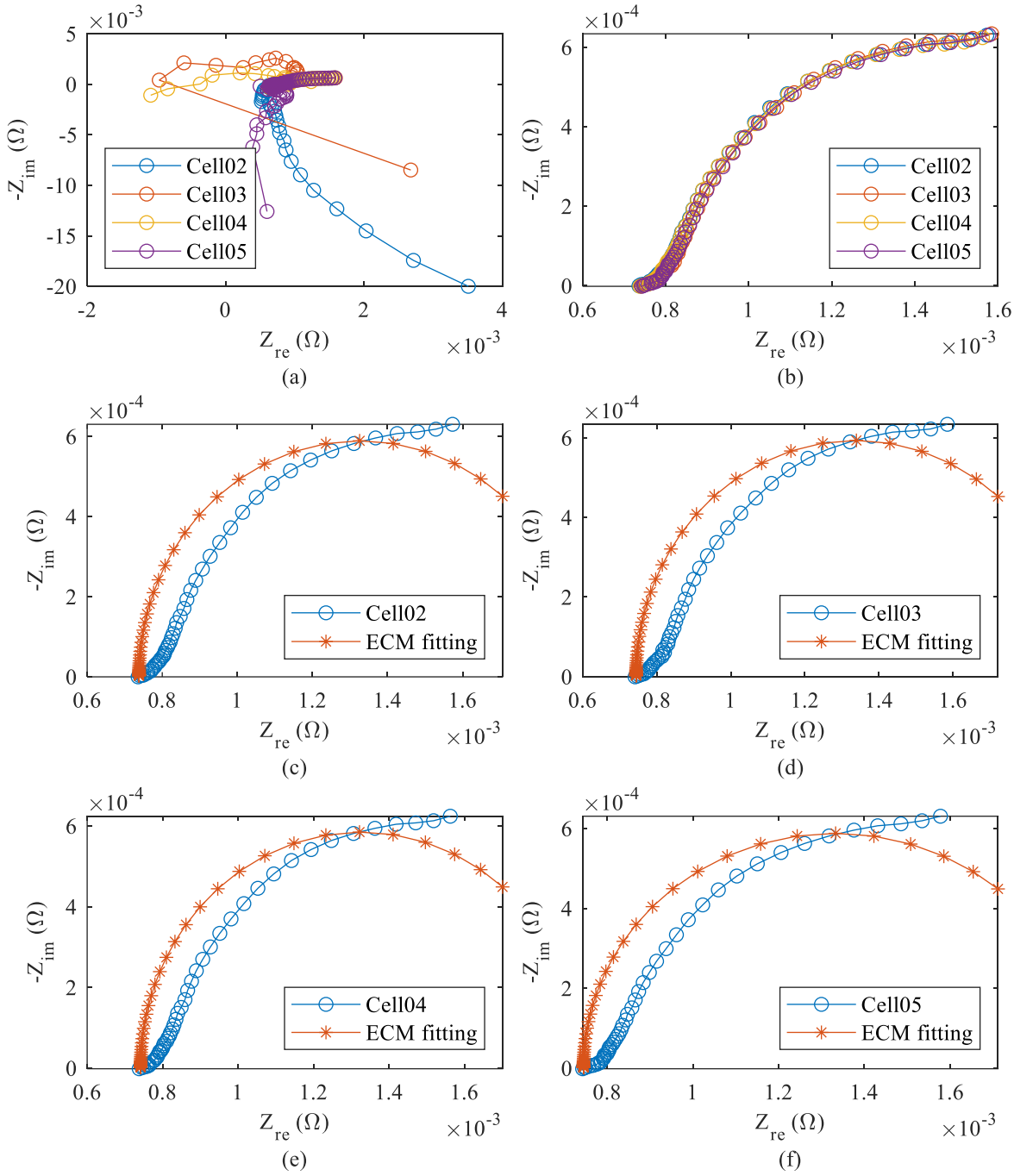

Figure B. 3 EIS and ECM fitting result of 4 LTO cells at 20% SoC: (a) overall result, (b) result when Zim < 0, (c) – (f) ECM fitting result from Cell02 to Cell05

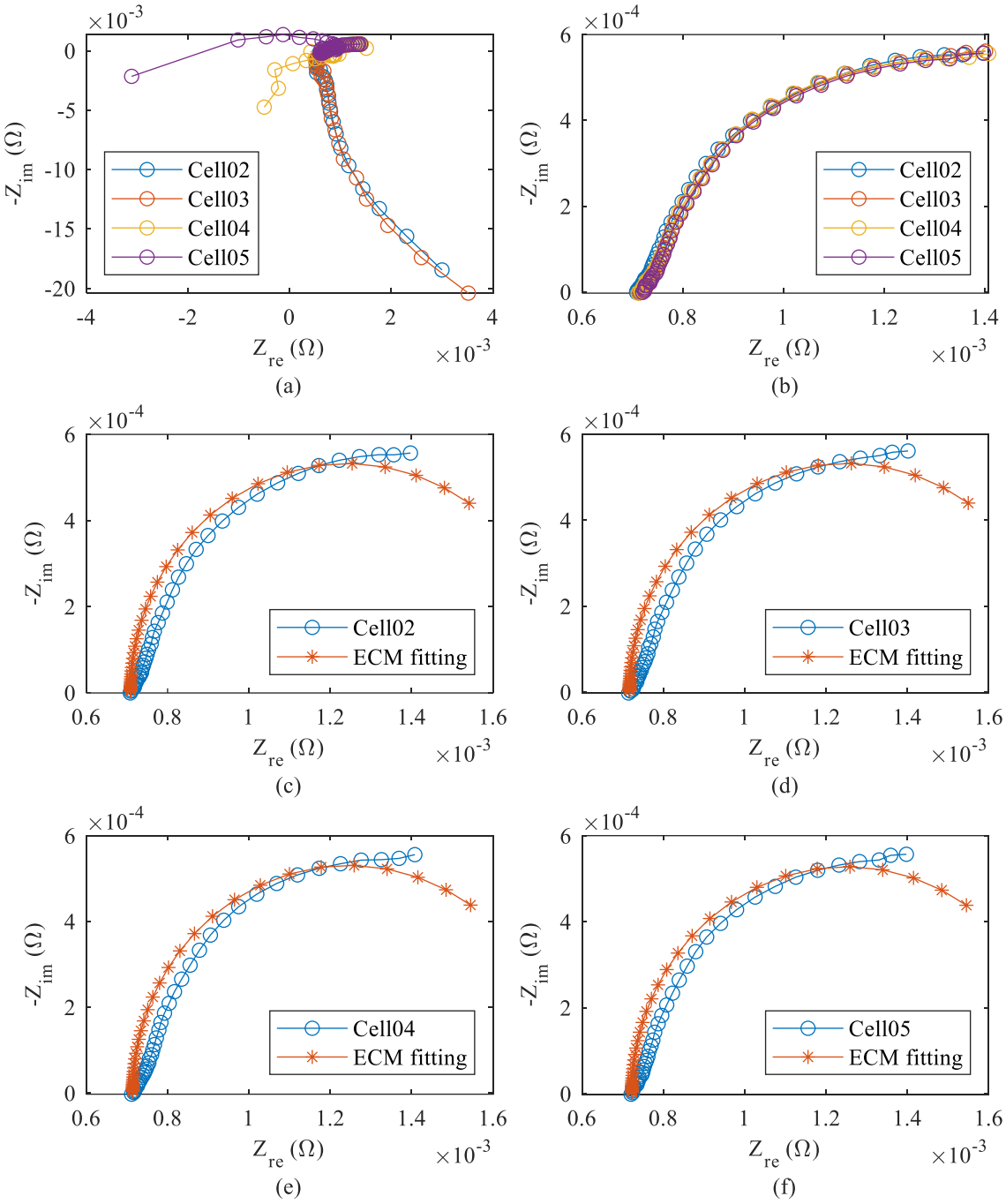

Figure B. 4 EIS and ECM fitting result of 4 LTO cells at 30% SoC: (a) overall result, (b) result when Zim < 0, (c) – (f) ECM fitting result from Cell02 to Cell05

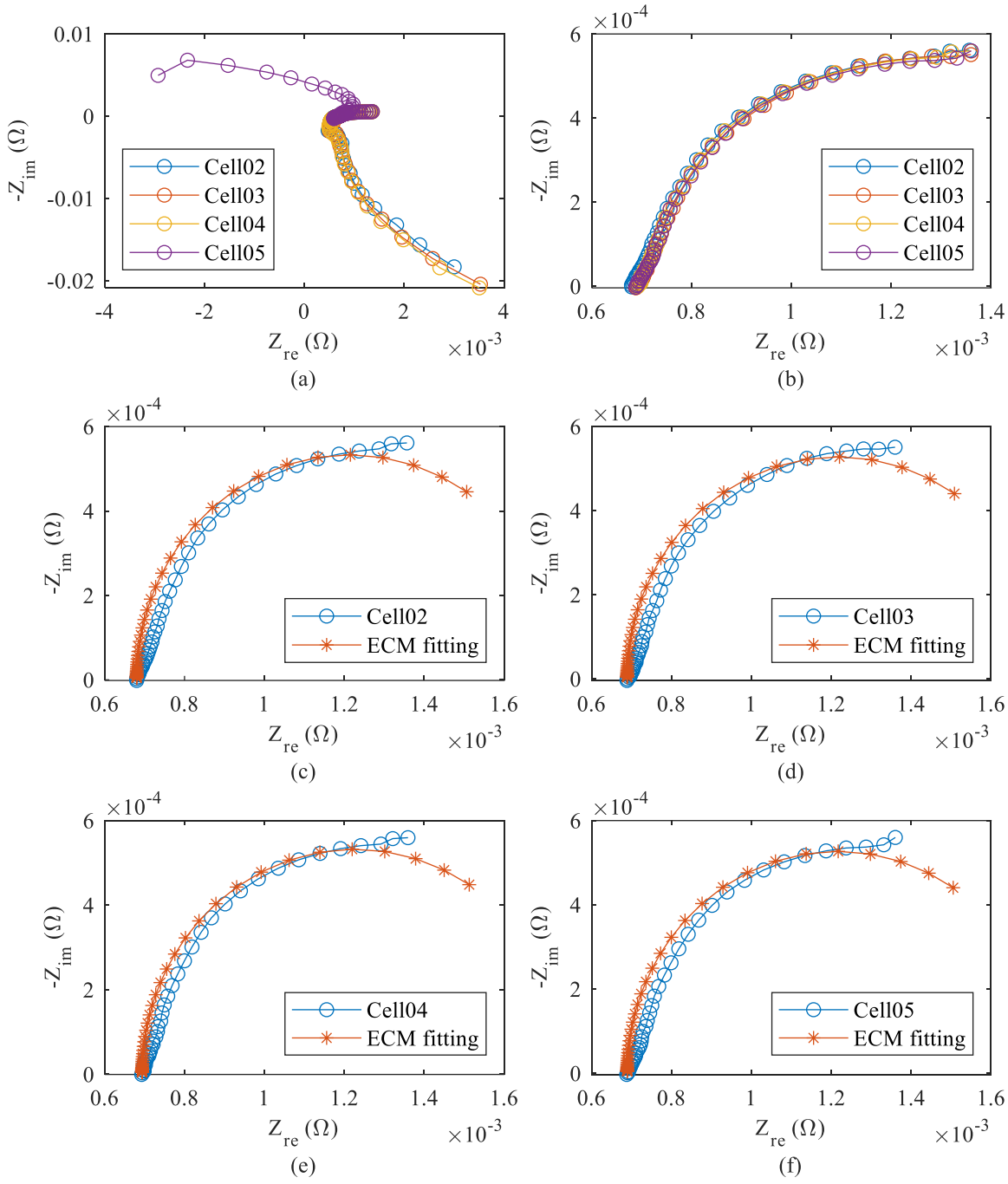

Figure B. 5 EIS and ECM fitting result of 4 LTO cells at 40% SoC: (a) overall result, (b) result when Zim < 0, (c) – (f) ECM fitting result from Cell02 to Cell05

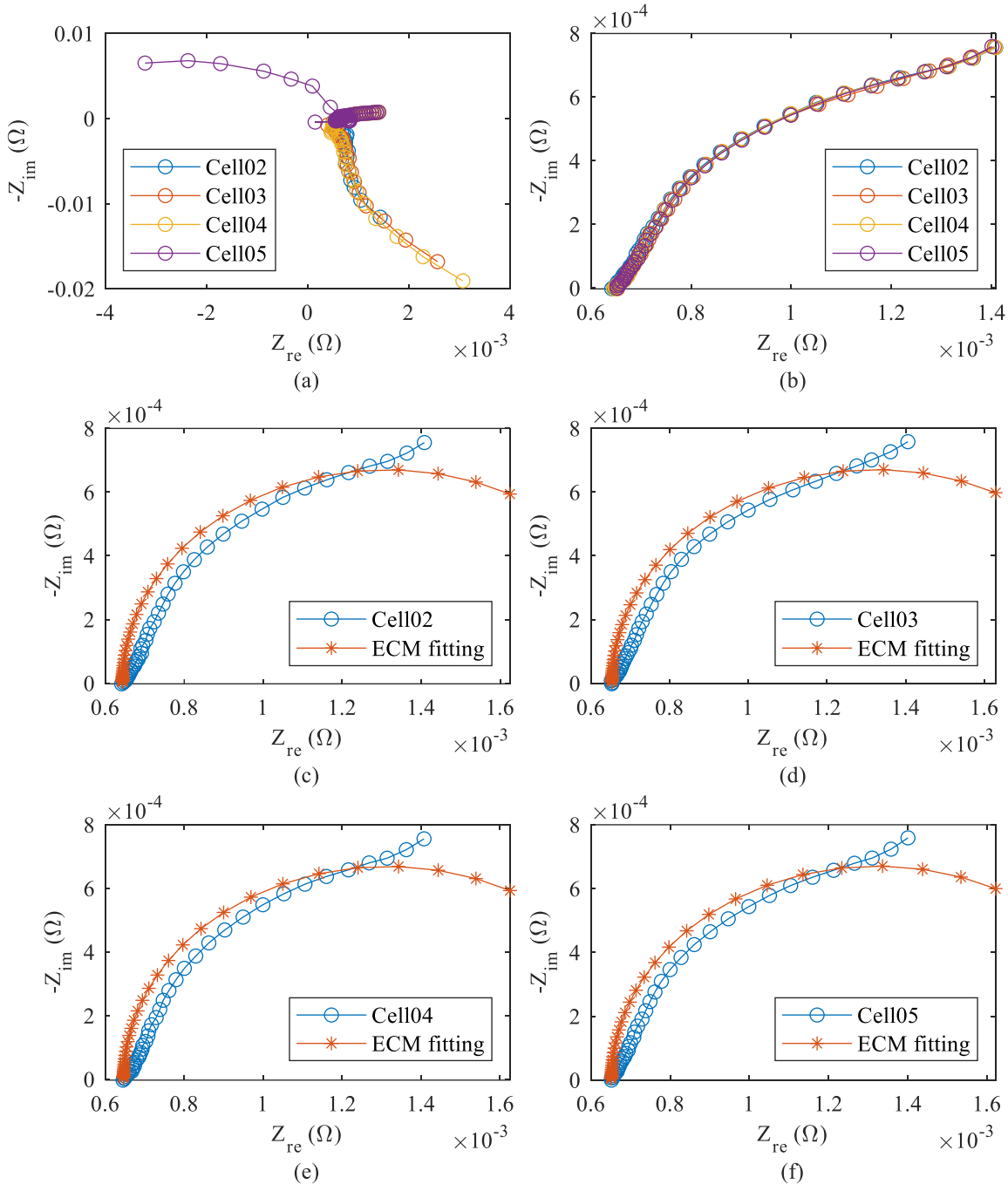

Figure B. 6 EIS and ECM fitting result of 4 LTO cells at 60% SoC: (a) overall result, (b) result when Zim < 0, (c) – (f) ECM fitting result from Cell02 to Cell05

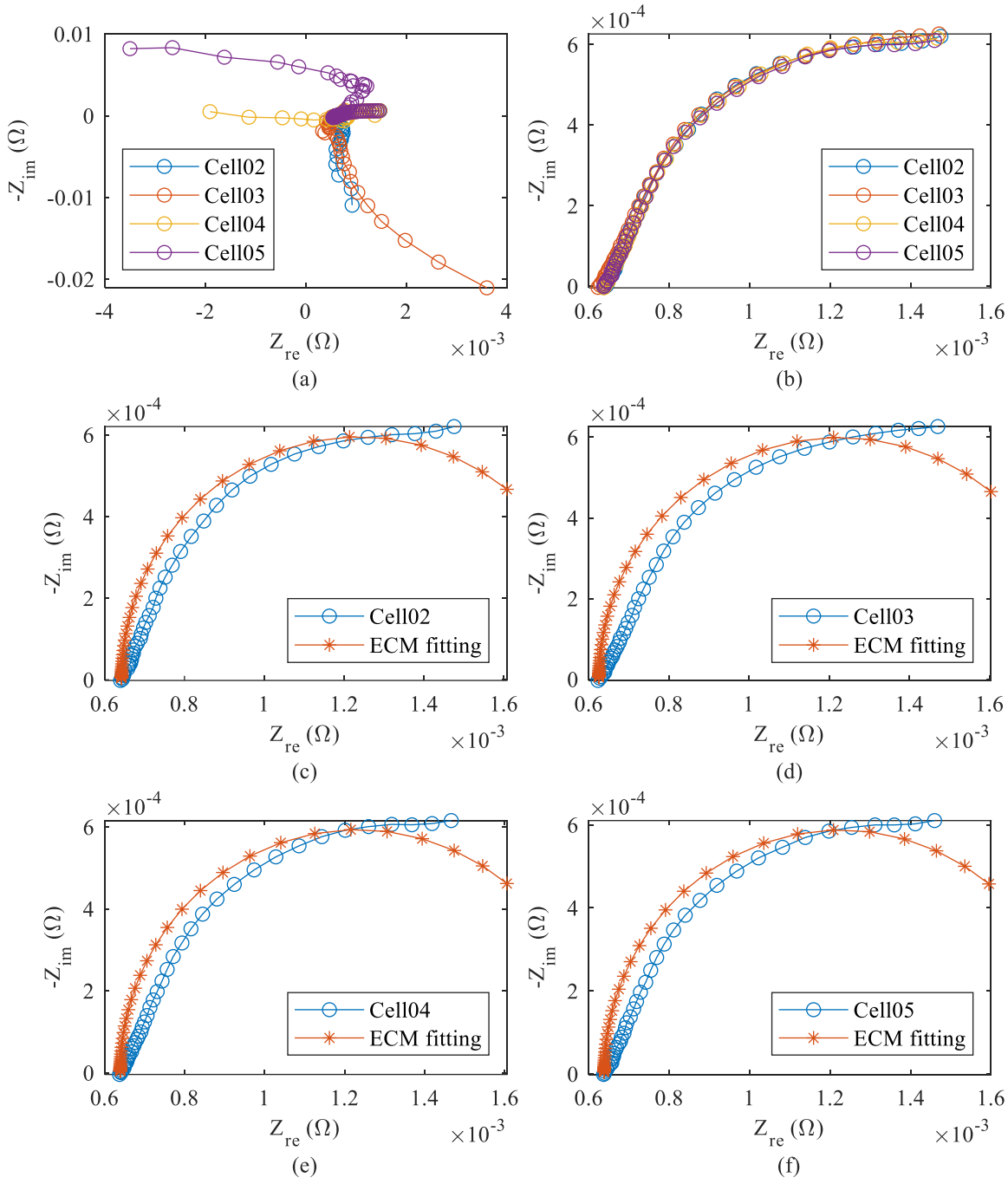

Figure B. 7 EIS and ECM fitting result of 4 LTO cells at 70% SoC: (a) overall result, (b) result when Zim < 0, (c) – (f) ECM fitting result from Cell02 to Cell05

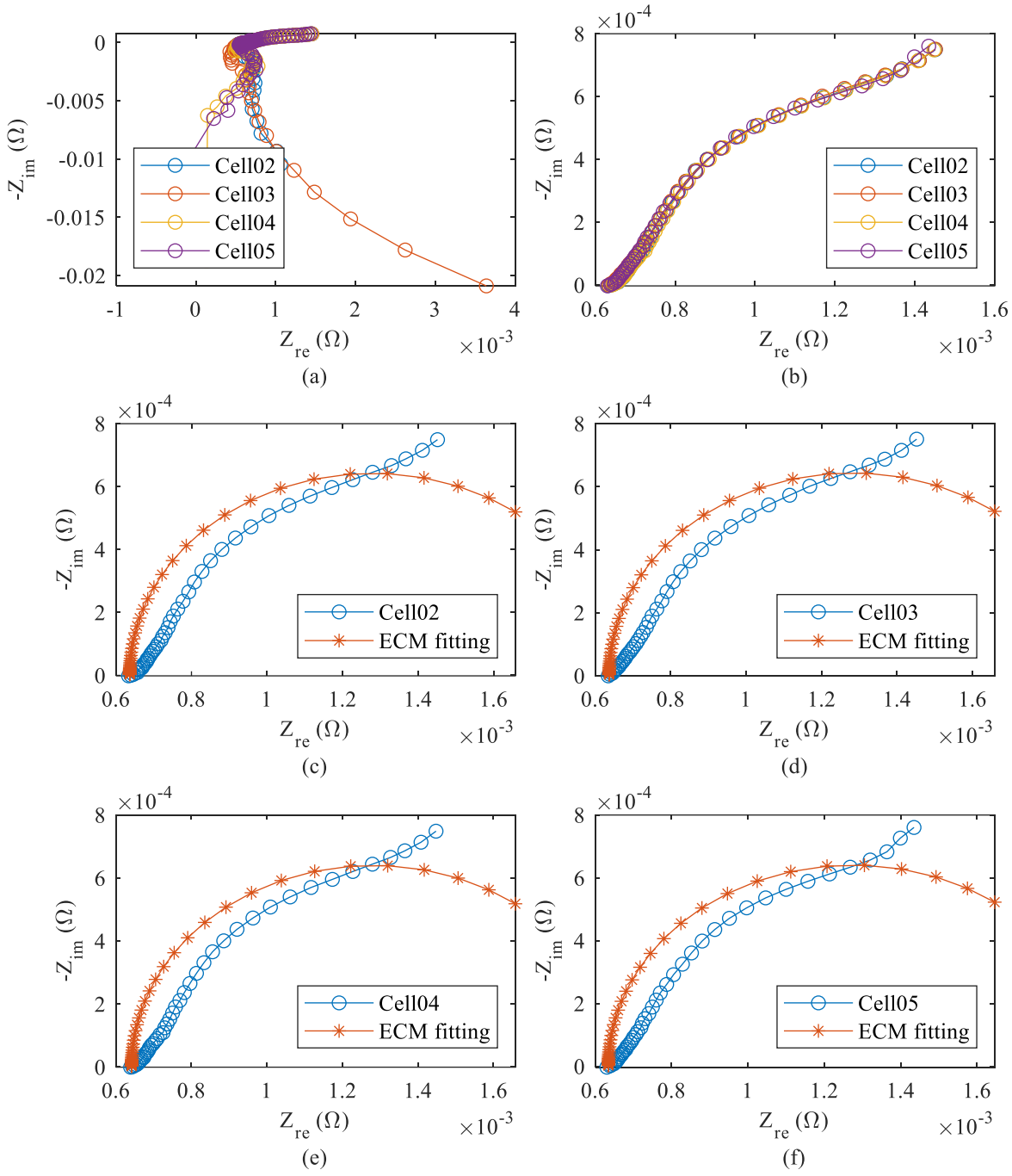

Figure B. 8 EIS and ECM fitting result of 4 LTO cells at 80% SoC: (a) overall result, (b) result when Zim < 0, (c) – (f) ECM fitting result from Cell02 to Cell05

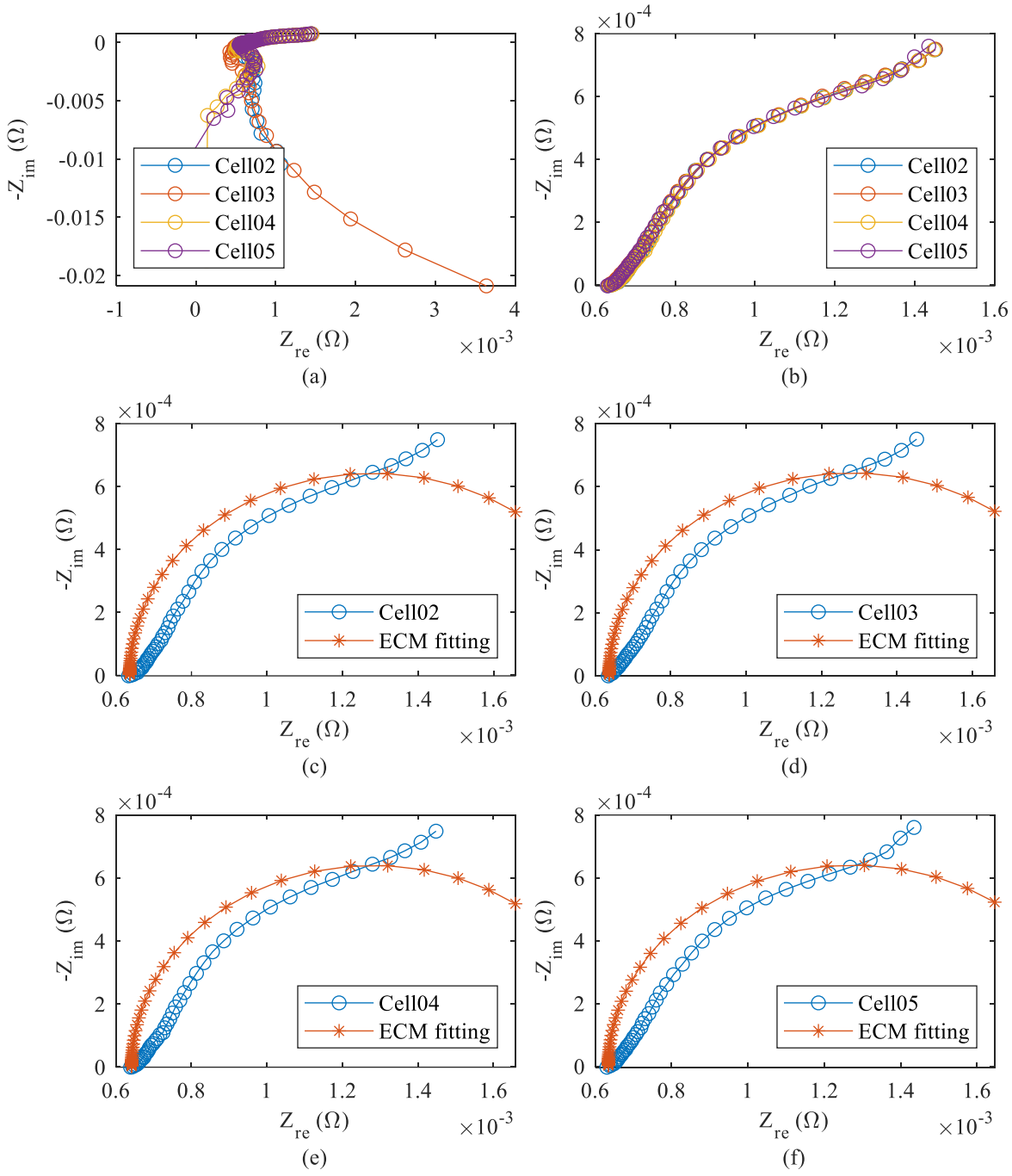

Figure B. 9 EIS and ECM fitting result of 4 LTO cells at 90% SoC: (a) overall result, (b) result when Zim < 0, (c) – (f) ECM fitting result from Cell02 to Cell05

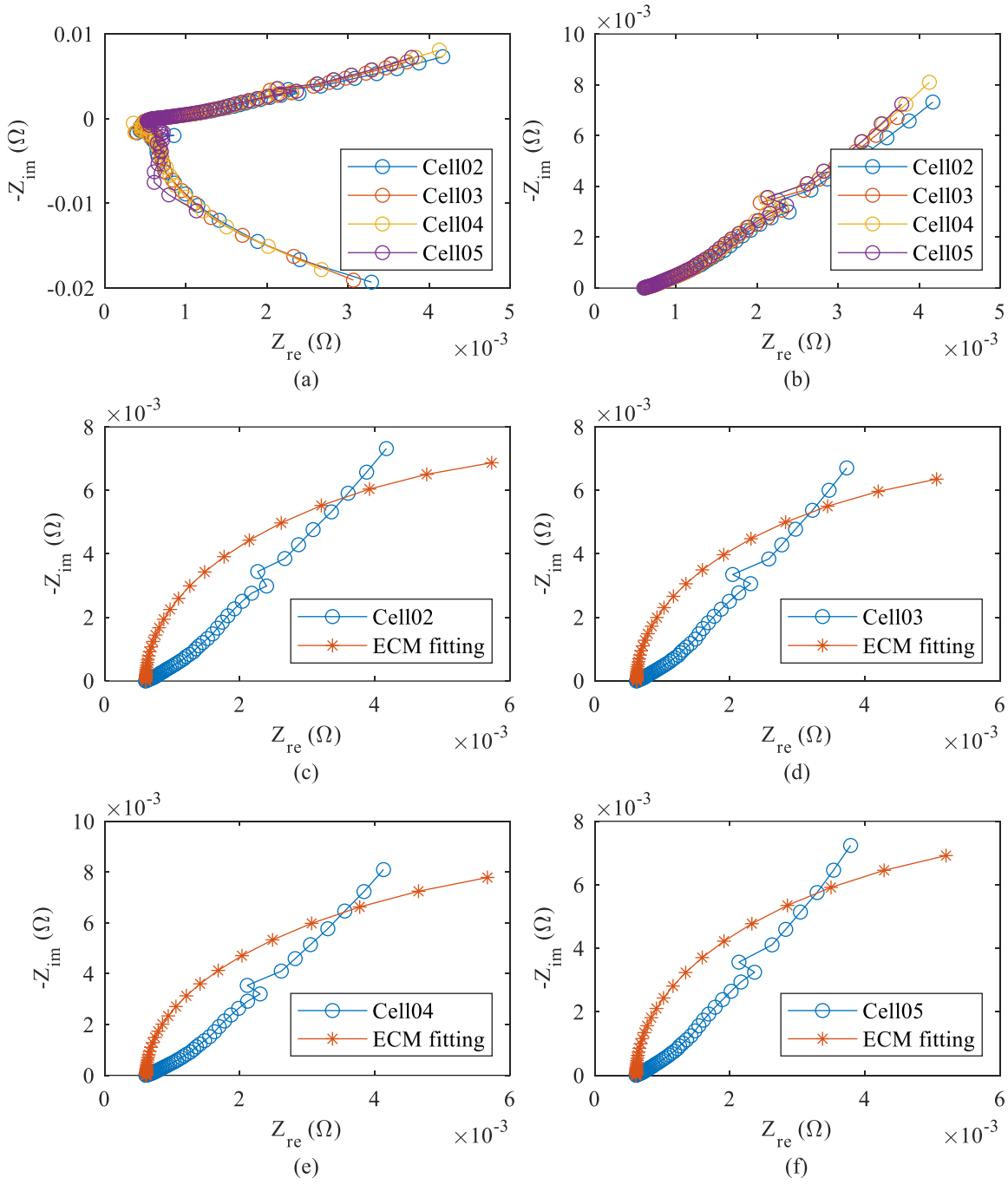

Figure B. 10 EIS and ECM fitting result of 4 LTO cells at 100% SoC: (a) overall result, (b) result when Zim < 0, (c) – (f) ECM fitting result from Cell02 to Cell05